UNIVERSITÄT HAMBURG
DEPARTMENT PHYSIK

Tests of the Electroweak Standard Model and Measurement of the Weak Mixing Angle with the ATLAS Detector

Dissertation
zur Erlangung des Doktorgrades
des Department Physik
der Universität Hamburg

vorgelegt von
Diplom-Physiker Martin Goebel
aus Dannenberg (Elbe)

Hamburg
2011

Gutachter der Dissertation:	Prof. Dr. Johannes Haller Prof. Dr. Joachim Mnich Prof. Dr. Stefan Söldner-Rembold
Gutachter der Disputation:	Prof. Dr. Johannes Haller Prof. Dr. Peter Schleper
Datum der Disputation:	19. September 2011
Vorsitzender des Prüfungsausschusses:	Dr. Georg Steinbrück
Vorsitzender des Promotionsausschusses:	Prof. Dr. Peter Hauschildt
Leiterin des Departments Physik:	Prof. Dr. Daniela Pfannkuche
Dekan der MIN-Fakultät:	Prof. Dr. Heinrich Graener

Abstract

In this thesis the global Standard Model (SM) fit to the electroweak precision observables is revisited with respect to newest experimental results. Various consistency checks are performed showing no significant deviation from the SM. The Higgs boson mass is estimated by the electroweak fit to be $M_H = 94\,^{+30}_{-24}$ GeV without any information from direct Higgs searches at LEP, Tevatron, and the LHC and the result is $M_H = 125\,^{+8}_{-10}$ GeV when including the direct Higgs mass constraints. The strong coupling constant is extracted at fourth perturbative order as $\alpha_s(M_Z^2) = 0.1194 \pm 0.0028\,(\text{exp}) \pm 0.0001\,(\text{theo})$. From the fit including the direct Higgs constraints the effective weak mixing angle is determined indirectly to be $\sin^2\theta^\ell_{\text{eff}} = 0.23147\,^{+0.00012}_{-0.00010}$. For the W mass the value of $M_W = 80.360\,^{+0.012}_{-0.011}$ GeV is obtained indirectly from the fit including the direct Higgs constraints.

The electroweak precision data is also exploited to constrain new physics models by using the concept of oblique parameters. In this thesis the following models are investigated: models with a sequential fourth fermion generation, the inert-Higgs doublet model, the littlest Higgs model with T-parity conservation, and models with large extra dimensions. In contrast to the SM, in these models heavy Higgs bosons are in agreement with the electroweak precision data.

The forward-backward asymmetry as a function of the invariant mass is measured for $pp \to Z/\gamma^* \to e^+e^-$ events collected with the ATLAS detector at the LHC. The data taken in 2010 at a center-of-mass energy of $\sqrt{s} = 7$ TeV corresponding to an integrated luminosity of 37.4 pb^{-1} is analyzed. The measured forward-backward asymmetry is in agreement with the SM expectation. From the measured forward-backward asymmetry the effective weak mixing angle is extracted as $\sin^2\theta^\ell_{\text{eff}} = 0.2204 \pm 0.0071\,(\text{stat})\,^{+0.0039}_{-0.0044}\,(\text{syst})$. The impact of unparticles and large extra dimensions on the forward-backward asymmetry at large momentum transfers is studied at generator level.

Zusammenfassung

In dieser Arbeit wird der globale Standard Modell (SM) Fit an die elektroschwachen Präzisionsdaten im Hinblick auf neueste experimentelle Ergebnisse erneut betrachtet. Die durchgeführten Konsistenztests zeigen keine signifikanten Abweichungen zur SM Vorhersage. Die Masse des Higgs Bosons wird durch den elektroschwachen Fit ohne Berücksichtigung der direkten Higgs Suchen bei LEP, Tevatron, und am LHC zu $M_H = 94\,^{+30}_{-24}$ GeV bestimmt, bzw. zu $M_H = 125\,^{+8}_{-10}$ GeV wenn die direkten Higgs Suchen mit einbezogen werden. Das Fit-Resultat für den Wert der starken Kopplungskonstante lautet $\alpha_s(M_Z^2) = 0.1194 \pm 0.0028\,(\text{exp}) \pm 0.0001\,(\text{theo})$. Der effektive schwache Mischungswinkel wird indirekt aus dem Fit mit den Informationen der direkten Higgs Suchen zu $\sin^2\theta^\ell_{\text{eff}} = 0.23147\,^{+0.00012}_{-0.00010}$ bestimmt. Für die Masse des W Bosons wird ein Wert von $M_W = 80.360\,^{+0.012}_{-0.011}$ GeV indirekt aus dem Fit mit den direkten Higgs Suchen ermittelt.

Die elektroschwachen Präzisionsdaten lassen sich darüber hinaus nutzen um neue Physik Modelle mit Hilfe des Konzepts der *oblique* Parameter einzuschränken. Folgende Modelle werden in dieser Arbeit untersucht: Modelle mit einer sequentiellen vierten Generation, das inert-Higgs Duplett Modell, das *littlest Higgs* Modell mit T-Parität Erhaltung, und Modelle mit großen extra Dimensionen. Im Gegensatz zum SM ist in diesen neuen Physik Modellen, die Existenz von schwere Higgs Bosonen mit den elektroschwachen Präzisionsdaten verträglich.

Desweiteren wird die Vorwärts-Rückwärts-Asymmetrie von $pp \to Z/\gamma^* \to e^+e^-$ Ereignissen, aufgezeichnet mit dem ATLAS Detektor am LHC, als Funktion der invarianten Masse bestimmt. Dazu werden die bei einer Schwerpunktsenergie von $\sqrt{s} = 7$ TeV im Jahre 2010 gesammelten Daten, die einer integrierten Luminosität von 37.4 pb^{-1} entsprechen, analysiert. Die gemessene Vorwärts-Rückwärts-Asymmetrie ist im Einklang mit der SM Vorhersage. Aus der gemessenen Vorwärts-Rückwärts-Asymmetrie wird der effektive schwache Mischungswinkel zu $\sin^2\theta^\ell_{\text{eff}} = 0.2204 \pm 0.0071\,(\text{stat})\,^{+0.0039}_{-0.0044}\,(\text{syst})$ bestimmt. Der Einfluss von *unparticles* und großen zusätzlichen Raum-Dimensionen auf die Vorwärts-Rückwärts-Asymmetrie bei hohen invarianten Massen wird auf Generator Niveau studiert.

Contents

CHAPTER 1

Introduction

The Standard Model (SM) of particle physics, describing the elementary particles and their interaction between each other, has been successfully tested at various collider experiments. Only the Higgs mechanism and its associated Higgs boson could not be confirmed so far. Nevertheless, intrinsic theoretical problems of the SM and cosmological measurements might point to the existence of physics beyond the SM.

The precision data measured at LEP, SLD, and Tevatron exhibits the most accurate test of the electroweak part of the SM. By comparing the measured observables to their theoretical prediction, taking into account radiative quantum loop corrections, unknown SM parameters (*e.g.* the mass of the Higgs boson) can be determined. In addition to the precision observables, the direct information from Higgs boson searches at LEP, Tevatron, and recently at the LHC constrain further the electroweak fit results. Additionally to the estimation of the Higgs mass, it is possible to determine indirectly the precision observables themselves, *e.g.* the W mass, the top mass, and the effective weak mixing angle. Together with the goodness-of-fit, the comparison of the indirect and direct determinations of the precision observables provides a proper test of the SM. In this thesis, the Gfitter software framework [1] is used to perform electroweak fits to the precision observables.[1]

The constraints from the electroweak precision observables allow also to estimate parameters of physics models beyond the SM. If the effect of the new particles appears only through vacuum polarization and the other corrections (*e.g.* vertex diagrams) are suppressed, the new physics contributions can be described by the oblique parameters. In this thesis the well-established S, T, U parameter set [3, 4] is used. The analysis, presented in this thesis, revisits several beyond SM theories: models with a sequential fourth fermion generation, the inert-Higgs doublet model, the littlest Higgs model with T-parity conservation, and models with large extra dimensions. Allowed regions in the new parameter space of these models can be determined by using the constraints from the electroweak precision data. In contrast to the SM, heavy Higgs bosons can often be realized in these SM extensions due to cancellations of Higgs and new physics corrections to the oblique parameters.

[1] The generic fitting framework Gfitter [1] is designed to provide a framework for model testing in high-energy physics. It is implemented in C++ and relies on ROOT [2] functionalities.

At CERN the Large Hadron Collider (LHC) is presently successfully under operation. It is mainly designed for the detection of the Higgs boson and for beyond SM searches. In addition, it is also possible to re-measure some of the electroweak precision observables, *e.g.* the top and W mass as well as the effective weak mixing angle. In this thesis a first measurement of the effective weak mixing angle with the ATLAS detector is performed with the data collected in 2010, corresponding to an integrated luminosity of 37.4 pb^{-1}. For this purpose the process $pp \to Z/\gamma^* \to e^+e^-$ is investigated. A forward-backward asymmetry of the produced leptons with respect to the incoming partons is predicted by the electroweak theory and depends directly on the value of the effective weak mixing angle. The shape of the forward-backward asymmetry can differ from the SM expectation when new physics models are assumed. A study of the impact from large extra dimensions and unparticles on the Drell–Yan spectrum as well as the forward-backward asymmetry is carried out using the Pythia8 [5] event generator.

This thesis is organized as follows:

Chapter 2: A brief theoretical overview of the SM is given. In addition the effective weak mixing angle is introduced and the di-electron production at the LHC is discussed.

Chapter 3: The results of the global electroweak fit are presented. Among them, the estimate of the Higgs mass and the indirect determinations of the W mass, the top mass, and the effective weak mixing angle.

Chapter 4: The concept of oblique parameters is introduced. Constraints from the electroweak precision observables on the S, T, U parameters and on the free parameter space of various new physics theories are presented.

Chapter 5: The components of the LHC and the ATLAS detector, in particular the ATLAS trigger system, are discussed. Additionally, luminosity determination, data quality, and Monte Carlo simulation are discussed being important ingredients for any physics analysis.

Chapter 6: The performance of electron triggers is studied with the data collected in 2010.

Chapter 7: The selection of electron positron pairs with the ATLAS detector is described. Several corrections are introduced for a proper comparison of data and simulated events. The estimate of the fraction of QCD background is discussed in detail. Several di-electron distributions are shown.

Chapter 8: The measurement of the forward-backward asymmetry and the extraction of the effective weak mixing angle are presented. Moreover, the measured forward-backward asymmetry is unfolded in order to obtain the real physical distribution. The impact on the forward-backward asymmetry of unparticles and large extra dimensions is discussed, as well.

Chapter 9: The values of the effective weak mixing angle determined from the electroweak fit and the forward-backward asymmetry of $pp \to Z/\gamma^* \to e^+e^-$ events are compared to various other determinations.

CHAPTER 2

Theoretical Background

This chapter starts with a brief theoretical overview of the Standard Model (SM) of particle physics. After presenting the fundamental constituents and their interactions, the electroweak theory and the Higgs mechanism are described in detail. The problems of the SM are discussed in the next section, which might point to physics beyond the SM. The effective Z couplings and the effective weak mixing angle are introduced by extending the tree level quantities by the electroweak form-factors containing the radiative loop corrections. Various determinations of the effective weak mixing angle are presented. Finally, the Drell–Yan process at the LHC is discussed. In particular, the forward-backward asymmetry between the incoming and outgoing fermion is introduced.

2.1 The Standard Model of Particle Physics

The SM of particle physics describes the interactions between the elementary particles, excluding gravity. The elementary particles are divided into leptons and quarks represented by fermion fields (spin 1/2). The mathematical description of the SM relies on the $SU(3)_C \otimes SU(2)_L \otimes U(1)_Y$ gauge group, where C denotes the color charge, L indicates that $SU(2)_L$ acts only on left-handed fermions, and Y stands for the electroweak hypercharge. The principal of local gauge invariance leads to the existence of gauge bosons: photon, $W^{\pm}$, Z, and gluons. In fig. 2.1 the fermions and the gauge bosons are depicted by black circles. The interactions among them are indicated by blue lines. Additionally, the Higgs boson is shown to be responsible for the generation of fermion and boson masses. The Higgs boson is the only particle of the SM which has not been observed yet.

The theory of the strong interaction is called Quantum Chromo Dynamics (QCD) represented by the non-abelian $SU(3)_C$ gauge group [7, 8]. The strong interaction is mediated via 8 massless gluons which have different combinations of color charges. Besides the gluons only quarks carry color charge and thus participate in the strong interaction. A characteristic of QCD is that for large momentum transfers the strong coupling (α_s) goes to zero and the quarks are quasi free particles (asymptotic freedom). At small energies, α_s is large and the quarks are glued together (confinement) in order to build colorless hadrons.

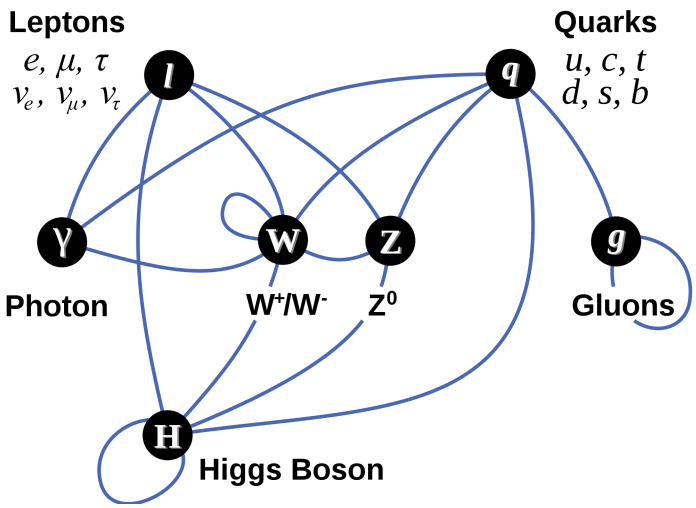

Figure 2.1: Elementary particles (black circles) and their interaction among each other (blue lines) [6]. The neutrinos do not couple to the photon.

The weak and electromagnetic interactions are mathematically described by the $SU(2)_L \otimes U(1)_Y$ symmetry group [9–11]. The $SU(2)_L$ symmetry couples to the third component of the weak isospin (I_3) of left handed fermions, while the $U(1)_Y$ acts on the hypercharge Y. The two quantities are connected via the Gell–Mann–Nishijima relation with the electric charge

$$Q = I_3 + Y/2\,. \tag{2.1}$$

The electroweak symmetry induces three $SU(2)_L$ and one $U(1)_Y$ gauge bosons. They are described by the massless fields $W_\mu^{1,2,3}$ and B_μ. The physical fields of the charged vector bosons $W_\mu^\pm$ are superpositions of the W_μ^1 and W_μ^2 fields

$$W_\mu^\pm \;=\; \frac{1}{\sqrt{2}}(W_\mu^1 \pm i W_\mu^2)\,, \tag{2.2}$$

while the photon field A_μ and the field of the neutral vector boson Z_μ are obtained by a rotation of the gauge fields B_μ and W_μ^3 with the weak mixing angle θ_W (often called Weinberg-angle)

$$\begin{pmatrix} Z_\mu \\ A_\mu \end{pmatrix} \;=\; \begin{pmatrix} \cos\theta_W & \sin\theta_W \\ -\sin\theta_W & \cos\theta_W \end{pmatrix} \begin{pmatrix} W_\mu^3 \\ B_\mu \end{pmatrix}. \tag{2.3}$$

In addition, the couplings of the electroweak theory are connected via the weak mixing angle

$$e = g' \cos\theta_W = g \sin\theta_W \tag{2.4}$$

where e is the elementary charge and the quantities g and g' represent the weak couplings. The electroweak theory requires in this from that the masses of the fermions as well as the bosons are zero, since mass terms are not invariant under $SU(2)_L \otimes U(1)_Y$ gauge transformations. However, this contradicts the experimental observation that all particles, except the photon and gluons, carry mass.

The simplest and most compelling solution to generate the physical masses without violating the properties of the electroweak theory is the introduction of the so-called Higgs mechanism [12–14]. A complex isospin doublet (Φ) with four degrees of freedom is introduced, called the Higgs field. The $SU(2)_L$ invariant potential of this Higgs field reads

$$V(\Phi^+\Phi) = \mu^2\Phi^+\Phi + \lambda(\Phi^+\Phi)^2\,. \tag{2.5}$$

In order to ensure that the potential goes to infinity when $|\Phi| \to \pm\infty$, the parameter λ needs to be positive. Choosing the parameter μ to be negative, the minimum of the potential is no longer at zero, instead it lies at

$$|\Phi_0| = \frac{\mu}{\sqrt{2}\lambda} = \frac{v}{\sqrt{2}}\,, \tag{2.6}$$

where $v/\sqrt{2}$ is the vacuum expectation value of the Higgs field. The $SU(2)_L$ symmetry of the Higgs potential leads to an infinite amount of non-trivial minima of the Higgs potential. By choosing a specific minimum as the vacuum ground state the symmetry is spontaneously broken. The Higgs field can then be expanded around the selected vacuum expectation value

$$\Phi(x) = e^{i\Theta_j(x)\frac{\sigma_j}{2}}\begin{pmatrix}0\\ [v+\phi(x)]/\sqrt{2}\end{pmatrix}. \tag{2.7}$$

The three degrees of freedom Θ_j ($j = 1, 2, 3$) lead to the so-called Goldstone bosons, which can be removed by a $SU(2)$ gauge transformation. The remaining degree of freedom ϕ results in a new spin 0 particle, the Higgs boson, analogous to the discrete excitation levels in quantum mechanics. The Higgs mechanism spontaneously breaks the $SU(2)_L \otimes U(1)_Y$ symmetry to the electromagnetic $U(1)_{\mathrm{EM}}$ at low energies. Hence, only the interactions of the particles with the photon are dominant at low energies.

When requiring local gauge invariance, the coupling between the Higgs field and the fields of the gauge bosons can be interpreted as mass terms. The masses of the gauge bosons are given in terms of the couplings and the vacuum expectation value

$$M_\gamma = 0, \qquad M_W = \frac{v}{2}g', \qquad M_Z = \frac{v}{2}\sqrt{(g'^2 + g^2)}\,. \tag{2.8}$$

The electroweak mixing angle can therefore be re-written as

$$\cos^2\theta_W = \frac{M_W^2}{M_Z^2}, \qquad \sin^2\theta_W = 1 - \frac{M_W^2}{M_Z^2}\,. \tag{2.9}$$

Additionally, a mass for the Higgs boson is generated

$$M_H = \sqrt{2\lambda}v \qquad \text{with} \qquad v = 246\ \text{GeV}\,. \tag{2.10}$$

The parameter λ or rather the mass of the Higgs boson is the only unknown quantity in the SM. Furthermore, the Higgs mechanism introduces mass terms for the fermions via Yukawa couplings of left and right-handed fermions to the Higgs boson. The fermion masses can be expressed by

$$m_f = \frac{v}{\sqrt{2}}\tilde{g}_f\,, \tag{2.11}$$

where $\tilde{g}_f$ are the couplings among the fermions and the Higgs boson. They are free parameters within the SM.

2.1.1 Problems of the Standard Model

The theoretical description of the SM could be confirmed by various experimental results. Only the observation of the Higgs boson is missing. However, in the SM there are some unsolved problems arising from theoretical and cosmological arguments pointing to possible extensions of the SM.

Gravity: In the SM there is no description of gravity. In particular, the unification of general relativity and quantum theory in a single theory can not be explained within the SM.

Unification: The unification of the electroweak and strong theory is not possible within the SM. In detail, the running of the weak, electromagnetic, and strong coupling does not intersect at a specific energy scale.[1]

Hierarchy Problem: The mass of the Higgs boson receives significant quantum corrections from SM particles, in particular from the top quark. These loop diagrams are usually calculated with respect to an ultraviolet cut-off scale. When choosing the Planck scale as cut-off, the Higgs mass would be much heavier than the expected value of approximately 100 GeV, unless there is an incredible fine-tuning between the radiative corrections. The cut-off scale is usually interpreted as the scale where new physics should appear.

Matter Anti-Matter Asymmetry: The CP[2] violation within the SM can not completely explain the matter anti-matter asymmetry in the universe.

Dark Matter and Dark Energy: There are several astrophysical observations indicating the existence of so-called dark matter and dark energy. By considering the cosmological Standard Model, it was found that the matter of the SM describes only around 5% of the content of the universe, while approximately 22% is composed of dark matter, and roughly 73% is made of dark energy [15]. Neutrinos are possible dark matter candidates within the SM, since they couple only weakly to the usual matter, but they cannot account for the entire relic density in the universe. For dark energy there is hardly no explanation also in new physics theories.

Throughout this thesis several new physics models are studied, which are able to solve at least some of the problems described above.

2.1.2 The Effective Weak Mixing Angle

The electroweak mixing angle at tree level is either expressed by the W and Z boson masses (*cf.* eq. (2.9)) or by the ratio of the vector and axial-vector couplings of the fermions

$$\frac{g^f_{V,\text{tree}}}{g^f_{A,\text{tree}}} = 1 - 4|Q_f| \sin^2 \theta_W \,, \tag{2.12}$$

[1] In grand unified theories (GUTs) the crossing point is usually around an energy of 10^{16} GeV.
[2] CP stands for charge and parity transformation.

where Q_f is the charge of the fermion and the couplings are defined by

$$g^f_{V,\text{tree}} = I^f_3 - 2Q_f \sin^2\theta_W \,, \tag{2.13}$$
$$g^f_{A,\text{tree}} = I^f_3 \,. \tag{2.14}$$

Contributions to the tree level notations arise from quantum loop diagrams, describing for example radiative corrections from the top quark and Higgs boson to the Z propagator. For practical use, these corrections are included into the so-called form-factors, ρ^f and κ^f. They depend mainly quadratically on the top mass and logarithmically on the Higgs mass. The effective weak mixing angle and the effective couplings read then

$$\sin^2\theta^f_{\text{eff}} = \kappa^f \sin^2\theta_W \,, \tag{2.15}$$
$$g^f_V = \sqrt{\rho^f}\left(I^f_3 - 2Q_f \sin^2\theta^f_{\text{eff}}\right) \,, \tag{2.16}$$
$$g^f_A = \sqrt{\rho^f} I^f_3 \,. \tag{2.17}$$

This results in

$$\frac{g^f_V}{g^f_A} = 1 - 4|Q_f| \sin^2\theta^f_{\text{eff}} \,. \tag{2.18}$$

The effective weak mixing angle depends on the flavor of fermions participating in the interaction and varies as a function of the momentum transfer. Usually, the value at the Z pole is quoted. The difference between the effective weak mixing angle of the leptons and the lightest quarks has been calculated by the authors of [16, 17] to be

$$\sin^2\theta^u_{\text{eff}} = \sin^2\theta^\ell_{\text{eff}} - 0.0001 \,, \tag{2.19}$$
$$\sin^2\theta^d_{\text{eff}} = \sin^2\theta^\ell_{\text{eff}} - 0.0002 \,. \tag{2.20}$$

Many measurements of the weak mixing angle at various energy scales Q^2 have been performed in the past. At low energies the value has been extracted from atomic parity violation ($Q^2 \approx 10^{-18}$ GeV^2) [19], from Møller scattering ($Q^2 \approx 0.03$ GeV^2) [20], from inelastic neutrino and anti-neutrino scattering on iron ($Q^2 \approx 4$ GeV^2) [21]. The CDF and D0 collaborations have extracted the effective weak mixing angle at the Z pole from the forward-backward asymmetry of the process $p\bar{p} \to Z/\gamma^* \to ee$. D0 has measured $\sin^2\theta^\ell_{\text{eff}} = 0.2309 \pm 0.0010$ by using an amount of data corresponding to 5 fb^{-1} [22]. The value from CDF is less precise due to less statistics (72 pb^{-1}), $\sin^2\theta^\ell_{\text{eff}} = 0.2338 \pm 0.0050$ [23]. In addition, the CMS collaboration has performed a first measurement by using di-muon events with an integrated luminosity of 40 pb^{-1}, $\sin^2\theta^\ell_{\text{eff}} = 0.2287 \pm 0.0085$ [24]. The LEP and SLD experiments have determined the effective weak mixing angle at the Z pole most precisely from asymmetry measurements [18]. The various values and the average, $\sin^2\theta^\ell_{\text{eff}} = 0.23153 \pm 0.00016$, are shown in fig. 2.2. The two most accurate measurements extracted from the b-quark forward-backward asymmetry at LEP ($\sin^2\theta^\ell_{\text{eff}} = 0.23221 \pm 0.00029$) and from the left-right asymmetry at SLD ($\sin^2\theta^\ell_{\text{eff}} = 0.23098 \pm 0.00026$) differ by about three standard deviations.

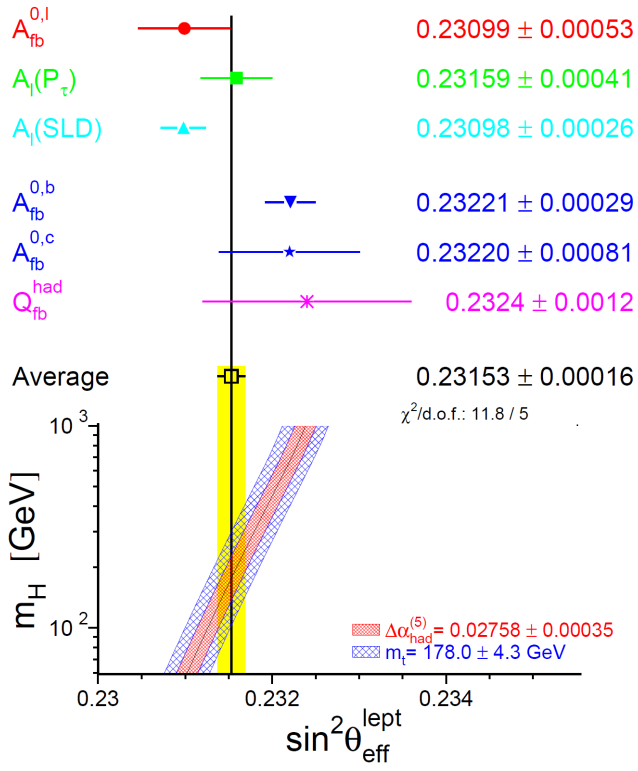

Figure 2.2: Different determinations of the effective weak mixing angle at LEP and SLD [18]. The SM prediction for $\sin^2\theta_{\text{eff}}^{\ell}$ as a function of the Higgs boson mass including the uncertainties from the top mass and $\Delta\alpha_{\text{had}}^5(M_Z^2)$ is shown, as well.

2.2 The Drell–Yan Process at the LHC

At the LHC two leptons with opposite charge are primarily produced via the annihilation of a quark and an anti-quark. Within the SM the Drell–Yan [25, 26] reaction proceeds via an s-channel exchange of either a virtual photon or a Z boson, $q\bar{q} \to Z/\gamma^* \to ll$.[1] While left and right-handed fermions have the same coupling to the photon, they act differently to the Z boson due to the presence of vector and axial-vector components. This fact results in an asymmetry in the polar angle (θ) of the lepton momentum relative to the incoming quark direction in the rest frame of the lepton pair. The differential cross-section for the Drell–Yan production in the rest frame of the lepton pair is given by (see for instance [23])

$$\frac{d\sigma}{d\cos\theta} = N_c \frac{4\pi\alpha^3}{3s} R_f \left[\frac{3}{8}\left(1+\cos^2\theta\right) + A_{\text{FB}}\cos\theta\right], \tag{2.21}$$

where N_c is the color factor, α the fine-structure constant, s the momentum transfer, $R_f = R^{VV} + R^{AA}$, and $A_{\text{FB}} = R^{VA}/R_f$ is the value of the forward-backward asymmetry. The

[1] From now on ll (ee) stands for two leptons with opposite charge (electron and positron).

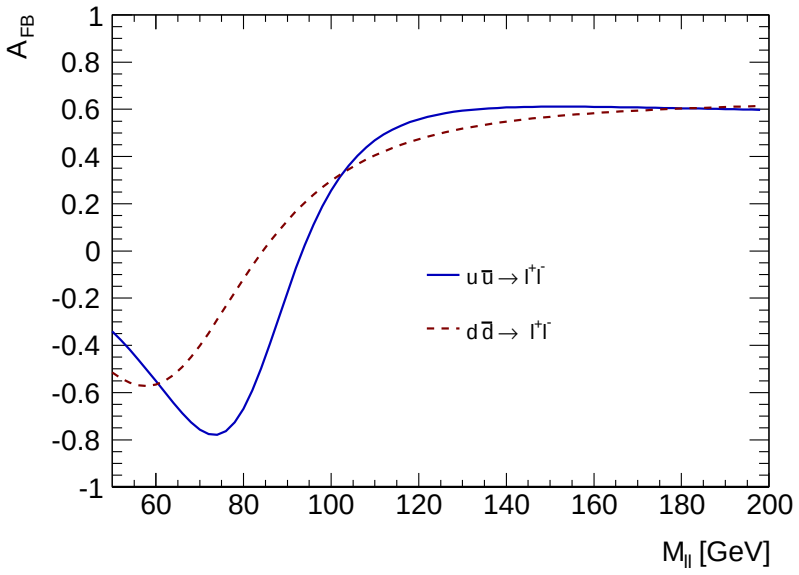

Figure 2.3: Tree level prediction of the forward-backward asymmetry for the annihilation of up-type and down-type quarks as a function of the momentum transfer ($s = M_{ll}$).

parameters R^{VV}, R^{AA}, and R^{VA} are defined by the vector and axial-vector couplings

$$R^{VV} = Q_l^2 Q_q^2 + 2 * Q_l Q_q g_V^\ell g_v^q Re(\chi(s)) + g_V^\ell \left(g_V^q + g_A^q\right) |\chi(s)|^2 , \tag{2.22}$$

$$R^{AA} = (g_A^\ell)^2 \left((g_V^q)^2 + (g_A^q)\right) |\chi(s)|^2 , \tag{2.23}$$

$$R^{VA} = \frac{3}{2} g_A^q g_A^\ell \left(Q_l Q_q Re(\chi(s)) + 2 g_V^q g_V^\ell |\chi(s)|^2\right) , \tag{2.24}$$

where the propagator function $\chi(s)$ reads

$$\chi(s) = \frac{1}{16 \cos^2\theta_W \sin^2\theta_W} \cdot \frac{s}{s - M_Z^2 + i\Gamma_Z M_Z} . \tag{2.25}$$

The $(1+\cos\theta)$-term in eq. (2.21) represents the total Drell–Yan cross-section, while the $(\cos\theta)$-term stands for the asymmetry induced by the vector and axial-vector couplings among the Z bosons and the fermions involved in the interaction. The forward-backward asymmetry can be also written as

$$A_{\mathrm{FB}} = \frac{\int_0^1 \frac{d\sigma}{d\cos\theta} d\cos\theta - \int_{-1}^0 \frac{d\sigma}{d\cos\theta} d\cos\theta}{\int_{-1}^1 \frac{d\sigma}{d\cos\theta} d\cos\theta} = \frac{\sigma_F - \sigma_B}{\sigma_F + \sigma_B} , \tag{2.26}$$

where σ_F and σ_B is the production cross-section of forward ($\cos\theta > 0$) and backward ($\cos\theta < 0$) events, respectively. This is equal to the widely used definition of the forward-backward asymmetry

$$A_{\mathrm{FB}} = \frac{N_F - N_B}{N_F + N_B} . \tag{2.27}$$

The forward-backward asymmetry depends on the momentum transfer, that defines the Z and photon fraction in the interference term. Additionally, it is sensitive to the particles

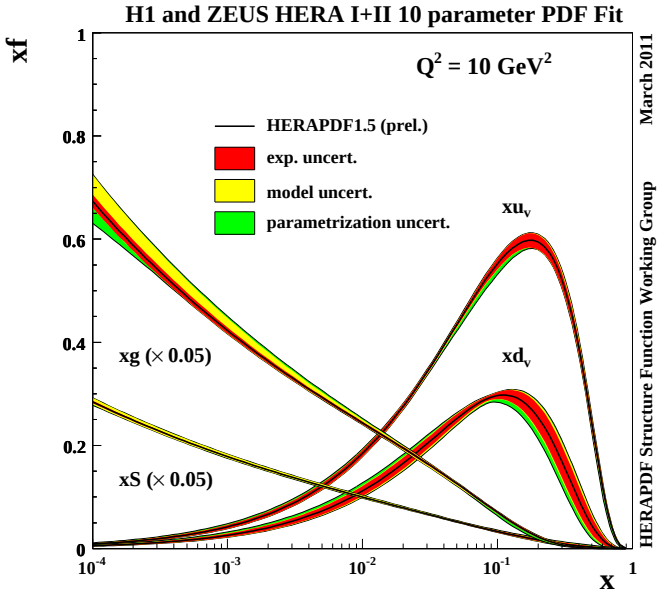

Figure 2.4: Parton density function in dependence of longitudinal momentum fraction (x) for $Q^2 = 10$ (GeV)^2 as obtained from a combined fit of H1 and ZEUS data [27]. The central value (solid line) is shown together with the experimental, model, and parametrization uncertainties.

involved in the interaction, since different types of fermions have different vector and axial-vector couplings (*cf.* eq. (2.16) and eq. (2.17)). Due to the dependence of Z couplings on the value of the weak mixing angle, the A_{FB} distribution is directly related to the electroweak mixing.

Figure 2.3 shows the value of A_{FB} at tree level as a function of the invariant mass of the lepton pair ($s = M_{ll}$) for the process $u\bar{u} \to Z/\gamma^* \to ll$ (blue solid line) and for $d\bar{d} \to Z/\gamma^* \to ll$ (red dashed line). The dependence on $s = M_{ll}$ is clearly visible for both curves. The different shapes of the up and down-type quark annihilation is due to different vector and axial-vector couplings of up and down quarks. The value of A_{FB} is zero, if R^{VA} vanishes.

In order to compute the cross-section and the forward-backward asymmetry of the process $pp \to Z/\gamma^* \to ll$, the composition of the protons has to be known. The fraction (xf) of gluons and quarks in the proton is described by parton density functions (PDFs), which have been measured precisely for instance at the electron-proton collider HERA. Figure 2.4 shows the PDFs as a function of longitudinal momentum fraction of the parton (x) at a momentum transfer of $Q^2 = 10$ (GeV)^2 as determined from H1 and ZEUS data. Partons at small Bjorken x values are mostly composed of gluons (xg) and sea-quarks (xS), while the valence quarks dominate at values around $x = 0.2$. As expected, the PDF for up quarks is approximately twice as large as for down quarks. At the LHC, the momentum transfers are usually much larger than $Q^2 = 10$ (GeV)^2, *cf.* fig. 2.5. Additionally, partons are involved in the interactions that are at very low momentum fractions. The DGLAP[1] [28–30] evolution equations are the

[1] Dokshitzer-Gribov-Lipatov-Alterelli-Parisi

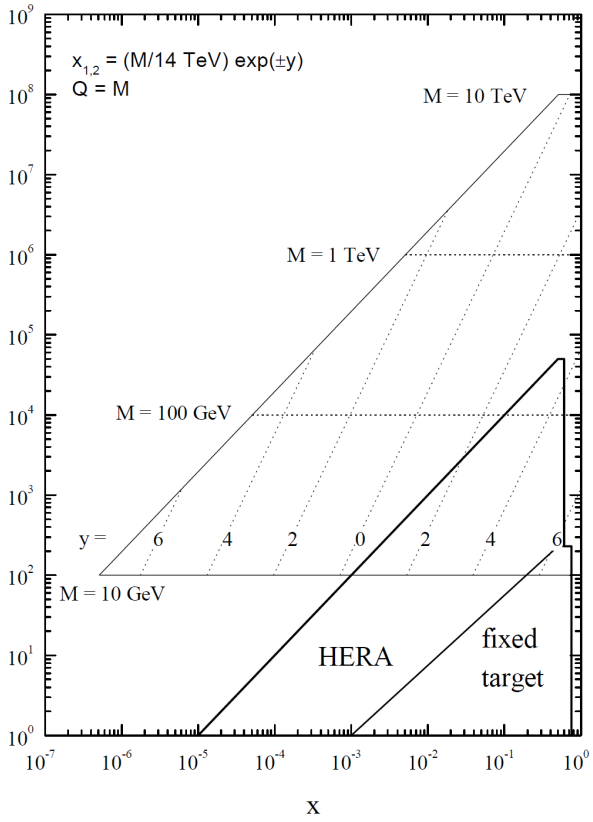

Figure 2.5: Values of x and Q^2 probed in the production of a particle of mass M and rapidity y at the LHC for $\sqrt{s} = 14$ TeV [33].

basis to describe hadron interactions at large momentum transfers, while the BFKL[1] [31, 32] equation provides the prescription for the evolution to small momentum fractions. The DGLAP as well as BFKL evolutions are together with the PDFs crucial ingredients to compute physical processes at the LHC.

[1] Balitsky-Fadin-Kuraev-Lipatov

CHAPTER 3

The Global Fit of the Electroweak Standard Model

Precision measurements, in line with accurate theoretical predictions, allow us to probe physics at much higher energy scales than the masses of the particles directly involved in experimental reactions by exploiting contributions from quantum loops. In case of the SM, unknown parameters of the SM (*e.g.* the Higgs boson mass) can be determined from multi-parameter fits. The analysis presented in this chapter relies on the Gfitter framework [1] and the presentation follows closely (though not identically) the presentation in the publications [1, 34]. This analysis has benefited from the enormous work in the past which has been done for the calculation of the electroweak precision observables. During this effort various software packages have been developed predicting the electroweak precision observables within the SM: ZFITTER [35, 36], TOPAZ0 [37, 38], LEPTOP [39, 40], and GAPP [41, 42] (see also the review [43]). Electroweak SM fits are also routinely performed by the LEP Electroweak Working Group [44] and for the electroweak review of the Particle Data Group [42].

This chapter is organized as follows. First, the statistical aspects of the fits as implemented in the Gfitter framework and the theoretical predictions of the electroweak observables are discussed. The experimental data used in the analysis is introduced. Especially, the treatment of the information from direct Higgs searches is explained in detail. The chapter concludes with the presentation of various fit results. Among them, constraints on the Higgs mass, a determination of the strong coupling, and indirect determinations of M_W, m_t, and $\sin^2\theta^\ell_{\text{eff}}$ are shown.

3.1 Statistical Aspects

The statistical analysis is performed with the Gfitter framework, which adopts a least-square like notation. The test statistics is defined as

$$\chi^2(y_{\text{mod}}) \equiv -2\ln\mathcal{L}(y_{\text{mod}})\,, \tag{3.1}$$

where the likelihood function ($\mathcal{L}$) depends on the free parameter (y_{mod}) of the physics model. The likelihood function of a parameter with its central measured value (x_0), positive (negative)

Gaussian error $\sigma^+_{\rm Gauss}$ ($\sigma^-_{\rm Gauss}$), and positive (negative) theoretical error $\sigma^+_{\rm theo}$ ($\sigma^-_{\rm theo}$), for a given set of $y_{\rm mod}$ parameters and the theoretical prediction $f(y_{\rm mod})$ is given by[1]

$$-2\ln\mathcal{L}(y_{\rm mod}) = \begin{cases} 0\,, & \text{if: } -\sigma^-_{\rm theo} \le f(y_{\rm mod}) - x_0 \le \sigma^+_{\rm theo}\,, \\ \left(\frac{f(y_{\rm mod})-\left(x_0+\sigma^+_{\rm theo}\right)}{\sigma^+_{\rm Gauss}}\right)^2\,, & \text{if: } f(y_{\rm mod}) - x_0 > \sigma^+_{\rm theo}\,, \\ \left(\frac{f(y_{\rm mod})-\left(x_0-\sigma^-_{\rm theo}\right)}{\sigma^-_{\rm Gauss}}\right)^2\,, & \text{if: } x_0 - f(y_{\rm mod}) > \sigma^-_{\rm theo}\,. \end{cases} \tag{3.2}$$

Theoretical uncertainties are treated according to the *R*Fit scheme [45, 46], *i.e.* the theoretical prediction can freely vary within the range of the theoretical uncertainty without contributing to the χ^2 estimator. The final test statistics of the global fit is defined as the sum over all $-2\ln\mathcal{L}(y_{\rm mod})$ contributions from each observable. Correlations between measurements are considered properly in the likelihood function.

In addition, it is possible to introduce dependencies among parameters in Gfitter, which can be used to parametrize correlations due to common systematic errors, or to rescale parameter values and errors with newly available results for parameters on which other parameters depend (rescaling mechanism).

For the parameter estimation the offset-corrected test statistics is used

$$\Delta\chi^2(y_{\rm mod}) = \chi^2(y_{\rm mod}) - \chi^2_{\rm min}(y_{\rm mod})\,, \tag{3.3}$$

where $\chi^2_{\rm min}(y_{\rm mod})$ is the absolute minimum of the test statistics. The minimum value of $\Delta\chi^2$ is zero, by construction. This ensures that, consistent with the assumption that the model is correct, exclusion confidence levels (CL) equal to zero are obtained when exploring the $y_{\rm mod}$ space.[2] The CL is computed for a Gaussian problem by

$$\mathrm{CL} = 1 - \mathrm{Prob}(\Delta\chi^2, n_{\rm dof})\,, \tag{3.4}$$

where $n_{\rm dof}$ is the number of degrees of freedom of the offset-corrected $\Delta\chi^2$. In case of a non-Gaussian problem a toy Monte Carlo analysis is required to estimate the CL. For the electroweak SM fit no significant deviations between the toy Monte Carlo analysis and eq. (3.4) are observed [1].

The p-value is an estimator for the goodness of the fit. It quantifies the probability of wrongly rejecting the theoretical hypothesis. For a Gaussian problem the p-value is compute by $\mathrm{Prob}(\Delta\chi^2, n_{\rm dof})$. In case of the electroweak fit, this naive p-value determinations have been confirmed with Monte Carlo toy experiments [1, 47].

In Gfitter the minimization of the test statistics is performed by TMinuit [48]. In addition, more involved global minima finders are used: Genetic Algorithm and Simulated Annealing, which are available with the TMVA [49] package in ROOT [2].

[1] The central value x_0 corresponds to the value with the largest likelihood, which is not necessarily equal to the arithmetic average in case of asymmetric errors.

[2] Throughout this thesis the term confidence level denotes 1 minus the p-value of a given $\Delta\chi^2$ (or χ^2) test statistics, and is hence a measure of the exclusion probability of a hypothesis. This is not to be confounded with a confidence interval, which expresses an inclusion probability.

3.2 Standard Model Predictions

The SM predictions for the electroweak observables measured by the LEP, SLC, and Tevatron experiments are implemented as a function of the floating fit parameters M_Z, M_H, m_t, $\overline{m_b}$, $\overline{m_c}$, $\Delta\alpha^5_{\text{had}}(M_Z^2)$, and $\alpha_s(M_Z^2)$. The predictions of the effective weak mixing angle and the W mass are the most important ones in order to constrain the mass of the Higgs boson. For the W mass eq. (6) and the coefficients of eq. (8) from [50] have been implemented. The calculation contains the full two-loop and leading beyond-two-loop corrections. The implementation of the effective weak mixing angle follows the full two-loop and leading beyond-two-loop computation of [51–53]. The asymmetry parameters can be computed by the effective weak mixing angle via

$$A_f = 2\frac{g_V^f/g_A^f}{1+(g_V^f/g_A^f)^2}\,, \tag{3.5}$$

where

$$\frac{g_V^f}{g_A^f} = 1 - 4|Q_f|\sin^2\theta^f_{\text{eff}}\,. \tag{3.6}$$

The forward-backward asymmetry where the superscript '0' indicates that the observed values have been corrected for radiative effects and photon exchange, can be determined from the asymmetry parameters as follows

$$A_{\text{FB}}^{0,f} = \frac{3}{4}A_e A_f\,. \tag{3.7}$$

Unlike the asymmetry parameters, the partial widths of the Z boson are defined inclusively, *i.e.* they contain all real and virtual corrections. They can be computed by[1]

$$\Gamma_Z^f = \frac{G_F M_Z^3}{6\sqrt{2}\pi}\left[(g_A^f)^2\left((1-4|Q_f|\sin^2\theta^f_{\text{eff}})R_V^f + R_A^f\right) + \delta^f_{Im(\kappa^f)}R_V^f\right] + \Delta^f_{\text{EW/QCD}}\,, \tag{3.8}$$

where G_F is the Fermi constant. For the analysis presented in this thesis, the vector and axial-vector couplings (g_A^f and g_V^f) are implemented using the parametrizations of [55–58], which are computed at one-loop level and partly at two-loop level for $\mathcal{O}(\alpha\alpha_s)$.[2] To account for a different Higgs mass dependence of the parametrizations and ZFITTER at large Higgs masses ($M_H \gtrsim 500$ GeV), a quadratic correction is added to $(\Delta T_Z)_{\text{SM}}$ of eq. (23b) in [58] (for further explanation of the T parameter see chapter 4)

$$(\Delta T_Z)_{\text{SM,Corr}} = \begin{cases} 0 & \text{if } M_H \leq 200 \text{ GeV}, \\ 0.00764(x_h - x_{h,200}) - 0.112(x_h - x_{h,200})^2 & \text{if } M_H > 200 \text{ GeV}, \end{cases} \tag{3.9}$$

where $x_h = \log(M_H/100\text{ GeV})$ and $x_{h,200} = \log(200/100)$.[3] This correction factor does not affect the electroweak SM fit, but it slightly influences the constraints on new physics parameters (*cf.* chapter 4). The term $\delta^f_{Im(\kappa^f)}$ in eq. (3.8) represents the corrections from the imaginary part

[1] See for instance [54] and [55–58].

[2] The above mentioned Gfitter publications use the implementations from ZFITTER [35, 36], which contains up to two-loop electroweak corrections [35, 36, 43, 54, 59–66] and all known QCD corrections [35, 36, 67].

[3] The coefficients are determined by comparing the values of the T parameter computed with eq. (23b) of [58] and with the Fortran ZFITTER package [35, 36] (version 6.42 [68]).

of loop-induced mixing of the photon and Z boson and its value is taken from [58]. The radiator functions R_V^f and R_A^f absorb final QED and QCD radiation to the vector and axial-vector current. In case of charged leptons they read [55]

$$R_V^\ell = \frac{\beta(3-\beta)}{2}, \tag{3.10}$$

$$R_A^\ell = \beta^3, \tag{3.11}$$

with $\beta = \sqrt{1-\frac{4m_l^2}{M_Z^2}}$. For hadronic Z decays the radiator functions are taken from [35, 54]. They have been extended by the fourth-order (3NLO) perturbative calculation of the massless QCD Adler function [69], leading to a determination of the strong coupling constant with very small theoretical uncertainties. The non-factorisable EW $\otimes$ QCD corrections ($\Delta_{\mathrm{EW/QCD}}$) only arise for quark final states. They are assumed to be constant [35, 70, 71], and their influence is rather small (less than 10^{-3}). The total Z width for three light neutrino generations is computed by the sum

$$\Gamma_Z = \Gamma_e + \Gamma_\mu + \Gamma_\tau + 3\Gamma_\nu + \Gamma_{\mathrm{had}}, \tag{3.12}$$

where $\Gamma_{\mathrm{had}} = \Gamma_u + \Gamma_d + \Gamma_c + \Gamma_s + \Gamma_b$ is the total hadronic Z width. The total hadronic cross-section at the Z pole is given by

$$\sigma_{\mathrm{had}}^0 = \frac{12\pi}{M_Z^2}\frac{\Gamma_e\Gamma_{\mathrm{had}}}{\Gamma_Z^2}. \tag{3.13}$$

To reduce systematic uncertainties, the LEP experiments have determined the partial Z width ratios $R_\ell^0 = \Gamma_{\mathrm{had}}/\Gamma_\ell$ and $R_q^0 = \Gamma_q/\Gamma_{\mathrm{had}}$, which are used in the fit.

The prediction of the total W width is implemented via eq. (20) of [58]. However, due to the comparatively large experimental uncertainty, this observable is not crucial for the electroweak fit.

In addition, uncertainties due to unknown higher order terms affecting the predictions of the W mass and the effective weak mixing angle [50–53] are taken into account in the fit, $\delta_{\mathrm{th}} M_W \simeq 4$ MeV and $\delta_{\mathrm{th}} \sin^2\theta_{\mathrm{eff}}^f \simeq 4.7 \cdot 10^{-5}$. They are treated according to the *R*Fit prescription, *i.e.* the theoretical prediction can freely vary within its uncertainty without contributing to the χ^2 estimator (*cf.* section 3.1).

3.3 Experimental Inputs

The experimental data used in the fit includes the electroweak precision observables measured at the Z pole [18] (asymmetry parameters, forward-backward asymmetry, partial Z widths) including their experimental correlations [18] and the latest W mass world average $M_W = (80.399 \pm 0.023)$ GeV [72] and width $\Gamma_W = (2.098 \pm 0.048)$ GeV [73]. Moreover, the most recent average of the direct Tevatron top mass measurement $m_t = (173.2 \pm 0.9)$ GeV [74] is taken into account. For the vacuum polarization contribution from the five lightest quark flavors to the electromagnetic coupling strength at M_Z the value of [75] is used, $\Delta\alpha_{\mathrm{had}}^5(M_Z^2) = (2749 \pm 10) \cdot 10^{-5}$. This measurement includes new $\pi^+\pi^-$ cross-section data from BABAR and KLOE, new

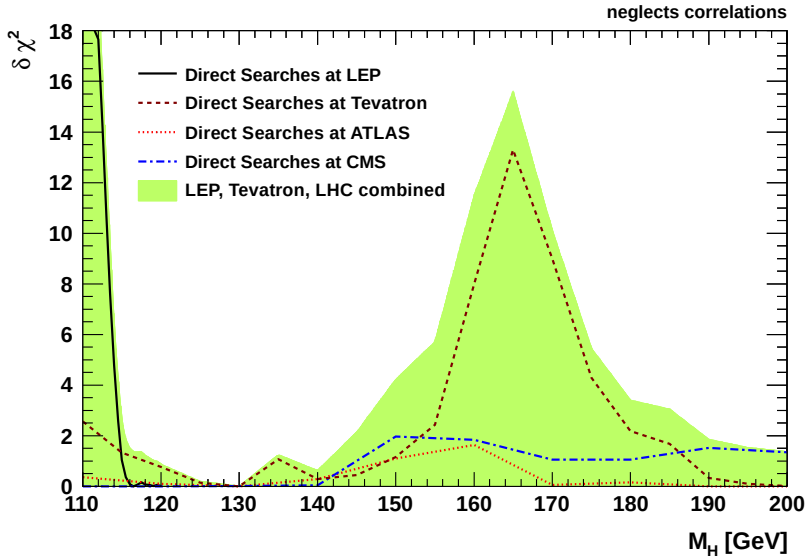

Figure 3.1: Contribution to the χ^2 estimator versus M_H derived from the experimental information on direct Higgs boson searches. The measured values are interpolated by straight lines. Correlations have been neglected in the combination. For further description consult the text.

multi-hadron data from BABAR, a re-estimation of missing low energy contributions using results on cross-sections and process dynamics from BABAR [75], and a re-evaluation of the continuum contribution from perturbative QCD at four loops. The functional dependence of the central value of $\Delta\alpha^5_{\rm had}(M_Z^2)$ on α_s of $0.37 \cdot 10^{-4} \times (\alpha_S(M_Z^2) - 0.1193)/0.0028$ [75] around the given central value of $\Delta\alpha^5_{\rm had}(M_Z^2)$ is included via a rescaling mechanism in the fit (*cf.* section 3.1).

Additionally, fits are performed including the information from direct Higgs searches at LEP [76], Tevatron [77], and first 2010 LHC results from ATLAS (combining six different final states) [78] and CMS ($H \to WW \to \ell\nu\ell\nu$) [79]. Recently, ATLAS and CMS have presented preliminary results for the SM Higgs search derived from the 2011 data corresponding to an integrated luminosity of up to 2.3 fb^{-1} [80, 81].[1] In this analysis, these preliminary results are not taken into account, since a proper combination of the ATLAS and CMS searches needs the detailed knowledge of the correlations between the two results.[2] The Higgs boson searches from the 2010 LHC data are however dominated by statistical uncertainties. Therefore, the correlations between ATLAS and CMS can be neglected. This assumption should not be too

[1] At ATLAS, Higgs masses between 146-232 GeV, 256-282 GeV, and 296-466 GeV are excluded at the 95% CL [80], while the CMS collaboration can exclude Higgs masses of 145-216 GeV, 226-288 GeV, and 310-400 GeV [81]. In both experiments a broad excess of events in the region of 140 GeV has been observed. The significance is approximately 2σ [80] for both experiments. However, more data is needed to confirm whether the observed excess is just a statistical fluctuation or not.

[2] An update of the electroweak fit results considering the recent ATLAS and CMS results will be provided at `www.cern.ch/Gfitter` when a combination of the LHC results is available.

inaccurate. The latest Tevatron combination for the Higgs boson production excludes a Higgs mass between 156-177 GeV at the 95% CL [77], while a small excess ($\sim 1\sigma$) of data events in the mass range 125-155 GeV with respect to the background estimation has been observed.

In order to include the direct Higgs searches in the fit, the one-sided confidence level ($\mathrm{CL_{s+b}}$) reported by the experiments,[1] is transformed into a two-sided confidence level ($\mathrm{CL_{s+b}^{2-sided}}$). This procedure ensures that positive fluctuations or signals beyond the SM prediction are penalized as are negative fluctuations. The contribution to the χ^2 estimator which is minimized in the fits is obtained via $\delta\chi^2 = 2 \cdot [\mathrm{Erf}^{-1}(1 - \mathrm{CL_{s+b}^{2-sided}})]^2$ and it is shown in fig. 3.1. The solid black and dashed dark red line show the contribution from LEP and Tevatron, while the dotted orange line and the dashed-dotted blue curve indicate the constraints from the 2010 data by ATLAS and CMS, respectively. The combination shown by the green area neglects the correlations between the different measurements (*cf.* discussion above). The minimum in the $\delta\chi^2$ distribution cannot be interpreted as most probable Higgs mass, rather it is due to the lack of sensitivity of the experiments in this region.

All input values can be found in the second column of table 3.1. For the $\overline{MS}$ masses of the bottom and charm quarks the values from [82] are used. The various other measurements of $\sin^2\theta^\ell_{\mathrm{eff}}$ as quoted in section 2.1.2 are not considered in the fit, since their impact on the fit is small in comparison to the combined Z pole data.

3.4 Fit Results

The electroweak fit is performed with and without the information from the direct Higgs searches. The fit converges at a global minimum of the test statistics of $\chi^2_{\mathrm{min}} = 17.9$ ($\chi^2_{\mathrm{min}} = 16.7$) for the fit with (without) the direct Higgs searches, resulting in a p-value of $\mathrm{Prob}(\chi^2_{\mathrm{min}}, 14) = 0.21$ ($\mathrm{Prob}(\chi^2_{\mathrm{min}}, 13) = 0.21$).

The results for the fits with and without the information from the direct Higgs searches for every observable are listed in the third and fourth column of table 3.1. The uncertainties are derived from the $\Delta\chi^2$ estimator using a Gaussian approximation. In the last column the indirect results for the observables are quoted when removing the specific measurement from the fit with the direct Higgs constraints. The correlation coefficients between the floating fit parameters are given in table 3.2. The large correlation between $\Delta\alpha^5_{\mathrm{had}}(M_Z^2)$ and $\alpha_s(M_Z^2)$ is due to the dependence of $\Delta\alpha^5_{\mathrm{had}}(M_Z^2)$ on the strong coupling. The largest correlation on the Higgs mass arises from m_t. Additionally, the correlation to the $\Delta\alpha^5_{\mathrm{had}}(M_Z^2)$ value and the Z mass is significant. The correlations of the light quark masses, $\overline{m_c}$ and $\overline{m_b}$, are small indicating their little impact on the fit.

Figure 3.2(a) shows the pull values for the fit with the information from direct Higgs mass constraints. The pull values are defined as the difference between the fit result and the measurement divided by the total experimental error. The known tension between the left-right asymmetry at SLD, A_l(SLD), and the b-quark forward-backward asymmetry at LEP, $A^{0,b}_{\mathrm{FB}}$, is

[1] In lack of published $\mathrm{CL_{s+b}}$ values by ATLAS [78], the log-likelihood ratio (llr) is normalized to zero and then it is used to compute the confidence level $\mathrm{CL_{s+b}} \simeq \mathrm{Prob}(\mathrm{llr}, 1)$.

Parameter	Input value	Free in fit	Results from global EW fits: *Standard fit*	*Complete fit*	*Complete fit w/o exp. input in line*
M_Z [GeV]	91.1875 ± 0.0021	yes	91.1874 ± 0.0021	91.1877 ± 0.0021	$91.1983^{+0.0133}_{-0.0155}$
Γ_Z [GeV]	2.4952 ± 0.0023	–	2.4959 ± 0.0015	2.4955 ± 0.0014	$2.4951^{+0.0017}_{-0.0016}$
$\sigma^0_{\rm had}$ [nb]	41.540 ± 0.037	–	41.478 ± 0.014	41.478 ± 0.014	41.469 ± 0.015
R^0_l	20.767 ± 0.025	–	20.743 ± 0.018	20.741 ± 0.018	$20.718^{+0.027}_{-0.026}$
$A^{0,l}_{\rm FB}$	0.0171 ± 0.0010	–	0.01641 ± 0.0002	$0.01620^{+0.0002}_{-0.0001}$	0.01606 ± 0.0001
A_ℓ $^{(\star)}$	0.1499 ± 0.0018	–	0.1479 ± 0.0010	$0.1472^{+0.0009}_{-0.0006}$	–
A_c	0.670 ± 0.027	–	$0.6683^{+0.00044}_{-0.00043}$	$0.6680^{+0.00040}_{-0.00028}$	$0.6679^{+0.00042}_{-0.00025}$
A_b	0.923 ± 0.020	–	$0.93470^{+0.00009}_{-0.00008}$	$0.93463^{+0.00008}_{-0.00005}$	$0.93463^{+0.00007}_{-0.00005}$
$A^{0,c}_{\rm FB}$	0.0707 ± 0.0035	–	0.0741 ± 0.0005	$0.0737^{+0.0005}_{-0.0004}$	0.0738 ± 0.0004
$A^{0,b}_{\rm FB}$	0.0992 ± 0.0016	–	0.1037 ± 0.0007	$0.1035^{+0.0003}_{-0.0004}$	$0.1038^{+0.0003}_{-0.0005}$
R^0_c	0.1721 ± 0.0030	–	0.17226 ± 0.00006	0.17226 ± 0.00006	0.17226 ± 0.00006
R^0_b	0.21629 ± 0.00066	–	$0.21578^{+0.00005}_{-0.00008}$	$0.21577^{+0.00005}_{-0.00008}$	$0.21577^{+0.00005}_{-0.00007}$
$\sin^2\theta^\ell_{\rm eff}(Q_{\rm FB})$	0.2324 ± 0.0012	–	0.23141 ± 0.00012	$0.23150^{+0.00008}_{-0.00011}$	$0.23152^{+0.00006}_{-0.00013}$
M_H [GeV] $^{(\circ)}$	Likelihood ratios	yes	$94^{+30[+74]}_{-24[-43]}$	$125^{+8[+22]}_{-10[-11]}$	$94^{+30[+74]}_{-24[-43]}$
M_W [GeV]	80.399 ± 0.023	–	$80.382^{+0.014}_{-0.015}$	$80.368^{+0.007}_{-0.010}$	$80.360^{+0.012}_{-0.011}$
Γ_W [GeV]	2.085 ± 0.042	–	2.093 ± 0.001	2.092 ± 0.001	$2.091^{+0.002}_{-0.001}$
$\overline{m}_c$ [GeV]	$1.27^{+0.07}_{-0.11}$	yes	$1.27^{+0.07}_{-0.11}$	$1.27^{+0.07}_{-0.11}$	–
$\overline{m}_b$ [GeV]	$4.20^{+0.17}_{-0.07}$	yes	$4.20^{+0.16}_{-0.07}$	$4.20^{+0.16}_{-0.07}$	–
m_t [GeV]	173.2 ± 0.9	yes	173.3 ± 0.9	173.5 ± 0.9	$177.2^{+3.0(\triangledown)}_{-3.1}$
$\Delta\alpha^{(5)}_{\rm had}(M_Z^2)$ $^{(\dagger\triangle)}$	2749 ± 10	yes	2750 ± 10	2748 ± 10	2716^{+60}_{-45}
$\alpha_s(M_Z^2)$	–	yes	0.1193 ± 0.0028	0.1194 ± 0.0028	0.1194 ± 0.0028
$\delta_{\rm th} M_W$ [MeV]	$[-4, 4]_{\rm theo}$	yes	4	4	–
$\delta_{\rm th} \sin^2\theta^\ell_{\rm eff}$ $^{(\dagger)}$	$[-4.7, 4.7]_{\rm theo}$	yes	4.7	4.7	–

$^{(\star)}$Average of LEP ($A_\ell = 0.1465 \pm 0.0033$) and SLD ($A_\ell = 0.1513 \pm 0.0021$) measurements. The fit w/o the LEP (SLD) measurement but with the direct Higgs searches gives $A_\ell = 0.1471^{+0.0010}_{-0.0005}$ ($A_\ell = 0.1467^{+0.0007}_{-0.0004}$). $^{(\circ)}$In brackets the 2σ. $^{(\dagger)}$In units of 10^{-5}. $^{(\triangle)}$Rescaled due to α_s dependency. $^{(\triangledown)}$Ignoring a second less significant minimum, *cf.* fig. 3.6 and the result of eq. (3.16).

Table 3.1: Input values and fit results for the observables and parameters of the global electroweak fit. The first and second columns list respectively the observables/parameters used in the fit, and their experimental values or phenomenological estimates (*cf.* section 3.3 for references). The subscript 'theo' labels theoretical error ranges. The third column indicates whether a parameter is floating in the fit. The fourth (fifth) column quotes the results of the fit without (with) the constraints from the direct Higgs searches at LEP, Tevatron and the LHC in the fit. In case of floating parameters the fit results are directly given, while for (non-floating) observables the central values and errors are obtained by individual profile likelihood scans. The last column gives the fit results for each parameter without using the corresponding experimental constraint in the complete fit (indirect determination).

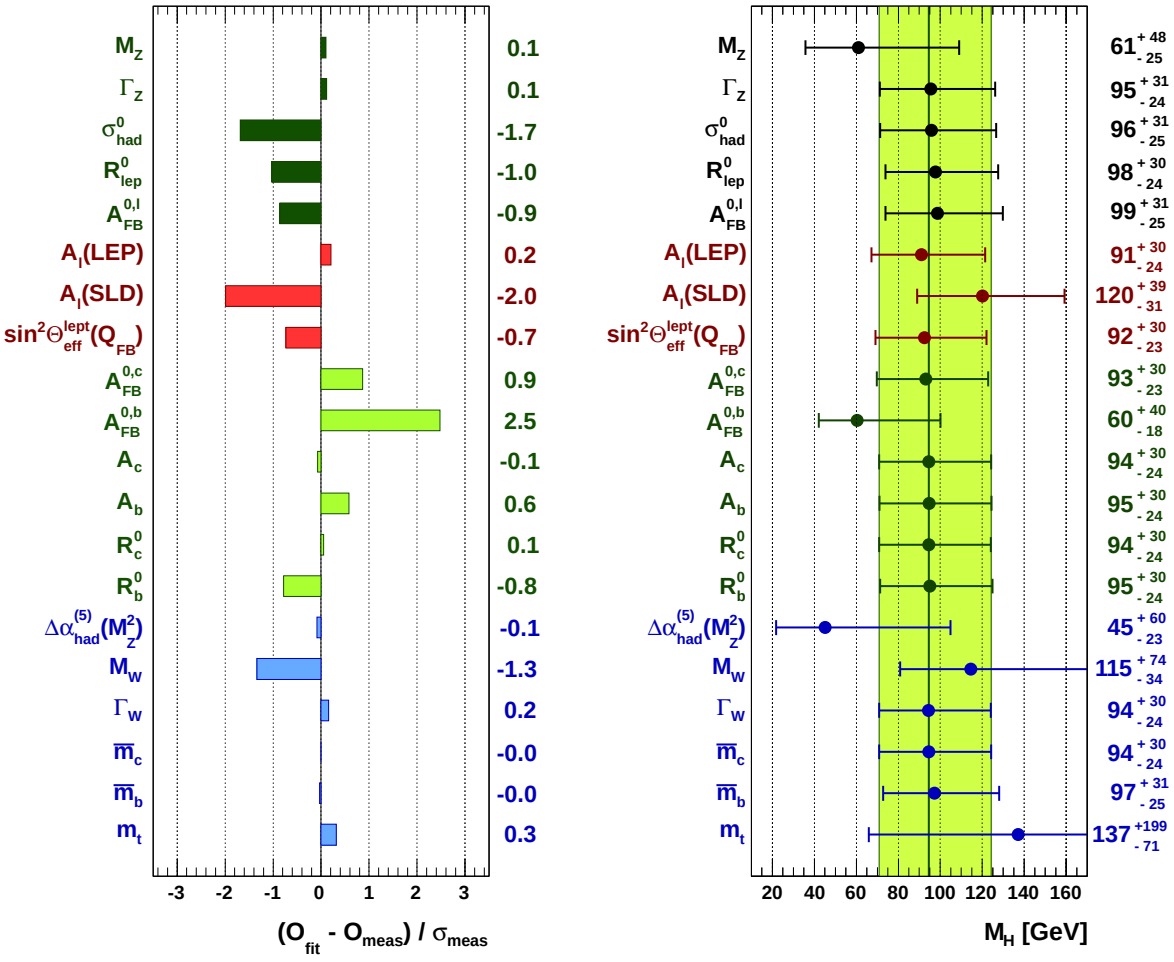

(a) (b)

Figure 3.2: Comparing fit results with direct measurements: (a) pull values for the fit with the direct Higgs constraints, (b) and results for M_H from the fit excluding the respective measurements from the fit and without any direct Higgs constraints.

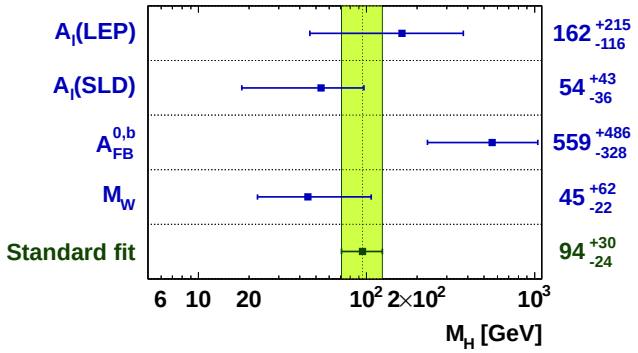

Figure 3.3: Determination of M_H excluding all the sensitive observables from the fit except the one given. No information from direct Higgs searches is taken into account. Note that the results shown are not independent.

Parameter	$\log M_H$	$\Delta\alpha^{(5)}_{\rm had}(M_Z^2)$	M_Z	$\alpha_s(M_Z^2)$	m_t	$\overline{m_c}$	$\overline{m_b}$
$\log M_H$	1	−0.17	0.13	0.03	0.32	−0.00	−0.01
$\Delta\alpha^{(5)}_{\rm had}(M_Z^2)$		1	−0.01	0.35	0.01	0.00	0.02
M_Z			1	−0.01	−0.01	−0.00	−0.00
$\alpha_s(M_Z^2)$				1	0.03	0.01	0.05
m_t					1	0.00	−0.00
$\overline{m_c}$						1	0.00
$\overline{m_b}$							1

Table 3.2: Correlation coefficients between the floating fit parameters in the fit without any information from direct Higgs searches. The correlations with and between the varying theoretical error parameters $\delta_{\rm th}$ are negligible in all cases.

clearly visible. However, no single pull value exceeds the 3σ level. Together with the reasonable p-value this fact indicates that the SM describes the electroweak precision data rather well.

3.4.1 Higgs Mass Constraints

Figure 3.4 and fig. 3.5 show the profile curves of the $\Delta\chi^2$ as a function of the Higgs mass for the fit without and with the information from the direct Higgs searches. The green solid lines are the results from fits including the theoretical uncertainties on $\sin^2\theta^f_{\rm eff}$ and M_W, while they are ignored for the dashed lines. The green shaded area indicates the difference between both treatments. In addition, the exclusion limits from the LEP and Tevatron experiments are shown by the gray shaded regions. The Higgs mass is extracted from fits including the theoretical uncertainties to be

$$M_H = \begin{cases} 94\,^{+30}_{-24}\ \text{GeV} & \text{(without the direct Higgs searches)}\,, \\ 125\,^{+8}_{-10}\ \text{GeV} & \text{(with the direct Higgs searches)}\,, \end{cases} \tag{3.14}$$

with the 95% (99%) upper bounds of 166 GeV (196 GeV) for the fit without any direct Higgs constraints, and 146 GeV (153 GeV) for the fit including the information from the direct Higgs searches, respectively.

In order to test the impact of the input values on the determination of the Higgs mass, in fig. 3.2(b) M_H is determined from fits without any direct Higgs constraints and where all input values except the one listed in the given line are used in the fit. It can be seen that precise measurements of M_W, $\Delta\alpha^5_{\rm had}(M_Z^2)$, and m_t are crucial for the Higgs mass estimate.

As default the direct top mass measurement from the Tevatron is used in the fit. However, this measurement is affected by several theoretical uncertainties arising from non-perturbative color-reconnection effects in the fragmentation process [83, 84], and from ambiguities in the top-mass definition [85, 86]. These additional uncertainties are not taken into account in the direct top mass determination. They amount to be 0.5 GeV each, where the systematic error due to shower effects could be larger [83]. The top pole mass extracted from the SM

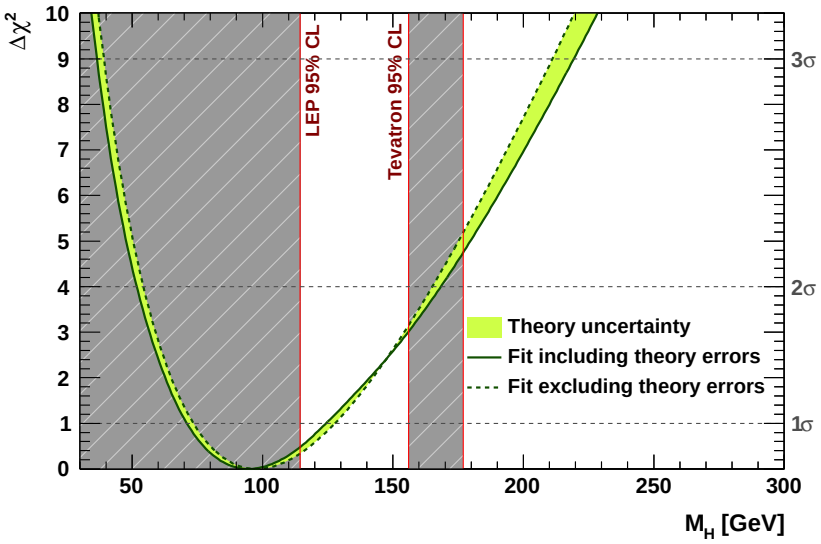

Figure 3.4: $\Delta\chi^2$ as a function of M_H for the fit without the direct Higgs searches. The solid line gives the results when including the theoretical errors, while the dashed line shows the result when ignoring the theoretical uncertainties.

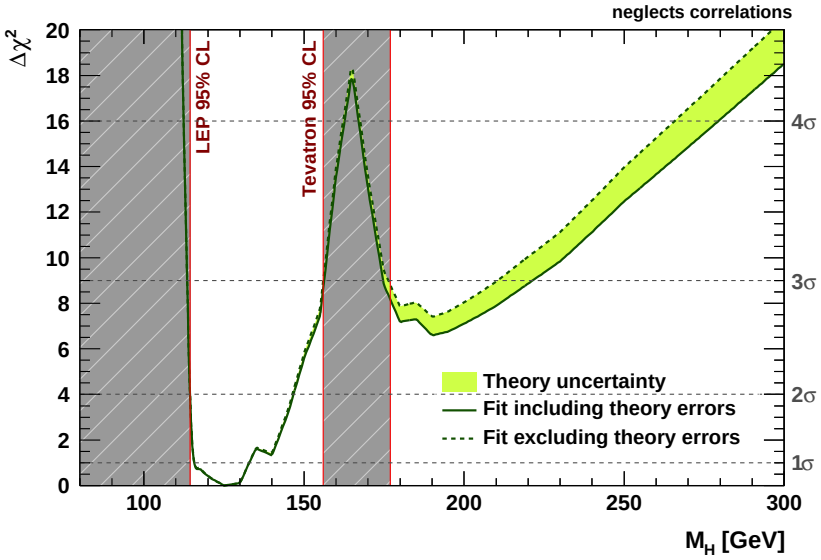

Figure 3.5: $\Delta\chi^2$ as a function of M_H for the fit with the direct Higgs searches. The solid line gives the results when including the theoretical errors, while the dashed line shows the result when ignoring the theoretical uncertainties.

$p\bar{p} \to t\bar{t} + X$ inclusive cross-section is not affected by these uncertainties. The top mass has been determined to be $m_t = 167.5\,^{+5.0}_{-4.5}$ GeV [87], when using the measured cross-section of $\sigma_{t\bar{t}} = 8.13\,^{+1.02}_{-0.90}$ pb [88] and its theoretical prediction based on approximate NNLO QCD calculations [89]. When considering this value instead of the direct top mass determination in the fit without any information from direct Higgs searches, the result on the Higgs boson mass is $76\,^{+40}_{-26}$ GeV, which is lower than the result of eq. (3.14). However, due to the larger error of the top mass the 95% CL upper bound is with 176 GeV even higher.

The electroweak fit has also been performed with an alternative value of $\Delta\alpha^5_{\rm had}(M_Z^2) = (2762.6 \pm 10.3) \cdot 10^{-5}$ [90]. The Higgs mass is extracted from this fit excluding the direct Higgs searches constraints to be $M_H = 88^{+29}_{-22}$ GeV.

In fig. 3.3 except the measurements for the floating fit parameters only the observable indicated in a given row is included in the fit. The four observables providing the strongest constraints on M_H are shown. The compatibility among these measurements can be estimated by repeating the global fit where the least compatible of the measurements (here $A^{0,b}_{\rm FB}$) is removed, and by comparing the $\chi^2_{\rm min}$ estimator obtained in that fit to the one of the full fit. To assign a probability to the observation, the $\Delta\chi^2_{\rm min}$ obtained in this way must be gauged with toy MC experiments to take into account the "look-elsewhere" effect introduced by the explicit selection of the outlier. In $(1.4 \pm 0.1)\%$ ("2.5σ") of the toy experiments, the $\Delta\chi^2_{\rm min}$ exceeds the value observed in the current data.

3.4.2 Determination of the Strong Coupling

The strong coupling is mainly sensitive to the value of R^ℓ_0 which is defined as the ratio of the hadronic and leptonic Z widths. This observable depends in particular on the radiator functions which have been implemented up to 3NLO. The strong coupling is determined from the fit with the information from the direct Higgs searches to be

$$\alpha_s(M_Z^2) = 0.1194 \pm 0.0028\,(\text{exp}) \pm 0.0001\,(\text{theo})\,, \tag{3.15}$$

where the first error is the uncertainty from the fit and the second one is due to the truncation of perturbative QCD series. It includes variations of the renormalization scale between $0.6 M_Z < \mu < 1.3 M_Z$ [91], of massless terms of order α_s^5 and higher, and of quadratic massive terms of order α_s^4 and beyond. This result is in excellent agreement with the 3NLO result from τ decays, $\alpha_s(M_Z^2) = 0.1212 \pm 0.0011$ [91]. These two determinations represent one of the best current test of the asymptotic freedom property of QCD, because of their precision and the almost two orders of magnitude scale difference between the τ and Z scale.

3.4.3 Determination of the Top Mass

In fig. 3.6 the $\Delta\chi^2$ estimator is shown as a function of the top mass for various fit scenarios. In all fits the direct top mass measurement is not included. The green band indicates the result of a fit without the information from the direct Higgs searches, while for the blue band also the direct Higgs constraints are taken into account. The result when assuming a SM Higgs at

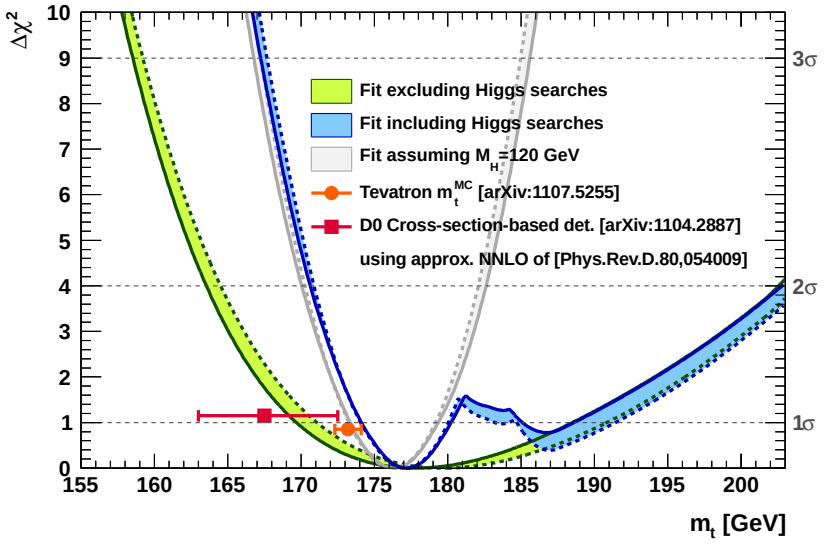

Figure 3.6: $\Delta\chi^2$ as a function of m_t for the fit scenarios given on the plot. In the fit the direct m_t measurements, indicated by the dots with 1σ errors, are not taken into account.

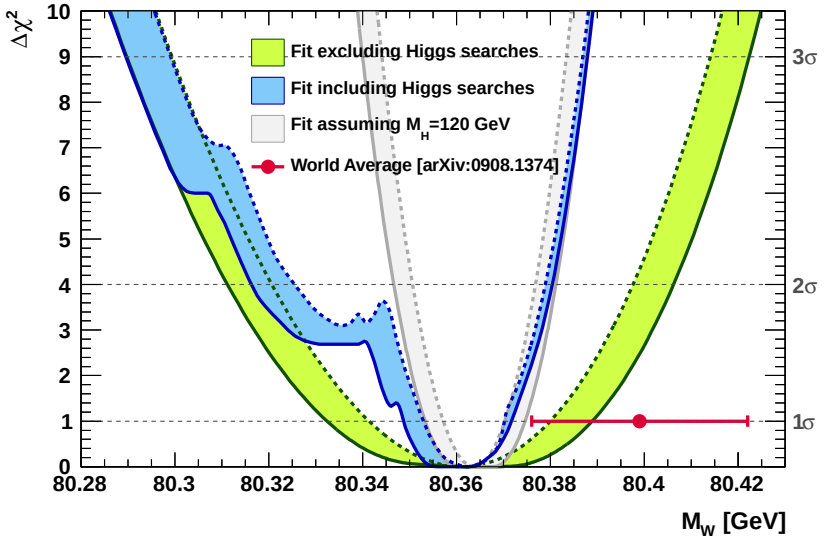

Figure 3.7: $\Delta\chi^2$ as a function of M_W for the fit scenarios given on the plot. In the fit the world average of M_W, indicated by the dot with 1σ error, is not taken into account.

120 GeV with negligible error on M_H is shown in gray. The width of the bands indicates the impact of the theoretical uncertainties, similar as for the Higgs mass estimate. Additionally, the direct top mass measurement [92] and the value extracted from inclusive $t\bar{t}$ cross-section measurement [87] are depicted by the dots and their error bars. The top mass is estimated from the fits without and with the information from the direct Higgs mass searches to be

$$m_t = \begin{cases} 177.8\,^{+10.7}_{-8.1}\ \text{GeV} & \text{(without the direct Higgs searches)}\,, \\ [174.1,\ 180.2]\ \text{GeV and}\ [185.1,\ 188.6]\ \text{GeV} & \text{(with the direct Higgs searches)}\,. \end{cases} \tag{3.16}$$

Both determinations agree with the direct Tevatron measurement. A possible Higgs discovery could increase the precision of the indirect determination significantly ($\Delta m_t = 3$ GeV for $M_H = 120$ GeV).

3.4.4 Determination of the W Mass

For the indirect determination of the W mass, several fits have been performed where the direct M_W measurement is removed from the fit. Figure 3.7 shows the $\Delta\chi^2$ estimator as a function of M_W for fits without any direct Higgs constraints (green band), with the direct Higgs constraints (blue band), and assuming a possible Higgs discovery at $M_H = 120$ GeV (gray band). The current world average [72] is shown by the red dot. The *R*Fit treatment of the theoretical uncertainty in the M_W prediction ($\delta_{\text{th}} M_W \simeq 4$ MeV) leads to a broadening of the fit minima, which is clearly visible by comparing the dashed and solid lines. The W mass is determined to be

$$M_W = \begin{cases} 80.363\,^{+0.026}_{-0.030}\ \text{GeV} & \text{(without the direct Higgs searches)}\,, \\ 80.360\,^{+0.012}_{-0.011}\ \text{GeV} & \text{(with the direct Higgs searches)}\,. \end{cases} \tag{3.17}$$

The latter value exceeds the precision of the experimental world average, $M_W = (80.399 \pm 0.023)$ GeV [72]. The indirect determinations are in agreement with the direct measurement. If the Higgs mass is finally measured (at $M_H = 120$ GeV), the precision of the indirect determination can be further improved.

3.4.5 Determination of the Effective Weak Mixing Angle

In order to determine indirectly the value of the effective weak mixing from the fit, all measurements have to be removed which are directly related to $\sin^2\theta^\ell_{\text{eff}}$ (*e.g.* the asymmetry parameters). The fits are performed by using only the experimental data for the following observables: m_t, M_W, M_Z, m_c, m_b, and $\Delta\alpha^5_{\text{had}}(M_Z^2)$. Since the measurement of R^ℓ_0 is not taken into account, the strong coupling is not constrained in the fit. Therefore, for $\alpha_s(M_Z^2)$ the result of eq. (3.15) is considered in the fit. In fig. 3.8 the $\Delta\chi^2$ estimator as a function of $\sin^2\theta^\ell_{\text{eff}}$ is shown for three different scenarios: without any information from direct Higgs searches (green band), with the direct Higgs searches (blue band), and assuming a possible Higgs discovery at $M_H = 120$ GeV (gray band). The LEP/SLD average of $\sin^2\theta^\ell_{\text{eff}} = 0.23153 \pm 0.00016$ [18] is

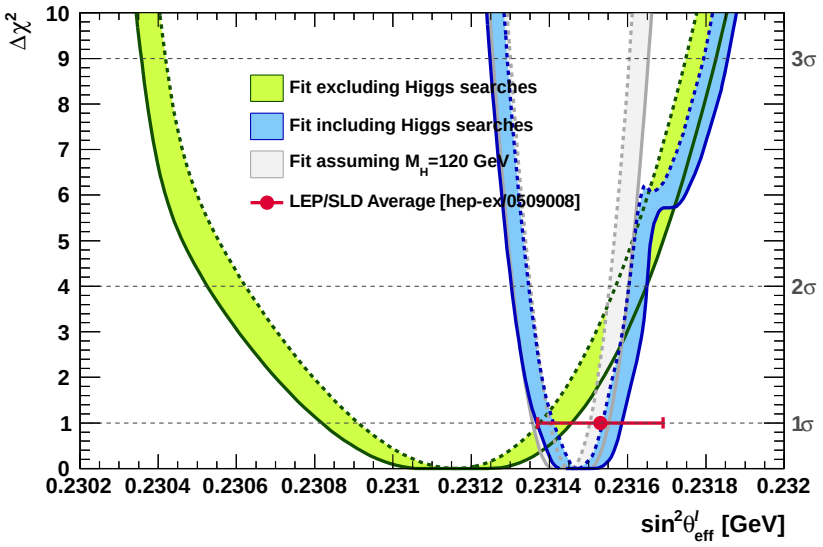

Figure 3.8: $\Delta\chi^2$ as a function of $\sin^2\theta^\ell_{\rm eff}$ for the fit scenarios given on the plot. In the fit the observables which are directly related to $\sin^2\theta^\ell_{\rm eff}$ are removed. The LEP/SLD average is indicated by the dot with 1σ error.

displayed by the red dot. Similar to the M_W determination, the fit minima are broadened due the inclusion of the theoretical uncertainty of the $\sin^2\theta^\ell_{\rm eff}$ prediction ($\delta_{\rm th}\sin^2\theta^\ell_{\rm eff} \simeq 4.7\cdot 10^{-5}$). The effective weak mixing angle is extracted to be

$$\sin^2\theta^\ell_{\rm eff} = \begin{cases} 0.23115\,^{+0.00031}_{-0.00033} & \text{(without the direct Higgs searches)}\,, \\ 0.23147\,^{+0.00012}_{-0.00010} & \text{(with the direct Higgs searches)}\,. \end{cases} \tag{3.18}$$

Both determinations agree with the LEP/SLD average [18]. The value extracted from the fit with the direct Higgs searches exceeds the precision of the LEP/SLD average and it is therefore currently the most precise determination of the effective weak mixing angle. The possible measurement of the Higgs mass could further reduce the uncertainty of the indirect determination.

3.4.6 Two-Dimensional Scan of the W and Top Mass

The comparison of the indirect and direct determinations of the W and top mass is a good probe of the electroweak SM, in particular once the Higgs mass is measured. In fig. 3.9 the two-dimensional 68%, 95% and 99% CL allowed regions obtained from scans of fits with fixed variable pairs of M_W and m_t are shown. The blue contours are made from a fit without any information from the direct Higgs searches and excluding the direct M_W and m_t measurements, while for the orange contours additionally the information of the direct Higgs searches are taken into account. Both indirect determinations agree with the direct measurements denoted by the green bands. The inclusion of the direct Higgs searches significantly decreases the allowed region. For illustration, the SM predictions for various Higgs masses are shown by

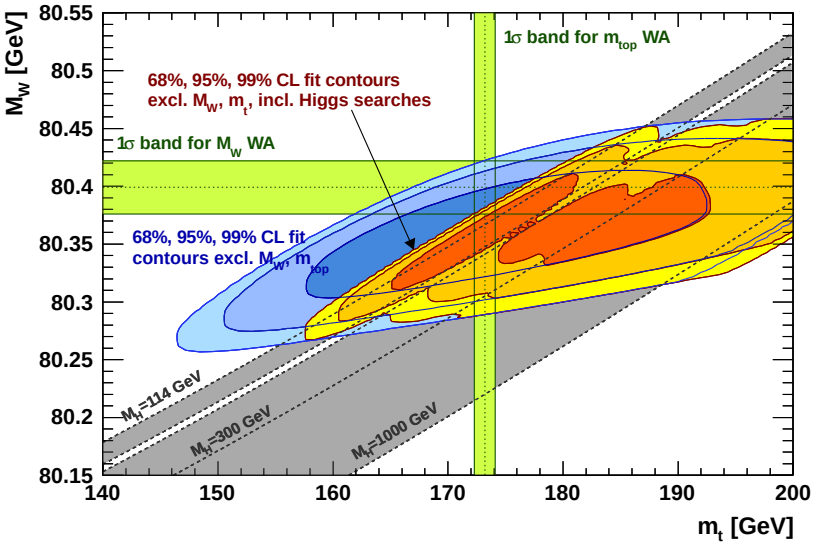

Figure 3.9: Contours of 68%, 95% and 99% CL obtained from scans of fits with fixed variable pairs M_W vs. m_t. The green bands represent the M_W and m_t world average with its 1σ uncertainty. The SM predictions for various Higgs masses are displayed by the gray isolines.

the gray isolines in fig. 3.9. As expected light Higgs bosons are preferred. The effect of the theoretical uncertainties is visible by the fact that the allowed region for the fit with the direct Higgs searches extends into the region of M_H smaller than the strict exclusion limit from LEP ($M_H < 114.4$ GeV). For the isolines no theoretical uncertainties are considered.

CHAPTER 4

Constraints on New Physics from the Electroweak Fit

The SM predictions of the electroweak precision observables can be extended by a parametrization of the oblique parameters, describing additional virtual-loop contributions. The oblique or S, T, U parametrization allows to constrain physics beyond the SM by the electroweak precision data. The analysis presented in this chapter has been recently published in [34] and the presentation in this chapter closely follows the presentation in this.

After the S, T, U parameters are introduced, their experimental constraints are discussed. By confronting the experimental S, T, U values with their predictions in a specific new physics model, allowed regions of the new model parameters can be estimated. The following models are revisited in this chapter: models with a sequential fourth fermion generation, the inert-Higgs doublet model, the littlest Higgs models with T-parity conservation, and models with large extra dimensions

4.1 Concept of Oblique Parameters

If the new physics mass scale is large and the new physics appears only through vacuum polarizations, the effects from physics beyond the SM can be parametrized by three gauge boson self-energy parameters called oblique parameters. Two different, but equivalent, sets of oblique parameters have been established in the past: $\varepsilon_{1,2,3}$ [93, 94] and S, T, U [3, 4]. Both sets are re-parametrizations of the form-factors $\Delta\rho$, $\Delta\kappa$ and Δr, which absorb the radiative corrections to the Z couplings, the effective weak mixing angle, and the W mass, respectively. If the scale of new physics is not much larger than the weak scale, additional parameters are required [95, 96]. However, they can be only independently determined when including data at higher center-of-mass energies than the Z pole, which is not carried out in this analysis. In addition, often an extra parameter is introduced in order to describe new physics contributions to the $Z \to b\bar{b}$ vertex, which receives non-negligible top quark corrections in the SM.

The $\varepsilon_{1,2,3}$ parameters [93, 94] include SM contributions dominated by top quark and Higgs boson corrections. By construction they vanish at Born level if the running of the QED coupling

is accounted for. They are defined by

$$\varepsilon_1 = \Delta\rho\,, \tag{4.1}$$

$$\varepsilon_2 = \cos^2\theta_W\Delta\rho + \frac{\sin^2\theta_G}{\cos^2\theta_W - \sin^2\theta_G}\Delta r - 2\sin^2\theta_G\Delta\kappa'\,, \tag{4.2}$$

$$\varepsilon_3 = \cos^2\theta_W\Delta\rho + (\cos^2\theta_W - \sin^2\theta_G)\Delta\kappa'\,, \tag{4.3}$$

with $\sin^2\theta_G = 1 - \sqrt{1 - \sqrt{8}\pi\alpha(M_Z^2)/(G_F M_Z^2)}$ and where $\Delta\kappa'$ relates $\sin^2\theta^f_{\text{eff}}$ to $\sin^2\theta_G$ instead of $\sin^2\theta_W$ (as in eq. (2.15)). The quadratic top mass dependence present in all form-factors has been removed explicitly from the parameters ε_2 and ε_3.

The S, T, U parameters [3, 4] can be directly related to the $\varepsilon_{1,2,3}$ parameters. They are constructed in a way that they vanish when a specific SM is assumed, *i.e.* fixed reference values for the top and Higgs mass. Therefore, the S, T, U parameters depend on a (somewhat arbitrary) SM reference point, while the physically relevant difference between the experimental S, T, U parameters and a model prediction is independent of the reference. The S, T, U parameters are defined via the $\varepsilon_{1,2,3}$ parameters and are normalized in a way that they are of order $\mathcal{O}(1)$

$$S = \varepsilon_3\frac{4\sin^2\theta_G}{\alpha(M_Z^2)} - d_S\,, \tag{4.4}$$

$$T = \varepsilon_1\frac{1}{\alpha(M_Z^2)} - d_T\,, \tag{4.5}$$

$$U = -\varepsilon_2\frac{4\sin^2\theta_G}{\alpha(M_Z^2)} - d_U\,, \tag{4.6}$$

where d_i are the SM predictions of the oblique parameters for the chosen M_H and m_t reference. In the following analysis the reference values $M_{H,\text{ref}} = 120$ GeV and $m_{t,\text{ref}} = 173$ GeV are used.

The S, T, U parameters describe different effects of new physics, which can be summarized as follows:

- The T parameter measures the difference between the new physics contributions of neutral and charged current processes at low energies, *i.e.* it is sensitive to weak isospin violation.
- The S (S+U) parameter describes new physics contributions to neutral (charged) current processes at different energy scales.
- The third parameter, U, is only constrained by the W boson mass and width. U is predicted to be small in most new physics models.

The determination of the S, T, U parameters is performed by comparing the measurements of the electroweak observables to their prediction in the S, T, U extended SM. The SM prediction of an observable, as described for the electroweak SM fit in section 3.2, is modified by the S, T, U parameters as follows

$$O = O_{\text{SM,ref}}(M_{H,\text{ref}}, m_{t,\text{ref}}) + c_S S + c_T T + c_U U\,, \tag{4.7}$$

where $O_{\text{SM,ref}}(M_{H,\text{ref}}, m_{t,\text{ref}})$ is the SM prediction of the observable in the reference SM. The values for the coefficients c_S, c_T, c_U are taken from [97].

4.2 Experimental Constraints on Oblique Parameters

The S, T, U parameters are extracted from a fit of the electroweak precision observables (*cf.* section 3.3) to their predictions (*cf.* eq. (4.7)). For the SM reference point $M_{H,\mathrm{ref}} = 120\,\mathrm{GeV}$ and $m_{t,\mathrm{ref}} = 173\,\mathrm{GeV}$ is used, while the other floating fit parameters including the S, T, U parameters can freely vary in the fit. The S, T, U parameters are constrained to

$$S = 0.04 \pm 0.10\,, \qquad T = 0.05 \pm 0.11\,, \qquad U = 0.08 \pm 0.11\,, \tag{4.8}$$

with the linear correlation coefficients of $+0.89$ between S and T, and -0.45 (-0.69) between S and U (T and U). Since in many new physics theories U is predicted to be zero, the results on S and T have been determined with the additional condition $U = 0$

$$S|_{U=0} = 0.07 \pm 0.09\,, \qquad T|_{U=0} = 0.10 \pm 0.08\,, \tag{4.9}$$

with a correlation coefficient of $+0.88$. The improved precision on S and T is due to the information of M_W and Γ_W, which otherwise is absorbed to determine the U parameter. The values are compatible with zero indicating that the chosen SM reference is in agreement with the experimental data. The values are also in agreement with studies performed by the LEP Electroweak Working Group [44] and for the electroweak review of the Particle Data Group [42].

In fig. 4.1 the 68%, 95% and 99% CL allowed regions in the (T, S)–plane are shown for $U = 0$ and the SM reference values $M_{H,\mathrm{ref}} = 120\,\mathrm{GeV}$ and $m_{t,\mathrm{ref}} = 173\,\mathrm{GeV}$. Additionally, the individual constraints from the asymmetry measurements, the Z partial and total widths, and the W mass and width are displayed for $U = 0$. Leaving U free would leave the former two constraints approximately unchanged, while the W mass and width would then constrain U rather than S or T. The 68%, 95% and 99% CL allowed regions in the (T, S)–plane for a freely floating U parameter (orange) are depicted in fig. 4.2. In both figures the gray shaded band represents the SM predictions for varying M_H and m_t. By construction, the SM prediction reproduces $S = T = U = 0$ at the $\mathrm{SM_{ref}}$ reference point. Since m_t is rather well known, the impact of the top mass on the SM prediction is small. In contrast, the variation of the Higgs mass can change the S and T values significantly. As expected, a light SM Higgs boson is favored over a heavy Higgs boson.

Figures 4.3(a)-(b) show the constraints in the (U,S)–plane and in the (T,U)–plane, respectively. In both figures the 68%, 95% and 99% CL allowed contours are presented. The third parameter can freely vary in the fits. The gray shaded areas indicate the SM prediction for varying M_H and m_t values. The Higgs mass dependence on the U parameter is rather small.

4.3 Constraints on New Physics Models

In many new physics models, the S, T, U parameters have been computed. By confronting the experimental S, T, U values with their theoretical predictions, one can either constrain the parameters of the new physics model or one can potentially exclude the entire model. The most prominent example is the analysis of technicolor models [98, 99], which introduce a

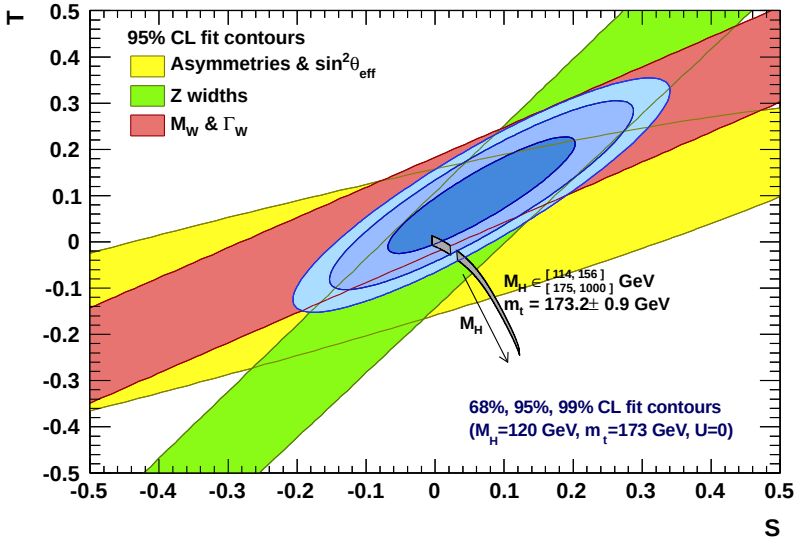

Figure 4.1: Allowed contours of 68%, 95% and 99% CL in the (T, S)–plane with U parameter fixed to zero. Additionally, the individual constraints are shown for $U = 0$ when considering only the given observables. The gray shaded area illustrates the SM prediction for varying M_H and m_t values.

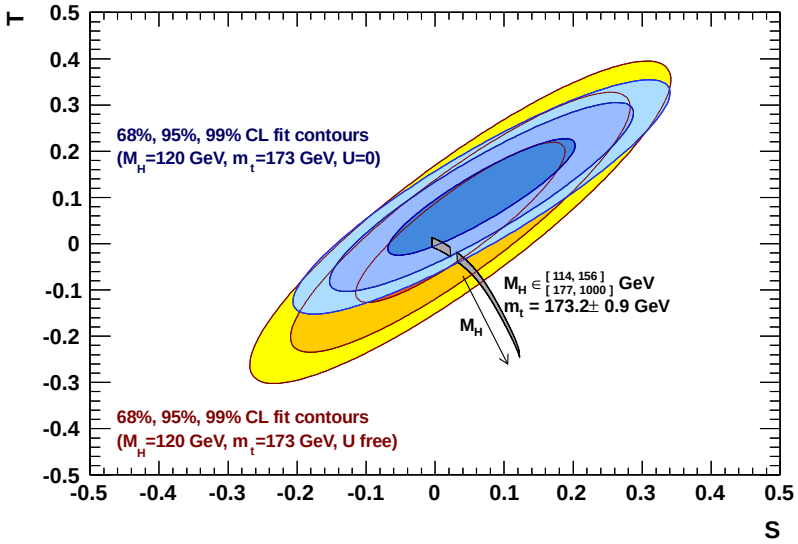

Figure 4.2: Allowed contours of 68%, 95% and 99% CL in the (T, S)–plane with a freely floating U parameter (orange) and $U = 0$, respectively. The gray shaded area illustrates the SM prediction for varying M_H and m_t values.

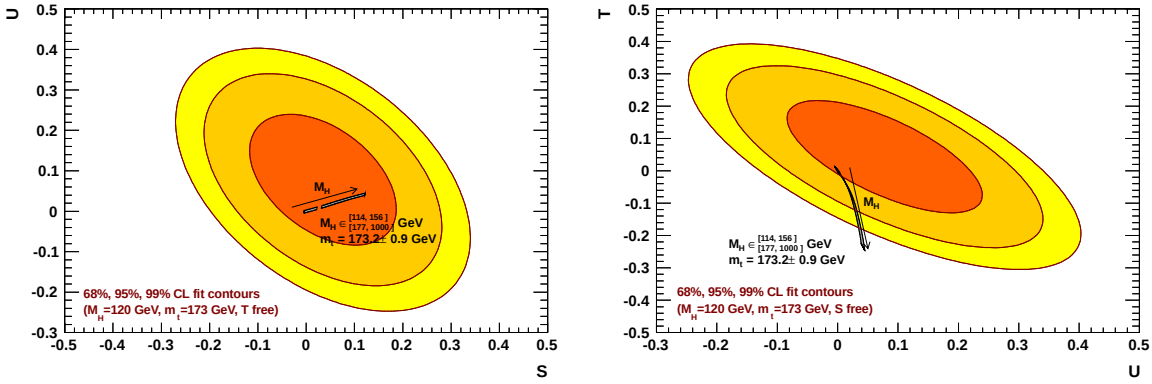

(a) (b)

Figure 4.3: Allowed contours of 68%, 95% and 99% CL (a) in the (U, S)–plane and (b) in the (T, U)–plane. The gray shaded area illustrates the SM prediction for varying M_H and m_t values.

new QCD-like gauge interaction. These QCD-like technicolor models are in conflict with the experimental S, T, U constraints and therefore they are excluded, see for instance [3, 4, 100–102] and recently [34].

The S, T, U values in a given new physics model are usually composed by the theoretical predictions of the new physics contributions and the non-vanishing SM remainders when the Higgs and top mass differ from those used for the SM reference. Within Gfitter it is possible to directly replace the S, T, U parameters in eq. (4.7) with the prediction of the new physics model. The Higgs and top mass dependence is introduced by the SM prediction O_{SM} in eq. (4.7). They read in one-loop approximation [4]

$$S \approx \frac{1}{12\pi} \ln \frac{M_H^2}{M_{H,\mathrm{ref}}^2} + \frac{1}{6\pi} \ln \frac{m_t^2}{m_{t,\mathrm{ref}}^2}\,, \tag{4.10}$$

$$T \approx -\frac{3}{16\pi \cos^2\theta_W} \ln \frac{M_H^2}{M_{H,\mathrm{ref}}^2} + \frac{3}{16\pi \sin^2\theta_W \cos^2\theta_W} \ln \frac{m_t^2 - m_{t,\mathrm{ref}}^2}{m_Z^2}\,, \tag{4.11}$$

$$U \approx \frac{1}{2\pi} \ln \frac{m_t^2}{m_{t,\mathrm{ref}}^2}\,. \tag{4.12}$$

Additionally to the S, T, U parameters physics beyond the SM can contribute to the $Z \to b\bar{b}$ vertex, which receives significant top quark corrections in the SM. These additional vertex corrections are implemented via two new parameters, $\delta g_L^{b\bar{b}}$ and $\delta g_R^{b\bar{b}}$, according to [103]. In the S, T, U fits they are set to zero. Only in new physics models with additional corrections to the $Z \to b\bar{b}$ vertex they are used.

Many new physics models feature a similar agreement with the data as observed for the SM. Nevertheless, the predictions of these models can cover large regions in the S, T, U space due to additional undetermined model parameters, which can be constrained via the oblique parameter formalism from the data. Most (though not all) models decouple at high scales from the SM so that the oblique corrections reproduce the SM values. New physics models providing

additional weak isospin violation can allow large Higgs boson masses, due to the cancellation of the Higgs mass induced negative T value and the model-induced positive contributions.

In the following analysis the electroweak constraints of various new physics models are revisited and consistently updated with respect to the most recent measurements of the electroweak precision observables. The original publications are listed in the corresponding sections.

4.3.1 Inert-Higgs Doublet Model

The inert-Higgs doublet model (IHDM) has been firstly developed by [104] and has been reconsidered by [105]. In this model the hierarchy problem, as discussed in section 2.1.1, is diluted due to the possibility of a heavy Higgs boson.[1] In order to be still in agreement with the electroweak precision data, which predicts a light Higgs boson mass, a second inert-Higgs doublet H_2 is introduced. Although H_2 has weak and quartic interactions, it does not acquire a vacuum expectation value, nor has it any other couplings to matter. This is ensured by a conserved parity symmetry Z_2. The H_2 doublet transforms odd under Z_2, while all SM fields have even Z_2-parity. As a consequence, the lightest inert scalar (LIP) is stable and a suitable dark matter candidate, if it is electrically neutral. In the literature three different mass regions of the LIP are discussed [105–113]: the low mass region (few GeV), the intermediate mass region (40-160 GeV), and the high mass region (above 500 GeV).

Besides the SM-like Higgs (h_0), the inert doublet H_2 induces two charged Higgs states of equal mass ($H^\pm$) and two neutral ones (H^0 and A^0), where the lightest neutral state, which could be either H^0 or A^0, is typically assumed to be the LIP. The free model parameters of the IHDM are the three Higgs masses, $M_{H^\pm}$, M_{H^0}, M_{A^0}, and two quartic couplings. One of the quartic couplings only affects the inert particles while the other one, involving both Higgs doublets, impacts measurable observables [105]. The oblique corrections induced by the IHDM have been computed in [105]

$$S = \frac{1}{2\pi}\left(\frac{1}{6}\ln\frac{M^2_{H^0}}{M^2_{H^\pm}} - \frac{5}{36} + \frac{M^2_{H^0}M^2_{A^0}}{3(M^2_{A^0}-M^2_{H^0})^2} + \frac{M^4_{A^0}(M^2_{A^0}-3M^2_{H^0})}{6(M^2_{A^0}-M^2_{H^0})^3}\ln\frac{M^2_{A^0}}{M^2_{H^0}}\right) \quad (4.13)$$

$$T = \frac{1}{32\pi^2\alpha v^2}\Big(F(M_{H^\pm},M_{H^0}) + F(M_{H^\pm},M_{A^0}) - F(M_{A^0},M_{H^0})\Big), \quad (4.14)$$

where $F(m_1,m_2) = (m_1^2+m_2^2)/2 - m_1^2m_2^2/(m_1^2-m_2^2)\cdot\ln(m_1^2/m_2^2)$. The function F is positive, symmetric with respect to an interchange of its arguments, and it vanishes for $m_1 = m_2$. For approximate H^0, A^0 mass degeneracy one finds $T \propto (M_{H^\pm}-M_{H^0})(M_{H^\pm}-M_{A^0})$ [105]. Contributions to the U oblique parameter are neglected.

In fig. 4.4 the experimental S, T fit results (for $U=0$) are compared to IHDM predictions shown by the green area. The SM predictions are displayed by the gray band. The bounds of the free model parameters are given on the plot. Good overlap between the experimental constraints and the IHDM prediction is observed. In addition, three representative mass parameter settings, fulfilling the electroweak constraints, are displayed by the symbols. In this analysis,

[1] A heavy Higgs boson of 500 GeV would lift the naturalness cut-off scale to roughly 1.5 TeV.

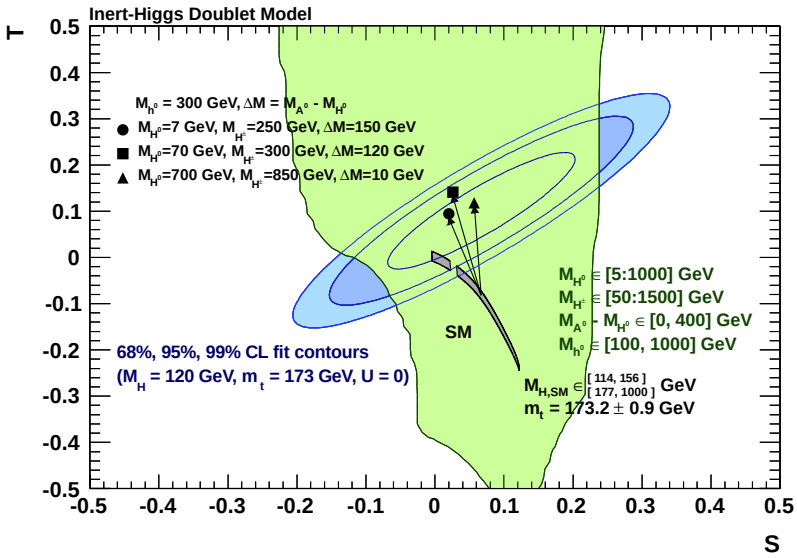

Figure 4.4: Comparison of the experimental S, T fit results (for $U = 0$) with the predictions from the SM (gray) and the inert-Higgs doublet model (green), respectively. The symbols illustrate the inert-Higgs doublet model predictions for three example settings, compared to the corresponding SM predictions via the arrows.

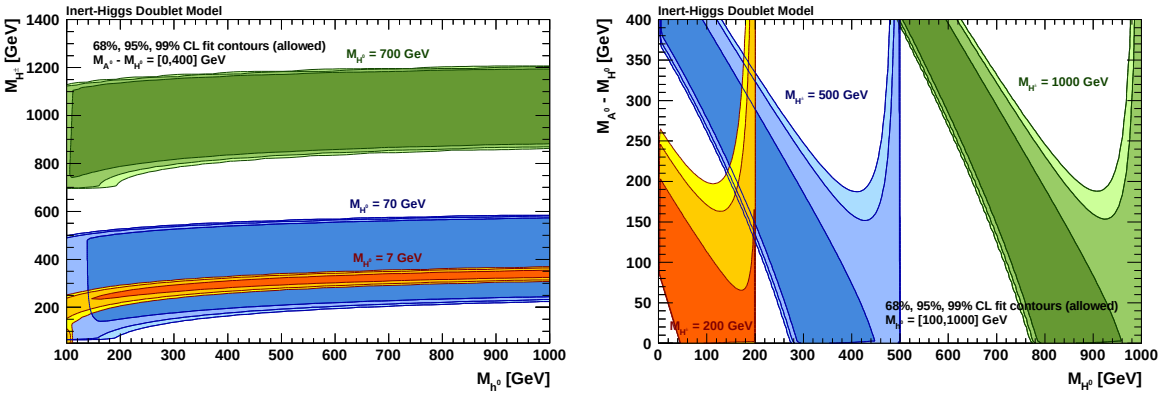

(a) (b)

Figure 4.5: Constraints in the inert-Higgs doublet model. Shown are the 68%, 95%, and 99% CL allowed fit contours in the (a) ($M_{H^\pm}$, M_{h^0})–plane and (b) ($M_{A^0} - M_{H^0}$, M_{H^0})–plane for the parameter settings given on the plots.

the H_0 Higgs state is considered as LIP, *i.e.* the conditions $M_{A^0} > M_{H^0}$ and $M_{H^\pm} > M_{H^0}$ are required.

Figure 4.5(a) displays the 68%, 95%, and 99% CL allowed regions in the ($M_{H^\pm}$, M_{h^0})–plane. The contours are shown for three different values of M_{H^0} (7 GeV, 70 GeV, and 700 GeV) representing the three different LIP mass regions as discussed above. The mass splitting between M_{A^0} and M_{H^0} is bounded to be within [0,400] GeV. By construction in all of the three settings large SM-like Higgs masses are allowed. For large M_{h^0} the allowed values for $M_{H^\pm}$ are approximately independent of M_{h^0}.

In fig. 4.5(b) the 68%, 95%, and 99% CL allowed regions in the ($M_{A^0} - M_{H^0}$, M_{H^0})–plane are displayed for three settings of $M_{H^\pm}$. The SM-like Higgs can freely vary between 100 and 1000 GeV. The neutral LIP requirement leads to the sharp vertical bound in the contours. The constraint from T puts bounds on the mass splitting between the inert Higgs states.

4.3.2 Models with a Sequential Fourth Fermion Generation

One of the simplest new physics models is the introduction of a sequential new generation of chiral matter. In this section a generic model with only one extra generation is investigated. The masses of the new fermions are generated via Yukawa couplings to the Higgs field. However, if the new fermions are too heavy the coupling would become so strong that the concept of a scalar Higgs field is no longer appropriate.[1] This can point to some new strong interaction being responsible for electroweak symmetry breaking via a condensation of the fourth generation fermions, *cf.* [114, 115]. The introduction of a new sequential fourth generation could solve the matter anti-matter asymmetry in the universe [116] by additional CP violation. Additionally, new stable hadrons, composed by the new quarks, could provide a possible dark matter candidate, see for example [117] and its references.

In a generic model with only one extra generation, two new fermions with the same properties as the original SM generations are added to the lepton and quark sector. The new unconstrained model parameters are the masses m_{u_4}, m_{d_4}, m_{ν_4}, m_{e_4} of the fourth generation quarks and leptons, and CP conserving and CP violating neutrino and quark mixing parameters. The fourth generation particles must have a mass of at least $M_Z/2$, to not contribute to the width of the Z boson.

Several experimental constraints on the masses of the new fermions have been determined. The most stringent lower limits on the masses of the fourth generation quarks arise from ATLAS [118], excluding d_4 and u_4 quark masses below 270 GeV with 95% CL, CMS [119], excluding d_4 masses between 255 and 361 GeV, and the Tevatron experiments where the latest analysis from CDF excludes u_4 quarks below 358 GeV and d_4 quarks below 372 GeV [120, 121]. The u_4 searches assume predominant decays into W bosons and SM quarks, requiring a small u_4–d_4 mass splitting to suppress the decay $u_4 \to W d_4$. The CMS and Tevatron d_4 searches assume a $d_4 \to Wt$ branching fraction of one on the basis of the observed unitarity of the three-generation quark mixing matrix suggesting small flavor-changing currents to light quarks. This

[1] A fourth generation would also enhance the hierarchy problem described in section 2.1.1.

also neglects the possibility of an inverted fourth generation mass hierarchy. The CDF limits have been re-analyzed in [122, 123] under more general quark mixing scenarios, leading to a weaker limit of 290 GeV for both quark flavors. The fourth generation leptons are mostly constrained by the LEP experiments. A lower limit of about 101 GeV for sequential heavy leptons decaying to $W\nu$ and $Z\ell$, or to $W\ell$ and $Z\nu$, depending on their electromagnetic charge, has been achieved [124]. In addition, the consequences of a fourth generation on the flavor sector of neutrinos, charged leptons and quarks have been extensively explored, see for instance [125–136] and the review [137].

Additionally, a sequential fourth generation of heavy quarks increases the gluon fusion to the Higgs production cross-section. The dominant triangular top-loop is increased by a factor of 9. Therefore, the Higgs boson discovery or exclusion potential is enlarged. The re-interpretation of the direct Higgs searches leads to following exclusion limits: $131 < M_H < 204\,\text{GeV}$ for the Tevatron experiments [138], $140 < M_H < 185\,\text{GeV}$ for ATLAS [78], and $144 < M_H < 207\,\text{GeV}$ for CMS [79].[1]

The impact of the fourth generation on the electroweak precision observables has been studied in various analyses [40, 131, 140–146]. In this analysis the oblique corrections, assuming negligible mixing of the fourth generation with the SM fermions,[2] are taken from [141]

$$\begin{aligned} S &= \frac{N_C}{6\pi}\Bigg\{(8Y+6)x_1-(8Y-6)x_2-2Y\ln\frac{x_1}{x_2} \\ &\quad + \left[\left(\frac{3}{2}+2Y\right)x_1+Y\right]G(x_1)+\left[\left(\frac{3}{2}-2Y\right)x_2-Y\right]G(x_2)\Bigg\}, \end{aligned} \tag{4.15}$$

$$T = \frac{N_C}{8\pi s_W^2 c_W^2}F(x_1,x_2)\,, \tag{4.16}$$

$$\begin{aligned} U &= -\frac{N_C}{2\pi}\Bigg\{\frac{1}{2}(x_1+x_2)-\frac{1}{3}(x_1-x_2)^2+\left[\frac{1}{6}(x_1-x_2)^3-\frac{1}{2}\frac{x_1^2+x_2^2}{x_1-x_2}\right]\ln\frac{x_1}{x_2} \\ &\quad + \frac{1}{6}(x_1-1)f(x_1,x_1)+\frac{1}{6}(x_2-1)f(x_2,x_2) \\ &\quad + \left[\frac{1}{3}-\frac{1}{6}(x_1+x_2)-\frac{1}{6}(x_1-x_2)^2\right]f(x_1,x_2)\Bigg\}, \end{aligned} \tag{4.17}$$

where $Y = 1/6\,(-1/2)$ is the weak hypercharge for quarks (leptons), $N_C = 3\,(1)$ for quarks (leptons), $x_i = (m_{i_4}/M_Z)^2$ with $i = 1, 2$ for the up and down-type fourth generation fermions, respectively.[1]

[1] The ATLAS and CMS collaborations have recently presented preliminary updates for the 2011 data [80, 139]. In the fourth generation model, both experiments can exclude Higgs masses between 120-600 GeV at the 95% CL. This new result is not taken into account in this analysis.

[2] A detailed numerical SM4 analysis [131] taking into account low-energy FCNC processes in the quark sector, electroweak oblique corrections, and lepton decays (but not lepton mixing) concludes that small mixing between the quarks of the first three and those of the fourth family is favored. The value of $|V_{tb}|$ is found in this analysis to exceed 0.93. The no-mixing assumption allows us to use the measured value of G_F, extracted from the muon lifetime under the SM3 hypothesis, to its full precision [135].

[1] The functions in eqs. ((4.15)–(4.17)) are defined as follows. $F(x_1,x_2) = (x_1+x_2)/2 - x_1x_2/(x_1-x_2)\cdot\ln(x_1/x_2)$, $G(x) = -4y\arctan(1/y)$, $y = \sqrt{4x-1}$, and $f(x_1,x_2) = -2\sqrt{\Delta}[\arctan((x_1-x_2+1)/\sqrt{\Delta}) -$

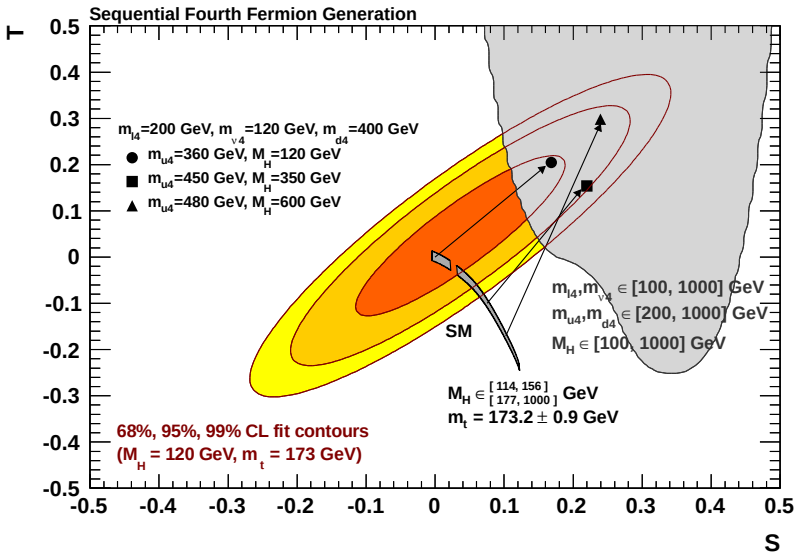

Figure 4.6: Comparison of the experimental S, T fit results (for U free) with the predictions from the SM (dark gray band) and the sequential fourth fermion generation model (light gray area), respectively. The symbols illustrate the predictions of the fourth fermion generation model for three example settings, compared to the corresponding SM predictions via the arrows.

In the limit of large and degenerate up and down-type fermion masses, the S parameter converges to $2/(3\pi) \simeq 0.21$. Larger positive values for S can be achieved by smaller fourth generation fermion masses. An increasing mass splitting of the leptons would further increase the S parameter, while the mass splitting of quarks would reduce it. Also negative values for S are allowed, *e.g.* for $m_{u_4} > m_{d_4}$ or $m_{l_4} > m_{\nu_4}$. The T parameter is always positive or zero. In case of approximate mass degeneracy, T is proportional to the difference between up and down-type mass-squared relative to M_Z^2. The U parameter takes also only positive values and it is at zero for degenerate fourth fermion masses. The maximum value is obtained at maximum mass splitting: $U \simeq 0.49(\text{quarks}) + 0.16(\text{leptons}) \simeq 0.66$ for freely varying masses within the range $[100, 1000]$ GeV.

Figure 4.6 shows a comparison in the (T, S)–plane between the experimental results (orange ellipses) and the predictions of the fourth fermion generation model (light gray area). The bounds of the model parameters used for the determination of the allowed regions are displayed on the plot. The experimental exclusion limits of the Higgs mass in the sequential fourth fermion model, as discussed above, are not taken into account. Nevertheless, the allowed region would not be affected by those Higgs exclusion limits. Additionally, three parameter settings are shown which fulfill the experimental constraints. The arrows indicate the change of the SM prediction (dark gray band) for the given Higgs mass when adding the contribution from the fourth fermions.

$\arctan((x_1-x_2-1)/\sqrt{\Delta})]$ for $\Delta > 0$, $f(x_1, x_2) = 0$ for $\Delta = 0$, and $f(x_1, x_2) = \sqrt{-\Delta}\cdot\ln((X+\sqrt{-\Delta})/(X-\sqrt{-\Delta}))$ with $X = x_1 + x_2 - 1$ for $\Delta < 0$, and where $\Delta = 2(x_1 + x_2) - (x_1 - x_2)^2 - 1$.

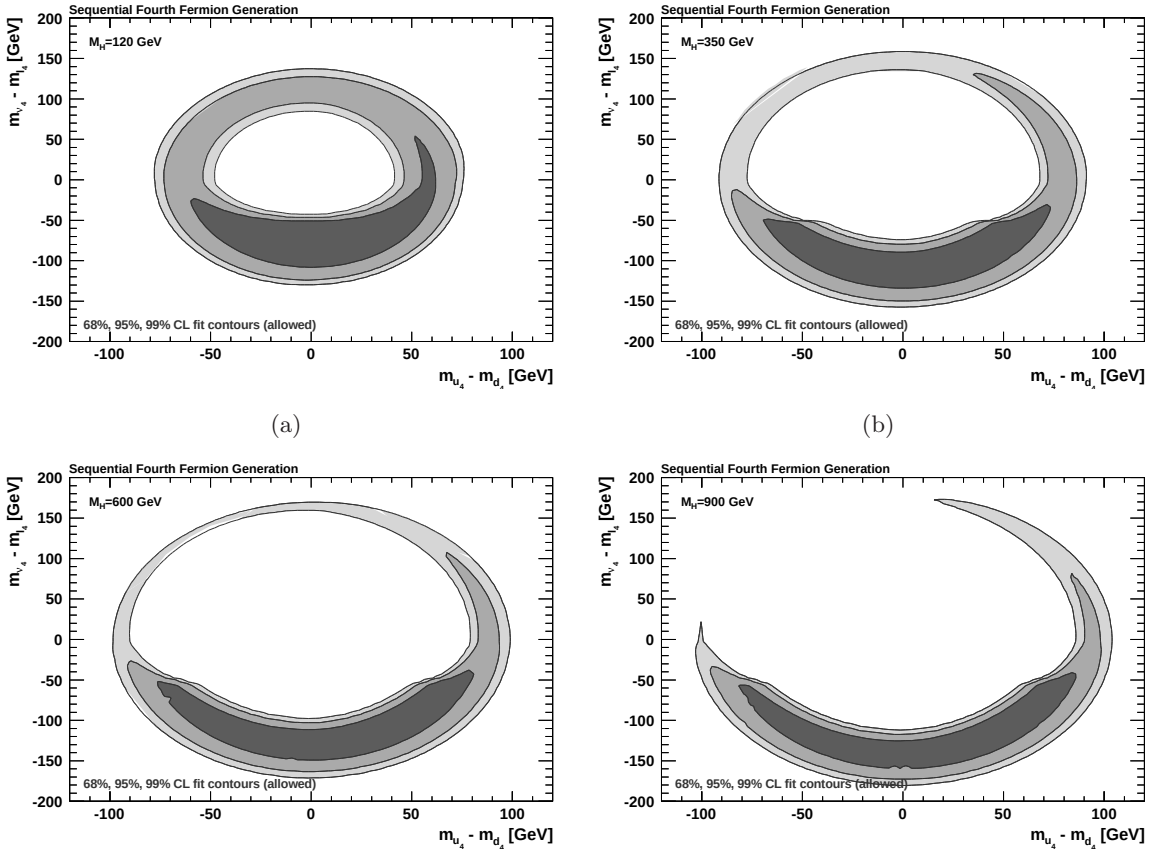

Figure 4.7: Constraints in a model with a fourth fermion generation. Shown are the 68%, 95% and 99% CL allowed fit contours in the $(m_{l_4} - m_{\nu_4},\, m_{u_4} - m_{d_4})$ plane as derived from the fit for (a) $M_H = 120$ GeV, (b) $M_H = 350$ GeV, (c) $M_H = 600$ GeV, and (d) $M_H = 900$ GeV.

The S, T, U parameters depend mainly on the mass splitting of up and down-type fermions instead of their absolute masses. In figs. 4.7(a)-(d) the 68%, 95% and 99% CL allowed regions in the $(m_{l_4} - m_{\nu_4},\, m_{u_4} - m_{d_4})$–plane are displayed for various Higgs mass values: (a) $M_H = 120$ GeV, (b) $M_H = 350$ GeV, (c) $M_H = 600$ GeV, and (d) $M_H = 900$ GeV. Large values of M_H, inducing a negative value of T, can be compensated by a positive shift due to large fermion mass splittings. In all plots the precision data prefers $m_{l_4} > m_{\nu_4}$. This behavior is amplified for large Higgs masses, since the positive shift in S, induced by large M_H values, needs to be canceled by a large mass splitting in the lepton sector.

4.3.3 Littlest Higgs with T-Parity Conservation

Little Higgs models have been introduced in particular to tackle the hierarchy problem of the SM [147, 148]. In these models the Higgs is a pseudo-Goldstone boson resulting from approximate symmetries, that are collectively broken by gauge, Yukawa and scalar couplings. One-loop radiative corrections to the Higgs mass are forbidden. Only at multi-loop order

quadratically divergent corrections to the Higgs mass arise featuring a naturally light Higgs boson [148]. The global symmetries are broken at a scale f, where new gauge bosons, fermions, and scalars arise which cancel the top-loop contribution to M_H in the SM (*cf.* section 2.1.1).

The littlest Higgs (LH) model [149] is one of the simplest little Higgs realizations. It relies on a non-linear 1σ model describing $SU(5)/SO(5)$ symmetry breaking at a scale f ($\sim$TeV). At an energy cut-off of $\Lambda = 4\pi f$, the non-linear 1σ model becomes strongly coupled and the LH model needs to be replaced by a more fundamental theory. Below the breaking scale f one finds the SM particles including a light Higgs, while the new LH particles are located above the breaking scale. It has been exposed that the original LH model does not satisfy the constraints from the electroweak precision data, mainly due to the allowed tree-level exchange of the new heavy gauge bosons [96, 150–154]. In order to avoid tree-level exchange a conserved discrete symmetry (T-parity) has been introduced [155, 156]. The LH model with T-parity conservation is characterized by two new top-like states which transform T-even and T-odd, respectively. Additionally, to each SM gauge boson a T-odd partner boson is introduced. The lightest and electrically neutral one is stable and could account for the relic dark matter density of the universe [157]. For every light SM fermion state a T-odd partner exists, as well.

The analysis presented here follows the one of [158]. The dominant oblique corrections in the LH model with T-parity conservation arise from the T-even top state T_+ which mixes to the SM top quark. In the limit $m_t \ll m_{T_+}$ these corrections are given by [158]

$$S_{T_+} = \frac{1}{3\pi}\left(\frac{1}{s_\lambda^2}-1\right)\frac{m_t^2}{m_{T_+}^2}\left(-\frac{5}{2}+\ln\frac{m_{T_+}^2}{m_t^2}\right), \tag{4.18}$$

$$T_{T_+} = \frac{3}{8\pi}\frac{1}{\sin^2\theta_W\cos^2\theta_W}\left(\frac{1}{s_\lambda^2}-1\right)\frac{m_t^4}{m_{T_+}^2 M_Z^2}\left(\ln\frac{m_{T_+}^2}{m_t^2}-\frac{3}{2}+\frac{1}{2s_\lambda^2}\right), \tag{4.19}$$

$$U_{T_+} = \frac{5}{6\pi}\left(\frac{1}{s_\lambda^2}-1\right)\frac{m_t^2}{m_{T_+}^2}, \tag{4.20}$$

with

$$m_{T_+} = m_t\sqrt{\frac{1}{s_\lambda^2\left(1-s_\lambda^2\right)}}\frac{f}{v}, \tag{4.21}$$

where v is the Higgs vacuum expectation value and f the symmetry breaking scale. The parameter s_λ is approximately the mass ratio of the new T-odd and T-even top states, $s_\lambda \approx m_{T^-}/m_{T^+}$,[1] which is restricted by the model to be smaller than one. The T parameter dominates over S and U by a factor of $\sim m_t^2/(\sin^2\theta_W\cos^2\theta_W M_Z^2) \sim 20$. The positive contribution to T in the LH model with T-parity conservation can be compensated by a negative SM correction due to large Higgs masses. When s_λ is close to one, *i.e.* when t–T_+ mixing is suppressed, the oblique corrections from the T-even top state are small. Thus, additional contributions to the S, T, U parameters become more important. The one-loop corrections to the T parameter

[1] The parameter s_λ is exactly defined by $s_\lambda = \lambda_2/\sqrt{\lambda_1^2+\lambda_2^2}$, where λ_1 and λ_2 are the top Yukawa couplings of the new top states.

from the new gauge sector reads [156, 158]

$$T_{\text{gauge}} = -\frac{1}{4\pi \sin^2\theta_W}\frac{v^2}{f^2}\left(\delta_c + \frac{9}{4}\ln\frac{2\pi v}{M_W}\right), \tag{4.22}$$

where δ_c is a coefficient of order one, whose exact value depends on the details of the unknown UV physics.[1] The authors of [159] have also computed the contribution from the new gauge sector in the LH model with T-parity conservation. They found a slightly different result, $T_{\text{gauge}} = -\frac{1}{4\pi \sin^2\theta_W}\frac{v^2}{f^2}\delta_c$. However, the final fit results do not significantly change for the two different calculations due to the ambiguity in δ_c and the fact that the corrections from the new gauge sector are rather small. In this analysis the result of eq. (4.22) is used. The contribution to the T parameter from the T-odd partners of the light SM fermions has been found to increase with the masses of the partners. From LEP constraints on four-fermion contact interaction (the *ddee* channel providing the most stringent lower bound), an upper bound on these masses can be derived leading to a maximum contribution to the T parameter of [158]

$$T_{T\text{-odd fermions}} < 0.05\,, \tag{4.23}$$

for each T-odd fermion partner of the twelve SM fermion doublets.

In addition, the T-even top state affects the $Z \to b\bar{b}$ vertex via Goldstone boson exchange. In the limit $m_{T_+} \gg m_t \gg M_W$ the additional leading order correction is [158]

$$\delta g_L^{b\bar{b}} = \frac{g}{c_w}\frac{\alpha}{8\pi \sin^2\theta_W}\frac{m_t^4}{M_W^2 m_{T_+}^2}\left(\frac{1}{s_\lambda^2} - 1\right)\ln\frac{m_{T_+}^2}{m_t^2}\,. \tag{4.24}$$

Figure 4.8 shows the S and T predictions from the LH model with T-parity conservation in comparison to their experimental constraints from the electroweak precision data. The used parameter ranges are given on the plot. The S dependence arises mostly from the varying Higgs mass between 114 and 1000 GeV. Because large positive values for T are allowed, a heavy Higgs boson can be realized in this model, see for instance the symbols on the plot indicating three possible parameter settings.

In fig. 4.9 the electroweak constraints are translated into the LH parameter space. The 68%, 95% and 99% CL allowed regions in the (f, s_λ)–plane for a fixed value of $M_H = 120$ GeV are displayed. The green contours are made from fits when neglecting the effects from the T-odd fermions, while for the blue contours the maximum contribution from the T-odd fermions (*cf.* eq. (4.23)) is assumed. The χ^2 of the fit when considering the maximal effect from the T-odd fermions is approximately two units larger than for the fit ignoring those contributions. In both cases large values of the symmetry breaking scale f are allowed.

The figs. 4.10(a)-(d) show the 68%, 95% and 99% CL allowed regions in the (f, M_H)–plane for fixed values of (a) $s_\lambda = 0.45$, (b) $s_\lambda = 0.55$, (c) $s_\lambda = 0.65$, and (d) $s_\lambda = 0.75$. From the green contours it is visible that small values of f allow large values for M_H. For $s_\lambda = 0.75$ Higgs masses above 400 GeV are excluded. By assuming the maximum contribution from the T-odd fermions the allowed regions (blue contours) are reduced significantly. For $s_\lambda = 0.65$

[1] The δ_c parameter is treated as theory uncertainty varying in the range $[-5, 5]$ in the fit.

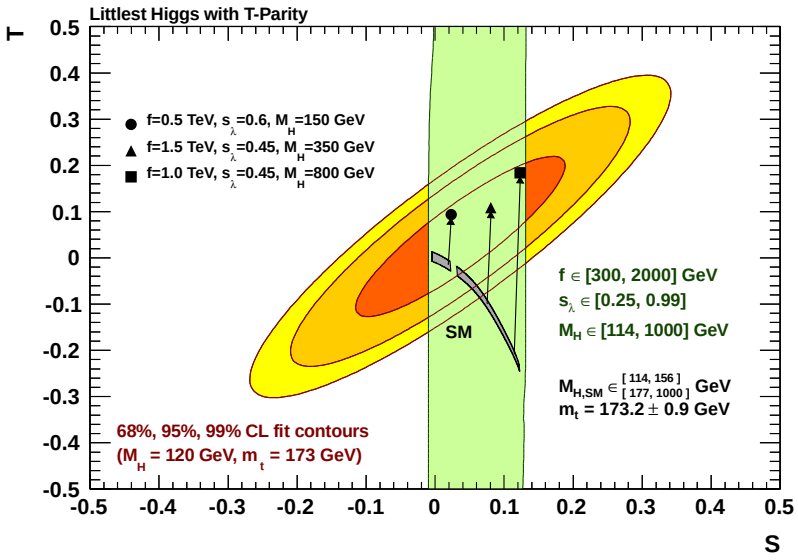

Figure 4.8: Comparison of the experimental S, T fit results (for U free) with the predictions from the SM (gray band) and the littlest Higgs with T-parity conservation (green area), respectively. The symbols illustrate the predictions of the littlest Higgs model with T-parity conservation for three example settings, compared to the corresponding SM predictions via the arrows.

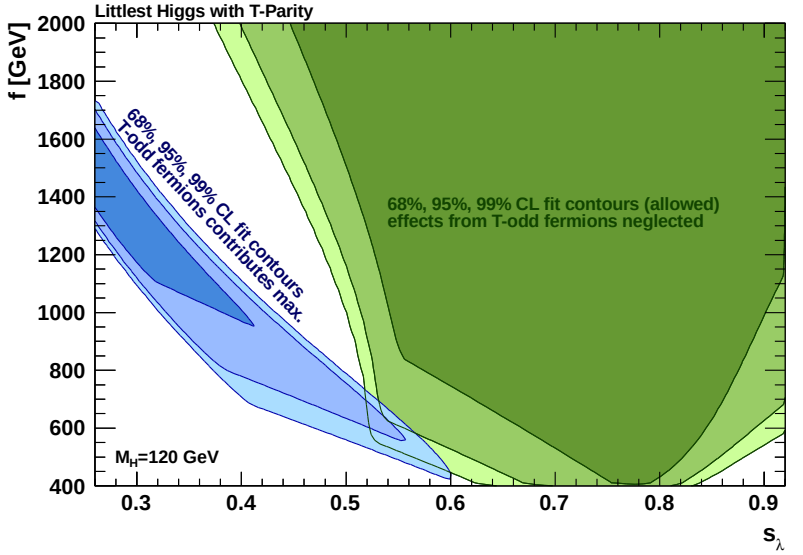

Figure 4.9: Constraints in the littlest Higgs model with T-parity conservation. Shown are the 68%, 95%, and 99% CL allowed fit contours in the (f, s_λ)–plane for the parameter settings given on the plots.

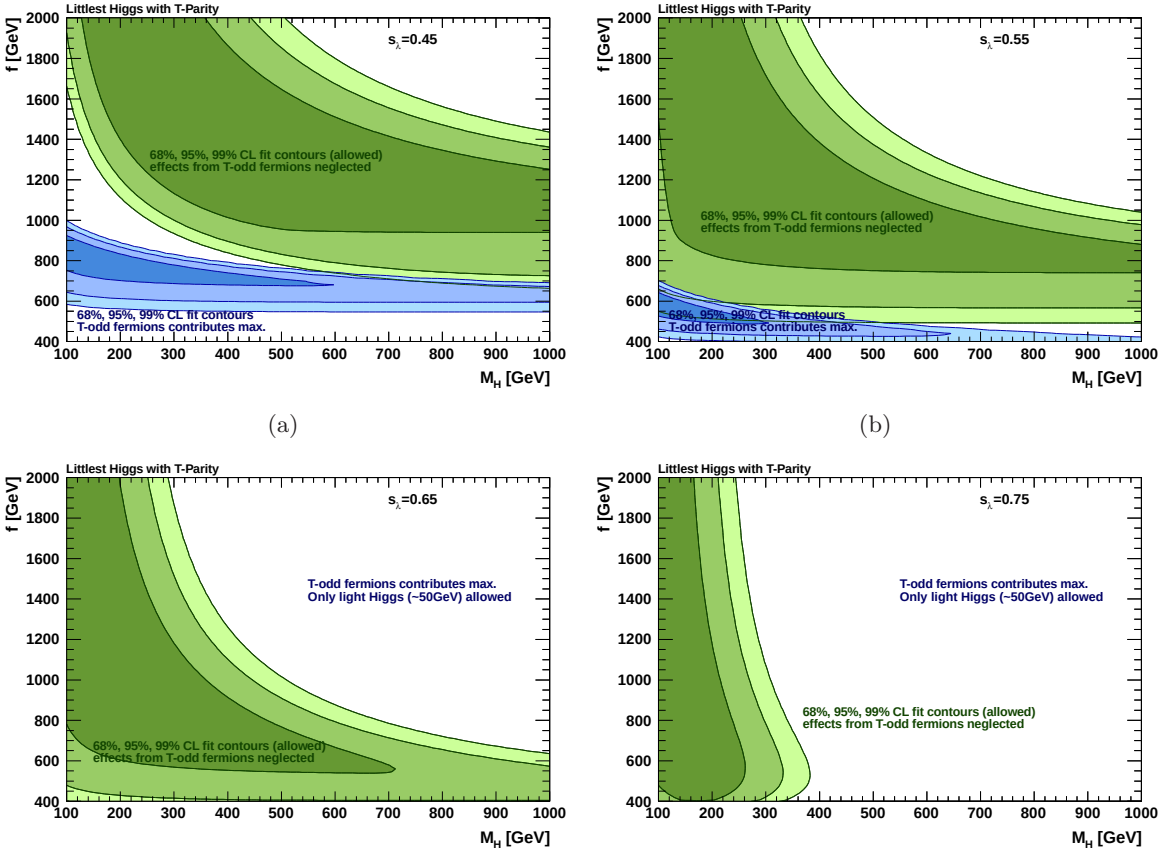

Figure 4.10: Constraints in the littlest Higgs model with T-parity conservation. Shown are the 68%, 95% and 99% CL allowed fit contours in the (f, M_H)–plane as derived from the fit for (a) $s_\lambda = 0.45$, (b) $s_\lambda = 0.55$, (c) $s_\lambda = 0.65$, and (d) $s_\lambda = 0.75$.

and $s_\lambda = 0.75$ only Higgs masses around 50 GeV are allowed, which are already excluded by the LEP experiments [76]. It should be also noticed that the amount of fine-tuning in the LH model decreases with increasing Higgs mass values [158, 160]. By considering this fact small values for s_λ are more favored, since they allow large values for M_H.

4.3.4 Models with Large Extra Dimensions

Models with large extra dimensions (LEDs) [161, 162] are a possibility to explain the weakness of gravity in comparison to the other forces. In these models the SM fields are confined to the four-dimensional membrane (brane), while gravity can also propagate in the extra dimensions (bulk). Thus, the strength of gravity is diluted in contrast to the other forces. The size of the Planck scale (M_{Pl}) is reduced to the visible scale[1]

$$M_D \approx \frac{1}{2\pi R} \left(2\pi R M_{Pl}\right)^{\frac{2}{\delta+2}} , \tag{4.25}$$

[1]The Planck scale is the energy scale at which gravity becomes strong and the quantum field description of particle physics breaks down ($\sim 10^{19}$ GeV).

where δ is the number of extra dimensions and R is the radius of an extra dimension that is compactified on a torus.[2] A single extra dimension is already ruled out, since if $\delta = 1$ and $M_D \sim 10$ TeV, then $R \lesssim 10^{12}$ cm which is not consistent with Newton's inverse-square law, that is well-established at such distances [163]. For $\delta = 2$ ($\delta > 2$) and requiring $M_D \sim$ TeV, the size of the extra dimension would be of order 100 μm ($< 10^{-7}$ cm). A direct search for a violation of the Newtonian law sets a 95% CL upper bound of $R \leq 44$ μm on the size of the large extra dimension [164], whereas for $\delta = 2$ the result on R is slightly tighter giving the lower bound $M_D > 3.6$ TeV [165]. Under certain model assumptions there exist strong astrophysical constraints on large extra dimensions, excluding Planck scales of up to $M_D > 1700\,(60)$ TeV for $\delta = 2\,(3)$ [166].

Gravitons propagating in the compact extra dimensions exhibit towers of Kaluza-Klein (KK) excitations with masses that are multiples of $\sim R^{-1}$. Since R is small in LED models, the mass spectrum is quasi–continuous and cannot be resolved in an accelerator experiment. The impact on physical observables (*e.g.* cross-section, forward-backward asymmetry) can be computed by summing over the large number of KK graviton states in a tower. However, this sum is ultraviolet divergent requiring a cut-off and the modeling of the ultraviolet completion. The cut-off scale Λ is related, but not necessarily equal to M_D [167–170]. It should, however, not be chosen much larger than M_D due to the unknown ultraviolet physics. Naive dimensional analysis, for example, sets upper limits at which gravity becomes strongly interacting of $\Lambda/M_D \simeq 5.4\,(2.7)$ for $\delta = 1\,(2)$, and further decreasing limits for a larger number of extra dimensions δ [170, 171].

Several direct accelerator-based searches for LEDs have been performed by the LEP, Tevatron, and LHC experiments (*cf.* for instance [172]). At LEP exclusion limits for M_D between 1.6 TeV for $\delta = 2$ and 0.66 TeV for $\delta = 6$ [173] have been determined by investigating direct graviton production and the virtual effects on the di-lepton and di-boson production. The Tevatron experiments have searched for large extra dimensions in di-electron, di-photon, mono-jet and mono-photon channels (*cf.* the review [172] and its references). These searches lead to M_D exclusion limits exceeding the LEP bounds for $\delta \geq 4$ [172]. The CMS collaboration excludes M_D values below 1.6–2.3 TeV at 95% CL [174], depending on the number of LEDs and the ultra-violet cut-off scale. While CMS has searched for deviations in the di-photon mass spectrum, at ATLAS the limit has been determined by looking for mono-jets, $M_D > 2.3$ TeV, 2.0 TeV and 1.8 TeV for $\delta = 2$, $\delta = 3$ and $\delta = 4$, respectively [175].

The S, T, U parameters are not sufficient to describe contributions from LEDs to the precision observables, since gravity does not appear only through vacuum polarization [171]. In contrast, the $\varepsilon_{1,2,3}$ parameters contain also corrections to the vector and axial-vector form-factors. However, those corrections cancel by a simple combination of the ϵ parameters [171]

$$\overline{\varepsilon} = \varepsilon_1 - \varepsilon_2 - \varepsilon_3 \cdot \tan^2\theta_W \,, \tag{4.26}$$

in which only the vacuum polarization correction difference remains. This combination can be easily translated into the S, T, U parameters, $\overline{\varepsilon} = \alpha(M_Z^2)(T + U/(4\sin^2\theta_W) - S/(4\cos^2\theta_W))$.

[2] It is assumed that all extra dimensions have the same curvature.

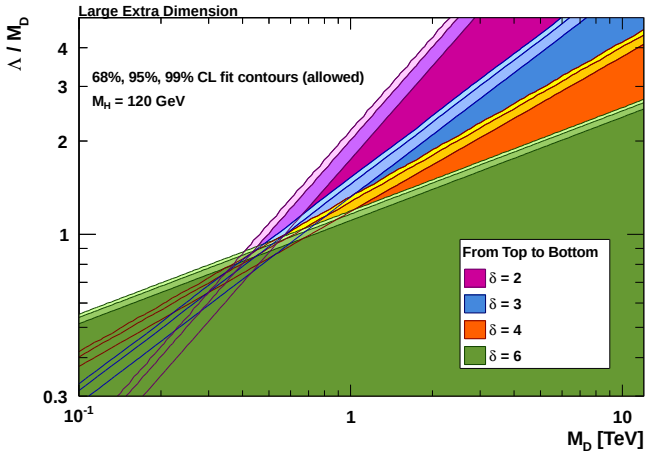

(a)

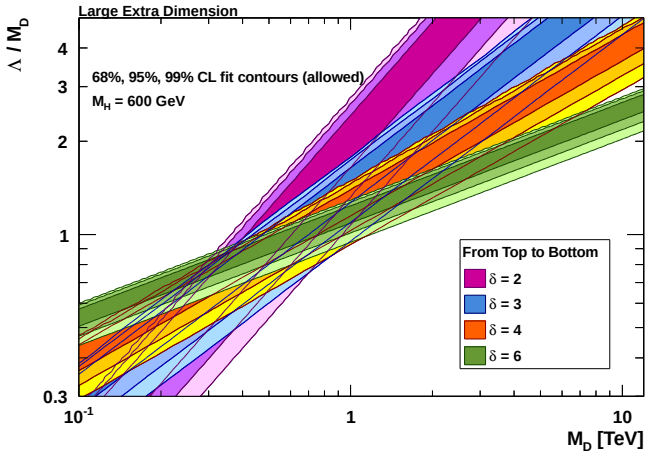

(b)

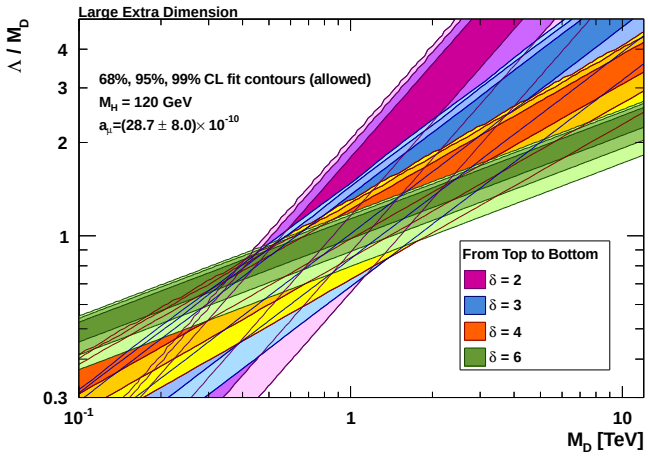

(c)

Figure 4.11: Constraints in models with large extra dimensions from the electroweak precision data. Shown are the 68%, 95% and 99% CL allowed fit contours in the (Λ/M_D, M_D)–plane for various numbers of extra dimensions δ. In (a) for a Higgs mass of 120 GeV, (b) for a Higgs mass of 600 GeV, and (c) for a Higgs mass of 120 GeV and with constraint from the muon anomalous magnetic moment.

From the electroweak precision data one extracts $\overline{\varepsilon} = (8.8 \pm 6.1) \cdot 10^{-4}$ ($\overline{\varepsilon} = (25.4 \pm 6.1) \cdot 10^{-4}$) for $M_H = 120\,\mathrm{GeV}$ ($M_H = 600\,\mathrm{GeV}$). The authors of [171] have computed the effects from LEDs by choosing the renormalization scale equal to Λ and cutting off the KK tower at $n < R \cdot \Lambda$, the graviton loop gives [171]

$$\delta\overline{\varepsilon} \simeq \sin^2\theta_W \frac{M_Z^2}{M_D^2} \left(\frac{\Lambda}{M_D}\right)^{\delta} \frac{5(8+5\delta)}{48\,\Gamma(2+\delta/2)\pi^{2-\delta/2}}\,. \tag{4.27}$$

From this equation and the experimental value for $\overline{\varepsilon}$ one can constrain Λ/M_D and M_D for different numbers of LEDs.

The 68%, 95% and 99% CL allowed regions in the (M_D, Λ/M_D) plane for various values of δ are shown in fig. 4.11(a) for $M_H = 120$ GeV and in fig. 4.11(b) for $M_H = 600$ GeV, respectively. The constraints for a rising number of extra dimensions are stricter for $\Lambda/M_D \lesssim 0.5$ and weaker for $\Lambda/M_D \gtrsim 0.5$. For $M_H = 600$ GeV the allowed regions are reduced to bands, in order to compensate a deviation of $\overline{\varepsilon}$ from zero. A similar behavior is observed in fig. 4.11(c) when using in addition the constraint from the anomalous magnetic moment of the muon (a_μ). The contribution of the large extra dimensions model to a_μ is also taken from [171]

$$\delta a_\mu = \frac{m_\mu^2}{M_D^2} \left(\frac{\Lambda}{M_D}\right)^{\delta} \frac{34+11\delta}{96\,\Gamma(2+\delta/2)\pi^{2-\delta/2}}\,. \tag{4.28}$$

This is compared to the recent evaluation of the difference between the measured [176] and the predicted value of a_μ in the SM, $\delta a_\mu = (28.7 \pm 8.0) \cdot 10^{-1}$ [75]. In fig. 4.11(b) and fig. 4.11(c) a proportional dependence between M_D and Λ/M_D is observed. It should be noticed that low M_D values are already excluded, see discussion above.

CHAPTER 5

The Experimental Set-Up

This chapter describes the experimental set-up used for the measurements of electron candidates at the ATLAS detector. First, the LHC and the associated experiments are introduced. Afterwards the main design of the ATLAS experiments and the principal detector components are explained. In a separate section, the electron reconstruction and identification are described in detail. Furthermore, the ATLAS trigger system is introduced, which is responsible for recording only interesting events from the large amount of collision data. In particular, the triggers on electron signatures are discussed. This is followed by a discussion of data quality and luminosity determination at the ATLAS experiment. The chapter concludes with a brief description of Monte Carlo generation and the ATLAS detector simulation, which are crucial ingredients for a proper understanding of the real collision data.

5.1 The Large Hadron Collider

The Large Hadron Collider (LHC) [177, 178] is a hadron ring collider located at CERN near Geneva (Switzerland). It is built in the former LEP tunnel and has a circumference of 27 km. Figure 5.1 shows the layout of the LHC and the location of the major experiments. The LHC is designed to collide protons with a center-of-mass energy of 14 TeV at a peak luminosity of 10^{34} cm^{-2}s^{-1}. In addition, it can be operated with heavy ions, that might be accelerated up to 2.8 TeV per nucleon. For this thesis only proton-proton collisions are considered.

Since spring 2010 the LHC has been operated with 3.5 TeV per proton beam resulting in a center-of-mass energy of 7 TeV. An upgrade to 14 TeV is only possible after a shut-down phase, planned for 2013. The protons in the beam are kept on track by 1232 superconductive dipole magnets, inducing a magnetic field of 8.33 T. They need to be set-up in such way that the protons in both directions are deflected correctly. Additional quadrupole and sextupole magnets focus and squeeze the beams. In total over 1600 superconductive magnets are installed which need to be cooled down with liquid helium to a temperature of 1.9 K.

The protons are initially accelerated by various pre-accelerators, including the Proton Synchrotron (PS) and the Super Proton Synchrotron (SPS). After the SPS has accelerated the beams up to an energy of 450 GeV, kicker magnets inject the protons to the LHC ring. The

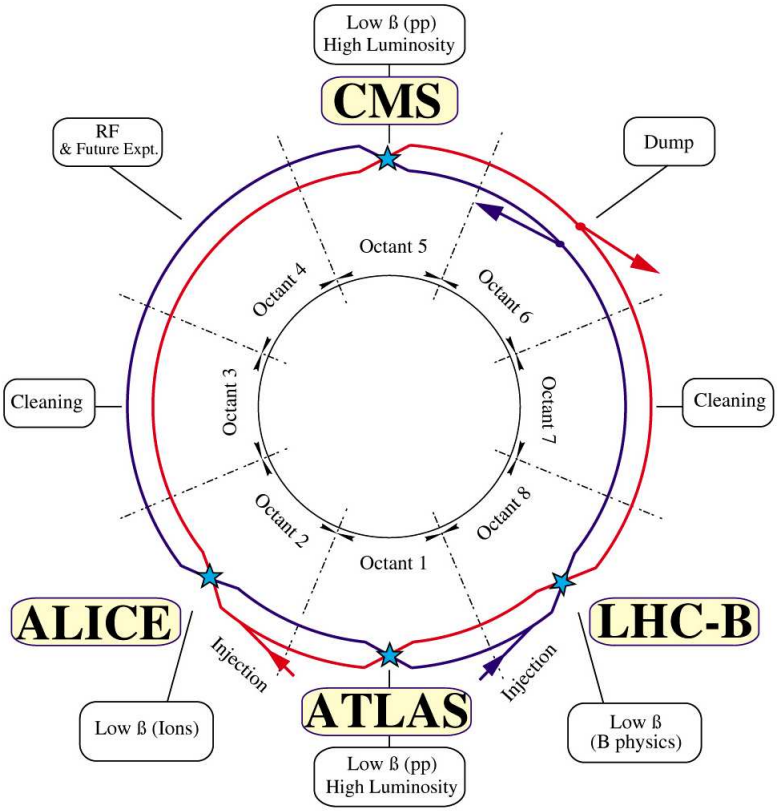

Figure 5.1: Schematic view of the LHC and the four major experiments [179].

acceleration to the final energy is carried out by superconductive radio frequency cavities in the LHC.

The four major experiments are located at the points where the LHC beam pipes cross to allow for collisions. The two general purpose detectors, ATLAS and CMS, are built especially for the direct detection of the Higgs boson and signatures from models beyond the SM. In addition, various SM properties can be confirmed or even measured for the first time. LHCb is a single arm spectrometer, designed to precisely measure the properties of B mesons in order to achieve a better understanding of flavor mixing. Additionally, effects of physics beyond the SM which are far beyond the direct reach might influence these observables. The ALICE detector is particularly designed for heavy ion collisions. A better understanding of strongly interacting systems (*e.g.* quark-gluon plasma) is the main aim.

The high interaction rate at the LHC poses a challenge for the resolution and radiation protection of the detector components. The interaction rate in a detector is defined by the product of the instantaneous luminosity $\mathcal{L}$ and the total cross-section σ, while the instantaneous luminosity is given by

$$\mathcal{L} = \frac{n_b f_r n_1 n_2}{2\pi \Sigma_x \Sigma_y} \,, \tag{5.1}$$

where n_1 and n_2 are the numbers of protons in each of the n_b bunches in each beam, Σ_x and

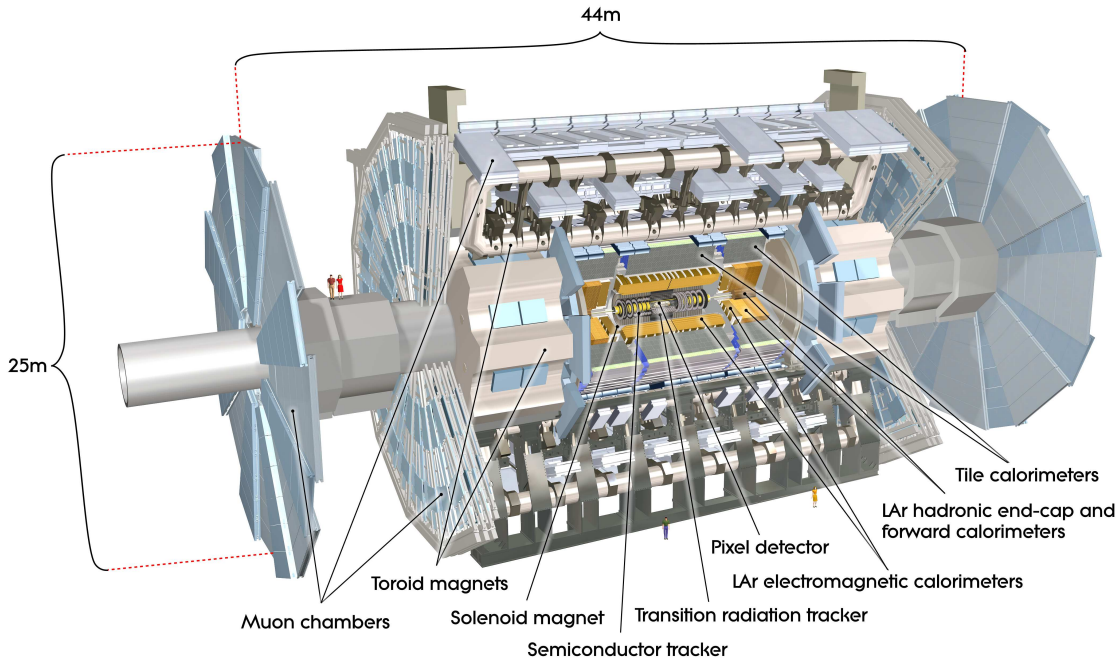

Figure 5.2: Schematic view of the ATLAS detector [181].

Σ_y characterize the widths of the horizontal and vertical beam profiles, and f_r is the LHC revolution frequency. At a center-of-mass energy of 14 TeV the total inelastic proton-proton cross-section is approximately 99 mb [180], which results in approximately 25 interactions per-bunch crossing (pile-up events) at the designed peak luminosity of 10^{34} cm^{-2}s^{-1}.

5.2 The ATLAS Detector

The ATLAS detector [181] is a multi-purpose detector. Figure 5.2 displays the ATLAS experiments with its several sub-detector systems. With a height of 25 m and a length of 44 m it is the largest detector of all LHC experiments. ATLAS is build up symmetrically around the beam pipe. The detector can be divided into three main parts: the barrel and the two end-caps. The tracking system (inner detector) uses silicon pixels, silicon microstrips, and straw-tube tracking detectors. It is surrounded by liquid-argon (LAr) electromagnetic sampling calorimeters and the hadronic scintillator-tile calorimeters. The muon spectrometer is at the very outer region of the detector. The performance goals of the various sub-detectors are listed in table 5.1.

5.2.1 The Coordinate System

In ATLAS a common set of variables is defined to describe detector components and physics processes. The nominal interaction point is defined as the origin of the coordinate system. The x axis points towards the center of the LHC ring, while the positive y axis goes upwards. The z direction is defined counter-clockwise along the LHC ring. The azimuthal angle ϕ is

Detector component	**Required resolution**	**η coverage**	
		Measurement	L1 Trigger
Tracking	$\frac{\sigma_{p_T}}{p_T} = 0.05\% \, p_T \oplus 1\%$	± 2.5	-
EM calorimetry	$\frac{\sigma_E}{E} = \frac{10\%}{\sqrt{E}} \oplus 0.7\%$	± 3.2	± 2.5
Hadronic calorimetry (jets)			
barrel and end-cap	$\frac{\sigma_E}{E} = \frac{50\%}{\sqrt{E}} \oplus 3\%$	± 3.2	± 3.2
forward	$\frac{\sigma_E}{E} = \frac{100\%}{\sqrt{E}} \oplus 10\%$	$3.1 < \eta < 4.9$	$3.1 < \eta < 4.9$
Muon Spectrometer	$\frac{\sigma_{p_T}}{p_T} = 10\% \, \text{at} \, p_T = 1 \, \text{TeV}$	± 2.7	± 2.4

Table 5.1: General performance goals of the ATLAS detector. The units for E and p_T are in GeV. Numbers are taken from [181].

measured around the beam axis, while θ is the angle from the z axis. The Lorentz invariant pseudo-rapidity is defined as

$$\eta = -\ln \tan(\frac{\theta}{2}) \, . \tag{5.2}$$

For massless particles the pseudo-rapidity is equal to the rapidity

$$y = \frac{1}{2} \ln \frac{E + p_z}{E - p_z} \, . \tag{5.3}$$

Radial distances are denoted by $\Delta R = \sqrt{\Delta\eta^2 + \Delta\phi^2}$. The transverse momentum is defined as $p_T = \sqrt{p_y^2 + p_x^2}$. The total transverse momentum in an event is a conserved quantity and its measurement is used in many new physics searches. In a highly relativistic limit, the transverse momentum is equal to the transverse energy. For electrons, the transverse energy is usually determined by the measured energy in the calorimeter and the position of the track measurement, $E_T = E_{cl}/\cosh(\eta_{tr})$.

5.2.2 The Magnet System

Magnetic fields are used to bend the tracks of charged particles in order to determine the momenta and the sign of the particle charge. ATLAS has two different superconductive magnet systems, the solenoid magnet and the toroid magnets [181]. In total an energy of 1.6 GJ is stored in the magnets.

The solenoid magnet is aligned to the beam axis and surrounds the inner detectors. It provides a 2 T field to bend the charged particles in the inner detector. In order to achieve the desired calorimeter performance, the radiative thickness of the solenoid needed to be minimized and amounts to approximately 0.66 radiation length [182]. The inner and outer diameters of the solenoid are 2.46 m and 2.56 m, while its axial length is 5.8 m.

The barrel toroid and the two end-cap toroids produce a magnetic field for bending muons in the muon spectrometers. The magnetic field in the barrel is 0.5 T, while in the two end-cap

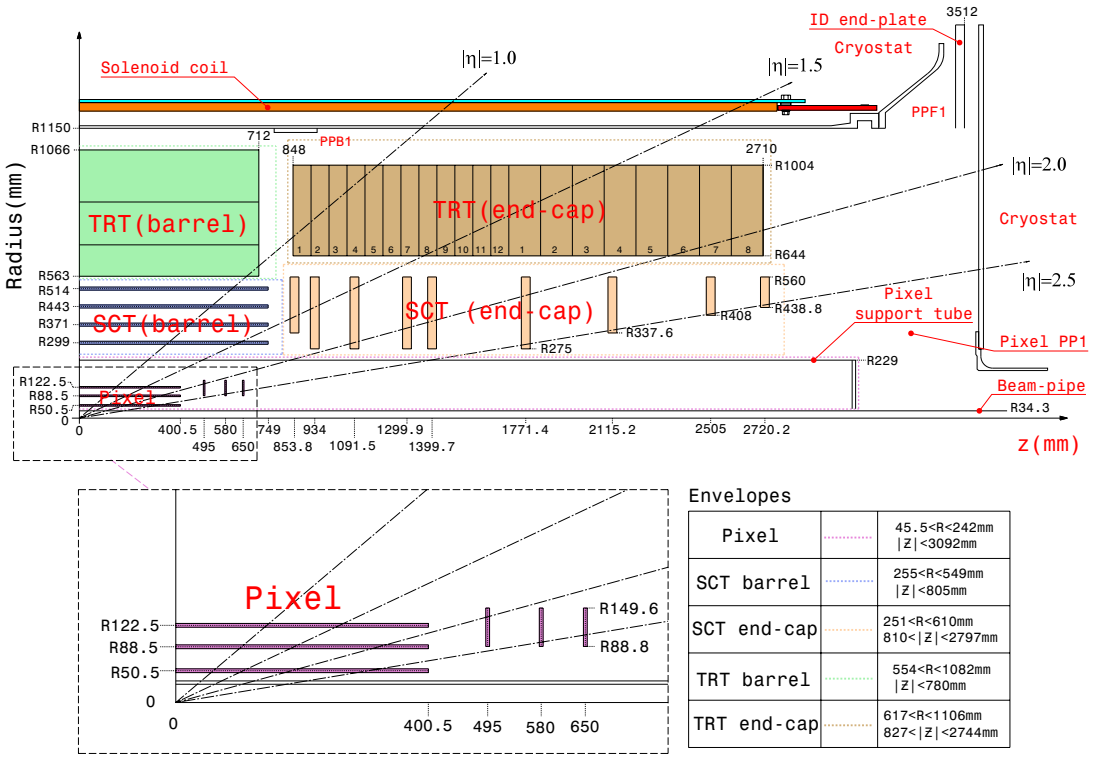

Figure 5.3: Schematic view of a quarter section of the inner detector. The major detector components are shown with its active dimensions and envelopes [181].

toroids a field of 1 T is induced. The barrel toroid consists of 8 coils each with a length of 25.3 m. The entire system has a inner (outer) diameter of 9.4 m (20.1 m).

5.2.3 The Inner Detector

Accurate tracking provides precise information about the curvature of the track of charged particles, which is used to determine the momenta and the sign of the particle charge. In addition, a good vertex reconstruction is important for the determination of the position of the primary vertex and the detection of possible secondary vertices arising for instance from B meson decays. Pixel and silicon microstrips (SCT), used in conjunction with the Transition Radiation Tracker (TRT), provide these features within the range of $|\eta| < 2.5$. Figure 5.3 illustrates the layout of the inner detector. The various sub-systems are displayed with its active dimensions and envelopes.

The Pixel Detector

The Pixel detector [183] lies at the innermost part of the detector. It is built to measure the primary vertex position precisely. The detector consists of a barrel and two end-cap parts, which cover together a range of $|\eta| < 2.5$. The barrel section can be divided into three parts. The innermost part is called b-layer and is only 5.05 cm away from the beam-pipe. The end-cap sections are composed of three discs.

The entire Pixel detector is composed of 1744 modules. Each module contains more than 60,000 Pixel elements with a size of 50×400 μm (50×600 μm at the edges). In total the Pixel detector has more than 80 million read-out channels. The system achieves a resolution of 10 μm in the R–ϕ plane and 115 μm in longitudinal direction (z direction for the barrel, R for the end-caps). The Pixel detector is the detector, which suffers most from radiation damage, due to the vicinity to the interaction point. The b-layer is expected to be replaced already after 3 years of nominal ATLAS running, while the other components survive 10 years.

The Silicon Tracker

The Semiconductor Tracker (SCT) is located behind the Pixel detector. In addition to the three hits from the Pixel detector, it provides four additional precision measurements per track. The SCT uses 80 μm wide and 12 cm long silicon microstrips [184]. In the barrel section, the sensor modules are arranged in four radial layers. One layer consists of two modules glued back-to-back together with an offset angle of 40 mrad. This methods leads to a better spatial resolution than for a single module. The modules used for the end-caps are similar in construction. The end-caps consists of three rings: the inner ring, the middle ring, and the outer ring. Each of them needs a special module geometry. In total the SCT has about 6 million readout channels with a spatial resolution of 17 μm in local R–ϕ and 580 μm in longitudinal direction.

The Transition Radiation Tracker

The outermost system of the inner detector is the Transition Radiation Tracker (TRT) [185, 186], designed to add in average 36 (22) additional hits per track in the barrel (end-cap) section. The TRT is a gaseous straw tube detector. The drift chambers consist of a 4 mm straw tube (cathode) and a 31 μm diameter tungsten gold-plated wire (anode). The cathode is operated at a voltage of -1530 V. A gas mixture of 70% Xe, 27% CO_2, and 3% O_2 is filled into the tubes. The TRT is divided into the barrel and end-caps sections. The barrel part consists of 52,544 tubes aligned parallel to the beam pipes. In each end-cap, 245,760 radial straws are assembled together. The spatial resolution in the R–ϕ plane is 130 μm. The TRT covers only the region of $|\eta| < 2.0$.

In addition to the tracking hits, the TRT can also detect transition radiation photons due to the installation of transition radiation fibers interleaved between the straws. Since ultra-relativistic electrons produce more transition radiation photons compared to hadrons (*e.g.* pions), a discrimination between electrons and hadrons is possible.

5.2.4 The Calorimetry

The Inner Detector is surrounded by calorimeters measuring the energy of electromagnetically and/or strongly interacting particles. The energy measurement of the calorimeters is based on the effect that particles produce secondary particles by interacting with the absorber material of the calorimeter. These secondary particles induce themselves new particles resulting in a particle shower. The entire energy of the shower is deposited in the calorimeter, while

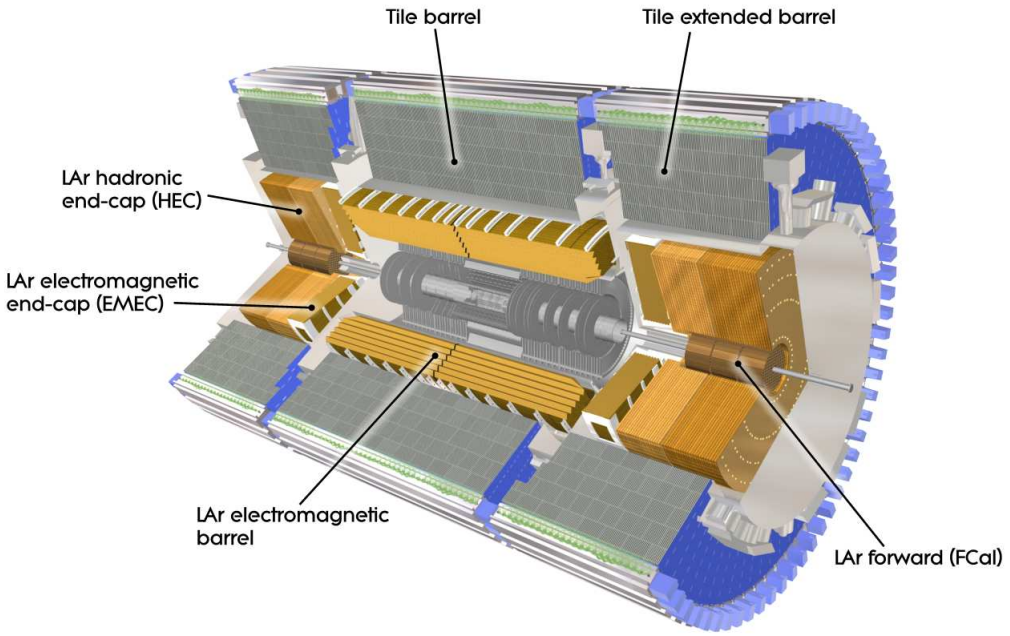

Figure 5.4: Schematic view of the ATLAS calorimeter system [181].

only a fraction is detected by the active material of the calorimeter. The measured energy is proportional to the energy of the original particle. The type of calorimeters with alternated layers of absorber and active material is called sampling calorimeter and is widely used in high energy physics.

Figure 5.4 shows the various components of the ATLAS calorimeter system. The high granularity liquid-argon (LAr) electromagnetic sampling calorimeters [187] cover the pseudo-rapidity range of $|\eta| < 3.2$. The hadronic scintillator-tile calorimeter is divided into a large barrel part and two smaller barrel cylinders. It covers the region $|\eta| < 1.7$. In the region $|\eta| > 1.5$ the hadronic calorimeters also use LAr technology. The LAr forward calorimeters (FCal) provide both electromagnetic and hadronic energy measurements. They extend the detection range up to $|\eta| = 4.9$.

The Electromagnetic Calorimeter

The ATLAS electromagnetic (EM) calorimeter system has an accordian geometry leading to an optimal coverage in ϕ without any cracks. Lead layers serve as absorber material, while the active material consists of liquid Argon connected with kapton electrodes. The EM calorimeter has a total thickness of more than 22 (24) radiation lengths in the barrel section (end-cap sections). This prevents any punch-throughs to the muon spectrometers. The EM calorimeter is divided into two half barrel parts ($|\eta| < 1.475$) as well as two outer ($1.375 < |\eta| < 2.5$) and two inner wheels ($2.5 < |\eta| < 3.2$) at the end-caps. There is a small gap at $\eta = 0$ and in the transition region between the barrel and the end-cap sections at $1.37 < |\eta| < 1.52$. The energy measurements in these regions are not reliable. A LAr-presampler is installed in the region

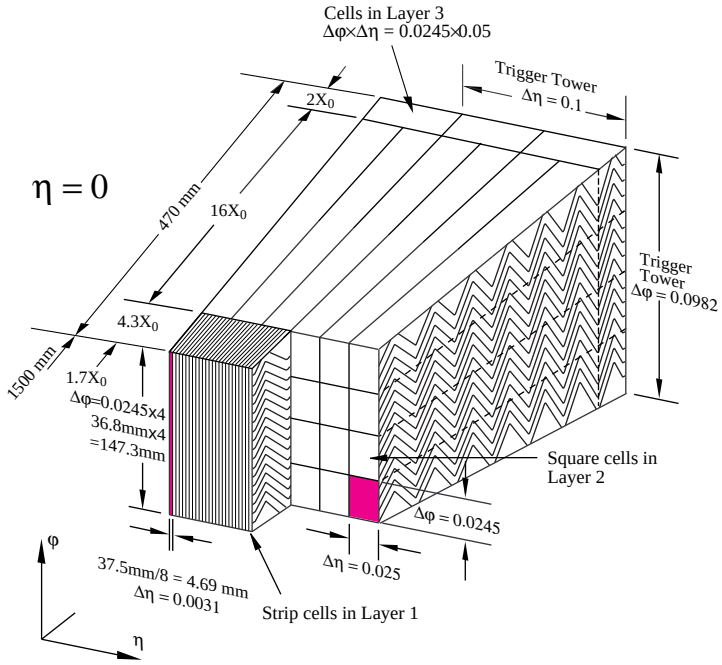

Figure 5.5: Schematic view of a section of the barrel LAr calorimeter. The accordian structure and the different granularities in each layer are visible [181].

$|\eta| < 1.8$ to determine the energy loss of electrons and photons due to the material in front of the EM calorimeter.

Figure 5.5 shows a section of the LAr calorimeter in the barrel, which is segmented into three radial layers. The granularity of the layers decreases as a function of the distance to the beam pipe. The first layer consists of strip cells and is designed to measure precisely the η direction of the electrons and photons. The second layer is with 16 radiation lengths the longest one and consists of cubic cells of size $\Delta\eta \times \Delta\phi = 0.025 \times 0.025$. Most of the energy of the EM shower is deposited in the second layer. The third layer is used to determine possible leakages of the shower into the hadronic calorimeter. In contrast to the barrel section and the outer wheel, the inner wheel consists of only two layers with a coarser transverse granularity.

To reconstruct the energy of an electron properly, cells in the second layer within a square window of 3×3 cells around the cell with the highest energy are clustered together. The energy of an electron is computed by the sum of the cluster energies in each layer [181], E_0 for the presampler and E_1, E_2, E_3 for the different layers

$$E = \text{offset} + w_0 \times E_0 + w_{01} \times \sqrt{E_0 E_1} + \lambda(E_1 + E_2 + E_3) \times w_3 \times E_3\,, \tag{5.4}$$

where offset, $w_{0,01,3}$, and λ are correction factors due to different kind of energy losses. They depend on the electron energy and the η region. In the barrel section, the linearity of response and the resolution have been studied with simulations as well as test beam measurements. The resolution can be parametrized as follows

$$\frac{\sigma(E)}{E} = \frac{a}{\sqrt{E(\text{GeV})}} \oplus b\,, \tag{5.5}$$

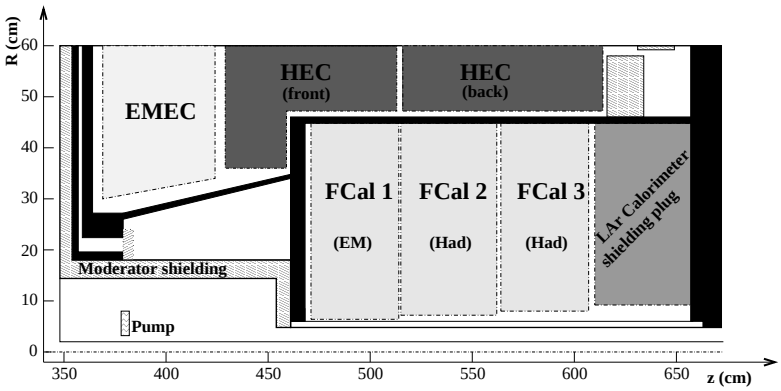

Figure 5.6: Schematic diagram showing the three FCal modules located in the end-cap cryostat [181].

where a is a stochastic term and b reflects local non-uniformities in the response of the calorimeter. The reconstructed energy response is linear within 0.1% in the energy range 15-180 GeV. A precise measurement of the electron shower shape allows to distinguish between real electrons and fakes coming from hadronic jets.

The forward calorimeter [188] (FCal) is installed to cover the pseudo-rapidity range up to $\eta = 4.9$. The FCal consists of three cylindrical modules, see fig. 5.6. The first layer is used for EM particles, while the last two layers measure the hadronic showers. Again LAr serves as active material. The first layer uses copper as absorber material, in order to optimize the resolution and heat removal. The two hadronic layers use mainly tungsten to provide containment, *i.e.* minimize the lateral spread of hadronic showers. Each FCal module consists of an absorber matrix with longitudinal tubes filled with a solid absorber rod. The cylindrical LAr gap has a thickness of 0.25 mm. For FCal1 modules the cell granularity is $\Delta\eta \times \Delta\phi = 0.1 \times 0.1$. The granularity in FCal2 and FCal3 is approximately $\Delta\eta \times \Delta\phi = 0.2 \times 0.2$.

The Hadronic Calorimeter

Hadronic showers are measured with three different calorimeters: the hadronic end-caps (HECs), the Tile Calorimeter, and the FCal. At $1.5 < |\eta| < 3.2$, the HECs use LAr technology. Each end-cap is composed of two independent wheels, which are built from 32 identical wedge-shaped modules. They use copper plates as absorber material. For $|\eta|$ ranges up to 4.9 the hadronic forward calorimeters FCal2 and FCal3 are used, as described in the previous paragraph. For pseudo-rapidities smaller than 1.7, the Tile Calorimeter is installed, which is a sampling calorimeter. It uses steel plates as absorber material interleaved with scintillating tiles as active material. Two sides of the scintillator tiles are read out by wavelength shifting fibers into separate photomultiplier tubes. The Tile Calorimeter consists of the barrel section covering $|\eta| < 1.0$ and the extended barrel sections located at $0.8 < |\eta| < 1.7$. All sections are composed of three layers. The first two layers have a granularity of $\Delta\eta \times \Delta\phi = 0.1 \times 0.1$, while the third layer has a coarser resolution of $\Delta\eta \times \Delta\phi = 0.2 \times 0.1$.

5.2.5 The Muon Spectrometer

The schematic layout of the muon spectrometer is presented in fig. 5.7. The system is designed with two independent sets of components: the trigger chambers and the precision chambers. The two separate systems provide a good momentum resolution without loss in trigger efficiency.

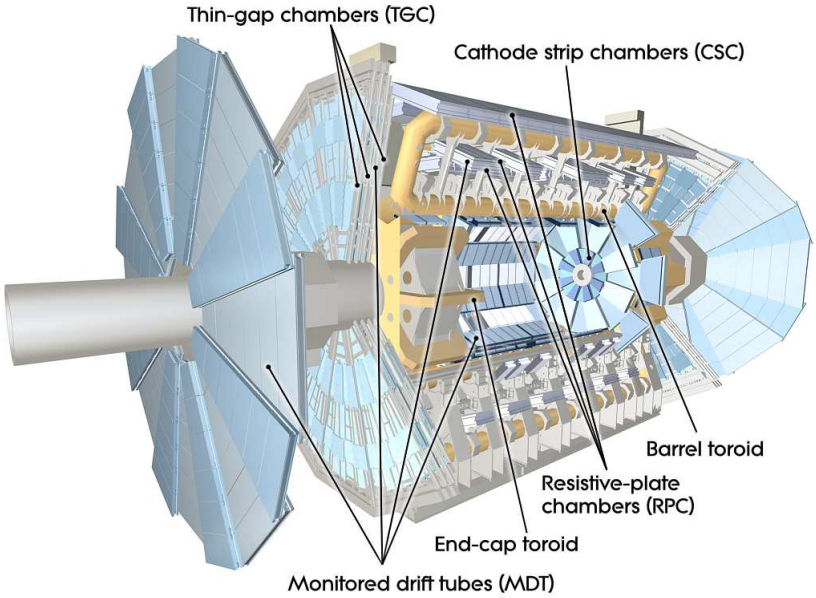

Figure 5.7: Cut-away view of the ATLAS muon system [181]. The toroid magnet system is visible in yellow.

The precise measurement of the muon tracks is performed by the Monitored Drift Tubes (MDTs) and the Cathode Strip Chambers (CSCs). The MDTs cover most of the region $|\eta| < 2.7$. Only for the innermost layer of the end-caps ($2.0 < |\eta| < 2.7$), the CSCs replace the MDTs. The MDTs are made of aluminum tubes with a diameter of approximately 30 mm (cathode) and 50 μm thick gold-plated tungsten wires (anode). The tubes are filled with a gas mixture of 93% Ar and 7% CO_2. The drift time from the cathode to the anode is relatively long, about 700 ns. A single tube measures the track position with an accuracy of 80 μm, while the combination of more tubes (3 layers in the barrel section and up to 8 layers in the end-caps) results in a resolution of 35 μm. In contrast to the MDTs, the CSCs have a higher rate capability and a better time resolution. Therefore, they are installed in the regions where higher particle fluxes are expected. The CSC is a multi-wire proportional chamber using perpendicularly segmented cathode planes. The chambers are filled with a gas mixture of 30% Ar, 50% CO_2, and 20% FE_4. To reach the required resolution of the tracking muon system, the position of the single components has to be known with an accuracy of 30 μm. For this purpose an optical alignment system controls the position and internal deformations of the MDTs and CSCs.[1]

[1]Deformations are for instance due to the magnetic field.

The muon trigger system consists of Resistive Plate Chambers (RPCs) and Thin Gap Chambers (TGCs). RPCs are installed in the barrel region ($|\eta| < 1.05$), while the TGCs have been placed in the end-caps ($1.05 < |\eta| < 2.4$). The time resolution is for the RPCs 1.5 ns and for TGCs 4 ns, respectively. The RPC uses parallel plates as electrodes, while the TGCs are multi-wire proportional chambers. A better time resolution for the TGCs in comparison to the CSCs is achieved by reducing the distance between the electrodes and by using a different gas mixture (CO_2 and n–C_5H_{12}).

5.3 Electron Reconstruction and Identification

The object reconstruction translates the electronic signals of the various detector components into physical quantities (*e.g.* type of particle, momentum, energy, and direction), while the identification process further reduces the background contamination of the signature.

5.3.1 Electron Reconstruction

Standard Electron Reconstruction

For the reconstruction of electrons in the central region ($|\eta| < 2.5$) two different algorithms exist [189, 190]. The standard algorithm starts from cell clusters in the EM calorimeter, which are then associated with reconstructed tracks from the inner detector. The second algorithm is optimized for low p_T electrons, originating for instance from J/Ψ decays. It selects tracks fulfilling certain quality criteria which are matched to relatively isolated clusters in the EM calorimeters. The low p_T algorithm is not further discussed here, since it is not used in this analysis.

The standard electron reconstruction [189, 190] starts with the selection of preliminary cluster seeds. These seeds are formed by a sliding window algorithm [191], which only takes into account clusters with an energy deposit of more than 2.5 GeV. The seed clusters have a size of 3×5 cells in the middle layer of the calorimeter, whereas one cell corresponds to $\Delta\eta \times \Delta\phi = 0.025 \times 0.025$. An electron is reconstructed, if one or more tracks from the inner detector are matched to the seed cluster. For this purpose, the last measured point of the reconstructed track is extrapolated to the second layer of the calorimeter. The η and ϕ coordinates are compared to the corresponding coordinates of the seed cluster. If the difference in $\Delta R = \sqrt{\Delta\eta^2 + \Delta\phi^2}$ is below a certain threshold, the track is matched to the cluster. For cases with more than one track matched to the cluster, the track with the smallest ΔR is taken. Tracks with silicon hits (Pixel and SCT) are preferred compared to tracks with no silicon hits. The matching of tracks without any silicon hit is restricted to the ϕ coordinate, since the precision of the TRT in η direction is limited. In the matching procedure energy losses due to Bremsstrahlung need to be regarded with special care. The Bremsstrahlung loss depends on the track tilt. To account for this effect the $\Delta\phi$ requirement in the track matching procedure is loosened for the side where the extrapolated track bends.

After the matching procedure the EM cluster is recomputed. For the barrel region a sliding window of 3×7 cells is used, while in the end-caps the cluster size is 5×5 in middle layer cell units. The preliminary 3×5 seed cluster is explicitly chosen as a subset of the final EM cluster size. In order to obtain the right energy of the electron, several corrections are applied to the final cluster. For the four momentum of the electron, the energy measurement of the cluster and the η and ϕ coordinates of the track are used. If the track has less than 4 silicon hits, the direction of the electron is also determined from the cluster. The transverse energy is defined by $E_T = E/\cosh(\eta)$.

The reconstruction algorithms cannot distinguish between prompt electrons (*e.g.* from Z decays) and converted electrons (from photons), since both signatures have tracks pointing to the EM cluster. As a result almost all converted photons are treated as electrons. The identification cuts, described in the next section, are used to reduce the contamination from converted photons as well as from hadronic jets in the electron sample.

Forward Electron Reconstruction

For the reconstruction of forward electrons ($2.5 < |\eta| < 4.9$) only information from the EM calorimeters are considered, because the tracking detectors are restricted to $|\eta| < 2.5$. Therefore, it is not possible to distinguish between electrons and photons in the forward region. The algorithm for forward electrons is called topological clustering [191]. This algorithm looks for cells with an energy significance (*i.e.* signal-to-noise ratio) above a certain threshold. Neighbored cells are added to the original cell energy, if their significance is again above a certain threshold. Hence, the clusters can have different sizes. In order to separate two clusters being close together, an algorithm has been developed which searches for local maxima and divides the original cluster into new separated clusters, if more than one maximum is found. A cluster is only reconstructed as an electron candidate, if its energy is above 5 GeV. The direction of the electron is defined by the barycenter of the cluster. To suppress contamination from QCD background, the differences in the EM shower shape induced by electrons and hadrons (*e.g.* pions) are exploited.

5.3.2 Electron Identification

Standard Electron Identification

A set of parameters is defined to separate real (isolated) electrons from fake electrons mostly arising from hadronic jets [190]. A list of all variables used for the cut based identification is given in table 5.2. The cut values have been optimized with simulated events as well as first data from 2009 and 2010. The cuts on the shower shape variables have been defined in 10 bins of eta (corresponding to the calorimeter geometry, the detector acceptance, and the regions of increasing material in the inner detector) and 11 bins of the cluster E_T (from 5 GeV to 80 GeV). Three reference sets of cuts have been defined: loose, medium, and tight [189, 190]. They provide progressively stronger QCD rejection, while the identification efficiency decreases with the tightness of the selection. The three selections are constructed in a way, that the

Type	Description	Variable
Loose cuts		
Acceptance of detector	⋆ pseudo-rapidity of cluster $\|\eta\| < 2.47$	
Hadronic leakage	⋆ Ratio of E_T in the first layer of the hadronic calorimeter to E_T of the EM cluster (used over the range $\|\eta\| < 0.8$ and $\|\eta\| > 1.37$) ⋆ Ratio of E_T in the hadronic calorimeter to E_T of the EM cluster (used over the range $\|\eta\| > 0.8$ and $\|\eta\| < 1.37$)	R_{had1} R_{had}
Second layer of EM calorimeter	⋆ Ratio in η of cell energies in 3×7 versus 7×7 cells. ⋆ Lateral width of the shower.	R_η $w_{\eta 2}$
Medium cuts (includes Loose)		
First layer of EM calorimeter.	⋆ Total shower width. ⋆ Ratio of the energy difference associated with the largest and second largest energy deposit over the sum of these energies	w_{stot} E_{ratio}
Track quality	⋆ Number of hits in the pixel detector (≥ 1). ⋆ Number of hits in the pixels and SCT (≥ 7). ⋆ Transverse impact parameter (<5 mm).	N_{Pi} N_{Si} d_0
Track matching	⋆ $\Delta\eta$ between the cluster and the track (< 0.01).	$\Delta\eta_1$
Tight cuts (includes Medium)		
b-layer	⋆ Number of hits in the b-layer (≥ 1).	N_{BL}
Track matching	⋆ $\Delta\phi$ between the cluster and the track (< 0.02). ⋆ Ratio of the cluster energy to the track momentum ⋆ Tighter $\Delta\eta$ cut (< 0.005)	$\Delta\phi_2$ E/p $\Delta\eta_1$
Track quality	⋆ Tighter transverse impact parameter cut (<1 mm).	d_0
TRT	⋆ Total number of hits in the TRT. ⋆ Ratio of the number of high-threshold hits to the total number of hits in the TRT.	N_{TRT} R_{TRT}
Conversions	⋆ Electron candidates matching to reconstructed photon conversions are rejected	

Table 5.2: Variables used for loose, medium, and tight electron identification cuts for central electron candidates ($|\eta| < 2.47$). Table is taken from [190].

probability that a jet is identified as an electron decreases by a factor of approximately 10 with increasing tightness, starting at a probability of roughly 0.001 for the loose selection.

The loose selection is based on variables which describe the shape of the EM shower. After the geometrical acceptance cut is applied, a cut on the hadronic leakage (ratio between E_T of hadronic and EM calorimeter) is performed. Furthermore, cuts on variables (R_η and $w_{\eta 2}$) are applied which limit the size of the EM shower. The loose set provides excellent identification efficiency but low background rejection.

The medium selection expands the cuts for the loose selection, and therefore improves the quality of the electron sample. The cuts on the first layer of the EM calorimeter improves the rejection of background events (*e.g.* $\pi^0 \to \gamma\gamma$ decays). In addition, the medium selection includes tracking related cuts to remove electron candidates with poorly reconstructed tracks.

The tight selection further rejects QCD background and secondary electrons from conversions. For this selection, it is foreseen to achieve a high rejection power by fully exploiting the electron identification possibilities of the ATLAS detector. Besides some further track quality conditions, the tight selection requires at least one b-layer hit to reject electrons from converted photons. A conversion-flagging algorithm is used to reduce further the contamination.

Isolation requirements can improve the purity of the electron sample. For this purpose usually a cone around the electron candidate is built. Electrons fulfill the isolation criteria, if there are no or only few other tracks with specific properties within this cone. A more detailed description can be found in [189, 190].

Forward Electron Identification

For the identification of electron candidates in the forward region ($2.5 < |\eta| < 4.9$), also a cut-based method is used [189, 190]. Most of the variables are defined as cluster moments or a combination of them. The cluster moment of degree n for a variable x is defined by

$$\langle x^n \rangle = \frac{1}{E_{\text{norm}}} \times \sum_i E_i x_i^n \,, \tag{5.6}$$

where i is the cell index of the cluster and $E_{\text{norm}} = \sum_i E_i$. Two subsets of selections have been defined for the forward electron identification: forward loose and forward tight. The variables used for these selections are listed in table 5.3. The forward loose selection cuts mainly on longitudinal and transverse shower profile variables, while the forward tight selection add further conditions to reject background more efficiently. The cut values have been optimized with simulated events, as well as with 2009 and 2010 data.

5.4 The ATLAS Trigger System

At the design luminosity, the LHC will have a 40 MHz bunch-crossing rate with an average of 25 interactions per bunch crossing. It is technically not feasible to record and process this

Type	Description	Variable
Forward Loose Cuts		
Acceptance	⋆ $2.5 < \|\eta\| < 4.9$	
E_T threshold	⋆ $E_T > 5$ GeV	
Shower depth	⋆ Distance of the shower barycenter from the calorimeter front face measured along the shower axis	λ_{center}
Longitudinal second moment	⋆ Second moment of the distance of each cell to the shower center in the longitudinal direction (λ_i)	$\langle\lambda^2\rangle$
Transverse second moment	⋆ Second moment of the distance of each cell to the shower center in the transverse direction (r_i)	$\langle r^2\rangle$
Forward Tight Cuts (includes Forward Loose)		
Maximum cell energy	⋆ Fraction of cluster energy in the most energetic cell	f_{max}
Normalized lateral moment	⋆ lat_2 is the second moment of r_i setting $r_i = 0$ for the two most energetic cells, while lat_{max} is the second moment of r_i setting $r_i = 4$ cm for the two most energetic cells and $r_i = 0$ for the others	$\frac{lat_2}{lat_2+lat_{max}}$
Normalized longitudinal moment	⋆ $long_2$ is the second moment of λ_i setting $\lambda_i = 0$ for the two most energetic cells, while $long_{max}$ is the second moment of λ_i setting $\lambda_i = 10$ cm for the two most energetic cells and $\lambda_i = 0$ for the others	$\frac{long_2}{long_2+long_{max}}$

Table 5.3: Variables used for forward loose and forward tight electron identification cuts in the region $2.5 < |\eta| < 4.9$. Table is taken from [190, 192].

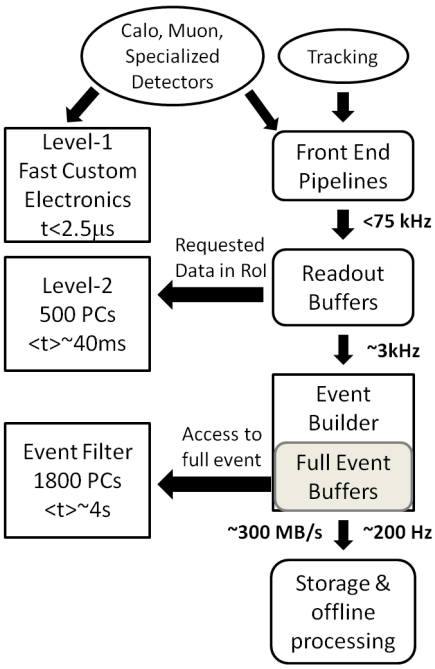

Figure 5.8: Schematic view of the ATLAS trigger system [193]. On the left-hand side the three levels of the trigger system are visible.

amount of data.[1] Therefore, the trigger system is used to reduce the collision rate to an output rate of 200 Hz, corresponding to an average data rate of 300 MB/s [193]. The trigger system should only keep those signatures important for physics and performance studies. In the 2010 data taking, it was possible to extend the output rate shortly to approximately 600 Hz, because offline processing could be completed between LHC fills and technical stops [193]. The average event size was roughly 1.3 MB at an instantaneous luminosity of $10^{32}\text{cm}^{-2}\text{s}^{-1}$.

The ATLAS Trigger system contains three levels: Level-1 (L1), Level-2 (L2), and the Event Filter (EF). Figure 5.8 shows the three levels and their interaction between each other. The L1 trigger is based on fast custom made hardware, while the L2 and EF, which form the High Level Trigger (HLT) system, rely on computer farms and software. Each level reduces the rate by running increasingly sophisticated algorithms. Only when an event is accepted at a certain level, this event is passed to the next level (early rejection principal). Triggers, which run in a pass-through mode, always pass the event to the next level.

5.4.1 The Level-1 Trigger System

The L1 trigger [193, 194] gets its information from various sub-detectors, *e.g.* the hadronic and EM calorimeters and the fast muon trigger chambers (TGC and RPC). The detector signals are stored in front-end pipelines pending a decision from the L1 trigger system. The

[1]The real bottle-necks for the event recording are the storage capacity and a possible reprocessing of the data.

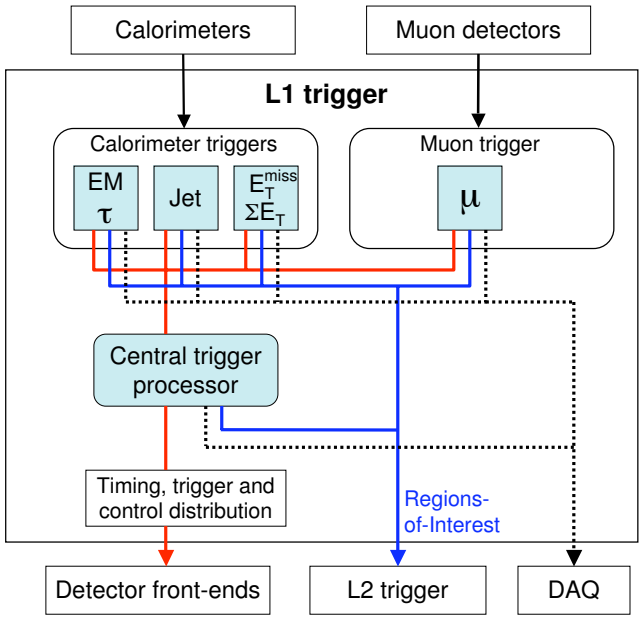

Figure 5.9: Diagram of the L1 trigger system. The overall L1 accept decision is made by the central trigger processor. Figure is taken from [181].

implementation of the fast custom electronics ensures a L1 decision time of 2.5 μs (about 1 μs is due to the propagation of the signals in the cables). The L1 trigger system reduces the rate to a maximum of 75 kHz. During the 2010 data taking, 30 kHz for the L1 output rate was not exceeded [193].

The L1 trigger decision is made by the central trigger processor (CTP) [194] based on information from the calorimeters and muon trigger systems.[1] The L1 calorimeter trigger (L1Calo) searches for high E_T objects, like electrons and photons, hadronic jets, τ-leptons decaying into hadrons, as well as events with large missing or total transverse energy [181]. The L1 muon trigger (L1Muon) consists of the RPCs and TGCs (as described in section 5.2.5) and looks for high p_T muons.[2] A schematic view of the L1 trigger system is shown in fig. 5.9. The CTP evaluates the information sent by the L1Calo and L1Muon system according to the defined trigger conditions (stored in look-up tables). These trigger conditions are then combined to maximum 256 L1 trigger items. In spite of a positive trigger decision the item can still be rejected due to a prescale or a dead-time veto. A prescale can be set to a trigger to select only a fraction of events fulfilling the trigger threshold. For instance, a trigger with a prescale factor of 5 would only accept every 5th event passing the trigger requirements. The ATLAS dead-time is applied by the CTP [193]. The three sources of dead-time are the simple dead-time (fixed number of bunch-crossings, default 4, are not evaluated after L1 was accepted), the complex dead-time (restricts the number of L1 accepts in a given period) and the back-

[1] The CTP gets also information from minimum bias scintillators, the LUCID detector, and zero degree calorimeter (ZDC).

[2] Six independent muon p_T thresholds can be configured.

pressure mechanism throttling the generation of L1 acceptances (due to busy signal from the data acquisition system). If one of the L1 items finally passes all conditions, a positive signal is sent to the detector front-ends to start the read-out. Region–of–interests (RoIs), describing the region in the detector where a particular trigger threshold is satisfied, are passed to the L2 trigger for further processing. Additionally, the information about the trigger decision (*e.g.* prescale and dead-time veto) are transferred to the data acquisition system (DAQ).

5.4.2 The High Level Trigger System

The HLT [195] consists of computer farms running software algorithms. During 2010 running, 800 nodes have been configured either for L2 or EF, while 300 dedicated nodes were only used by the EF [193]. The computer farms can be expanded to about 500 L2 nodes and 1800 EF nodes. The L2 trigger system is designed to reduce the rate to roughly 3 kHz with an average processing time of 40 ms.[1] The EF decreases the rate further to the designed output rate of 200 Hz. The processing time is 4 s.[2]

The L2 selection is based on only 2-6% of the entire data information. The data from each trigger system is provided by the Readout System (ROS), consisting of one or more Readout Buffers (ROB). The RoI builder merges the input from the L1 trigger systems into one single data structure, which is send to the L2 supervisors (L2SV). The L2 trigger decision is evaluated at the L2 trigger processing units (L2PU). Only in case of a positive L2 decision the entire event information is transferred to the event builder. This way, the amount of data transfers is minimized resulting in faster processing time.

The event builder (*cf.* fig. 5.8) provides the entire event information for the EF. The EF decision is usually based on the standard ATLAS reconstruction algorithms. Accepted events are finally send to the output nodes of the DAQ system. If an event does not pass a certain level, it is rejected at this stage and it is not further processed. The trigger conditions for a specific signature defines a trigger chain (for an example see (5.7)). Depending on the type of the trigger chain that triggered the event, the events are written to different data streams. Besides the calibration streams four physical streams exist: Egamma, Muon, JetTauEtmiss, MinBias. The additional express stream contains approximately 10% of all accepted events and it is used for prompt offline processing to monitor the data quality.

5.4.3 Electron Trigger Selection

The electron trigger selection [181, 196] at the three trigger levels is discussed in more detail, since electrons are the important objects used in this thesis. Figure 5.10(a) shows a schematic diagram of a trigger chain for the selection of electrons. Electrons can only be triggered in the region $|\eta| < 2.5$, since the tracking detectors are limited to this region. An example of an electron trigger chain is

$$\text{L1\_EM10} \rightarrow \text{L2\_e15\_medium} \rightarrow \text{EF\_e15\_medium}\,. \tag{5.7}$$

[1] In 2010 the L2 processing time was about 50 ms at an instantaneous luminosity of $10^{32}\text{cm}^{-2}\text{s}^{-1}$ [193].
[2] In 2010 the EF processing time was 0.4 s at an instantaneous luminosity of $10^{32}\text{cm}^{-2}\text{s}^{-1}$ [193].

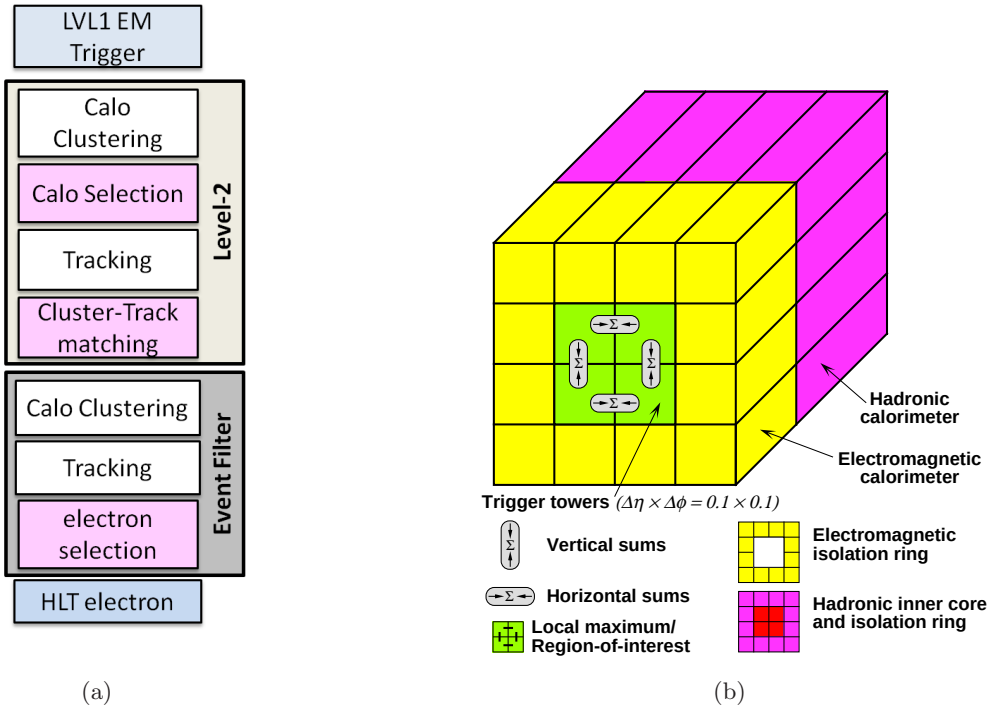

(a) (b)

Figure 5.10: (a) Illustration of an electron trigger chain [193]. (b) Level-1 electron trigger algorithm [181]. The central cluster and the three isolation regions are also shown.

The prefix represents the trigger level, the numbers stand for the applied E_T thresholds, and the last part indicates the identification criteria that is applied to the signature.

At L1, only the calorimeter information is available. Therefore, no discrimination between electrons and photons can be made. The EM and hadronic calorimeters are divided into Trigger Towers (TT) each with a reduced granularity of $\Delta\eta \times \Delta\phi \approx 0.1 \times 0.1$, as it is depicted in fig 5.10(b). The energy of a TT is composed of the energy of the EM and hadronic calorimeter cells, excluding the cells from the fourth layer of the hadronic end-caps. A RoI consists of four TTs arranged in a 2×2 square. The RoI is identified by a sliding window algorithm. The L1 item is accepted if at least two neighbored TTs exist in the RoI, which have a larger combined energy deposit than the trigger threshold.

In addition to the energy condition, isolation criteria can be applied to L1. Primary produced electrons are unlikely close to hadronic particles. Hence, signatures originating from jets can be suppressed by requiring an isolated EM signal. At L1, there are three cut variables describing the size of the EM shower and the leakage into the hadronic calorimeter:

- The energy deposit in the EM isolation ring (**L1_EMIsol**), shown in yellow in fig. 5.10(b).
- The energy deposit behind the RoI in the hadronic calorimeter (**L1_hadCore**), shown in red in fig. 5.10(b).
- The energy deposit in the hadronic isolation ring (**L1_hadIsol**), displayed in pink in fig. 5.10(b).

Like all L1 variables, the L1 isolation parameters are discrete and can take only integer values. A performance study of L1 isolation variables is presented in section 6.1.3. For the 2010 data taking no isolation requirements were applied at L1.

At L2, also tracking information is taken into account. First, the L2 performs a fast calorimeter reconstruction on the L1 RoIs. A cluster of 3×7 cells around the most energetic cell in the second layer of the EM calorimeter is build. In order to reduce data transfer only the region around the RoI is investigated. A fast pattern recognition is used to find tracks within the RoI [197]. The electron L2 trigger is accepted if a track has been matched to the calorimeter cluster and the corresponding E_T threshold is fulfilled.

Finally, the selection on the EF works in the same way as it has been described for the offline reconstruction and identification, *i.e.* the EF requires the loose, medium, and tight conditions in order to accept or reject events. The selection cut values are the same as used for the offline reconstruction.

5.4.4 The Trigger Menu and Configuration

The trigger system is configured via a trigger menu containing all trigger chains and their current hardware (L1) and software (HLT) settings. A trigger menu is stored in the online database (TriggerDB) [198, 199]. Additionally, the menus are replicated in various other databases for simulation and trigger aware data analyses. A specific trigger menu is identified by its super-master-key (SMK), consisting of a single L1-master-key and a single HLT-master-key. The assignment of a SMK to a menu provides an explicit identification. In addition, prescale sets can be assigned to the menus. More than one prescale set can be identified with a SMK. A user-friendly graphical Java program (TriggerTool) has been developed [199], in order to interact with the TriggerDB. The TriggerTool provides browsing features as well as the possibility to generate or manipulate menus. Furthermore, it avoids duplications of SMKs in the TriggerDB. A snapshot of the main panel of the TriggerTool is shown in fig 5.11. In the upper part of the figure the various trigger menus are listed, while the configured trigger chains of the selected menu are visble in the lower part.

A trigger menu contains between 200 and 500 different trigger chains. One distinguishes between different types of trigger chains [193]:

- **Single object triggers** are used for final states with at least one characteristic object, *e.g.* EF_e15_medium for $Z \to ee$ or $W \to e\nu$.
- **Di-object triggers** (or multiple object triggers) are used for final states with two (or more) objects, *e.g.* EF_2e_tight for $J/\Psi \to ee$.
- **Combined triggers** search for different trigger signatures, like a combination of electrons and muons (*e.g.* EF_e10_medium_mu6).
- **Topological triggers** apply selections based on information on two or more RoIs.

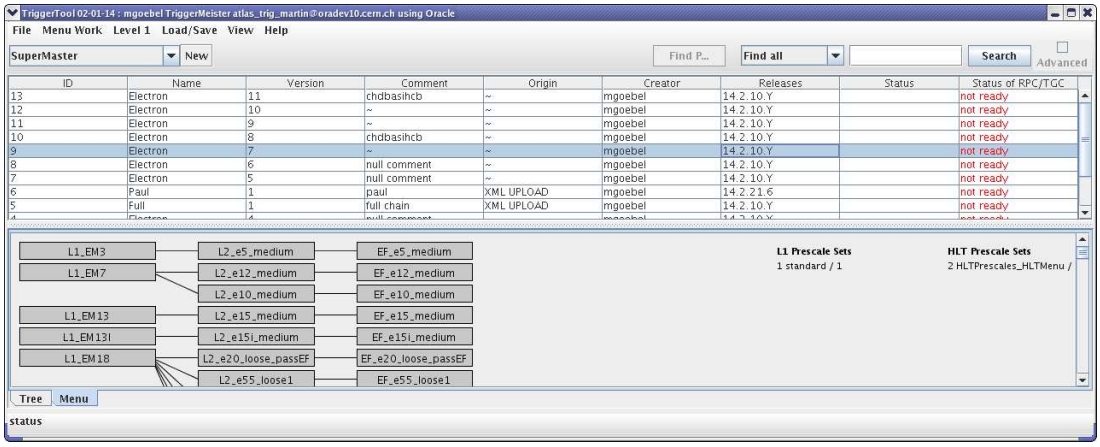

Figure 5.11: A snapshot of the main panel of the TriggerTool.

An example of a trigger menu as applied in 2010 together with the used L1 trigger thresholds is shown in table 5.4.

The trigger rate rises with increasing instantaneous luminosity. In order to control the output rate of the three trigger levels, one can either tighten the selection cuts (*e.g.* E_T threshold, isolation cuts) or assign prescales to the trigger chains. While changes of trigger definitions can only be done before ATLAS starts data taking, prescale factors for each trigger level can be applied during data taking. Moreover, changes of the trigger definitions complicate the comparison and combination of data [200]. Various prescale sets are prepared in order to react to different luminosities. Principal physics triggers should not be prescaled to avoid signal losses. In addition, the LHC bunch information can be added to the trigger system to be able to trigger events under certain bunch crossing conditions, for instance colliding bunches for physics triggers or empty bunches for cosmic ray, random noise or pedestal triggers.

5.5 Data Quality and Luminosity Determination

In ATLAS the data taking is divided into different periods. Each period, named by capital letters, is characterized by comparable beam conditions (*e.g.* number of colliding bunches) and similar detector configurations (*e.g.* the trigger menu). A period consists of several runs. A run is indicated by a coherent detector configuration and named by a sequential number. Runs are again sub-divided into luminosity blocks which have a length of approximately 2 mins. The luminosity block is the shortest data taking unit in ATLAS. Hence, the configuration of the detector is constant during a luminosity block. For instance, trigger prescales can only be changed before starting a new luminosity block. For every luminosity block the following conditions are stored in a database: trigger prescales, trigger dead times, detector and beam conditions, as well as luminosity information.

The data quality is defined by the current detector and beam conditions. Depending on the analysis one requires that certain sub-detectors have worked smoothly during the data taking phase. The luminosity blocks passing specific data quality requirements are stored in so-called

Trigger Signature	Representation L1	HLT	L1 Thresholds [GeV]							
electron	EM	e	2	3	5	10	10i	14	14i	85
photon	EM	g	2	3	5	10	10i	14	14i	85
muon	MU	mu	0	6	10	15	20			
jet	J	j	5	10	15	30	55	75	95	115
forward jet	FJ	fj	10	30	55	95				
tau	TAU	tau	5	6	6i	11	11i	20	30	50
E_T^{miss}	XE	xe	10	15	20	25	30	35	40	50
$\sum E_T$	TE	te	20	50	100	180				
total jet energy	JE	je	60	100	140	200				
b jet	$--$	b								
Minimum Bias	MBTS	mbts								
Beam Condition Monitor	BCM	$--$								
Zero Degree Calorimeter	ZDC	$--$								
LUCID	LUCID	$--$								
Beam Pickup	BPTX	$--$								

Table 5.4: The key trigger objects, the abbreviations used to represent them in the trigger menu at L1 and the HLT, and the L1 thresholds used for each trigger object in the menu at an instantaneous luminosity of $10^{32}\text{cm}^{-2}\text{s}^{-1}$ [193]. Thresholds are applied to E_T for calorimeter triggers and p_T for muon triggers.

good-runs-lists (GRLs) [202]. In this thesis, GRLs are used containing all luminosity blocks, in which the detector components used for the reconstruction and identification of standard and forward electron candidates were operating stable (egamma GRLs). Figure 5.12 shows how efficient the various detector components ran during the 2010 data taking.

The luminosity can be determined from several different measurements. So far, all methods are based on the event counting technique [203], *i.e.* one determines the fraction of bunch crossings in which a specified detector registers an event satisfying certain selection requirements. For instance, the precise timing of the LAr calorimeter ($\sim$1 ns) provides the possibility to count events arising from collisions. The LUCID [204, 205] detector is specifically designed to measure the relative luminosity. It uses Cherenkov radiation from charged particles to measure inelastic pp scattering. Two of those detectors are placed at each side of the interaction point (at a distance of 17 m). However, the event counting methods determine only the relative luminosity. To obtain the absolute luminosity the relative measurement needs to be normalized to the total pp cross-section. In the future, the ALFA detector [204], placed at 240 m distance from the interaction point, will monitor the absolute luminosity through the measurement of elastic pp scattering at small angles in the Coulomb-Nuclear interference region. Currently the absolute luminosity is determined by using accelerator parameters [206, 207]. The horizontal (Σ_x) and vertical (Σ_y) width of the beam profile (*cf.* eq. (5.1)) are determined by using van-der-Meer scans [208]. By scanning the beams across each other, Σ_x and Σ_y can be extracted and the absolute luminosity can be computed. More details about the various techniques and the algorithms of luminosity determination can be found in [203].

The integrated and instantaneous luminosity is stored for every luminosity block and needs

Inner Tracking Detectors			Calorimeters				Muon Detectors			
Pixel	SCT	TRT	LAr EM	LAr HAD	LAr FWD	Tile	MDT	RPC	CSC	TGC
99.1	99.9	100	90.7	96.6	97.8	100	99.9	99.8	96.2	99.8

Luminosity weighted relative detector uptime and good quality data delivery during 2010 stable beams in pp collisions at √s=7 TeV between March 30th and October 31st (in %). The inefficiencies in the LAr calorimeter will partially be recovered in the future.

Figure 5.12: Luminosity weighted relative fraction of good quality data delivered by the various ATLAS subsystems during LHC fills with stable beams in 2010, and after switching the tracking detectors on [201].

to be corrected for prescales and dead-times of the trigger chain used in the specific analysis. Table 5.5.1 shows the integrated luminosity per data period for the egamma GRL. The first data periods contribute only a small fraction to the total integrated luminosity, while the last period accounts for more than 60% of the integrated luminosity. The relative uncertainty on the luminosity has been determined to be 3.4% [209]. Up to period E, the L1 item L1_EM14 has been used, since period F the trigger chain EF_e15_medium has been taken to correct the integrated luminosity.[1] Both triggers were not prescaled in 2010.

5.5.1 Electron Object Quality

The energy measurement of the EM calorimeter is a crucial ingredient for the electron reconstruction and identification. During the 2010 run, three different types of problems have occurred, which impact the reconstruction and identification of electron candidates [192].

- Some calorimeter regions were affected by high voltage problems. In this thesis electrons are rejected if a part of the cluster lies in such a region.
- The energy of isolated cells producing a high signal or no signal at all are set to 0. Electrons are rejected if the core cluster (3×3 cells in the second layer) contains one of these cells.
- The energy reconstruction can be affected by electronic front-end board (FEB) cards which provide no output signal (mostly due to non-functioning optical readout lines). In this analysis electrons are rejected if a part of the cluster falls into a dead FEB region of the first or second layer of the calorimeter. If the problematic region is in the third layer, an energy correction is applied and the electron is used.

The problematic regions are stored in two dimensional η–ϕ object quality maps. These maps are time-dependent and need to be accounted properly for the analysis. The loss of the electron efficiency has been estimated to be 6% [192].

[1] The HLT was not activated in the early data taking phase and the electron HLT triggers have changed since run number 160613 to recover inefficiencies.

Data Period	Integrated Luminosity	Physics Trigger
Period A	$0.26 \cdot 10^{-}3\ \mathrm{pb}^{-1}$	L1_EM14
Period B	$6.90 \cdot 10^{-}3\ \mathrm{pb}^{-1}$	L1_EM14
Period C	$8.15 \cdot 10^{-}3\ \mathrm{pb}^{-1}$	L1_EM14
Period D	$0.29\ \mathrm{pb}^{-1}$	L1_EM14
Period E	$0.98\ \mathrm{pb}^{-1}$	L1_EM14
Period F	$1.74\ \mathrm{pb}^{-1}$	EF_e15_medium
Period G	$6.65\ \mathrm{pb}^{-1}$	EF_e15_medium
Period H	$7.03\ \mathrm{pb}^{-1}$	EF_e15_medium
Period I	$20.74\ \mathrm{pb}^{-1}$	EF_e15_medium
Total	$37.43\ \mathrm{pb}^{-1}$	–

Table 5.5: Integrated luminosity per run period using the egamma good-runs-list and the trigger given in the last column.

5.6 Monte Carlo Generation and Detector Simulation

For a proper understanding of the detector response, a detector simulation of generated events is performed. For this purpose, events (*e.g.* $Z \rightarrow ee$, Minimum Bias) need to be generated by a Monte Carlo (MC) event generator program. The interaction of the generated particles with the detector material is carried out by the detector simulation. After the positions of the particles in the sub-detectors are computed, the digitization procedure simulates the output of the readout channels of the various detector components.

Event Generation

A full calculation of the physical interaction is usually not possible. Therefore, MC techniques, implemented in computer algorithms, are used for the generation of events [210, 211]. In fig. 5.13 the different steps of a MC event generation are illustrated. They are described in more detail in the following:

The hard process is usually the process of interest. For this purpose the problem is factorized into several components (see for instance [8])

$$d\sigma = \sum_{i,j} d\sigma_{ij}^{\mathrm{part}} \otimes f_i(x_a) \otimes f_j(x_b)\,, \tag{5.8}$$

where f_i and f_j are the PDFs of the incoming partons ($i, j = u, d, c, s, ...$) carrying momentum fraction x_a and x_b and $d\sigma_{ij}^{\mathrm{part}}$ is the partonic cross-section. Initial (ISR) and final state radiation (FSR) describe the emission of gluons and photons from the initial and final particles. For ISR the momentum transfer can be of the order of the original

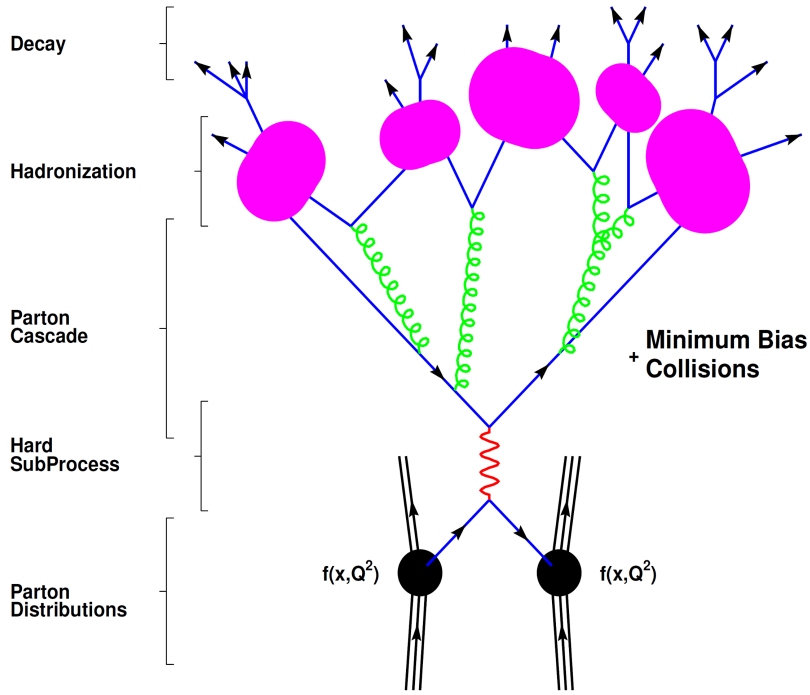

Figure 5.13: Illustration of computational steps of a Monte-Carlo event generation [212, 213].

hard process, while for FSR the particles have usually low momenta. The ISR is mainly responsible for a large part of the transverse momentum in the event. ISR and FSR can be either implemented via the matrix element (hard particles) or by a parton shower approach [210] (soft and collinear particles). ISR is also often included in the PDFs.

Parton showers describe the showering of the partons involved in the event. The primary produced quarks and gluons radiate further partons until final state particles are at an energy of 1 GeV. Below this limit the strong coupling becomes too large and the perturbative calculations are not valid anymore. Parton shower algorithms are based on the approximation, that parton radiation is soft and collinear.

The **hadronization** procedure ensures that the final state particles are composed of colorless hadrons. This process cannot be computed from the first principals. Several techniques have been developed for this step. The two main models are described below. In the string fragmentation [214, 215] the strongly interacting particles are connected via strings, representing the potential energy between them. If the potential energy excesses a certain limit new particle are generated. They build color-singlets with the original particles. This procedure repeats until only colorless hadrons remain. In the cluster fragmentation [216, 217] gluons split into quark pairs after the parton showering. Quarks and anti-quarks are composed of color-singlet clusters. They decay into smaller clusters until primary hadrons remain. After the hadronization unstable particles decay according to their branching ratios.

Multiple interactions describe the probability that more than one parton of the proton makes a hard interaction. This process follows the same rules as the primary hard scattering described above.

In this thesis two different programs are used for the MC event generation. Pythia is one of the most widely used generators. It provides a large number of SM and beyond SM processes. The hadronization is implemented via the LUND string fragmentation [215]. Two independent programs of Pythia exist. The Fortran code Pythia6.4 [218] is used for ATLAS data analysis in this thesis. Unparticle and large extra dimension di-fermion production have been studied with the C++ Pythia version, Pythia8.1 [5].

In the MC@NLO generator [219, 220] the full next-to-leading order QCD matrix elements are implemented for the hard process. Therefore, it provides a more sensible description of QCD effects than Pythia. The showering and hadronization process is performed by the Herwig [221] generator, which uses a cluster fragmentation model for the hadronization. Since soft emission is already implemented via the next-to-leading matrix element, a procedure is needed to avoid double counting. A mechanism of negative event weights has been developed to account for this problem.

Detector Simulation and Pile-Up Events

For the ATLAS detector simulation, all possible interactions (*e.g.* energy loss, Bremsstrahlung, photon conversion) between particles and the detector material or the magnetic fields need to be taken into account. The widely used GEANT4 package [222, 223] has been especially developed for this purpose. The settings of the GEANT4 package in the ATLAS simulation have been optimized by taking into account test beam data, as well as first data from 2009 and 2010. Additionally, damaged and inefficient regions of the detector are considered. From the GEANT4 output the position (hits) of the interactions between the detector and the particles are known. Theses hits are then passed to the digitization process, which translates the simulated signatures to signals in the readout channels. The output of the detector simulation is equivalent to the real raw detector output, *i.e.* before reconstruction and identification.

The high luminosity at the LHC leads to additional pp interactions taking place in the same or adjoining bunch-crossings. The additional interactions are called pile-up events and differ from the process of multiple interactions, describing interactions of partons from the same protons involved in the hard scattering. One distinguishes between in-time pile-up, resulting in additional primary vertices in the bunch-crossing, and out-of-time pile-up, describing particles from adjoining bunch-crossing overlapping with the particles from the current event due to time delays in the electronics. For the simulation of pile-up events, minimum bias events are overlaid over the primary process. The amount of additional minimum bias interactions is Poisson distributed with the expectation value of 2.2 for the MC samples used in this thesis.

CHAPTER 6

Electron Trigger Performance

In this chapter the electron trigger performance of the 2010 data is studied. In the first section, the dependence of various L1 calorimeter trigger rates on the instantaneous luminosity is investigated as well as the L1 trigger efficiencies for some principal electromagnetic L1 trigger items. Additionally, the performance of low E_T threshold L1 trigger items as a function of the integrated luminosity is studied and the effect from the L1 isolation variables on the trigger rate is analyzed. In the second section, the HLT performance is explored. The trigger efficiencies as a function of E_T and η are studied for two HLT trigger chains, followed by the determination of scale factors accounting for differences between MC and data. The chapter concludes with a study of the time stability of the trigger chain EF_e20_loose. Parts of the analysis have been published in [196].

6.1 L1 Performance

6.1.1 L1 Trigger Rates

The verification of the scaling of the trigger with increasing luminosity is a proper test of a stable running of the L1 trigger items. In fig. 6.1 the L1 trigger rates as a function of the instantaneous luminosity are shown for some low-threshold calorimeter trigger items.[1] In order to correct for different bunch configurations in the runs, the trigger rates and luminosity are divided by the number of bunches. In this figure each dot corresponds to the rate observed in a single luminosity block. The luminosity is assumed to be constant within a luminosity block. The electromagnetic (EM), tau (TAU), and jet (J) L1 items show a linear relation between luminosity and rate. As expected the rates of the global quantities, like total energy (TE) and missing transverse energy (XE), rise stronger with increasing instantaneous luminosities. They are strongly affected by the number of pile-up events, which increase with higher luminosities.[2]

Figure 6.2 shows the rates as a function of the instantaneous luminosity for some principal electromagnetic L1 items. A perfect linear behavior is observed between rate and luminosity, indicating that pile-up collisions do not affect the rates of the electromagnetic L1 items. In

[1] Only collision data from period G is investigated.

[2] At $\mathcal{L} = 10^{32}$ cm^{-2}s^{-1} up to 3 additional pile-up events occur in one bunch-crossing [196].

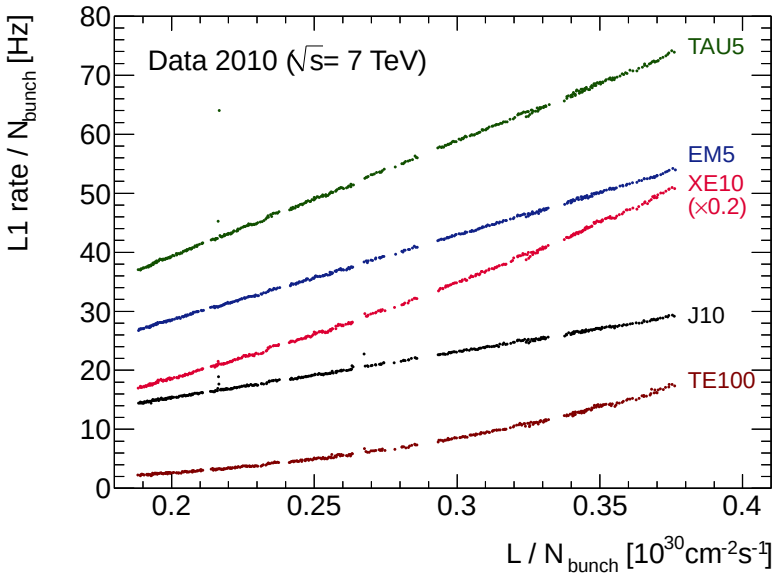

Figure 6.1: Unprescaled L1 rates for some low threshold calorimeter triggers as a function of the instantaneous luminosity per bunch-crossing. The rate for XE10 is scaled by 0.2. For simplicity the prefix L1 is omitted in the trigger names.

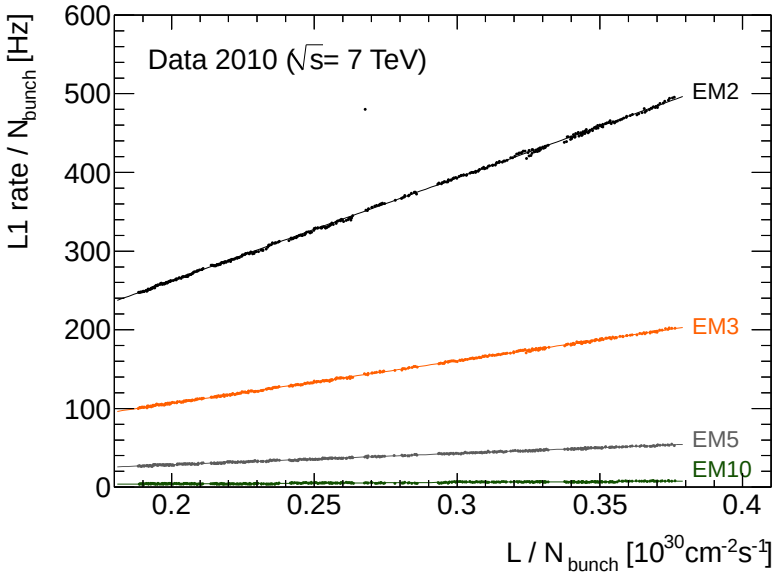

Figure 6.2: Unprescaled L1 rates for electromagnetic trigger items as a function of the instantaneous luminosity per bunch-crossing. For simplicity the prefix L1 is omitted in the trigger names.

addition, it is clearly visible that the L1 rate decreases with increasing L1 threshold. Thus, the raising of E_T thresholds provides a possibility to reduce the L1 output rate.

6.1.2 L1 Trigger Efficiency

The L1 trigger efficiencies are determined from data period A to E.[1] In this analysis, collision candidates are taken into account which have at least one vertex with at least three tracks and which pass the egamma good-runs-list (GRL). In order to obtain sufficient statistics of selected electrons, no identification cuts (loose, medium, tight) are applied in the offline selection. As a result most of the reconstructed electrons are mis-identified hadronic jets (faked electrons). Only electrons in the central region ($|\eta| < 2.47$), excluding the transition region between the barrel and the end-caps ($1.37 < |\eta| < 1.52$), are accepted.

The trigger efficiency of electrons is determined using events initially triggered by a trigger orthogonal to the electron triggers. Only events are considered passing a minimum bias (MBTS) trigger, whose decision is independent of any L1 calorimeter trigger. The reconstructed electrons are matched to the trigger RoIs by requiring that the distance in η–ϕ is less than 0.15 ($\Delta R < 0.15$). The trigger efficiency is defined as the ratio between the number of reconstructed electrons that pass the trigger and all reconstructed electrons

$$\text{efficiency} = \frac{\#(\text{reconstructed electrons passing the trigger})}{\#(\text{all reconstructed electrons})} \,. \tag{6.1}$$

When using binomial error propagation, the uncertainty vanishes, if the efficiency is 0 or 1 even at low statistics. In order to avoid this problem, in this analysis the method developed in [224] is used. It is based on Bayes' theorem and results in an asymmetric uncertainty. In case of large statistics, the error calculation converges to the normal binomial uncertainty.

Figure 6.3 shows the L1 efficiencies as a function of the uncalibrated offline E_T of the electromagnetic cluster for the L1_EM2, L1_EM3, and L1_EM5 trigger items. The efficiency curves sharply rise at the threshold of the L1 item and are fully efficient above the turn-ons. In the MC simulations, the turn-ons start at slightly larger values of E_T, but the overall shape of the curve is well simulated. The bumps at low E_T for the L1_EM2 and L1_EM3 trigger items are due to calibration differences between the L1 system and the offline reconstruction [196]. At L1 a larger cluster than in the offline reconstruction is used for calculating the transverse energy. This could result in the fact, that an offline electron candidate with a reconstructed E_T below the trigger threshold might pass the L1 threshold (in particular if two clusters are close together).

A similar behavior as for low threshold triggers, is observed for the L1_EM10 and L1_EM14 items. The corresponding efficiencies are displayed in fig. 6.4. Besides the fact that the turn-ons of the data curves start at lower E_T values than for the non-diffractive MC events, the shapes of the efficiencies are well modeled in the simulation. The L1 trigger items are fully efficient above the turn-on. No bumps at low E_T values are observed for L1_EM10 and L1_EM14.

[1] Since the efficiencies are determined by requiring a MinBias trigger and for later periods MinBias triggers are highly prescaled, later periods are not taken into account. Additionally, only runs after run number 15277 are considered, because the L1 timing configuration has been update since then [196].

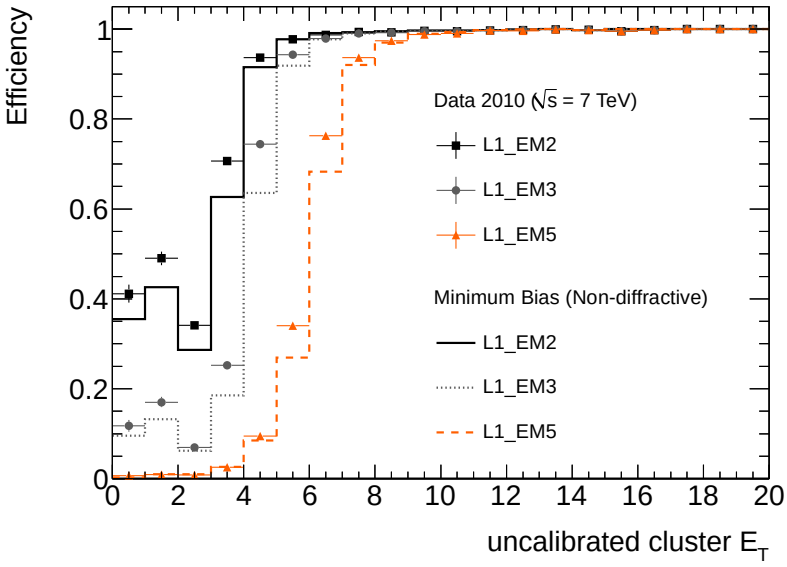

Figure 6.3: L1 trigger efficiencies for reconstructed electrons as a function of the uncalibrated cluster E_T for the items L1_EM2, L1_EM3, and L1_EM5. The turn-on curves are compared to MC simulation.

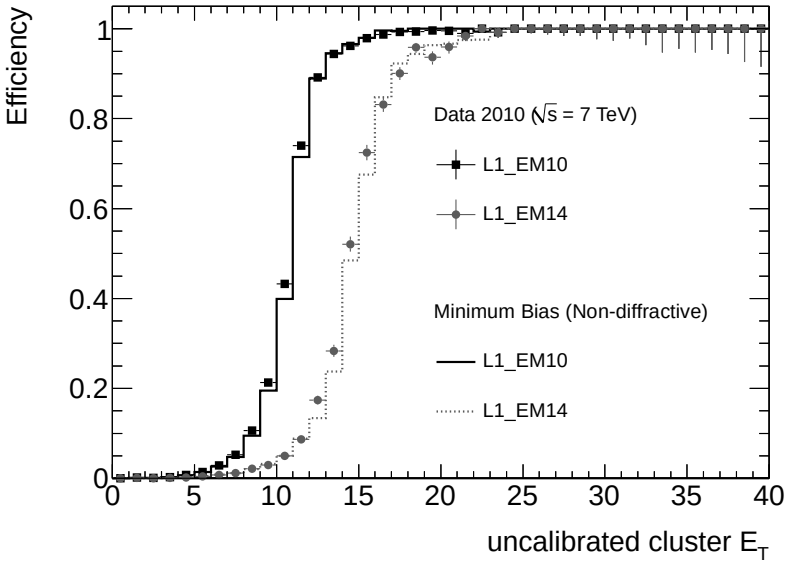

Figure 6.4: L1 trigger efficiencies for reconstructed electrons as a function of the uncalibrated cluster E_T for the items L1_EM10 and L1_EM14. The turn-on curves are compared to MC simulation.

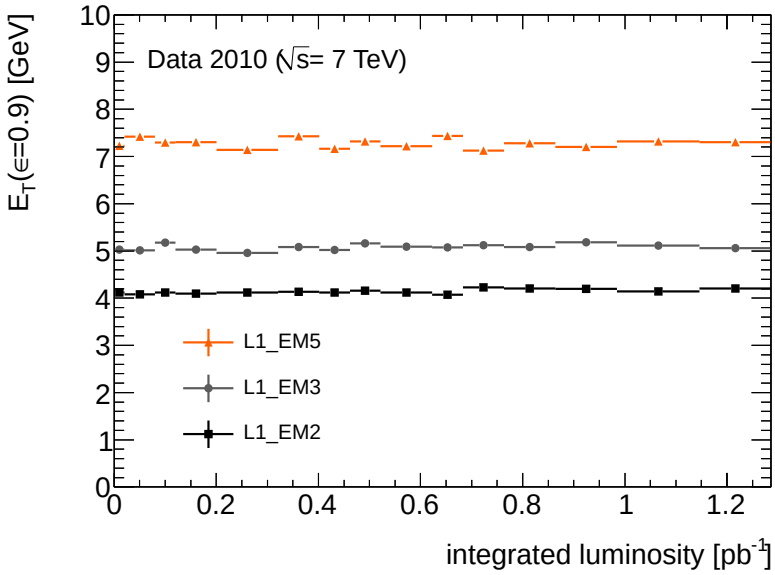

Figure 6.5: E_T value for which the L1 trigger items reach the 90% efficiency level as a function of the integrated luminosity.

In order to test a stable operating of the L1 items, the E_T value for which the L1 trigger items reach the 90% efficiency level is determined as a function of time (integrated luminosity). For this study the L1_EM2, L1_EM3, and L1_EM5 trigger items have been investigated. For L1_EM10 and L1_EM14, the statistics of events selected with the MBTS triggers are not sufficient for this study. Figure 6.5 shows the E_T value when the L1 trigger items reach the 90% efficiency level as a function of the integrated luminosity. Each bin is composed of several luminosity blocks in such a way that a bin contains at least 1000 events passing the L1_EM5 requirements. The width of the bins is therefore determined by a combination of the L1_EM5 and MBTS trigger rate. For instance, in period E (at roughly 1 pb^{-1}) the used MBTS trigger is highly prescaled, resulting in a wider bin since less events have been selected. The 90% efficiency level is determined by fitting the turn-on curve of each luminosity bin with a Fermi-Dirac distribution. As alternative also the Gaussian error function is used as fit function. The difference between both fit methods is taken as systematic uncertainty and is added in quadrature to the statistical uncertainty. The smooth behavior of the 90% efficiency level thresholds in fig. 6.5 indicates that the L1_EM2, L1_EM3, and L1_EM5 trigger items have been operated rather stable in time.

6.1.3 L1 Isolation

As explained in section 6.1.1 the rates of the L1 items increase with instantaneous luminosity. There are several methods to lower the L1 output rate in order to fulfill the L1 design output rate of 75 kHz for a further increase of the luminosity. With the assignment of prescales to a L1 trigger item only a fraction of the events passing the trigger is selected. The enhancement of the L1 trigger thresholds also decreases the L1 rate. However, due to the larger E_T threshold

interesting physics signals might not be recorded. Another possibility is to tighten the trigger requirements. In this section, the impact of cutting on L1 isolation variables, introduced in section 5.4.3, is studied.

The analysis has been performed with events from data periods H and I, which have in average 7 additional pile-up interactions. Each event has to be triggered by a HLT pass-through trigger, in order to avoid any bias from HLT selection.[1] Three observables are defined in order to study the impact of the L1 isolation variables. The first variable is defined by the number of selected RoIs after applying the isolation cuts over the original number of RoIs

$$R_{\text{frac}} = \frac{\#(\text{RoIs after cut})}{\#(\text{all RoIs})} \,. \tag{6.2}$$

The change in the L1 rate is computed by

$$R_{\text{rate}} = \frac{\#(\text{events after cut})}{\#(\text{all events})} \,, \tag{6.3}$$

while the efficiency that an offline electron survives the L1 isolation requirements is given by

$$\epsilon = \frac{\#(\text{offline electrons after cut})}{\#(\text{all offline electrons})} \,. \tag{6.4}$$

In figs. 6.6(a)-(c) R_{frac}, R_{rate}, and ϵ are shown as a function of the L1 cut value for the L1_EM10 trigger item. In each plot, the values of L1_hadIsol, L1_hadCore, and L1_EMIsol need to be smaller than the given value on the x-axis. For all isolation variables a rate reduction (R_{frac} and R_{rate}) can be only achieved, if the cut value is below 5 GeV. For larger values, the R_{frac} and R_{rate} are close to one. Most reduction can be achieved by applying a cut on the L1_EMIsol variable. However, a too small value for L1_EMIsol can decrease the electron efficiency ϵ. The electron efficiencies in fig. 6.6(c) are determined from electron candidates selected by a tag-and-probe method, as described in the next section 6.2. This method provides a clean electron sample that does not suffer from a high background contamination. Without loosing good electron candidates, one can achieve a reduction of approximately 20% for R_{frac} and R_{rate} when cutting at 3 GeV for the L1_EMIsol variable. A similar performance is obtained with the L1_hadCore variable when going to small cut values (1-2 GeV). The L1_hadIsol variable provides only little rate reduction.

A combination of the cut variables further improves the performance of the L1 isolation. A rate reduction of roughly 30% with a good electron efficiency can be achieved by using a combination of L1_EMIsol and L1_hadCore [225]. Studies have also shown that the rate reduction increases with increasing L1 E_T thresholds, *i.e.* for low E_T threshold triggers the L1 isolation variables play a minor role.

[1] The HLT pass-through trigger EF_e10_noCut is used, which is seeded by the L1_EM5 item.

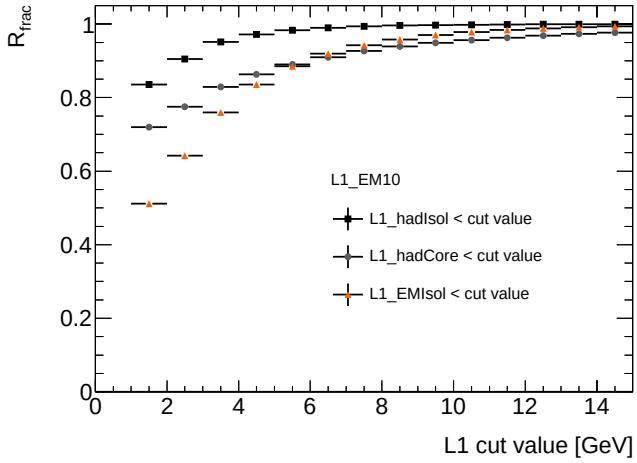

(a)

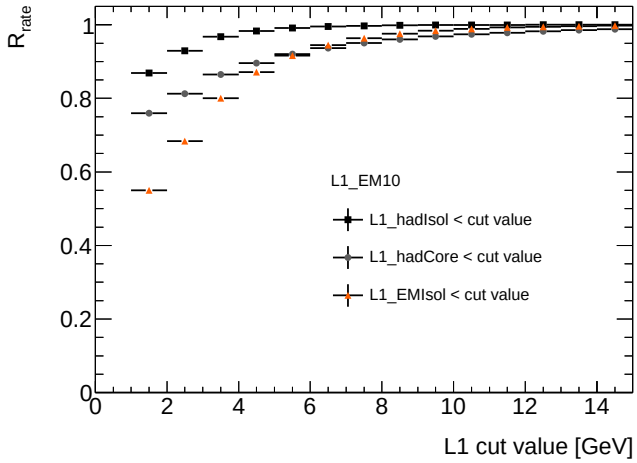

(b)

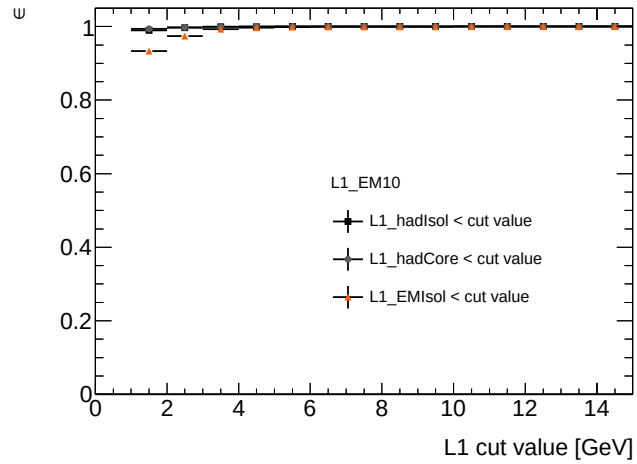

(c)

Figure 6.6: Study of the L1 isolation variables L1_hadIsol, L1_hadCore, and L1_EMIsol. The values of the isolation variables have to be smaller than the value given on the x-axis. The observables, (a) R_{frac}, (b) R_{rate}, and (c) ϵ are defined in the text.

6.2 HLT Performance

The study of the trigger efficiencies of HLT chains is important to account for possible discrepancies between data and MC in the physics analysis. The following two HLT trigger chains are investigated in this section

$$\text{L1\_EM10} \rightarrow \text{L2\_e15\_medium} \rightarrow \text{EF\_e15\_medium}\,, \tag{6.5}$$

$$\text{L1\_EM14} \rightarrow \text{L2\_e20\_loose} \rightarrow \text{EF\_e20\_loose}\,. \tag{6.6}$$

The HLT trigger efficiencies are determined by using tag-and-probe techniques.[1] For the tag electron a reconstructed tight electron with $E_T > 20$ GeV triggered by EF_e15_medium is taken. As probe electron, only medium electron candidates with $E_T > 15$ GeV are considered. Electrons are only accepted if they are in the central region ($|\eta| < 2.47$) excluding the transition region between the barrel and the end-caps ($1.37 < |\eta| < 1.52$). To be sure that the electron pairs arise from the process $Z/\gamma^* \rightarrow ee$, the invariant mass of the system must lie between 80 and 100 GeV. Within this range only negligible background contamination is expected. The reconstructed electrons are matched to the trigger objects, if $\Delta R < 0.15$.

For the analysis the entire 2010 data is investigated since run number 160613.[2] This corresponds to an integrated luminosity of approximately 37.1 pb^{-1}. The events have to pass the egamma GRL and need to have at least one vertex associated with at least three tracks. The trigger efficiency and its uncertainty are computed as described for the L1 efficiency determination in section 6.1.2. The data results are compared to the expectations from Pythia $Z \rightarrow ee$ events.

In fig. 6.7 and fig. 6.8 the trigger efficiencies as a function of the transverse energy are presented for the EF_e15_medium and EF_e20_loose trigger chain, respectively. Both trigger chains show a stable plateau region above the turn-on for all three trigger levels. The comparison to the MC simulation shows reasonable agreement. For the EF_e20_loose trigger the sharp turn-on is clearly visible, while for EF_e15_medium the E_T cut of 15 GeV does not allow to see the entire turn-on behavior. The shapes of the turn-ons are modeled well in the MC simulation.

The integrated trigger efficiency for electrons with a E_T larger than 20 GeV as a function of the cluster η is shown in fig. 6.9 for the trigger chain EF_e15_medium. The efficiencies at all three levels are compared to the MC simulation. The EF efficiency of the data events is below the one simulated in MC. The deviations are of similar size for the different η bins. Hence, the difference can be corrected by a global factor. The situation for the trigger chain EF_e20_loose in fig. 6.10 is quite similar. In MC, all three levels are almost fully efficient, except in the very outer tracking region, while in data the efficiency is below the one for the EF.

[1] The use of the orthogonal trigger method suffers from low statistics, since due to the large prescales assigned to the MBTS triggers only very few events are selected containing a reconstructed (medium) electron.

[2] The HLT was not activated in the early data taking phase and the electron HLT triggers have changed since run number 160613 to recover inefficiencies.

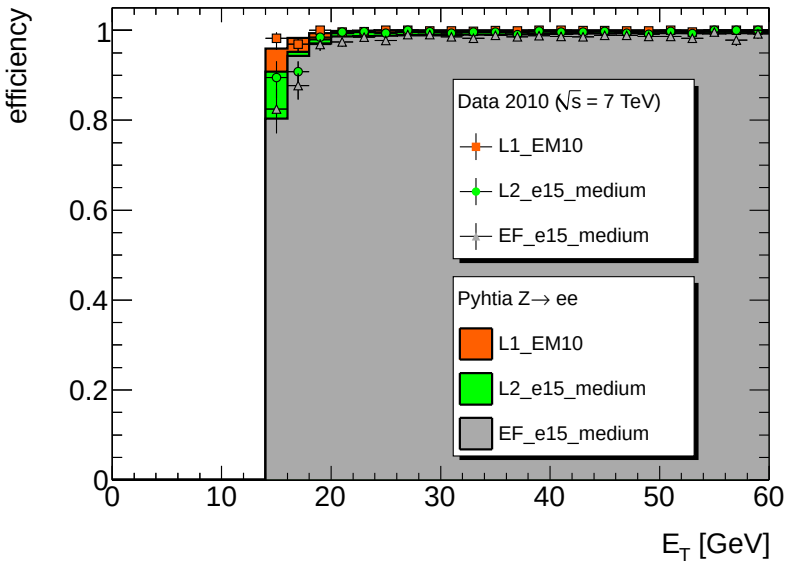

Figure 6.7: Trigger efficiencies for medium electrons as a function of the electron E_T for the trigger chain EF_e15_medium. The efficiencies are compared to Pythia $Z \rightarrow ee$ MC simulation.

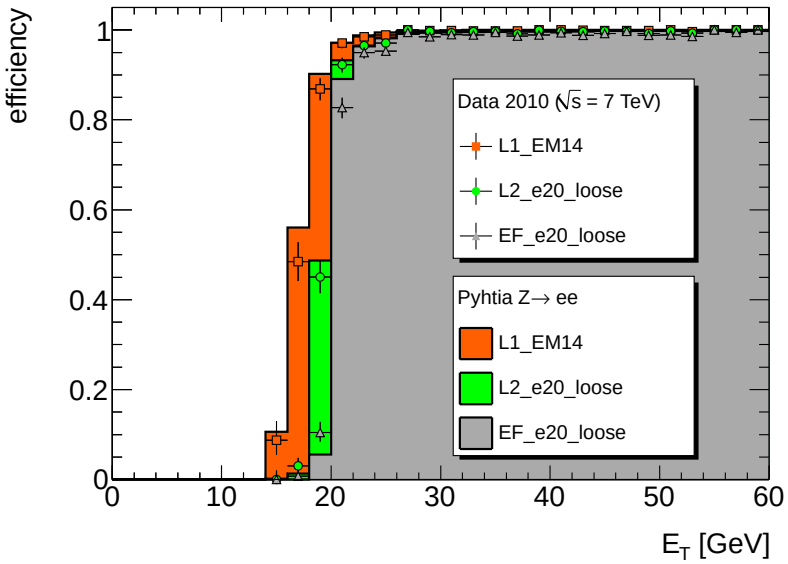

Figure 6.8: Trigger efficiencies for medium electrons as a function of the electron E_T for the trigger chain EF_e20_loose. The efficiencies are compared to Pythia $Z \rightarrow ee$ MC simulation.

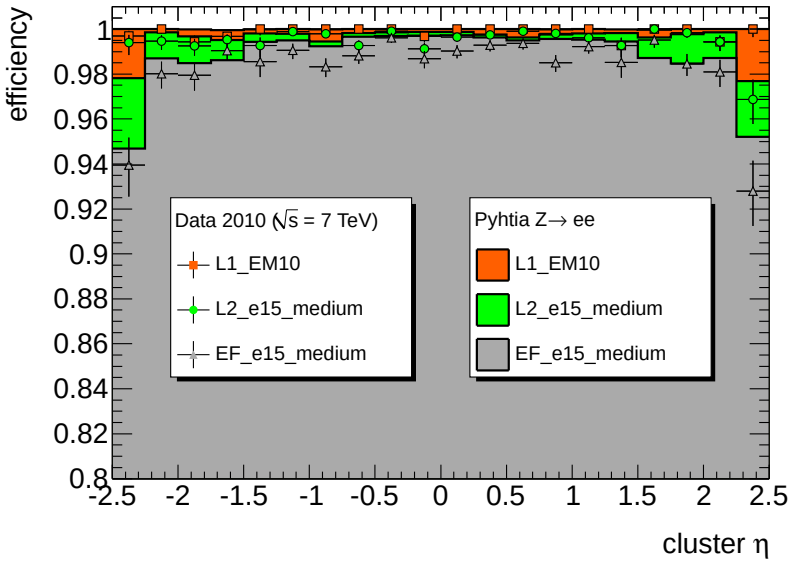

Figure 6.9: Trigger efficiencies for medium electrons with $E_T > 20$ GeV as a function of the cluster η for the trigger chain EF_e15_medium. The efficiencies are compared to Pythia $Z \rightarrow ee$ MC simulation.

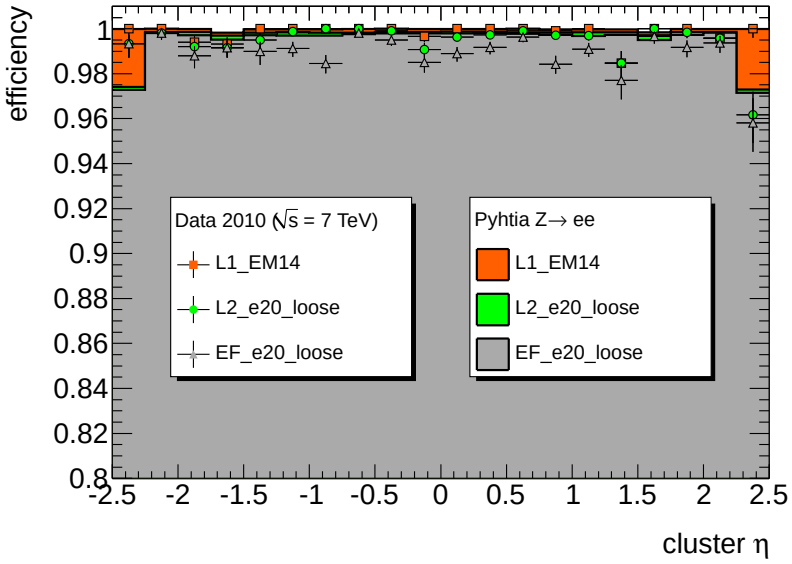

Figure 6.10: Trigger efficiencies for medium electrons with $E_T > 25$ GeV as a function of the cluster η for the trigger chain EF_e20_medium. The efficiencies are compared to Pythia $Z \rightarrow ee$ MC simulation.

Trigger	Integration Threshold	Efficiency in %	
		Data	Pythia $Z \to ee$
L1_EM10	$E_T > 20$ GeV	99.90 ± 0.03	99.9946 ± 0.0005
L1_EM14	$E_T > 25$ GeV	99.87 ± 0.03	99.9749 ± 0.0011
L2_e15_medium	$E_T > 20$ GeV	99.57 ± 0.05	99.6625 ± 0.0040
L2_e20_loose	$E_T > 25$ GeV	99.60 ± 0.04	99.7281 ± 0.0037
EF_e15_medium	$E_T > 20$ GeV	98.63 ± 0.09	99.1427 ± 0.0064
EF_e20_loose	$E_T > 25$ GeV	99.03 ± 0.08	99.6250 ± 0.0044

Table 6.1: The integrated efficiencies for the trigger chain EF_e15_medium and EF_e20_loose. Only statistical uncertainties are given.

In table 6.1 the integrated efficiencies of all trigger levels for the chains EF_e15_medium and EF_e20_loose are given, respectively.[1] As already seen in fig. 6.9 and fig. 6.10 the efficiencies in the MC simulation are larger than the ones in data. For the EF, a global scale factor of 0.995 ± 0.001 (0.994 ± 0.001) for the trigger chain EF_e15_medium (EF_e20_loose) is determined. The results of the HLT trigger chains have been confirmed with $W \to e\nu$ events [192, 196], where missing transverse energy is used as tag trigger.

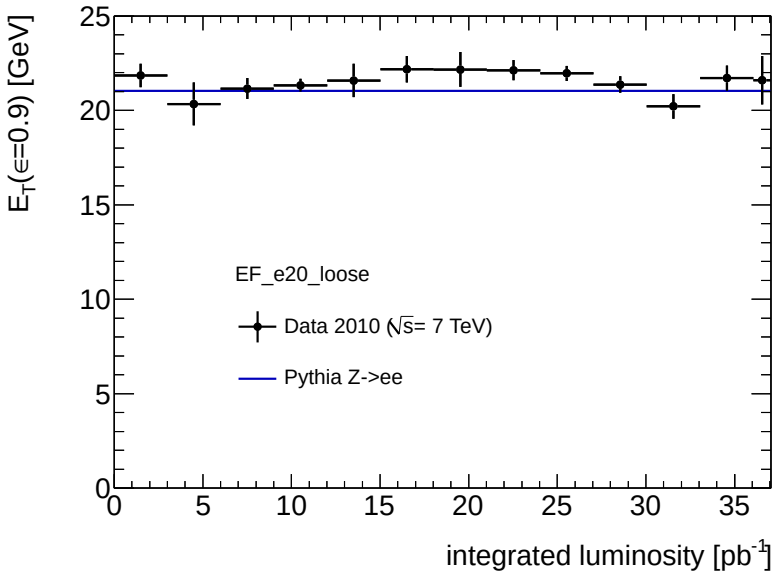

Figure 6.11: E_T value when the EF_e20_loose trigger reaches the 90% efficiency level as a function of the integrated luminosity.

[1] Studies of systematic uncertainties, including the change of requirements for the tag electron, different values for the ΔR matching, and the change of the invariant mass cut, have shown that the systematic uncertainty is of the same order as the statistical one [196, 226].

The E_T value for which the EF_e20_loose trigger reaches the 90% efficiency level is determined by the same fitting procedure as described for L1 in section 6.1.2. The E_T threshold value at the 90% efficiency level as a function of the integrated luminosity is displayed in fig. 6.11. In addition, the MC expectation of Pythia $Z \rightarrow ee$ events is shown by the blue line. The data points agree well with the MC expectation within the uncertainties. Moreover, the smooth behavior of the data points indicates a quite stable operating of the EF_e20_loose trigger chain.

CHAPTER 7

Di-Electron Event Selection

In this chapter the selection of $pp \to Z/\gamma^* \to ee$ candidates is discussed, which are later used for the measurement of the forward-backward asymmetry and the effective weak mixing angle. In the beginning the selection requirements of central–central and central–forward electron pairs are presented. In order to compare data and MC simulation, corrections are introduced to account for possible differences in efficiencies and energy measurements. In a separate section the rates of selected di-electron events as a function of the integrated luminosity are shown, indicating stable data taking conditions. The expected number of simulated events from signature and background processes is studied, as well. In order to estimate the QCD background, the results of a data-driven method are presented. Finally, the chapter concludes with data MC comparisons of various di-electron control distributions.

7.1 Selection of $Z/\gamma^* \to ee$ candidates

The event selection is divided into the pre-selection, the electron selection, and the di-electron selection. In the pre-selection collision events are separated from non-collision background:

Good-Runs-List: Only events associated with a luminosity block which is in the egamma GRL are selected (*cf.* section 5.5).

Primary Vertex Cut: In order to reject cosmic ray signatures only events with at least one vertex associated with at least 3 tracks are investigated.

Trigger: Since the HLT was not operated with a stable configuration in the early data taking phase, the trigger condition is special for early runs (*cf.* section 5.5 and section 6.2).

- Runs with run numbers smaller than 160613 (corresponding to approximately 0.3 pb^{-1}): **L1_EM14**
- Since 160613 (corresponding to approximately 37.1 pb^{-1}): **EF_e15_medium**
- For simulated events the two triggers are applied corresponding to the fraction of events in data.

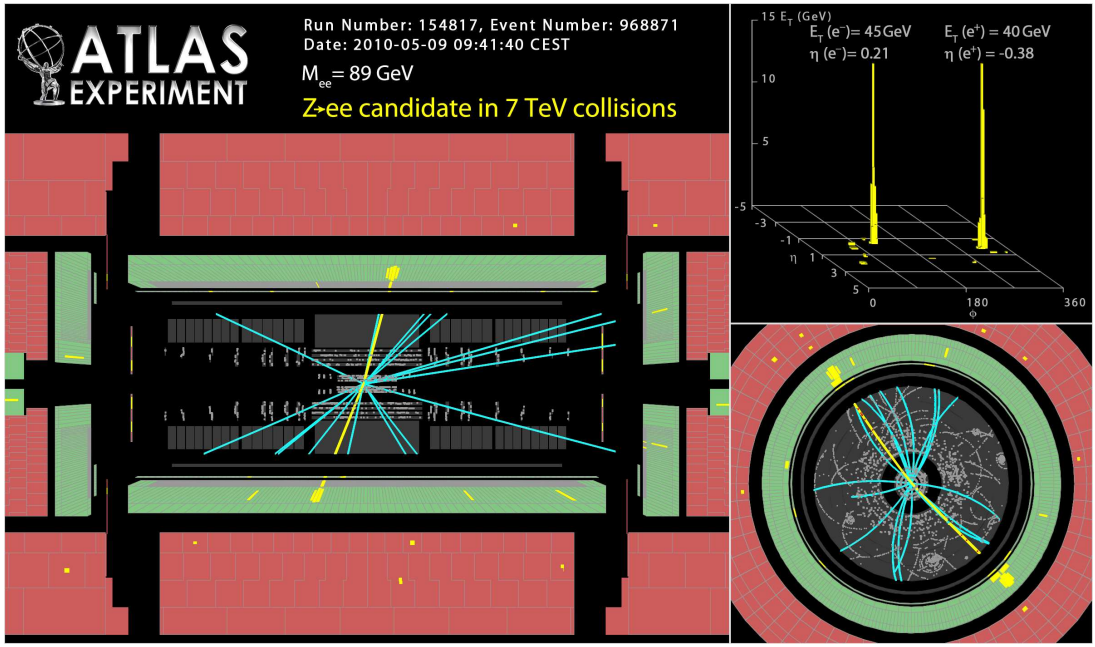

Figure 7.1: Event display of a $Z/\gamma^* \rightarrow ee$ candidate with two central medium electrons [201].

In this thesis electron candidates are selected which are reconstructed by the standard as well as the forward algorithms. For simplicity, one usually refers to central and forward electrons. To ensure that the selected electrons lie in the plateau region of the trigger efficiencies (*cf.* section 6.2), only central electrons with a transverse energy larger than 20 GeV are taken into account (kinematic cut). The same cut is also applied to the forward electrons in order to be consistent with the central selection. The central electron candidates are restricted to the pseudo-rapidity coverage of the EM calorimeter ($|\eta| < 2.47$), while for forward electrons objects within $2.5 < |\eta_{cl}| < 4.9$ are selected. Additionally, the transition regions between the barrel and the end-caps of the EM calorimeter ($1.37 < |\eta_{cl}| < 1.52$) are excluded, since a reliable electron reconstruction is difficult in this region. Each electron has to pass the object quality cuts, representing non-reliable regions in the EM calorimeter (as described in section 5.5.1). These regions are stored in time-dependent η–ϕ maps. For MC events the maps are used corresponding to the fraction of events in data.

For the di-electron selection, either two central electrons or one central with a forward electron are combined. A combination of two forward candidates is not possible, since the electron trigger is limited to the central region. The category of $Z/\gamma^* \rightarrow ee$ candidates are defined by:

Two Central Electrons (CC): Two electron candidates with opposite charge passing the medium identification cuts (as described in section 5.3.2).

One Central Electron and one Forward Electron (CF): A central electron candidate passing the tight identification cuts and a forward electron identified by the forward tight algorithm (as described in section 5.3.2).

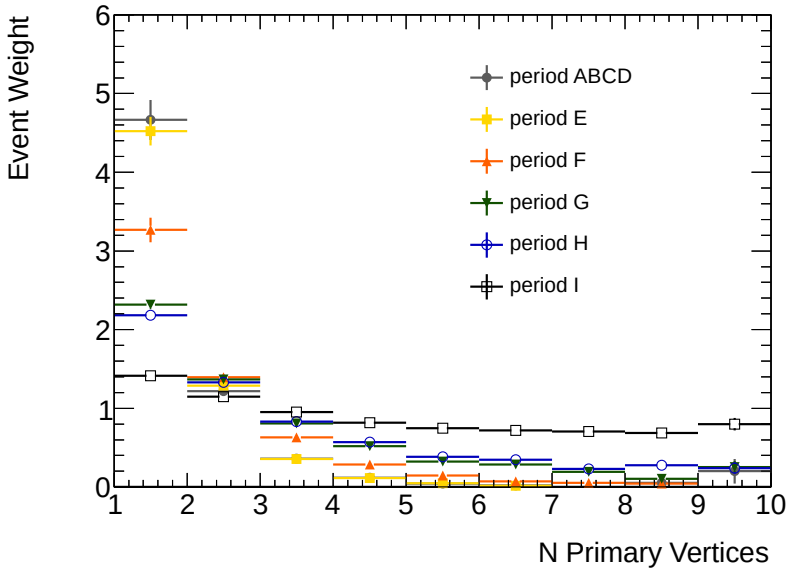

Figure 7.2: Pile-up MC re-weighting factors for the different data taking periods.

Figure 7.1 shows the event display of a $pp \rightarrow Z/\gamma^* \rightarrow ee$ candidate. Two medium electron tracks (yellow) with opposite charge have been reconstructed. The inner detector (gray) is surrounded by the EM calorimeter (green) and the hadronic calorimeter (red). Other charged particles (turquoise) are also depicted in the event display. In the upper right corner the η and transverse energy of the electrons are given. The invariant mass of the two electrons is determined to be 89 GeV.

7.1.1 Corrections and Efficiencies

In order to compare MC predictions to data, several corrections need to be applied to MC as well as data events. While data events only need to be corrected for the energy scale in the EM calorimeter, in MC several correction factors arise due to differences in energy resolution, efficiency measurements, and a different simulation of pile-up events in MC compared to data.

The number of additional pile-up events can influence the physical results. As described in section 5.6, in the MC samples used in this thesis the amount of additional minimum bias interactions is Poisson distributed with an expectation value of 2.2. The number of interactions in an event passing the GRL and the trigger conditions is estimated by counting the number of reconstructed primary vertices that have at least three tracks. The ratio between the number of vertices for data and Pythia $Z \rightarrow ee$ events is shown as a function of the number of primary vertices in fig. 7.2. Since the number of pile-up events increases with increasing instantaneous luminosity, the pile-up event weights are determined for each data period separately. In the analysis the MC events are weighted by the corresponding pile-up weights from fig 7.2, to reproduce the number of additional pile-up interactions in data properly.

η **regions**	**medium scale factor**	**tight scale factor**
$-2.47 < \eta < -2.01$	0.973 ± 0.010	1.002 ± 0.012
$-2.01 < \eta < -1.52$	0.972 ± 0.010	1.032 ± 0.019
$-1.37 < \eta < -0.8$	0.976 ± 0.011	1.065 ± 0.014
$-0.8 < \eta < 0$	0.971 ± 0.007	0.989 ± 0.009
$0 < \eta < 0.8$	0.978 ± 0.008	0.996 ± 0.009
$0.8 < \eta < 1.37$	0.976 ± 0.010	1.059 ± 0.011
$1.52 < \eta < 2.01$	0.986 ± 0.010	1.048 ± 0.028
$2.01 < \eta < 2.47$	0.974 ± 0.025	1.037 ± 0.026

Table 7.1: Scale factors for combined $Z \to ee$ and $W \to e\nu$ medium and tight identification efficiencies in η bins and integrated over the 2-50 GeV E_T range [192].

In order to correct for different trigger, reconstruction, and identification efficiencies in data and MC, scale factors have been determined to account for possible discrepancies in the MC simulation [192]. For the efficiency calculations tag-and-probe techniques have been applied to $Z \to ee$ as well as to $W \to e\nu$ events. For the reconstruction efficiency no deviations between data and MC could be observed so far. The trigger efficiency has been determined from $Z \to ee$ events in section 6.2. A global scale factor of 0.995 ± 0.001 has been estimated for the trigger chain EF_e15_medium.[1] For the identification efficiency deviations in different η regions have been observed [192]. The scale factors which are applied to MC events are listed in table 7.1. The errors are composed of statistical as well as systematic uncertainties.

Table 7.2 contains the scale factors used for forward electron candidates. The difference of the identification efficiency between data and MC is larger for forward electrons than for central electrons.

η **regions**	**loose forward scale factor**	**tight forward scale factor**
$2.5 < \|\eta\| < 3.2$	0.916 ± 0.053	0.800 ± 0.053
$3.2 < \|\eta\| < 4.9$	0.983 ± 0.086	0.896 ± 0.81

Table 7.2: Scale factors for loose forward and tight forward efficiencies in two η bins [192].

The energy scale of the EM calorimeter depends on the environmental conditions, *e.g.* the temperature. These conditions can change during data taking and in particular they can differ from the conditions assumed in the electron reconstruction. So far no time-dependent study has been performed due to the lack of statistics. Only correction factors for the entire 2010

[1] The data efficiency of the L1_EM14 trigger agrees with the MC expectation within the uncertainties [227].

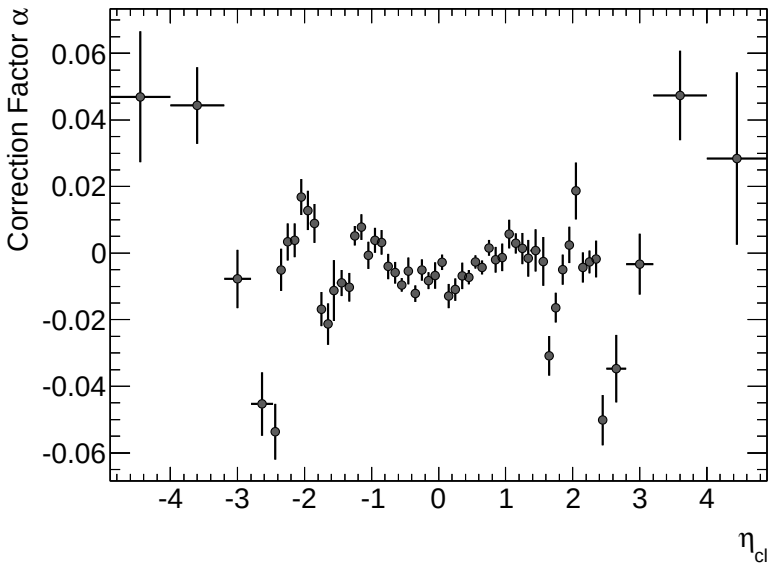

Figure 7.3: Electron energy scale correction factors in η bins to be applied to data [192].

data taking period have been determined [192]. The calorimeter energy is corrected as follows

$$E_{\text{corr}} = \frac{E_{\text{meas}}}{1-\alpha}\,, \tag{7.1}$$

where α is the correction factor, that has been determined in 58 η bins from J/Ψ and Z events as well as from E/p studies of isolated electrons from $W \rightarrow e\nu$ candidates. In case of Z events, the scale corrections are derived by requiring that the invariant mass distribution follows the Z line shape in MC. For this purpose several methods have been developed and compared [192]. As depicted in fig. 7.3, the correction is around 1% in the barrel region ($|\eta_{cl}| < 1.37$), while in the end-caps a larger correction 2-4% has to be applied. In the forward region the correction factor is approximately 5-6%. The largest systematic uncertainty arises from the limited knowledge of the material in front of the calorimeter as well as the energy from the presampler. The uncertainty arising from the dead regions in the calorimeter has been studied in detail and found to be small [192].

In MC, the Z mass resolution does not reproduce the one in data after the appropriate energy of the electrons has been re–scaled. To achieve a proper agreement the energy resolution of the MC electrons needs to be smeared. The smearing parameters are extracted by comparing the invariant mass distributions of data and MC events. A detailed description of the methods and the values of the smearing parameters can be found in [192].

7.1.2 Yield of $Z/\gamma^* \rightarrow ee$ candidates

In fig. 7.4(a) and fig. 7.4(b) the rates for CC and CF $Z/\gamma^* \rightarrow ee$ candidates are shown as a function of the integrated luminosity. Each dot represents approximately 0.1 pb^{-1}. The dots are distributed around the average for the 2010 data, shown by the orange bands. The largest

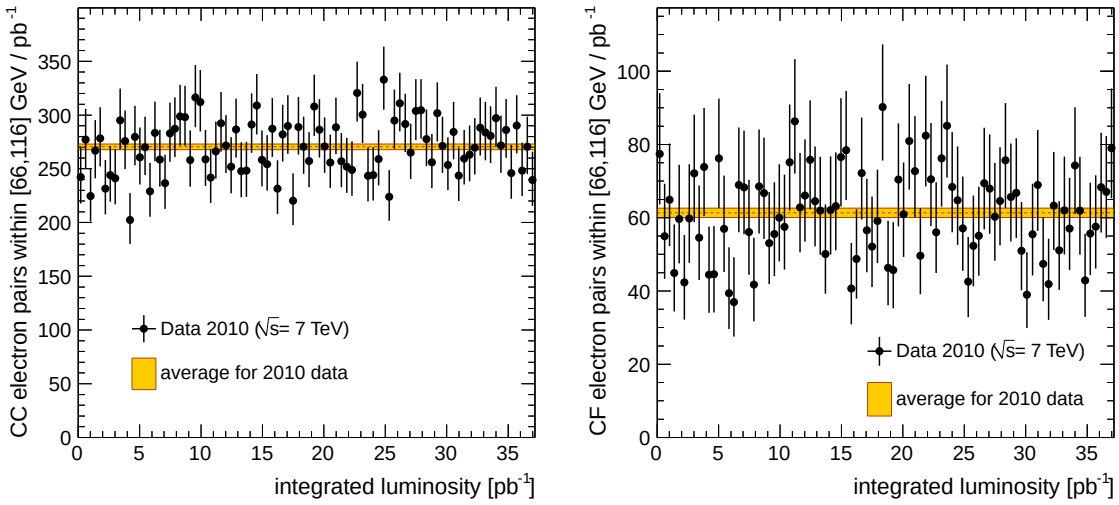

(a) (b)

Figure 7.4: Rate of selected $Z/\gamma^* \rightarrow ee$ candidates versus the integrated luminosity for (a) two central electrons as well as (b) a central and a forward electron.

outlier deviates 3.0σ from the average for CC selection and 2.2σ for the CF selection, respectively. Overall the rates indicate that the detector components responsible for the electron selection operated rather stable in 2010.

7.2 Background Contamination

The Drell–Yan signal suffers from several sources of background contamination. They can be divided into electroweak backgrounds ($W \rightarrow e\nu$, $Z \rightarrow \tau\tau$, and $t\bar{t}$) and the background arising from hadronic jets (QCD). The background contamination is usually estimated from simulated events. The MC samples used for the ATLAS analysis in this thesis are listed in table 7.3. The Pythia MC generator is used with a special tune of the MRST LO** PDF [228–230], while the MC@NLO generator has been employed with the CTEQ6.6 PDF set [231]. The signal MC samples $Z \rightarrow ee$ contain Drell–Yan events generated with an invariant mass larger than 60 GeV. The generator–computed cross-sections as listed in the second column are used to normalize the expected CC and CF $Z/\gamma^* \rightarrow ee$ events given in the last two columns of table 7.3. It is already visible that the electroweak background is rather small compared to the Drell–Yan signal samples. The QCD background arises mostly from the mis-identification of jets as electrons. A di-jet sample containing approximately 9 millions events has been investigated. The cross-section of this process is huge and suffers from significant uncertainties. In addition, only very few events survive the CC and CF selection. Therefore, a data-driven method is required to get an estimate of the QCD background.

Sample	Cross-Section	Used PDF	CC Events	CF Events
Data 2010	–	–	10124	2296
Pythia $Z \to ee$	855 ± 20 pb	MRST LO** [228–230]	8906.38 ± 8.44	2209.02 ± 4.20
MC@NLO $Z \to ee$	953 ± 26 pb	CTEQ6.6 [231]	8478.65 ± 9.33	2120.57 ± 4.69
Pythia QCD	$(8.57 \pm 0.25) \cdot 10^7$ pb	MRST LO** [228–230]	no events selected	223.60 ± 223.60
Pythia $W \to e\nu$	8937 ± 306 pb	MRST LO** [228–230]	8.14 ± 0.69	19.07 ± 1.08
MC@NLO $t\bar{t}$	144 ± 5 pb	CTEQ6.6 [231]	12.01 ± 0.21	0.93 ± 0.06
Pythia $Z \to \tau\tau$	854 ± 20 pb	MRST LO** [228–230]	5.79 ± 0.35	2.42 ± 0.24

Table 7.3: Number of events containing at least one $Z/\gamma^* \to ee$ candidate with an invariant mass between 66 and 116 GeV for data and MC samples. The numbers are for an integrated luminosity of 37.4 pb^{-1}. The errors are statistical uncertainty only. The generator–computed cross-section and the PDF set are given, as well.

7.2.1 Data-Driven QCD Background Estimation

To obtain the normalization of the QCD background, a template fit method is applied to the invariant mass distributions. For this purpose, the QCD background is artificially enhanced by loosening the electron requirements. Finally, the resulting enhanced background level needs to be scaled down in order to account for the original selection.

For the CC selection, instead of requiring a medium electron, a loose electron with the additional requirement that the track has at least 4 hits in the silicon tracking detectors ('loose+SilHits') is chosen.[1] Two different selections have been investigated: two 'loose+SilHits' electrons as well as one medium and one 'loose+SilHits' electron.[2] The estimated number of QCD events is determined by fitting the invariant mass distributions of these two selections. The resulting number needs to be scaled down by the probability that a hadronic jet identified as a 'loose+SilHits' electron candidate passes also the medium requirements (rejection factor). The result derived with two 'loose+SilHits' electron candidates is multiplied by the square of the rejection factor

$$N_{\mathrm{QCD}}^{\mathrm{medium-medium}} = N_{\mathrm{QCD}}^{\prime\mathrm{loose+SilHits}^{\prime}-\prime\mathrm{loose+SilHits}^{\prime}} \cdot (r_{\prime\mathrm{loose+SilHits}^{\prime}}^{\mathrm{medium}})^2 \,, \tag{7.2}$$

while for the medium plus 'loose+SilHits' selection the QCD background is estimated by

$$N_{\mathrm{QCD}}^{\mathrm{medium-medium}} = N_{\mathrm{QCD}}^{\mathrm{medium}-\prime\mathrm{loose+SilHits}^{\prime}} \cdot r_{\prime\mathrm{loose+SilHits}^{\prime}}^{\mathrm{medium}} / (2 - r_{\prime\mathrm{loose+SilHits}^{\prime}}^{\mathrm{medium}}) \,. \tag{7.3}$$

The rejection factor is determined from a control sample, containing only events with a single reconstructed electron and a transverse missing energy less than 15 GeV.[3] These conditions

[1] The requirement of at least 4 hits in the silicon tracking detectors is not included in the loose criteria, but at L2 this condition is required.

[2] In case of two 'loose+SilHits' electrons one needs to switch to the trigger chain EF_e20_loose, otherwise the online trigger conditions would be tighter than the offline selection.

[3] Only data period H and I are used.

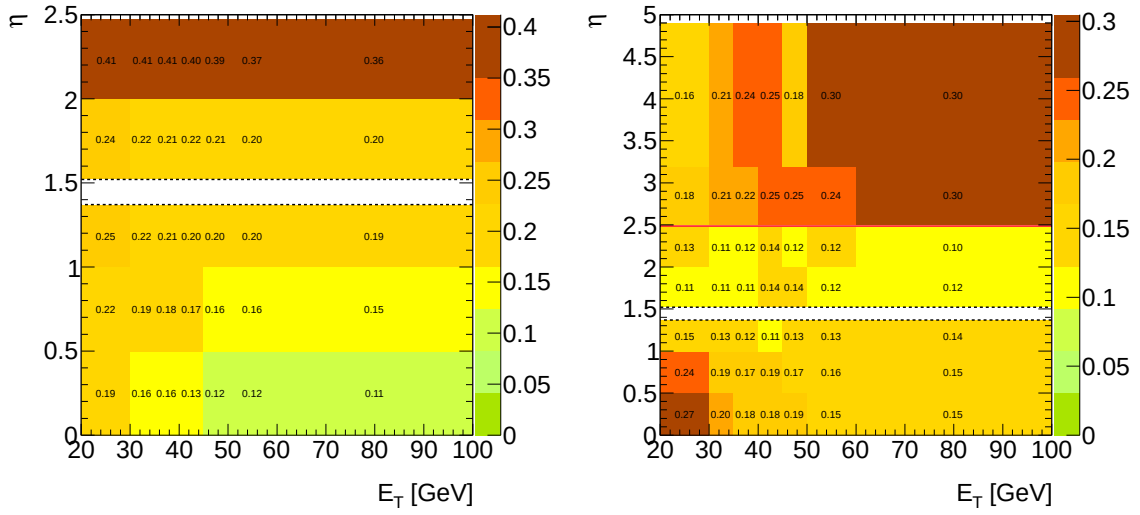

(a) (b)

Figure 7.5: Rejection factors as a function of η and E_T: (a) For 'loose+SilHits' to medium electron candidates and (b) medium to tight and loose forward to tight forward electron candidates. The rejection factors have been determined from electron samples dominated by electron candidates faked by hadronic jets.

ensure a sample composed of reconstructed electrons mostly faked by hadronic jets. The rejection factor is defined as the ratio of the number of medium electron candidates over the number of 'loose+SilHits' candidates. The result is shown in fig. 7.5(a) as a function of η and E_T. The mis-identification rate is larger in the end-caps ($|\eta| > 1.52$), since less tracking information is available in this region. The overall integrated factor amounts to be $r^{\text{medium}}_{\text{loose+SilHits}} = 0.2467 \pm 0.0003$.

For the CF selection, also two different selections have been investigated: one medium and one loose forward electron as well as one tight and one loose forward electron candidate. The corresponding rejection factors are determined from the same sample as for the CC selection. The results are shown in fig. 7.5(b) as a function of η and E_T. The central and forward regions are separated by the red solid line. The average values are $r^{\text{medium}}_{\text{tight}} = 0.1613 \pm 0.0004$ and $r^{\text{loose forward}}_{\text{tight forward}} = 0.2012 \pm 0.0027$. In case of a medium and a loose forward electron the number of background events needs to be scaled by

$$N^{\text{tight}-\text{tight forward}}_{\text{QCD}} = N^{\text{medium}-\text{loose forward}}_{\text{QCD}} \cdot r^{\text{medium}}_{\text{tight}} \cdot r^{\text{loose forward}}_{\text{tight forward}}\,, \tag{7.4}$$

while for tight and forward loose selection the number of QCD background events is estimated by

$$N^{\text{tight}-\text{tight forward}}_{\text{QCD}} = N^{\text{tight}-\text{loose forward}}_{\text{QCD}} \cdot r^{\text{loose forward}}_{\text{tight forward}}\,. \tag{7.5}$$

The background extraction relies on fits of the invariant mass distributions. The Z signal is described by a Crystal-Ball convoluted with a Breit-Wigner function, while for the QCD background a Landau function is added. The background extraction is performed either by

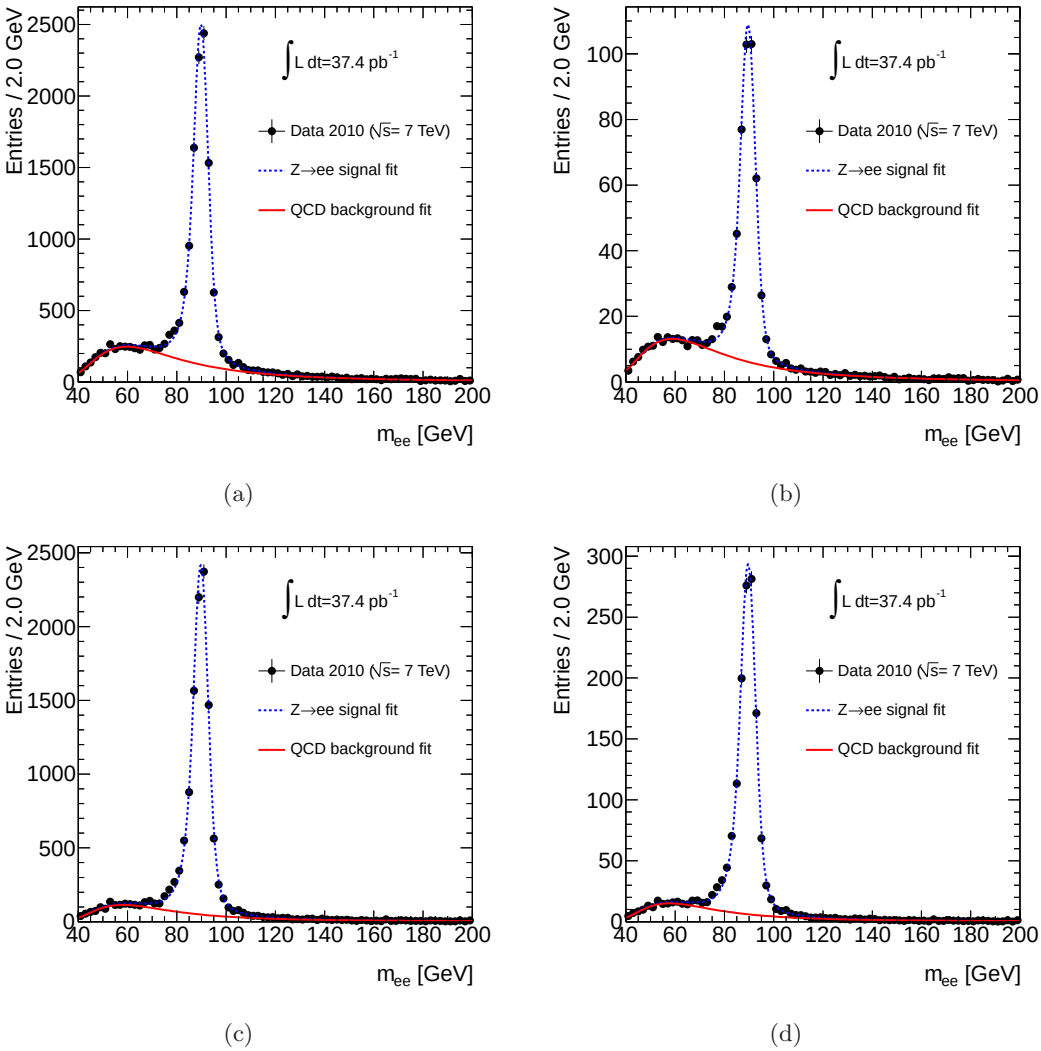

Figure 7.6: Fits of central–central invariant mass distributions: (a) 'loose+SilHits' – 'loose+SilHits', (b) 'loose+SilHits' – 'loose+SilHits' weighted with the rejection factor, (c) medium – 'loose+SilHits', and (d) medium – 'loose+SilHits' weighted with the rejection factor. For more details consult the text.

fitting the invariant mass distributions and scaling the background results by the corresponding rejection factors or by directly weighting the events according to the maps shown in fig. 7.5(a) and fig. 7.5(b) and then fitting the invariant mass distributions. The fits of CC and CF invariant mass distributions are shown in figs. 7.6 (a)-(d) and figs. 7.7 (a)-(d). As default the number of QCD background events is estimated from the fit of the unweighted distributions of two 'loose+SilHits' electrons for the CC selection (*cf.* fig. 7.6 (a)) and the unweighted distribution of a medium and a loose forward electron for the CF selection (*cf.* fig. 7.7 (a)). The difference to the other methods is taken as systematic uncertainty. In case of the CC selection, the QCD background is estimated in the invariant mass window between 66 and 116 GeV to be

$$N_{\mathrm{QCD}}^{\mathrm{medium-medium}} = 194.8 \pm 3.8\,(\mathrm{stat}) \pm 32.7\,(\mathrm{syst})\,, \tag{7.6}$$

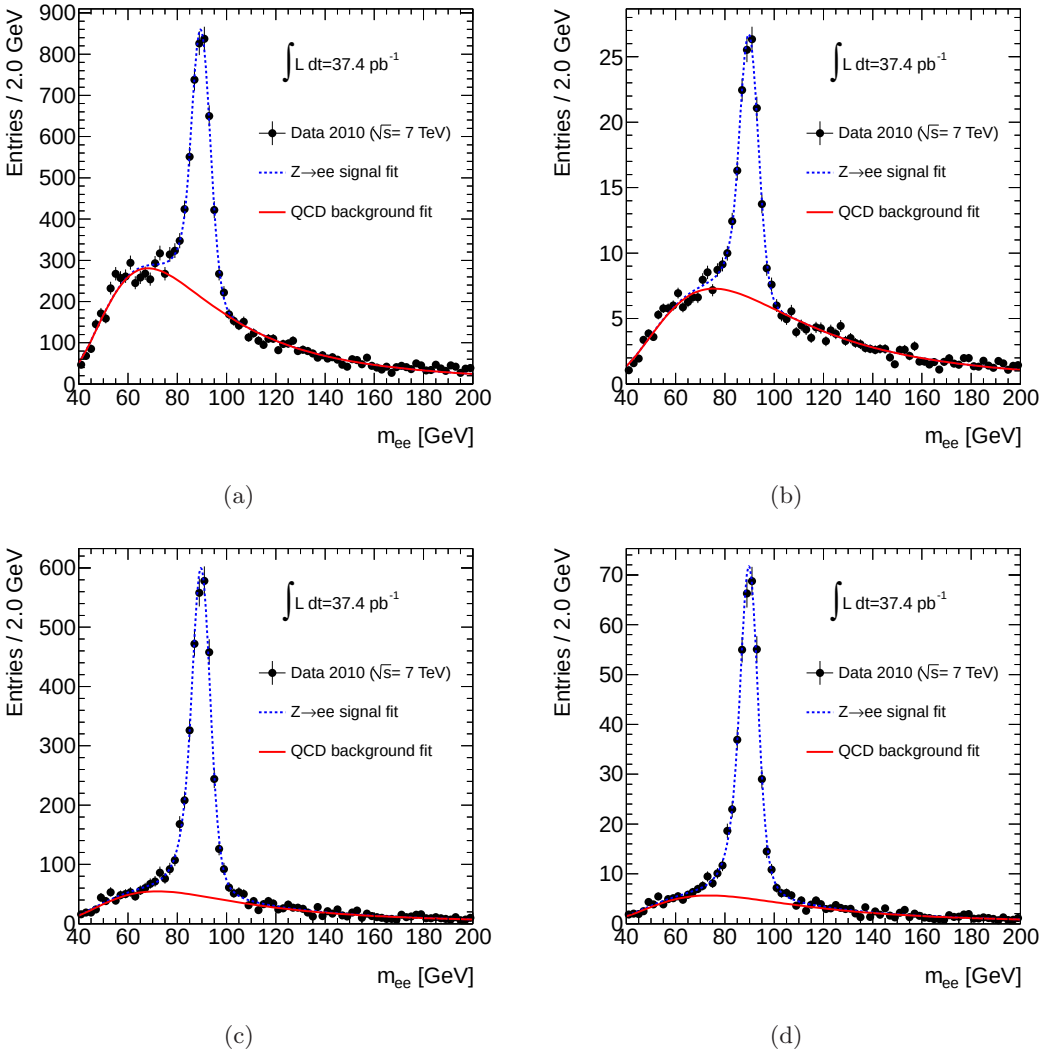

Figure 7.7: Fits of central–forward invariant mass distributions: (a) medium – loose forward, (b) medium – loose forward weighted with the rejection factors, (c) tight – loose forward, and (d) tight – loose forward weighted with the rejection factor. For more details consult the text.

and for CF selection it is

$$N_{\mathrm{QCD}}^{\text{tight}-\text{tight forward}} = 124.7 \pm 4.5\,(\text{stat}) \pm 46.4\,(\text{syst})\,. \tag{7.7}$$

In addition to the QCD contribution, the background shapes for the invariant mass distributions contain also electroweak backgrounds and Drell–Yan signal events. The electroweak background is determined from the MC samples and the corresponding cross-section as listed in table 7.3. The amount of Drell–Yan events is estimated by the difference of same-sign to opposite-sign pairs for the CC selection. Since the charge mis-identification rate (*cf.* section 8.2) and the production rate of Drell–Yan events (excluding the Z peak) are small, the number of signal events in the background function is negligible for same-sign events. Therefore, the difference of the background shape of same-sign and opposite-sign events should give

an estimate of the Drell–Yan contribution. The contamination of Drell–Yan events could be determined from fits to be approximately 13% of the number of extracted background events. The value is also used in the CF case. The electroweak and Drell–Yan contribution is summed in quadrature and is taken into account as additional systematic uncertainty. The final QCD background within the invariant mass window of 66 and 116 GeV is estimated for the CC selection to be

$$N_{\mathrm{QCD}}^{\mathrm{medium-medium}} = 194.8 \pm 3.8\,(\mathrm{stat}) \pm 32.7\,(\mathrm{syst,fit})\,{}^{+\,0.0}_{-82.1}\,(\mathrm{syst,ew/DY})\,, \tag{7.8}$$

and for the CF selection it is

$$N_{\mathrm{QCD}}^{\mathrm{tight-tight\ forward}} = 124.7 \pm 4.5\,(\mathrm{stat}) \pm 46.4\,(\mathrm{syst,fit})\,{}^{+\,0.0}_{-82.0}\,(\mathrm{syst,ew/DY})\,, \tag{7.9}$$

where the third uncertainty is due to the electroweak and Drell–Yan contamination and only accounts as negative error.

The QCD background outside the invariant mass window of 66 to 116 GeV is estimated by normalizing the invariant mass distributions of two electrons without any identification cuts of QCD MC events to the expected number of QCD events in the mass range 66-116 GeV. The result is shown in fig. 7.8. The same procedure has been carried out with a data sample containing almost only reconstructed electrons faked by hadronic jets.[1] The difference between the two shapes is small and is completely covered by the uncertainty from the QCD background estimation. In this thesis, the QCD background shapes for various distributions are always taken from the QCD MC sample and scaled to the number of estimated background events in the mass window of 66-116 GeV.

7.3 Di-Electron Distributions

After the QCD background has been estimated by the data-driven method, all ingredients are available to compare data to MC simulation. For the electroweak background, the MC samples described in section 7.2 are used. Figure 7.9(a) and fig. 7.9(b) show the invariant mass distribution between 60 and 1000 GeV of Z/γ^* candidates for the CC and CF selection, respectively. The number of MC entries is scaled to the number of data entries in the Z peak region (invariant mass range 66-116 GeV). The Z peak around 90 GeV is clearly visible for both selections. The uncertainty arising from the data-driven QCD background estimation is displayed by the red/yellow shaded region for the MC expectation. Uncertainties from the electroweak background (*e.g.* cross-section, luminosity) are neglected. Additionally, the ratio between data and MC is shown at the bottom of the figures. The errors are computed by using the statistical uncertainty of the data and the uncertainty of the MC prediction. Data and MC expectation agree quite well over the entire mass range, indicating that the QCD background determination is also valid for large invariant masses.

[1] One 'loose+SilHits' electron candidates and one electron without any identification cuts have been selected. Events with the actual selection have been excluded.

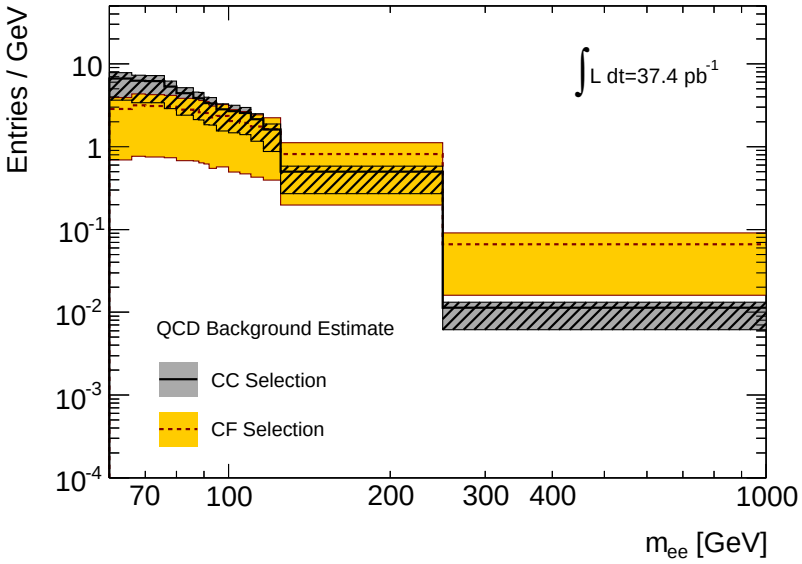

Figure 7.8: Number of QCD background events as a function of the invariant mass for the central–central and the central–forward selection.

A zoom of the invariant mass distributions is displayed in fig. 7.10(a) and fig. 7.10(b). They show the invariant mass distributions with a linear scale and only near the Z mass peak for the CC and the CF selection, respectively. Only the QCD background is considered, since the electroweak background is negligible in comparison to the signal and QCD background as already seen in fig. 7.9(a) and fig. 7.9(b). The data and MC Z line shapes agree well. No resolution and energy scale uncertainties have been considered in these distributions.

In fig. 7.11(a) and fig. 7.11(b) the distributions of the E_T of both electrons arising from $Z/\gamma^* \rightarrow ee$ candidates with an invariant mass between 66 and 116 GeV are depicted. Again, a reasonable agreement between data and MC is observed. For the CC selection, the Jacobian peak is clearly visible, *i.e.* the distribution peaks at half of the Z mass and the distribution declines for $\mathrm{E_T} > 45$ GeV. The Jacobian peak for the CF selection is shifted to lower values and is smeared out due to the fact that CF pairs are usually boosted, *i.e.* they are not produced with small rapidities.

The distributions of the transverse momentum of $Z/\gamma^* \rightarrow ee$ candidates with an invariant mass between 66 and 116 GeV are presented in fig. 7.12(a) and fig. 7.12(b). Most of the events carry only very little transverse momenta. This follows the expectation, since large transverse momenta are usually introduced by ISR. The probability of ISR decreases with increasing momentum of the emitted particle. Again, a reasonable agreement could be found between data and MC.

Figure 7.13(a) and fig. 7.13(b) show the rapidity distributions of the di-electron pairs for the CC and the CF selection, respectively. Again, only pairs with an invariant mass between 66 and 116 GeV are taken into account. The difference between CC and CF pairs is clearly visible. The CC pairs favor small rapidities and due to the fiducial cuts the rapidity is restricted

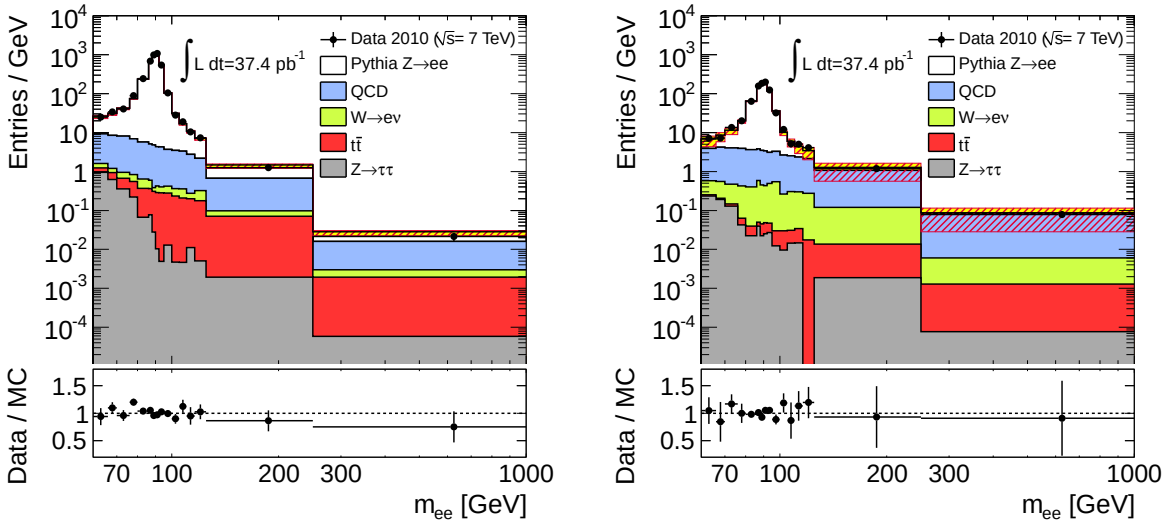

(a) (b)

Figure 7.9: Invariant mass distribution for (a) the central–central and (b) the central–forward electron selection, respectively. The red/yellow shaded areas indicate the uncertainty of the MC prediction arising from the QCD background estimation. The number of MC entries is scaled to the number of data events in the invariant mass range 66-116 GeV. The ratio between data and MC expectation is depicted at the bottom of the figures.

to $|y_{ee}| < 2.5$. In comparison, the CF events are much more boosted, leading to large values of the rapidity ($|y_{ee}| > 1$). The data MC agreement is reasonable. One should keep in mind that the scale factors for the forward electron identification have rather large uncertainties (*cf.* table 7.2).

In conclusion the data agrees quite well with the MC simulation including the data-driven estimate of the QCD background. No significant deviation between the SM predictions and the measured data could be observed.

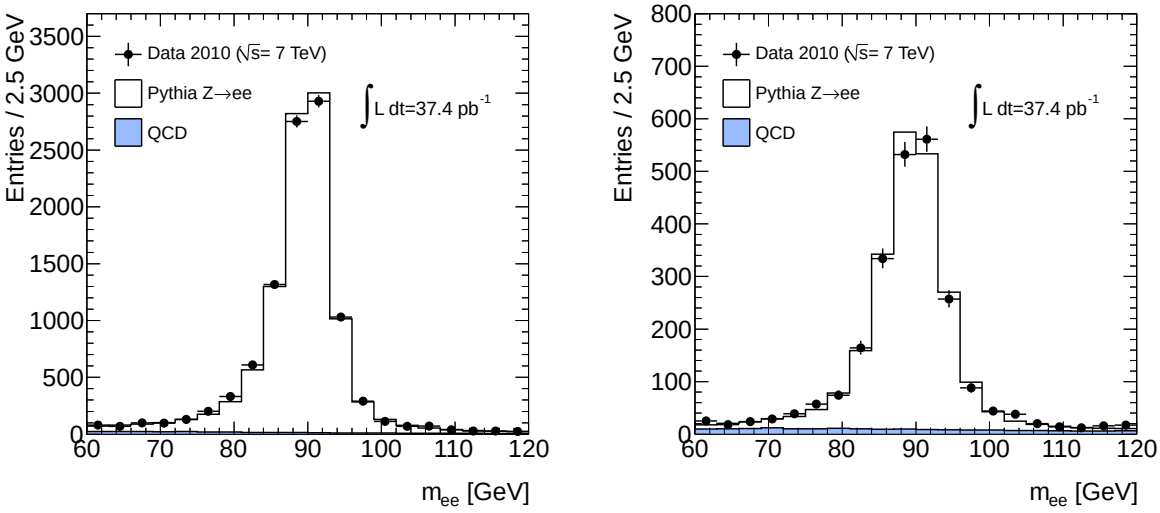

(a) (b)

Figure 7.10: Data–MC shape comparison for the invariant mass distribution near the Z peak for (a) the central–central and (b) the central–forward selection. The number of entries in MC is scaled to the one in data.

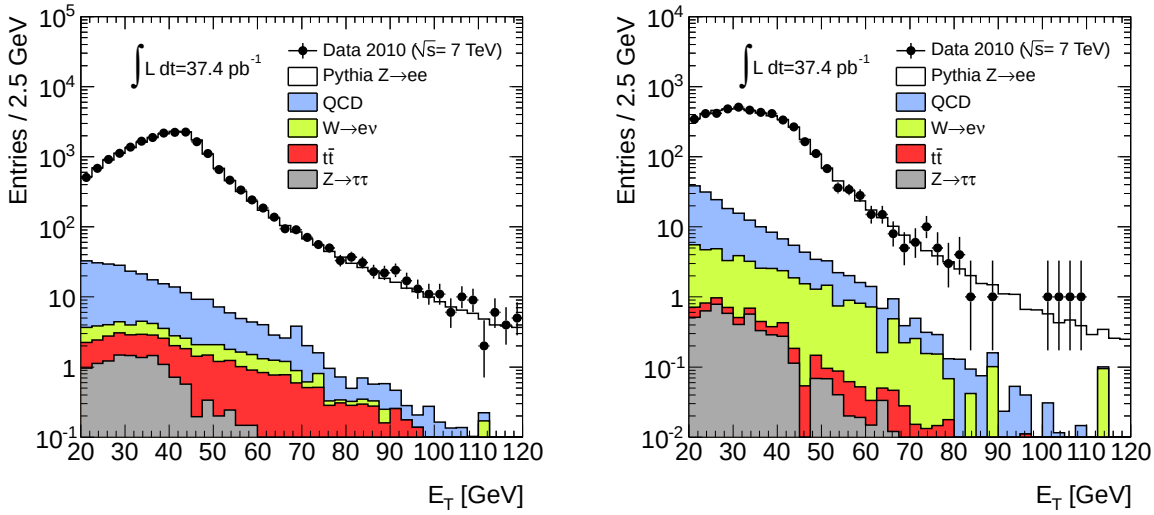

(a) (b)

Figure 7.11: Distributions of the E_T of both electrons arising from $Z/\gamma^* \rightarrow ee$ candidates with an invariant mass between 66 and 116 GeV for (a) the central–central and (b) the central–forward selection. The number of entries in MC is scaled to the one in data.

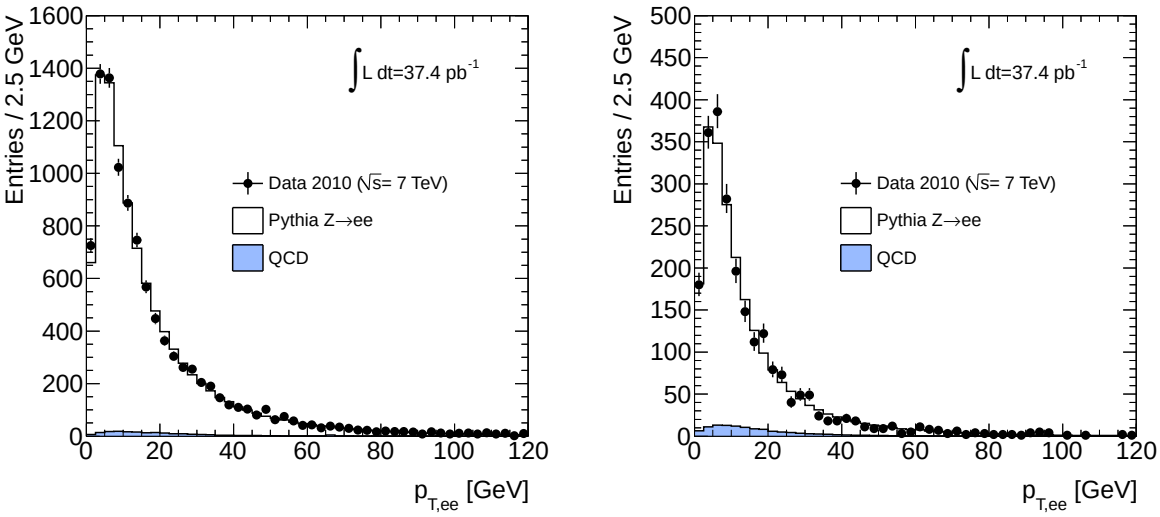

(a) (b)

Figure 7.12: Transverse momentum distributions of the $Z/\gamma^* \rightarrow ee$ candidates with an invariant mass between 66 and 116 GeV for (a) the central–central and (b) the central–forward selection. The number of entries in MC is scaled to the one in data.

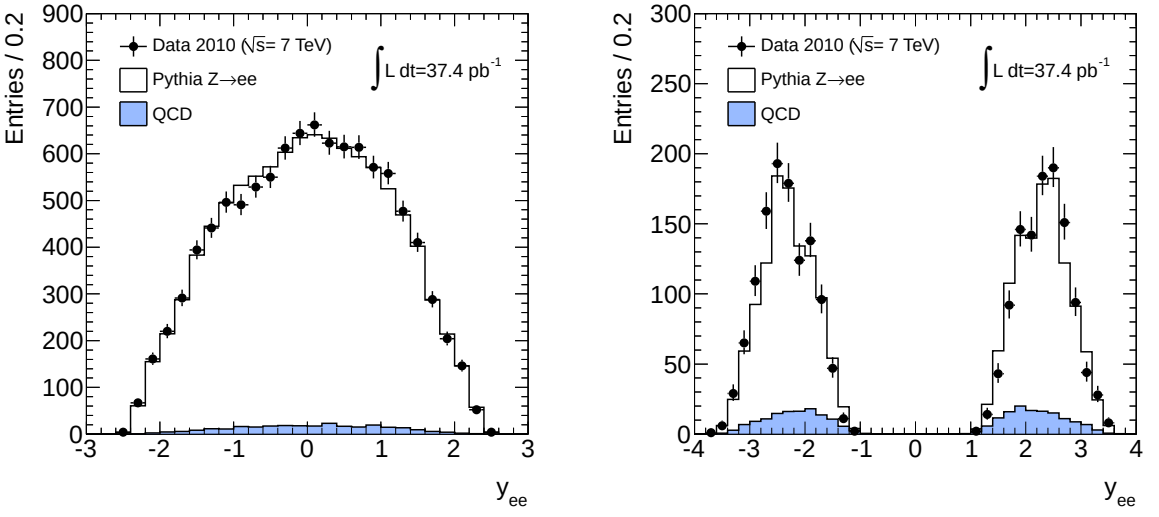

(a) (b)

Figure 7.13: Rapidity distributions of the $Z/\gamma^* \rightarrow ee$ candidates with an invariant mass between 66 and 116 GeV for (a) the central–central and (b) the central–forward selection. The number of entries in MC is scaled to the one in data.

CHAPTER 8

Measurement of A_{FB} and $\sin^2\theta^{\ell}_{eff}$

This chapter describes the measurement of the forward-backward asymmetry and the effective weak mixing angle using the ATLAS detector. In the beginning, the strategy of the analysis is discussed in detail. Results on the charge mis-identification are presented, which can influence the A_{FB} measurement. In the following section, the forward-backward asymmetry at detector level is shown. From the A_{FB} distribution the effective weak mixing angle is determined by using a template method. The forward-backward asymmetry at detector level is corrected for the detector resolution and acceptance as well as ambiguities in the analysis, to obtain the true distribution at parton level. The unfolded distribution is directly compared to predictions from MC generators. The chapter concludes with a Pythia8 study demonstrating the influence of unparticles and large extra dimensions to the Drell–Yan cross-section as well as on the forward-backward asymmetry.

8.1 Analysis Strategy

The aim of this analysis is to measure the forward-backward asymmetry as a function of the invariant mass of the process $pp \to Z/\gamma^* \to ee$ and to extract the effective weak mixing angle. As already described in section 2.2 the angle between the incoming quark and the outgoing electron has to be known, in order to distinguish forward and backward events. However, in case of proton-proton collisions the directions and the transverse momenta of the incoming partons are unknown. However, the boost of the di-electron system gives a hint of the direction of the incoming quark. For the production of Drell–Yan events at the LHC usually a valence quark annihilates with a sea anti-quark. Since the valence quark has in average a larger Bjorken x than the sea anti-quark, the di-electron system should be boosted in the direction of the valence quark. However, this statement is only true on average and for individual events it might not always be correct. In particular, no statement can be made of the annihilation of two sea quarks.

The uncertainty of the unknown transverse momenta of the incoming quarks can be minimized by using the Collins–Soper (CS) reference frame [232], where the polar axis is defined as the bisector of the two quark momenta in the rest frame of the electron-positron system.

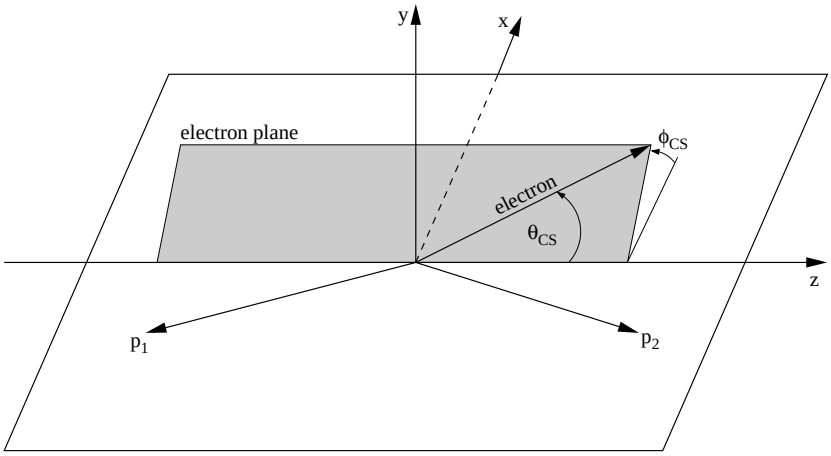

Figure 8.1: The Collins–Soper reference frame used in this analysis to reduce the ambiguity due to the unknown transverse momenta of the incoming quarks. P_1 and P_2 are the quark momenta.

The angle θ_{CS} is defined as the angle between the polar axis z and the electron, as shown in fig. 8.1. The angle can be computed from the four-momenta of the electron and positron

$$\cos(\theta_{\mathrm{CS}}) = \frac{2}{m_{ee}\sqrt{m_{ee}^2 + p_{T,ee}^2}} \left[p^+(e^-)p^-(e^+) - p^+(e^+)p^-(e^-)\right] , \tag{8.1}$$

where $p^\pm = \frac{1}{\sqrt{2}}(E \pm p_z)$. E is the energy and p_z the longitudinal component of the momentum of the electron or positron, respectively. To account for the assumption that the boost of the di-electron system and the direction of the incoming quark are the same, the sign of the boost has to be added

$$\cos(\theta_{\mathrm{CS}}) = \frac{p_{z,ee}}{|p_{z,ee}|} \cdot |\cos(\theta_{\mathrm{CS}})| . \tag{8.2}$$

Electron pairs in the forward direction are then defined by $\cos(\theta_{\mathrm{CS}}) > 0$, while for backward pairs the relation $\cos(\theta_{\mathrm{CS}}) < 0$ holds. The forward-backward asymmetry is defined by the number of forward (N_F) and backward events (N_B)

$$A_{\mathrm{FB}} = \frac{N_F - N_B}{N_F + N_B} , \tag{8.3}$$

with the statistical uncertainty[1]

$$\Delta A_{\mathrm{FB}} = \sqrt{\frac{1 - A_{\mathrm{FB}}^2}{N_F + N_B}} . \tag{8.4}$$

In fig. 8.2 the probability that the incoming quark direction is equal to the direction of the Z/γ^* boost is shown as a function of the rapidity of the electron pair. For electron pairs

[1] If $N_F = 0$ or $N_B = 0$, *i.e.* $A_{\mathrm{FB}} = \pm 1$, the uncertainty is determined by $\Delta A_{\mathrm{FB}} = 4/(N_F + N_B)^4 \cdot (N_F^2(\Delta N_B)^2 + N_B^2(\Delta N_F)^2)$, where $\Delta N = \sqrt{N}$ for $N \neq 0$ and for $N = 0$ the 68% CL upper limit for 0 observed events is taken as uncertainty ($\Delta N = 1.84$).

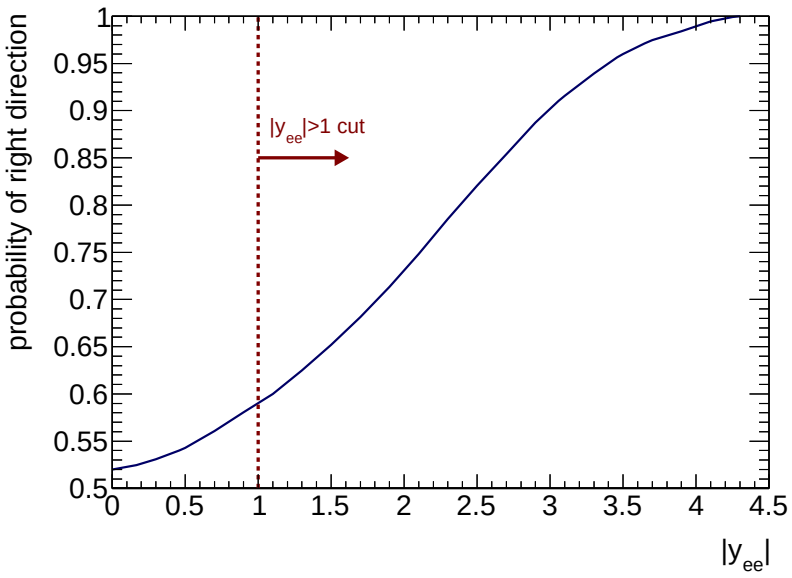

Figure 8.2: Probability that the incoming quark direction is equal to the direction of the Z/γ^* boost as a function of the rapidity. Truth generator level information from Pythia $Z \rightarrow ee$ events is used.

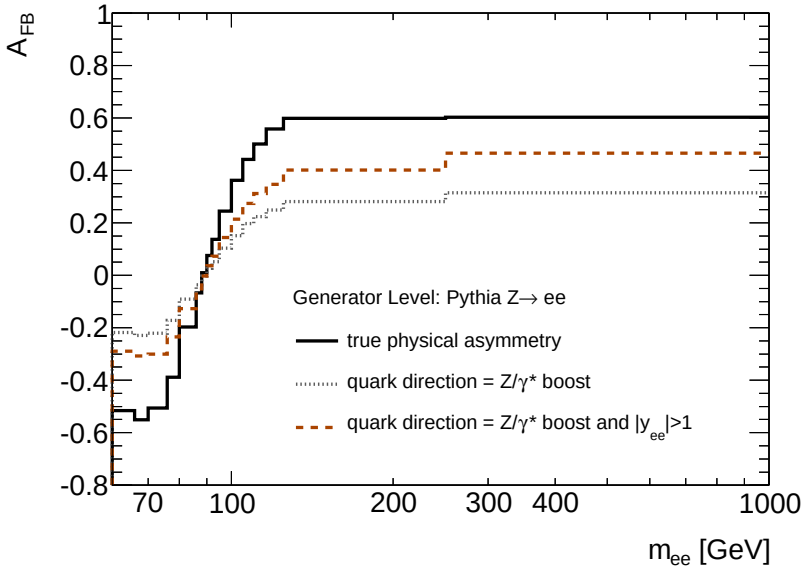

Figure 8.3: Forward-backward asymmetry as a function of the invariant mass for the three scenarios given. Truth generator level information from Pythia $Z \rightarrow ee$ events is used.

produced with small rapidities the probability is only slightly larger than 50%, *i.e.* in approximately half of the cases the assumption is incorrect. For events with large rapidities, the probability increases, since one quark (usually the valence quark) needs to have more momentum.

The ambiguity that the incoming quark direction is not always equal to the direction of the Z/γ^* boost, affects the shape of the measured forward-backward asymmetry. In fig. 8.3 the black solid line shows the true asymmetry, while for the gray dotted line the assumption, that the quark direction is equal to the Z/γ^* boost, is used. The dilution of the asymmetry is clearly visible. In order to enhance the asymmetry, the analysis is additionally performed with a rapidity cut of $|y_{ee}| > 1$, which removes events with low probability that the incoming quark direction is correctly determined (*cf.* fig. 8.2). The corresponding A_{FB} distribution is displayed by the orange dashed line in fig. 8.3. The additional cut ($|y_{ee}| > 1$) has been already proposed by several authors [16, 17, 233].

For the analysis of the forward-backward asymmetry CC as well as CF $Z/\gamma^* \rightarrow ee$ candidates are investigated. The advantage of CF electron pairs is that they are more boosted than CC pairs leading to larger rapidities and therefore to larger probabilities that the quark direction is equal to the Z/γ^* boost. In contrast, CC pairs can be measured more precisely and their production rate is higher than for CF pairs. In this thesis, the analysis is performed with a combination of CC and CF $Z/\gamma^* \rightarrow ee$ candidates. The forward-backward asymmetry and the resulting value of the effective weak mixing angle are determined with and without the additional rapidity cut of $|y_{ee}| > 1$.

8.2 Charge Mis–Identification

The charge of the electron is a crucial ingredient for the computation of the Collins–Soper angle in eq. (8.1). While for CC electron pairs both charges are measured and therefore the charge mis-identification of such events is rather small, for CF pairs only the charge of the central electron is known. The primary reason for charge mis-identification is that electrons interacting early in the detector produce multiple high p_T tracks. The track cluster matching algorithm could finally assign the wrong track to the electron, resulting in a possible incorrect charge identification.

The charge mis-identification rate is measured with a tag-and-probe method using $Z \rightarrow ee$ events. The tag-and-probe electrons need to pass the pre-selection as well as the fiducial and kinematic cuts described in chapter 7. To select a well measured tag electron with a small charge mis-identification rate, the tag electron needs to pass the tight as well as some isolation requirements. Additionally, only tags in the barrel region ($|\eta| < 1.37$) are selected, since the charge mis-identification rate is larger in the end-caps than in the barrel region due to less tracking information than in the barrel. To account for background contamination, a simple side-band subtraction is applied. The invariant mass range between 80 and 100 GeV is defined as signal region, while the background side-bands lie 20 GeV below and above the signal region.

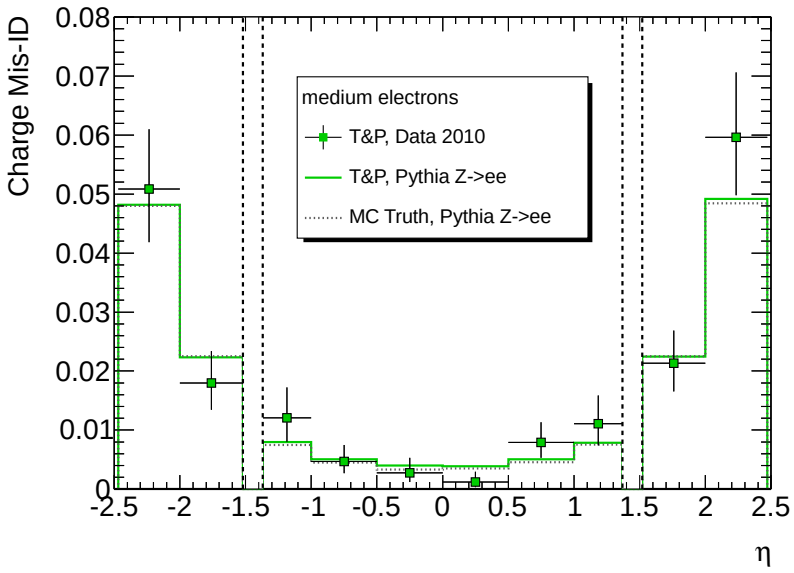

Figure 8.4: The charge mis-identification rate in η bins for medium electron candidates.

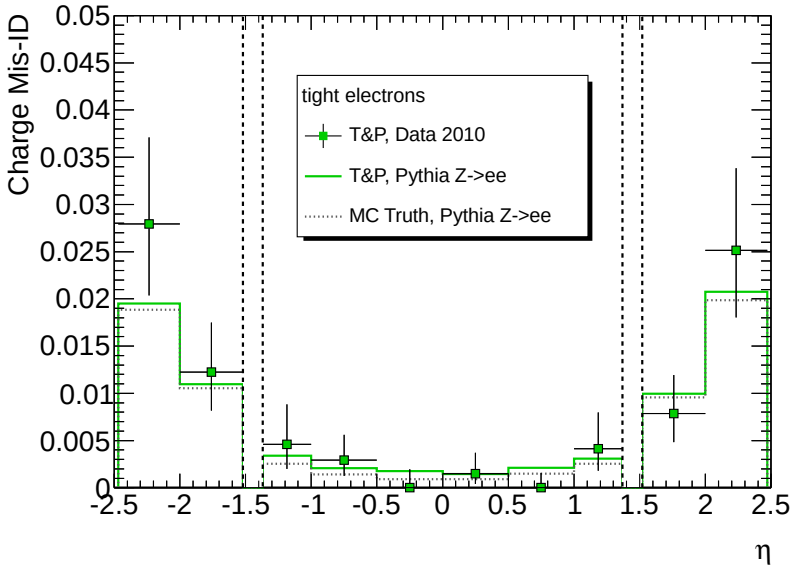

Figure 8.5: The charge mis-identification rate in η bins for tight electron candidates.

The charge mis-identification rate is defined as the ratio of the number of same-sign tag-and-probe pairs over all di-electron pairs.

In fig. 8.4 and fig. 8.5 the charge mis-identification rate in various η bins is shown for medium and tight electrons, respectively. The mis-identification rate is larger in the end-caps than in the barrel region for both selections due to less tracking information in the end-caps. The tag-and-probe results for MC and data are in good agreement.[1]

In conclusion, the charge mis-identification rates for medium and tight electrons are small and should not affect the measurement of A_{FB} significantly. The MC simulation describes rather well the charge mis-identification in data. Therefore, no correction factors are applied to simulated events.

8.3 Forward-Backward Asymmetry at Detector Level

For the computation of the forward-backward asymmetry, the angular distribution of the $Z/\gamma^* \rightarrow ee$ candidates needs to be determined.[2] In the following always a combination of CC and CF pairs is used. Figure 8.6(a) shows the $\cos(\theta_{CS})$ distribution for electron pairs with an invariant mass between 66 and 116 GeV, while for fig. 8.6(b) in addition the rapidity cut of $|y_{ee}| > 1$ is applied. Very forward or very backward events are quite rare due to the kinematic and fiducial cuts of the electrons (*cf.* section 8.5.2). A slightly stronger asymmetry between forward and backward events is already visible for the analysis with the additional rapidity cut.

The forward-backward asymmetry is determined in various invariant mass bins. The number of selected forward and backward events in each mass bin and the corresponding background events are listed in appendix A. The expected background contamination needs to be subtracted from the number of measured events to obtain the pure A_{FB} distribution of $Z/\gamma^* \rightarrow ee$ events. The forward-backward asymmetry is shown in fig. 8.7 for the invariant mass range between 60 and 1000 GeV and in fig. 8.8 for invariant masses near the Z peak. The uncertainty arising from background subtraction is added in quadrature to the statistical errors. The resulting uncertainties are indicated by the gray error bars. Since the background is dominated by QCD events and the electroweak background is almost negligible, only the uncertainty from the data-driven QCD estimate is taken into account. The measured asymmetry is compared to the MC simulation of Pythia and MC@NLO $Z \rightarrow ee$ events. The data distribution agrees quite well with the expectations from the MC simulations.

A similar behavior is observed for pairs with $|y_{ee}| > 1$. The corresponding distributions are shown in fig. 8.9 and fig. 8.10. Again, no significant deviations between the measurement and the MC simulations are observed. In contrast to the previous distribution without any rapidity

[1] The small difference between the MC tag-and-probe result (green solid line) and the result using MC truth information (gray dotted line) is due to a non-vanishing probability that the tag electron is mis-identified.

[2] As already mentioned the sign of $\cos(\theta_{CS})$ defines if an event is considered as forward or backward (*cf.* section 8.1).

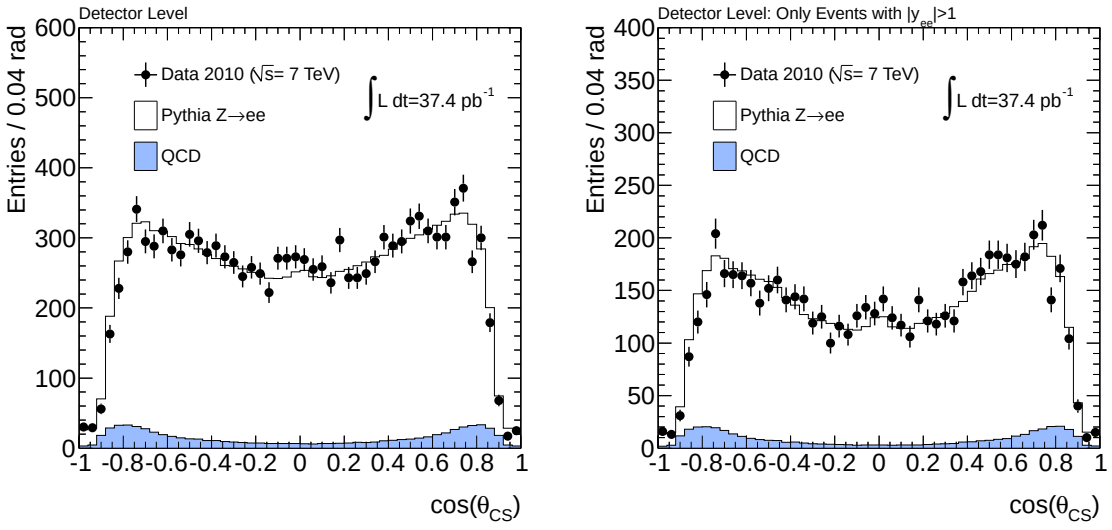

(a) (b)

Figure 8.6: Angular distributions of the Collins–Soper angle for $Z/\gamma^* \rightarrow ee$ candidates with an invariant mass between 66 GeV and 116 GeV (a) for all rapidities and (b) only pairs with $|y_{ee}| > 1$.

cut, the asymmetry is enhanced due to the rejection of events with a low probability that the incoming quark direction is equal to the di-electron boost.

8.4 Determination of the Effective Weak Mixing Angle

As discussed in section 2.2 the shape of the forward-backward asymmetry depends on the value of the effective weak mixing angle. In this thesis a MC template method is used to extract the value of $\sin^2\theta^{\ell}_{\text{eff}}$ from the forward-backward asymmetry at detector level.[1] For this purpose 100 Pythia $Z \rightarrow ee$ MC samples with 5 million events each have been generated for $\sin^2\theta^{\ell}_{\text{eff}}$ values between 0.2 and 0.25. As default, the CT10 PDF set [235] is used. For each $\sin^2\theta^{\ell}_{\text{eff}}$ sample the ratio of the normalized number of events in the two-dimensional space m_{ee}–$\cos(\theta_{\text{CS}})$ of the default ATLAS MC Pythia $Z \rightarrow ee$ simulation (generated with $\sin^2\theta^{\ell}_{\text{eff}} = 0.232$) and the generated $\sin^2\theta^{\ell}_{\text{eff}}$ samples are computed. The undiluted MC truth information is used to compute the physical quantities. Each event of the full ATLAS MC simulation is then re-weighted by the corresponding factor of the two-dimensional m_{ee}–$\cos(\theta_{\text{CS}})$ map, resulting in 100 ATLAS MC simulation samples each with a different $\sin^2\theta^{\ell}_{\text{eff}}$ value. Finally, the data distributions are compared to the different $\sin^2\theta^{\ell}_{\text{eff}}$ MC samples to determine the effective weak mixing angle with the best matching distribution.

The χ^2 estimator of the comparison between the detector level A_{FB} distribution of data and the specific $\sin^2\theta^{\ell}_{\text{eff}}$ Pythia $Z \rightarrow ee$ MC samples is defined by the sum of the contributions

[1] This method has also been used by the D0 collaboration [22, 234].

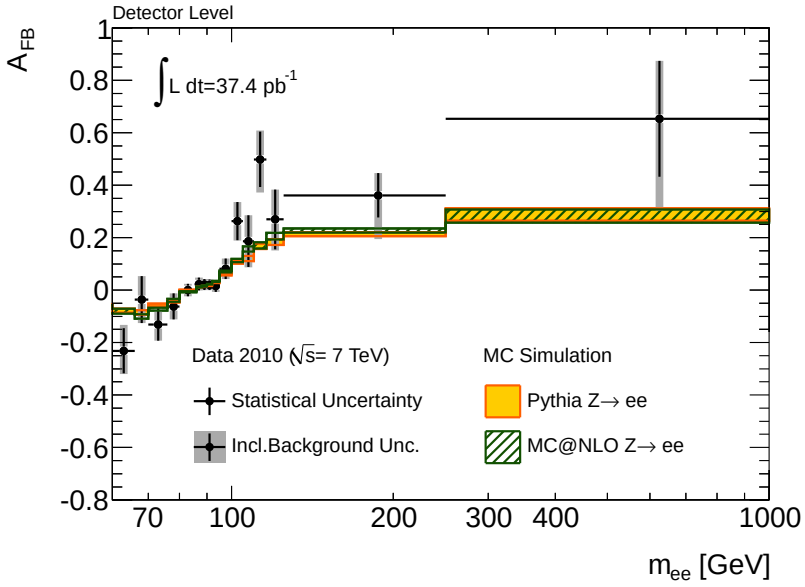

Figure 8.7: Forward-backward asymmetry at detector level as a function of the invariant mass in the range of 60 to 1000 GeV.

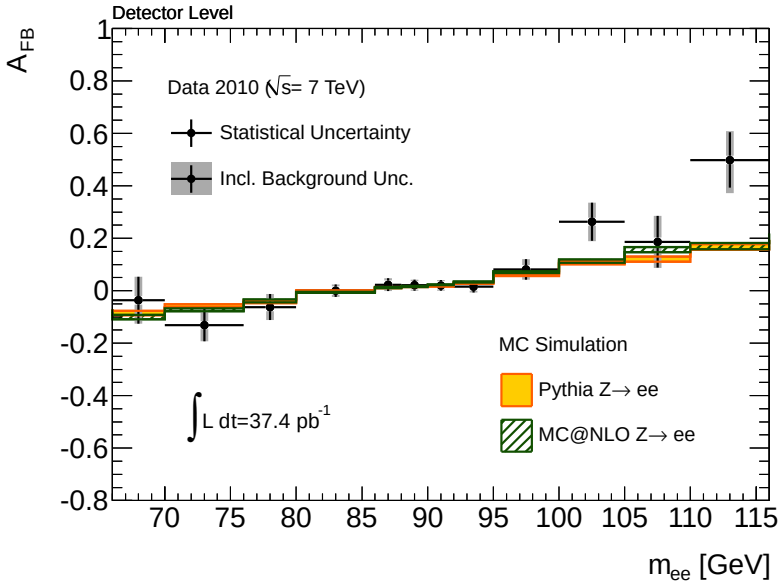

Figure 8.8: Forward-backward asymmetry at detector level as a function of the invariant mass in the range of 66 to 116 GeV.

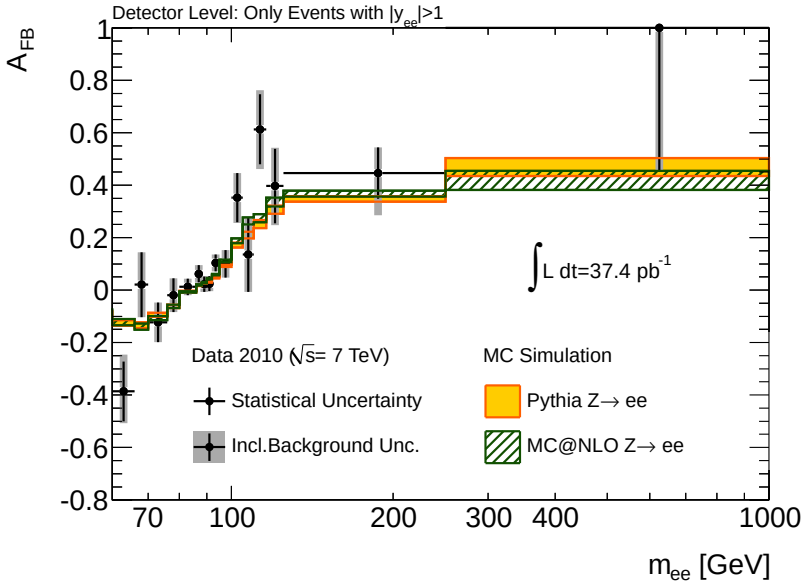

Figure 8.9: Forward-backward asymmetry at detector level as a function of the invariant mass in the range of 60 to 1000 GeV. Only pairs with $|y_{ee}| > 1$ are taken into account.

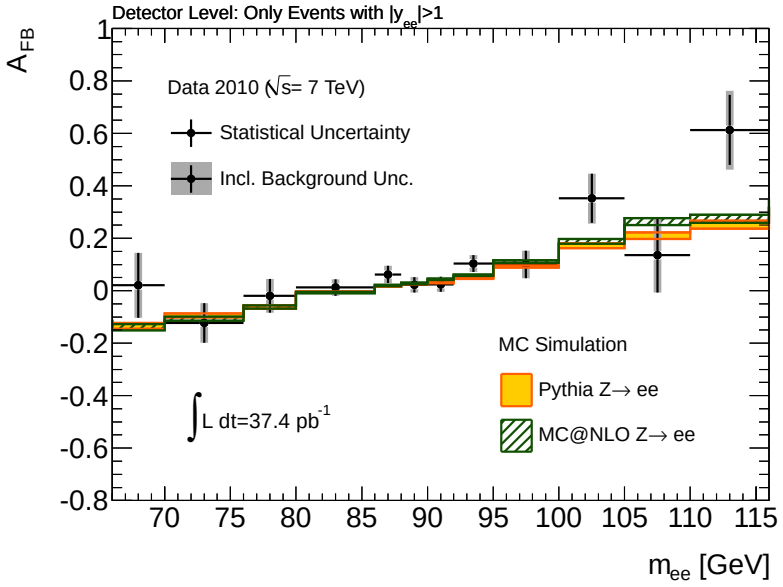

Figure 8.10: Forward-backward asymmetry at detector level as a function of the invariant mass in the range of 66 to 116 GeV. Only pairs with $|y_{ee}| > 1$ are taken into account.

from each mass bin i

$$\chi^2(\sin^2\theta^\ell_{\text{eff}}) = \sum_i \frac{\left(A^i_{\text{FB}}(\text{data}) - A^i_{\text{FB}}(\sin^2\theta^\ell_{\text{eff}})\right)^2}{\left(\Delta A^i_{\text{FB}}(\text{data})\right)^2 + \left(\Delta A^i_{\text{FB}}(\sin^2\theta^\ell_{\text{eff}})\right)^2}\,, \tag{8.5}$$

where the errors in the denominator are purely statistical uncertainties. Since the uncertainties of the forward-backward asymmetry are small for bins near the Z peak, the value of $\sin^2\theta^\ell_{\text{eff}}$ is mainly determined by these mass bins. The χ^2 estimator as a function of $\sin^2\theta^\ell_{\text{eff}}$ is shown in fig. 8.11 for all di-electron pairs and in fig. 8.12 for pairs with $|y_{ee}| > 1$, respectively. The χ^2 distribution is fitted by a quadratic function, shown by the black dashed curves. The resulting $\sin^2\theta^\ell_{\text{eff}}$ values and their 1σ uncertainties can be easily derived. They are displayed by the red arrows in the two figures.[1] Taking into account all electron pairs the value reads

$$\sin^2\theta^\ell_{\text{eff}} = 0.2290 \pm 0.0081\,, \tag{8.6}$$

while for $Z/\gamma^* \to ee$ candidates with $|y_{ee}| > 1$ the value is determined to be

$$\sin^2\theta^\ell_{\text{eff}} = 0.2204 \pm 0.0071\,. \tag{8.7}$$

Although less events are selected with the additional cut the effective weak mixing angle can be determined more precisely due to the enhanced asymmetry that is more sensitive to the $\sin^2\theta^\ell_{\text{eff}}$ value. The difference in both $\sin^2\theta^\ell_{\text{eff}}$ values can be explained by statistical fluctuations.

In a closure test the effective weak mixing angle is determined from the original ATLAS Pythia $Z \to ee$ sample (generated with $\sin^2\theta^\ell_{\text{eff}} = 0.232$). The $\sin^2\theta^\ell_{\text{eff}}$ value for all electron pairs is $\sin^2\theta^\ell_{\text{eff}} = 0.2327 \pm 0.0010$ and when applying the cut $|y_{ee}| > 1$ one obtains $\sin^2\theta^\ell_{\text{eff}} = 0.2326 \pm 0.0009$. Both values agree with each other and with the one used in the MC generation.

In the determination of the effective weak mixing angle several sources of systematic uncertainties arise. The values of the systematic uncertainties from the energy scale, the energy resolution, and identification scale factors are estimated by shifting the correction factors by their uncertainties, as listed in section 7.1.1. The maximum shifts in the $\sin^2\theta^\ell_{\text{eff}}$ value are taken as systematic uncertainty. In case of pile-up re-weighting the difference between the results with the additional pile-up re-weighting and with the default pile-up configuration (in average 2.2 vertices) is considered as systematic uncertainty. Similar for background subtraction the maximum shifts in the $\sin^2\theta^\ell_{\text{eff}}$ determination, when applying the uncertainties from appendix A, are used as systematic errors. For the PDF uncertainty, 52 error PDF sets are used, which are provided by the CT10 collaboration [235]. They have been determined by varying the PDF parameters in positive and negative direction along the i-th eigenvector. Following the description in [235] the PDF uncertainty can be computed by

$$\Delta^\pm \sin^2\theta^\ell_{\text{eff}} = \sqrt{\sum_{i=1}^{26} (\sin^2\theta^\ell_{\text{eff}}(f_i^\pm) - \sin^2\theta^\ell_{\text{eff}}(f_0))^2}\,, \tag{8.8}$$

[1] The value is defined as the minimum of the χ^2 distribution and the error is derived by going one unit upwards in the χ^2 distribution.

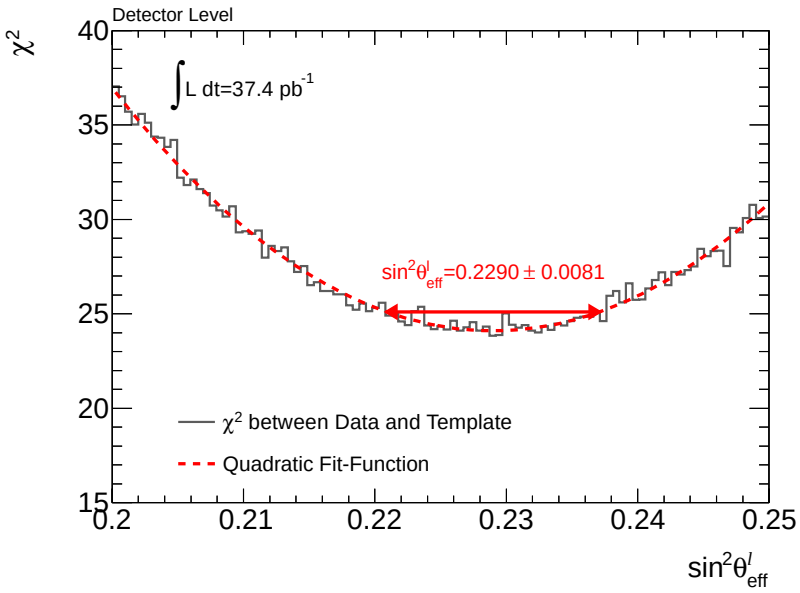

Figure 8.11: χ^2 estimator between the A_{FB} distribution at detector level from data and the different $\sin^2\theta^{\ell}_{\text{eff}}$ Pythia $Z \rightarrow ee$ MC simulations. The resulting $\sin^2\theta^{\ell}_{\text{eff}}$ value is displayed by the red arrow.

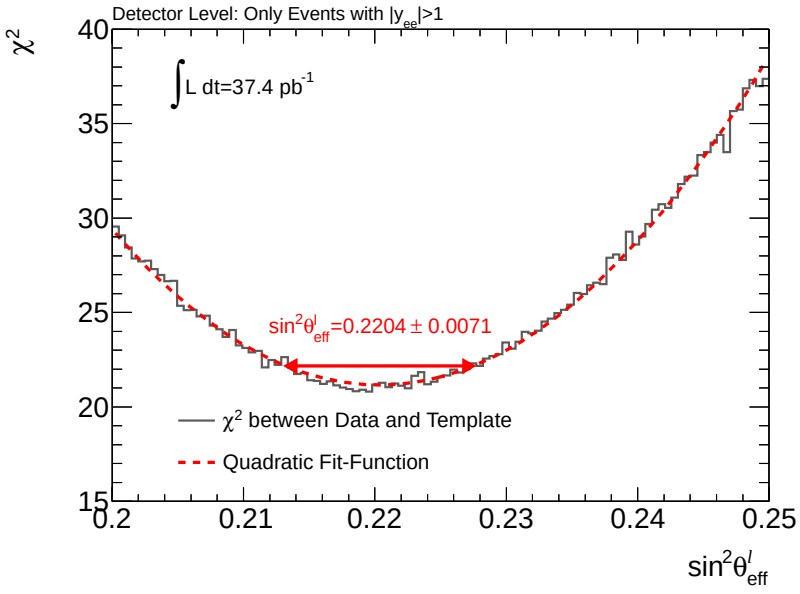

Figure 8.12: χ^2 estimator between the A_{FB} distribution at detector level from data and the different $\sin^2\theta^{\ell}_{\text{eff}}$ Pythia $Z \rightarrow ee$ MC simulations. Only di-electron pairs fulfilling $|y_{ee}| > 1$ are taken into account. The resulting $\sin^2\theta^{\ell}_{\text{eff}}$ value is displayed by the red arrow.

Source	$\Delta \sin^2 \theta_{\text{eff}} \times 10^3$	
	all rapidities	**only $\|y_{ee}\| > 1$**
PDF	+7 / -7	+5 / -5
Background	+15 / -7	+11 / -8
Energy Scale	+29 / -33	+34 / -40
Energy Resolution	+8 / -8	+11 / -12
ID Scale Factor	+5 / -4	+6 / -6
Pile-Up	+4 / -4	+6 / -6
Total	+35 / -36	+39 / -44

Table 8.1: Sources of systematic uncertainties for $\sin^2\theta^\ell_{\text{eff}}$ and their contributions. For each uncertainty, the asymmetric error is given (+/-).

where f_i^+ (f_i^-) stands for a PDF with a positive (negative) variation along the i-th eigenvector. The default PDF is denoted by f_0. Hence, two different uncertainties are derived, one for positive and one for negative variations. The maximum value of both uncertainties is taken as systematic PDF uncertainty.

A full list of the sources of the systematic uncertainties and their values for both determinations (with and without the additional rapidity cut) is given in table 8.1. The total systematic uncertainty is defined by the square root of the quadratic sum of the single contributions. It is slightly larger when applying the rapidity cut. In both cases, the main systematic uncertainty arises from the energy scale of the measured electrons. In future analyses, this uncertainty as well as the uncertainties from the other sources can probably be reduced due to a better understanding of the detector. In a similar study using only MC simulations [233], the total uncertainty for pp collisions at $\sqrt{s} = 14$ TeV with an integrated luminosity of 100 fb^{-1} has been estimated to be $\Delta \sin^2\theta^\ell_{\text{eff}} = (\pm 1.5\,(\text{stat}) \pm 0.3\,(\text{syst}) \pm 2.4\,(\text{PDF})) \times 10^{-4}$. Here the largest uncertainty arises from the PDF uncertainty.

The determination of the weak mixing angle is performed by comparing data with different Pythia $Z \to ee$ samples. However, Pythia contains only leading order calculations. In [22, 234] the authors have proposed to compare the A_{FB} distributions of generators containing higher orders to the different $\sin^2\theta^\ell_{\text{eff}}$ Pythia $Z \to ee$ templates at generator truth level. The difference between the $\sin^2\theta^\ell_{\text{eff}}$ value of the best Pythia template match and the value used in the higher order generator is taken to correct the extracted $\sin^2\theta^\ell_{\text{eff}}$ value for higher order effects. For the MC@NLO $Z \to ee$ sample no difference between $\sin^2\theta^\ell_{\text{eff}}$ used in the generation ($\sin^2\theta^\ell_{\text{eff}} = 0.2311$) and the one determined from the Pythia templates is observed. To achieve a precise determination in future analyses one should also take into account other higher order generators, *e.g.* POWHEG [236].

The final result for the effective weak mixing angle without any rapidity cut is

$$\sin^2\theta^{\ell}_{\text{eff}} = 0.2290 \pm 0.0081\,(\text{stat})\,{}^{+0.0035}_{-0.0036}\,(\text{syst}), \tag{8.9}$$

and with the additional rapidity cut ($|y_{ee}| > 1$) the value is determined to be

$$\sin^2\theta^{\ell}_{\text{eff}} = 0.2204 \pm 0.0071\,(\text{stat})\,{}^{+0.0039}_{-0.0044}\,(\text{syst})\,. \tag{8.10}$$

Both values are dominated by the statistical uncertainty. The value determined by considering all rapidities is 0.3σ below the LEP/SLD average [18], while for the value taking into account only pairs with $|y_{ee}| > 1$ a 1.4σ difference is observed. Therefore, both values are in agreement with the LEP/SLD average. A comparison to other determinations is given in the conclusions (*cf.* chapter 9).

8.5 Unfolded Forward-Backward Asymmetry

The real physical forward-backward asymmetry can be obtained by correcting for detector resolution and acceptance as well as intrinsic ambiguities of the analysis. The unfolding procedure is divided into two steps. First, the A_{FB} distribution is corrected for mass migration and for charge mis-identification. In a second step, the forward-backward asymmetry is corrected for the detector acceptance and for the dilution of the A_{FB} distribution due to the wrong assignment of the incoming quark direction. The unfolding procedure is applied to all electron pairs, *i.e.* no rapidity cut is considered. The corrections are determined from Pythia $Z \to ee$ events. The extraction of the effective weak mixing angle from the unfolded asymmetry is possible in principal, but it will suffer from larger uncertainties arising from the unfolding procedure. Thus, this method is not performed in this thesis. Similar unfolding techniques have been deployed by the CDF and D0 collaborations [22, 23, 234, 237].

8.5.1 Mass Migration and Charge Mis–Identification

The reconstructed invariant mass can differ from the generated one due to final state Bremsstrahlung and the energy resolution of the detector. Events in a specific invariant mass bin could therefore migrate to a different mass bin. In addition, electron pairs reconstructed as forward events could be in real a backward event due to a wrong charge identification.[1] In order to correct for these effects, the probability for an electron pair reconstructed as forward in mass bin i to be actually a forward pair in mass bin j is derived from Pythia $Z \to ee$ MC events. This defines the response matrix M^{FF}_{ij}. Similar, the response matrices for a backward event being actually a backward event (M^{BB}_{ij}), a forward a backward event (M^{FB}_{ij}), and a backward a forward event (M^{BF}_{ij}) are computed.

The response matrices are derived under the assumption that the detector is well described in the MC simulation. This should be satisfied, since differences between data and MC simulation are corrected and the control plots in section 7.3 show no significant deviations between

[1] The possible incorrect assignment of the incoming quark direction is not considered in this step.

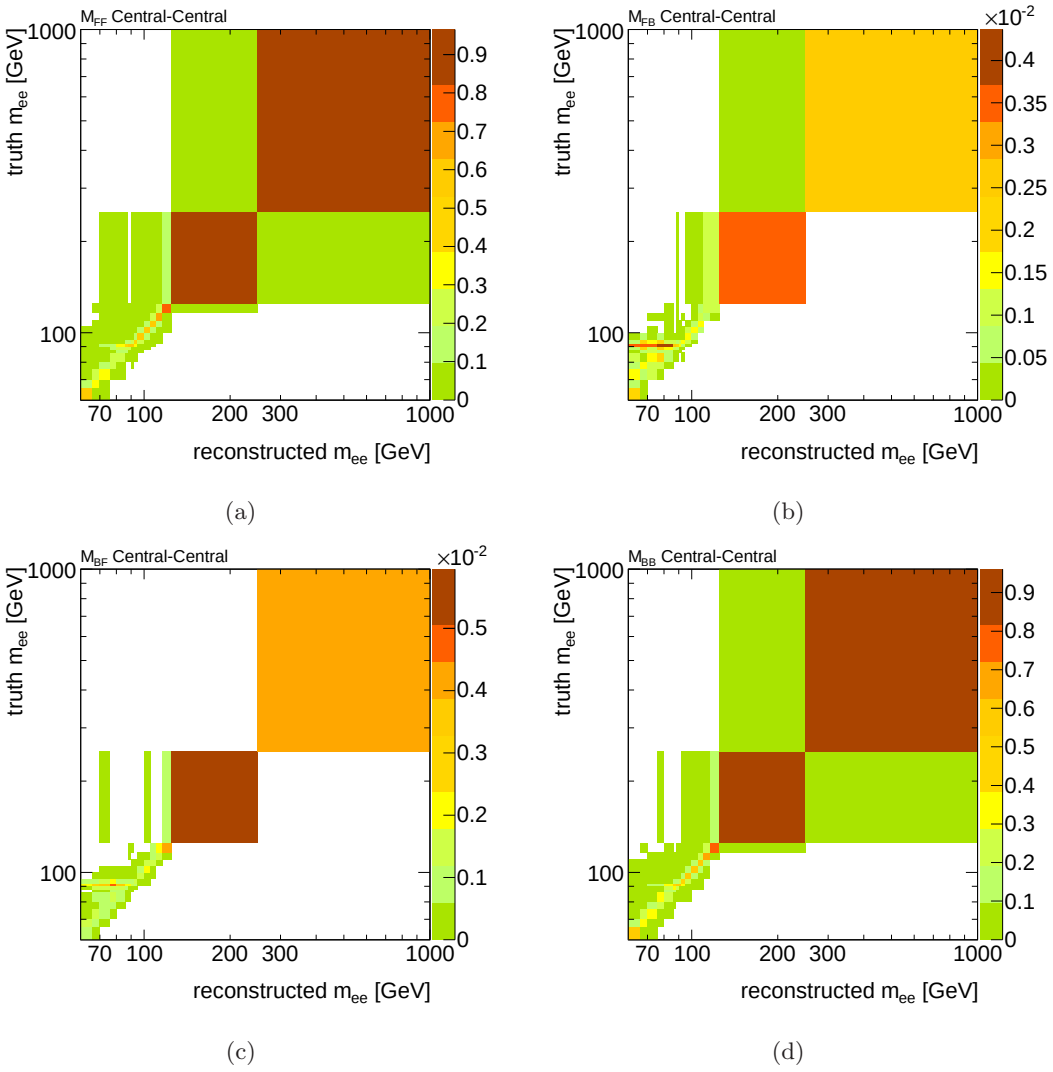

Figure 8.13: Response matrices for central–central $Z/\gamma^* \rightarrow ee$ candidates. From left to right and top to bottom: (a) forward–forward, (b) forward–backward, (c) backward–forward, (d) backward–backward.

MC and data. Additionally, the charge mis-identification shows similar results in data and MC (*cf.* section 8.2). The matrices are computed separately for the CC and CF selection. They are presented in figs. 8.13 and figs. 8.14. As expected, if mass migration occurs, the migration to neighboring bins is preferred. The probability that a forward (backward) event is actually a backward (forward) event is small, being consistent with the small charge mis-identification rate determined in section 8.2.

8.5.2 Correction for Acceptance and incorrect Quark Direction

The kinematic and fiducial requirements applied to the electrons influence the angular distribution of the $Z/\gamma^* \rightarrow ee$ candidates. In particular, the very forward and very backward events are cut away. In addition, the fact that the incoming quark direction is not always equal to the

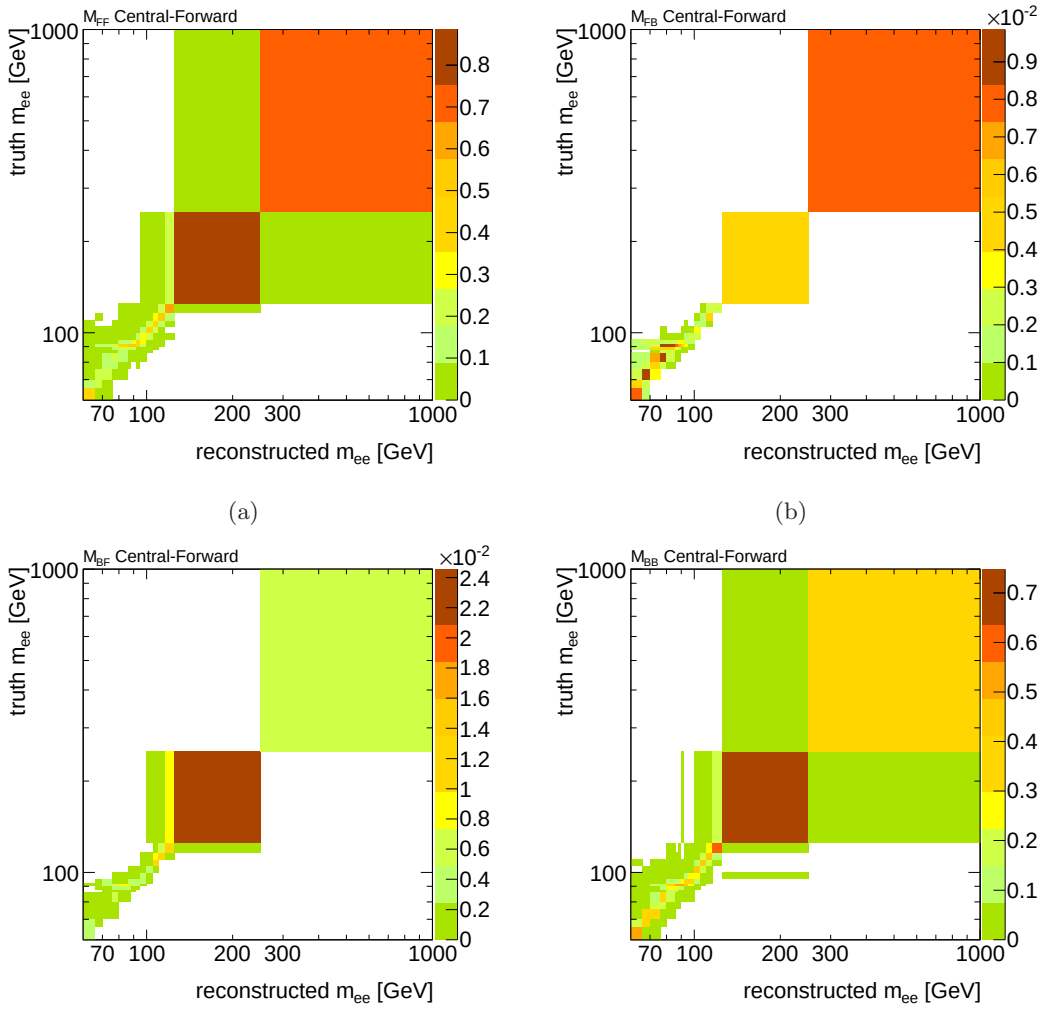

Figure 8.14: Response matrices for central–forward $Z/\gamma^* \rightarrow ee$ candidates. From left to right and top to bottom: (a) forward–forward, (b) forward–backward, (c) backward–forward, (d) backward–backward.

Z/γ^* boost results in a dilution of the asymmetry. The effects of the detector acceptance and the dilution due to the incorrect determination of the quark direction are displayed for three different invariant mass regions in fig. 8.15(a)-(c). The red solid lines show the true angular distributions, while the black dashed histograms use the assumption that the quark direction is equal to the Z/γ^* boost. The gray shaded histograms represent the events which are reconstructed and identified (CC and CF) after the detector simulation. For each histogram the true kinematic values at generator level are used to compute $\cos(\theta_{\mathrm{CS}})$.

Each of the three different invariant mass ranges shown in fig. 8.15(a)-(c) represents different $\mathrm{A_{FB}}$ values: a negative value (60 GeV $< m_{ee} <$ 66 GeV), almost no asymmetry near the Z peak (90 GeV $< m_{ee} <$ 92 GeV), and a positive value (125 GeV $< m_{ee} <$ 250 GeV). In particular for bins with large positive or negative $\mathrm{A_{FB}}$ values, the effect, that some events are

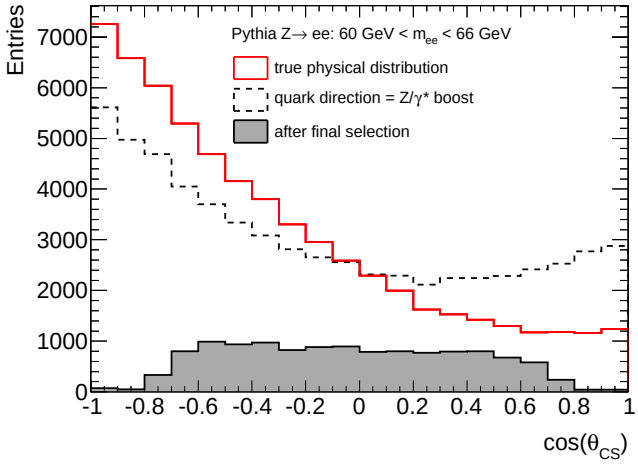

(a)

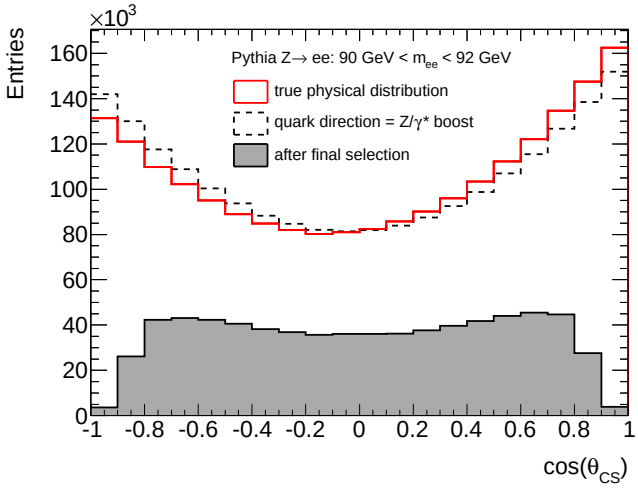

(b)

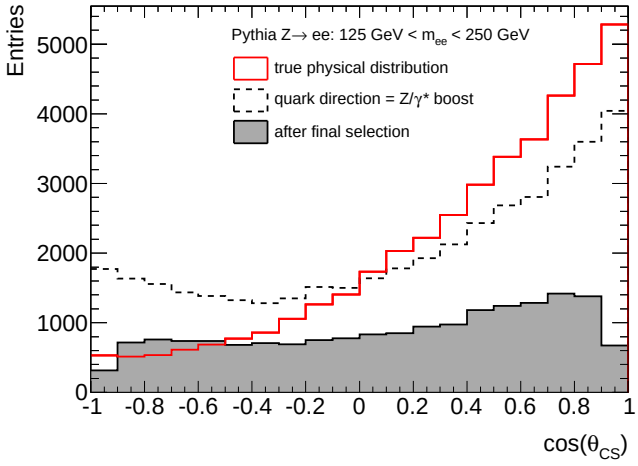

(c)

Figure 8.15: Angular distribution for Pythia $Z \to ee$ MC events. Three different mass ranges are shown, in order to represent different values for A_{FB}.

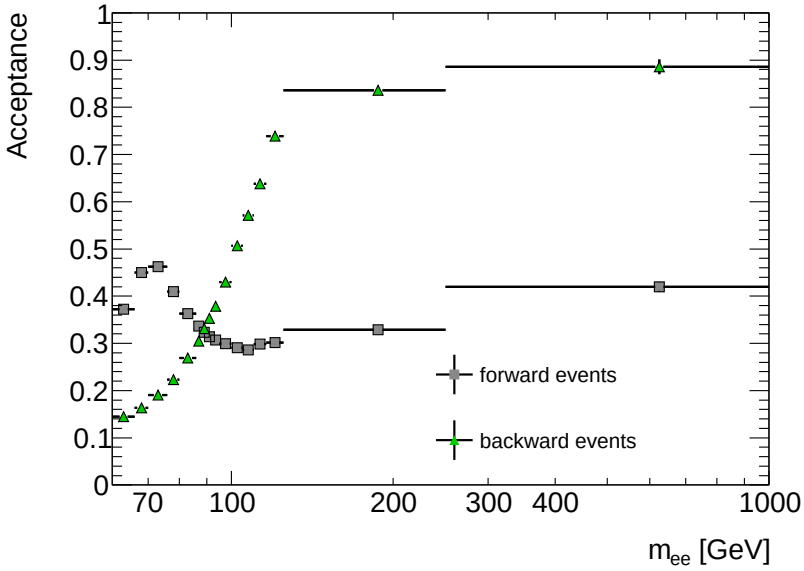

Figure 8.16: Acceptance of forward and backward events as a function of the invariant mass. For the acceptance definition please consult the text.

assigned with the wrong quark direction, is clearly visible. For bins with a small asymmetry the effect is almost compensated, since the number of wrongly identified forward and backward electron pairs is similar. The detector acceptance finally reduces the number of selected events. Especially very forward and very backward events are removed from the sample.

The acceptance correction is defined by the ratio of the number of forward (backward) events selected after detector simulation (gray shaded histograms) and the true number of forward (backward) events at generator level (red solid lines) for each mass bin. The result is shown in fig 8.16. If very few backward events are generated, the acceptance is large due to the fact that forward events are wrongly reconstructed as backward events, and vice versa. The acceptances for forward and backward events cross exactly at the point where the asymmetry vanishes. However, one should keep in mind that the angular distribution and therefore the number of forward and backward events depends on the $\sin^2\theta^{\ell}_{\text{eff}}$ value used in the MC generation.

8.5.3 Unfolding Procedure

In order to obtain the real number of forward and backward events in each invariant mass bin the measured numbers need to be unfolded with the corrections determined in the two previous sections. The unfolded number of events in mass bin i is calculated by applying the following equations [234]

$$N_F^{i,\text{unf}} = \frac{1}{\text{acc}_F^i} \sum_j \left(M_{ij}^{FF} N_F^j + M_{ij}^{BF} N_B^j \right) , \tag{8.11}$$

$$N_B^{i,\text{unf}} = \frac{1}{\text{acc}_B^i} \sum_j \left(M_{ij}^{FB} N_F^j + M_{ij}^{BB} N_B^j \right) , \tag{8.12}$$

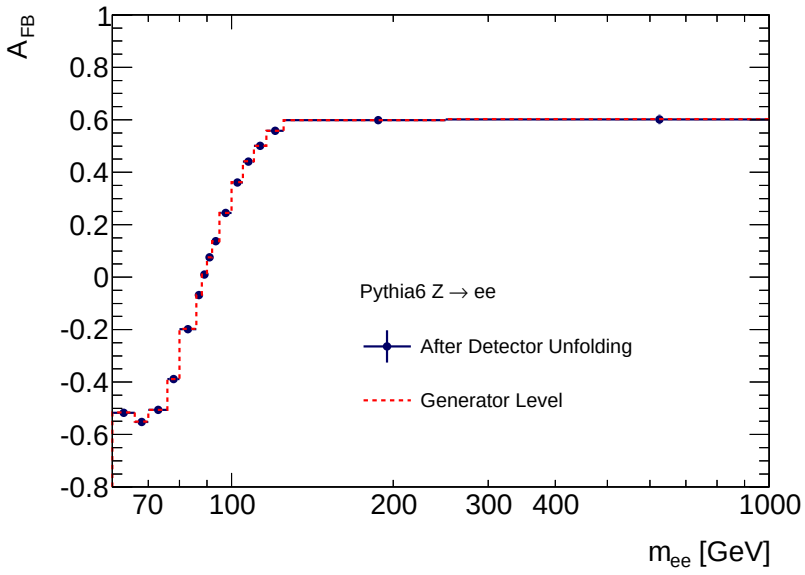

Figure 8.17: Closure test of the unfolding procedure with Pythia $Z \to ee$ events. The unfolded A_{FB} distribution is compared to the one at generator level.

where $\mathrm{acc}_{F/B}$ are the acceptances for forward and backward events as shown in fig. 8.16. The response matrices M_{ij} are determined in section 8.5.1, and $N^j_{F/B}$ stands for the measured number of forward and backward events in mass bin j. If the electron pair is a CC or a CF pair, the associated response matrices are taken. The unfolded A_{FB} distribution is finally computed via eq. (8.3). The error calculated via error propagation is determined to be

$$\Delta A^i_{\mathrm{FB}} = \sqrt{\sum_j \left(\frac{\partial A^i_{\mathrm{FB}}}{\partial N^j_F}\Delta N^j_F\right)^2 + \sum_j \left(\frac{\partial A^i_{\mathrm{FB}}}{\partial N^j_B}\Delta N^j_B\right)^2}\,, \tag{8.13}$$

where

$$\frac{\partial A^i_{\mathrm{FB}}}{\partial N^j_F} = \frac{-2M^{ij}_{FF}N^{i,\mathrm{unf}}_B}{\mathrm{acc}^i_F\left(N^{i,\mathrm{unf}}_F + N^{i,\mathrm{unf}}_B\right)^2} + \frac{-2M^{ij}_{BF}N^{i,\mathrm{unf}}_F}{\mathrm{acc}^i_B\left(N^{i,\mathrm{unf}}_F + N^{i,\mathrm{unf}}_B\right)^2}\,, \tag{8.14}$$

$$\frac{\partial A^i_{\mathrm{FB}}}{\partial N^j_B} = \frac{-2M^{ij}_{FB}N^{i,\mathrm{unf}}_B}{\mathrm{acc}^i_F\left(N^{i,\mathrm{unf}}_F + N^{i,\mathrm{unf}}_B\right)^2} + \frac{-2M^{ij}_{BB}N^{i,\mathrm{unf}}_F}{\mathrm{acc}^i_B\left(N^{i,\mathrm{unf}}_F + N^{i,\mathrm{unf}}_B\right)^2}\,. \tag{8.15}$$

The uncertainty converges to the one of the forward-backward asymmetry at detector level in section 8.3, if no matrix and acceptance corrections are applied.

A closure test has been performed with Pythia $Z \to ee$ events. The resulting forward-backward asymmetry is shown in fig. 8.17. As expected, the unfolded A_{FB} distribution is in perfect agreement with the one predicted by the Pythia generator. The unfolding procedure has also been applied only to CC and CF events, respectively. In both cases the distributions agree perfectly with the one at generator level.

8.5.4 Results

Finally, the unfolding procedure as discussed in the previous section is applied to data. The unfolded forward-backward asymmetry as a function of the invariant mass is shown in fig. 8.18 for the invariant mass range 60-1000 GeV and near the Z peak in fig. 8.19, respectively. The data distributions are compared to the generator level predictions from the Pythia as well as the MC@NLO generator. In both cases, very good agreement is observed with the unfolded forward-backward asymmetry. It should be noticed that due to the unfolding procedure the mass bins are correlated, leading to larger statistical errors.

The systematic uncertainties arise (similar to the determination of the effective weak mixing angle) from the energy scale, the energy resolution, the identification scale factors, pile-up re-weighting, PDFs, and the background subtraction. Additionally, the $\sin^2\theta^{\ell}_{\text{eff}}$ value assumed in the MC generation biases the calculation of the acceptance corrections. To account for this ambiguity the unfolded A_{FB} distributions of the re-weighted $\sin^2\theta^{\ell}_{\text{eff}}$ samples used for the effective weak mixing angle determination in section 8.4 are calculated. The difference in each mass bin between the unfolded result of the ATLAS simulated Pythia $Z \rightarrow ee$ events and the unfolded distributions when using the result of eq. (8.9) and shifting it by its statistical uncertainty is taken as systematic error. The systematic uncertainties in each mass bin are summarized in appendix B. The total systematic error near the Z peak is dominated by the uncertainty arising from the ambiguity of the $\sin^2\theta^{\ell}_{\text{eff}}$ value in the acceptance calculation, while for large invariant masses the error from the background subtraction contributes most. For each mass bin the statistical uncertainty is still the dominant one. The total uncertainties in fig. 8.18 and fig. 8.19 are indicated by the gray shaded error bars.

8.6 Impact of Models Beyond the SM

Various models beyond the SM might contribute to the Drell–Yan cross-section and can possibly influence the shape of the forward-backward asymmetry. In the following, the impact of large extra dimensions and unparticles is studied. The analysis has been performed at generator level by using the Pythia8 [5] MC generator (version 8.125). The implementation of these models in Pythia8 are discussed in the publications [238, 239]. The presentation in this chapter follows closely the presentation of the results in the publication [239]. In the analysis, pp interactions at a center-of-mass energy of 14 TeV are assumed.

8.6.1 Large Extra Dimension

The idea of large extra dimensions (LEDs) is already discussed in section 4.3.4. However, in this analysis a slightly modified theory is investigated. The graviton exchanges are described with the aid of a form-factor, that improves the perturbative behavior of general relativity in the ultraviolet regime [240]. The existence of the form-factor can be interpreted as the running

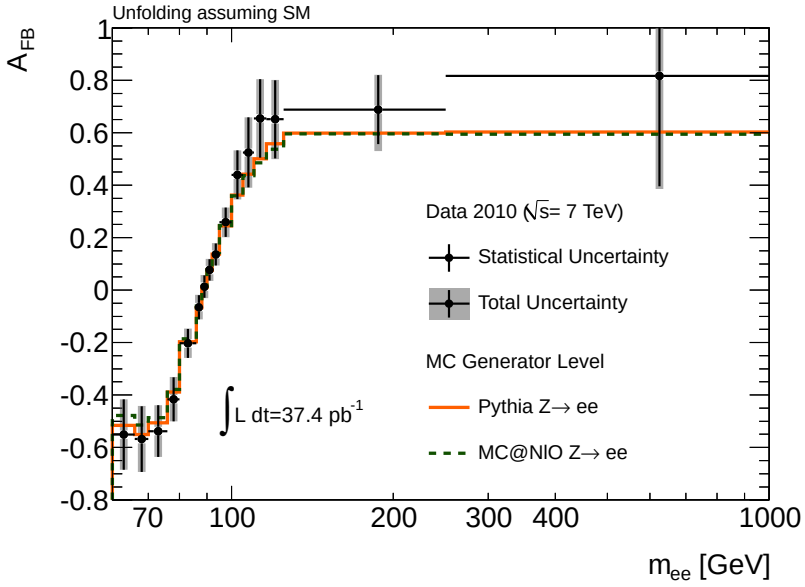

Figure 8.18: Unfolded forward-backward asymmetry as a function of the invariant mass, compared to the SM prediction from Pythia and MC@NLO for the invariant mass range of 60-1000 GeV.

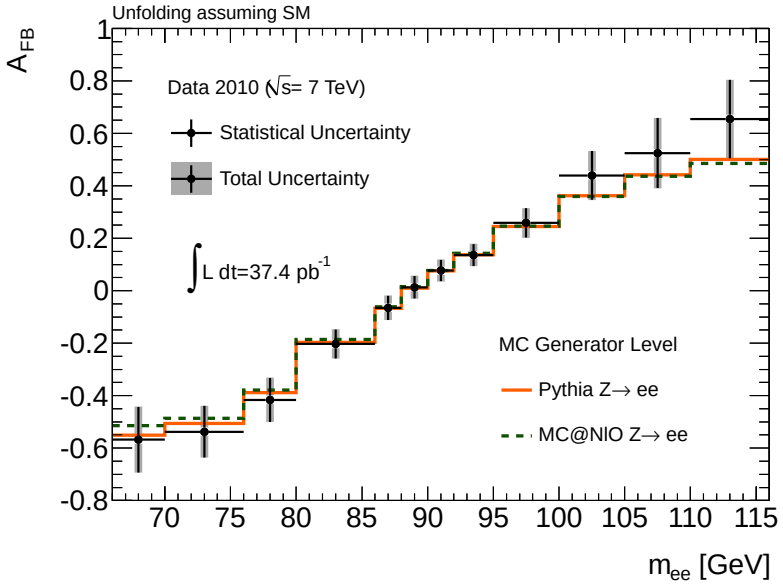

Figure 8.19: Unfolded forward-backward asymmetry as a function of the invariant mass, compared to the SM prediction from Pythia and MC@NLO for the invariant mass range of 66-116 GeV.

of the gravitational coupling. The form-factor is defined by

$$F(\mu; t, M, n) = \left[1 + \left(\frac{\mu^2}{t^2 M^2}\right)^{1+n/2}\right]^2 , \tag{8.16}$$

where n is the number of extra dimensions, μ is a renormalization scale and t is a $\mathcal{O}(1)$ free parameter which accounts for the unknown details of the running of the gravitational coupling. The parameter M is associated with the cut-off scale of the effective theory. In case of virtual graviton exchange, the free parameters of the theory are t and the cut-off scale Λ_H. In order to avoid that virtual graviton exchange amplitudes violate unitarity, the authors of [240] have argued that t must be smaller than 2.

The production of two leptons can be influenced by the effects of virtual graviton exchange. Therefore, the invariant mass distribution of the two final-state leptons has been studied for a large number of different parameter settings of the LED model. As an example, fig. 8.20 shows the differential cross-section as a function of the invariant mass of the lepton pair for the cut-off scale $\Lambda_H = 2.5$ TeV in scenarios with $n = 3$. The results show the strongly t-dependent increase of the cross section at high masses for the LED scenarios with respect to the SM. As expected from eq. (8.16), the differential cross section converges towards the SM prediction for decreasing values of t, while for larger t values, *e.g.* $t = 2$, it approaches the LED scenarios where the form-factor is not used (NoFF). In addition, the dependence of the cross section on the number of extra dimensions has been studied in fig. 8.20. The distributions decrease faster with more extra dimensions at larger invariant masses and they intersect at $m_{ll} = \sqrt[4]{0.5\pi}\Lambda_H$ corresponding to 2.8 TeV. Higher values of Λ_H would shift the deviation from the SM to larger invariant masses.

The existence of LEDs can impact the forward-backward asymmetry, as well. The results presented in fig. 8.22 are determined under the assumption that the incoming quark direction corresponds to the boost of the di-electron system. In addition it is required that at least one electron is in the central region ($|\eta| < 2.5$). No rapidity cut to the electron pair is applied. The forward-backward asymmetry is shown for various t values with fixed $n = 3$ and $\Lambda_H = 2.5$ TeV. At high invariant masses the deviation from the SM is clearly visible. In contrast to the differential cross-section, also the distribution for $t = 0.5$ shows a significant deviation compared to the SM expectation.

8.6.2 Unparticles

Unparticle models [241, 242] are introduced in order to build a realistic framework for unconventional signatures of new physics being detectable at future or current collider experiments. These theories relate to physics originating from a scale invariant new sector coupling weakly to the SM through a connector sector with a high mass scale. Below a cut-off scale Λ_U the models can be described by a conformal field theory called unparticle. Similar to LED models unparticles of scale dimension d_U behave like a non-integral number of invisible particles. The

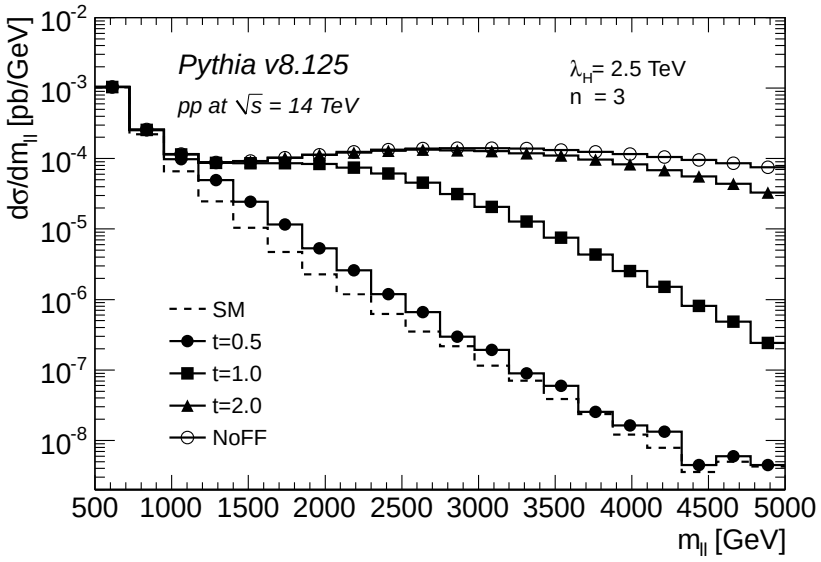

Figure 8.20: Differential cross-section for the production of two charged leptons at the LHC ($\sqrt{s}$ = 14 TeV) as a function of their invariant mass. The results are shown for various LED scenarios with various t values.

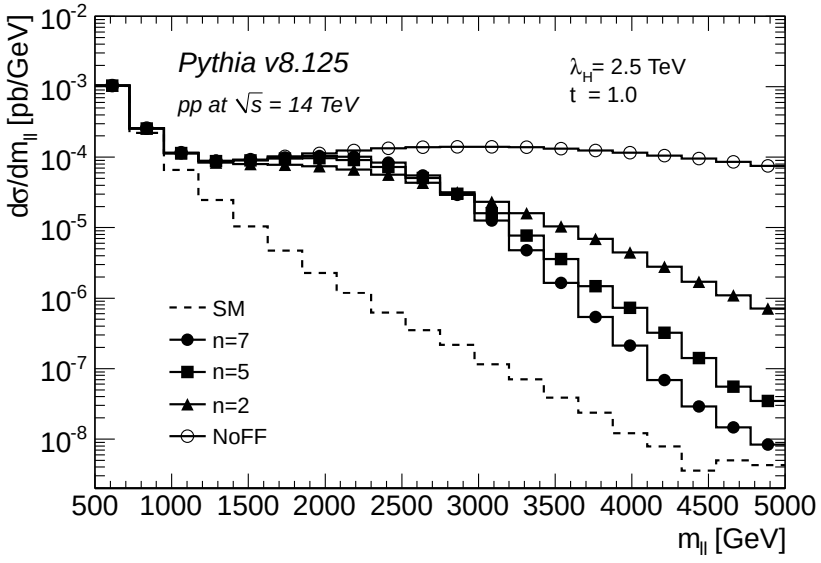

Figure 8.21: Differential cross-section for the production of two charged leptons at the LHC ($\sqrt{s}$ = 14 TeV) as a function of their invariant mass. The results are shown for various LED scenarios with various n values.

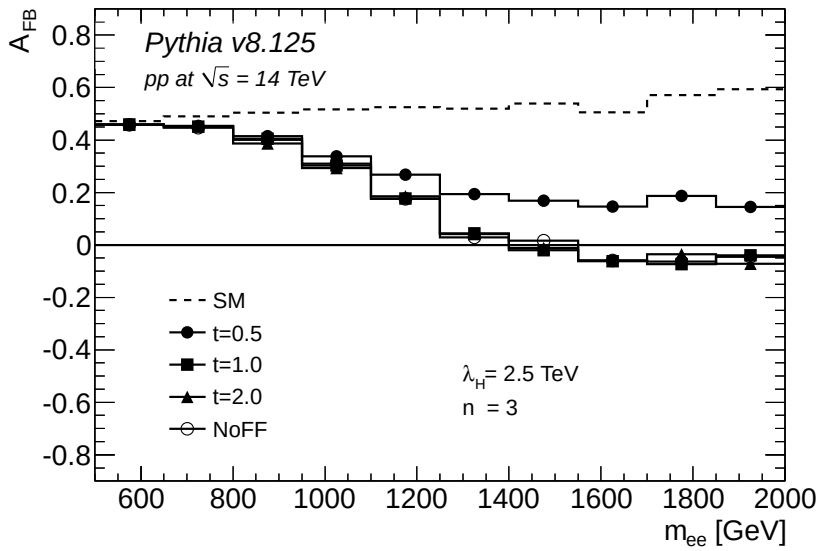

Figure 8.22: A_{FB} as a function of the invariant mass of the electron pair at the LHC ($\sqrt{s}$ = 14 TeV). The results are shown for various LED scenarios with $n = 3$ and $\Lambda_H = 2.5$ TeV.

interplay of unparticles with the Higgs sector can influence the Higgs boson properties dramatically [243], *e.g.* the Higgs mass can be shifted from its SM value $2\lambda v^2$. Studies show that unparticles could also provide a solution for the dark matter problem [244, 245].

Besides the scale dimension parameter d_U and the cut-off scale Λ_U, the coupling constant λ of the unparticles to the SM fields is the main parameter of the model. In order to avoid the collapse of the effective theory, the dimension parameter is restricted to $1 < d_U < 2$ in case of virtual unparticle exchange [239, 246–248]. In the following, the impact of virtual exchange of spin-1 unparticles with different types of 4-fermion interaction couplings on the Drell–Yan process is investigated.[1]

Figure 8.23 shows the differential Drell–Yan cross-sections at the LHC as a function of the invariant mass of the lepton pair for various values of d_U, assuming unparticles with spin-1 and vector-like 4-fermion interactions. A cut on the lepton pair rapidity ($|y| < 1$) has been applied, ensuring that only central leptons are selected. As expected, the characteristic increase of the differential cross section due to the unparticle signal is more prominent for small values of d_U, *e.g.* $d_U = 1.3$, both above and below the Z pole.

The forward-backward asymmetry is determined in the same way as it has been done for the LED scenarios. In fig. 8.24 the forward-backward asymmetry is shown for various unparticle scenarios and the SM. The impact of the different 4-fermion interactions is clearly visible.

8.6.3 Conclusion

In addition to the cross-section measurement of the Drell–Yan spectrum, the forward-backward asymmetry can provide a possibility to confirm contributions from physics beyond the SM to

[1] A description of the different 4-fermion interactions and their treatment in Pythia8 can be found in [239].

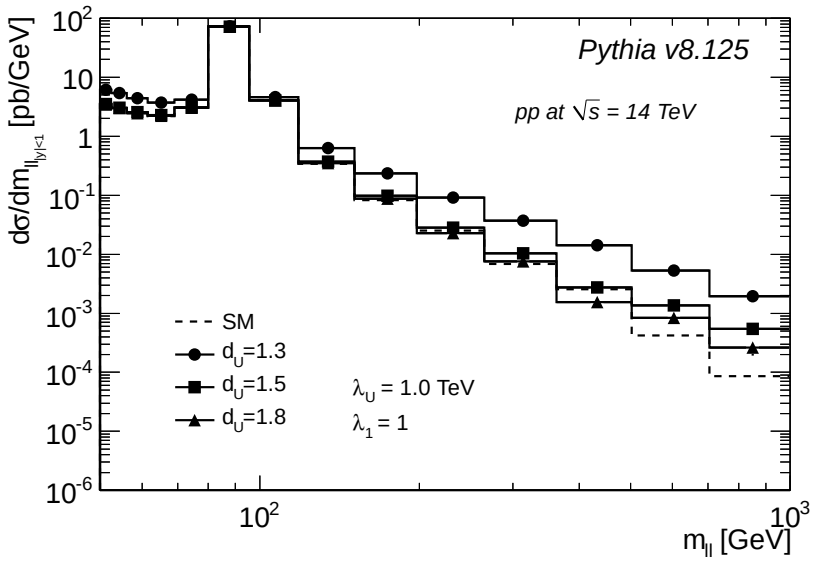

Figure 8.23: Differential cross-section for the production of two charged leptons at the LHC ($\sqrt{s}$ = 14 TeV) as a function of their invariant mass. The results are shown for scenarios with different values of d_U assuming unparticles with spin-1 and vector-like 4-fermion coupling.

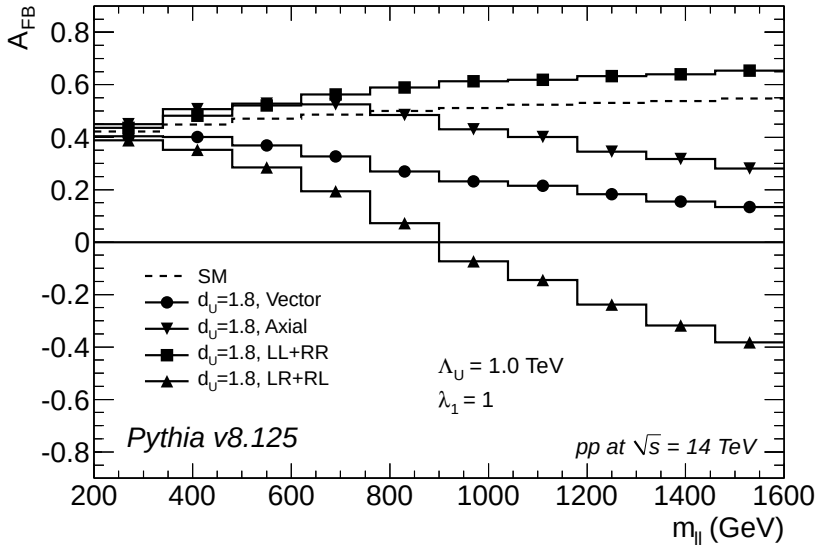

Figure 8.24: A_{FB} as a function of the invariant mass of the electron pair at the LHC ($\sqrt{s}$ = 14 TeV). The results are shown for $d_U = 1.8$ and spin-1 unparticles with various chiral interactions.

the di-lepton production. Additionally, the coupling parameters of the new physics model could be constrained by it. However, experimental effects, in particular statistics, will pose a significant challenge for the reconstruction of A_{FB}. A detailed study including the detector simulation is therefore needed to estimate the feasibility.

CHAPTER 9

Conclusions

In this thesis various tests of the Standard Model of particle physics have been performed. Among them are the determination of the effective weak mixing angle from the electroweak precision data as well as from the forward-backward asymmetry of the process $pp \to Z/\gamma^* \to e^+e^-$ at the ATLAS detector. No significant deviations to the SM predictions have been observed. Effects from models beyond the SM have been investigated and constraints in new physics models have been derived.

The global SM fit to the electroweak precision data as measured at the LEP, SLD, and Tevatron colliders — for some fits also the direct Higgs searches from LEP, Tevatron, and the LHC are considered — has demonstrated the predictive power of the electroweak unification. The fit results shown in this thesis are in agreement with the results from the LEP Electroweak Working Group [44] and for the electroweak review of the Particle Data Group [42]. The p-values of the fits, the pull-values of the single observables, and a compatibility test of the most sensitive observables determining the Higgs mass do not indicate any significant deviation from the SM. Additionally, the determination of the strong coupling constant from the electroweak precision data, $\alpha_s(M_Z^2) = 0.1194 \pm 0.0028\,(\text{exp}) \pm 0.0001\,(\text{theo})$, is in conjunction with the value from τ-decays [91], one of the best tests of the asymptotic freedom property of QCD. The indirect determinations of the top and W mass as well as the effective weak mixing angle agree with the direct measurements. From fits considering the information from the direct Higgs searches, the following 1σ values have been determined indirectly

$$m_t = [174.1,\ 180.2]\ \text{GeV and}\ [185.1,\ 188.6]\ \text{GeV}\,, \tag{9.1}$$

$$M_W = 80.360\ ^{+0.012}_{-0.011}\ \text{GeV}\,, \tag{9.2}$$

$$\sin^2\theta^\ell_{\text{eff}} = 0.23147\ ^{+0.00012}_{-0.00010}\,. \tag{9.3}$$

The latter two values exceed the precision of the direct determinations.

As a summary the indirect determination of the effective weak mixing angle from the fit with and without the direct Higgs constraints is compared to various precision measurements (from LEP and SLD) in fig. 9.1(a). Both values agree with the LEP/SLD average [18] displayed by the green band. The mass of the Higgs boson has been extracted from the fit without the constraints from the direct Higgs searches to be $M_H = 94\,^{+30}_{-24}$ GeV with the 95% CL upper

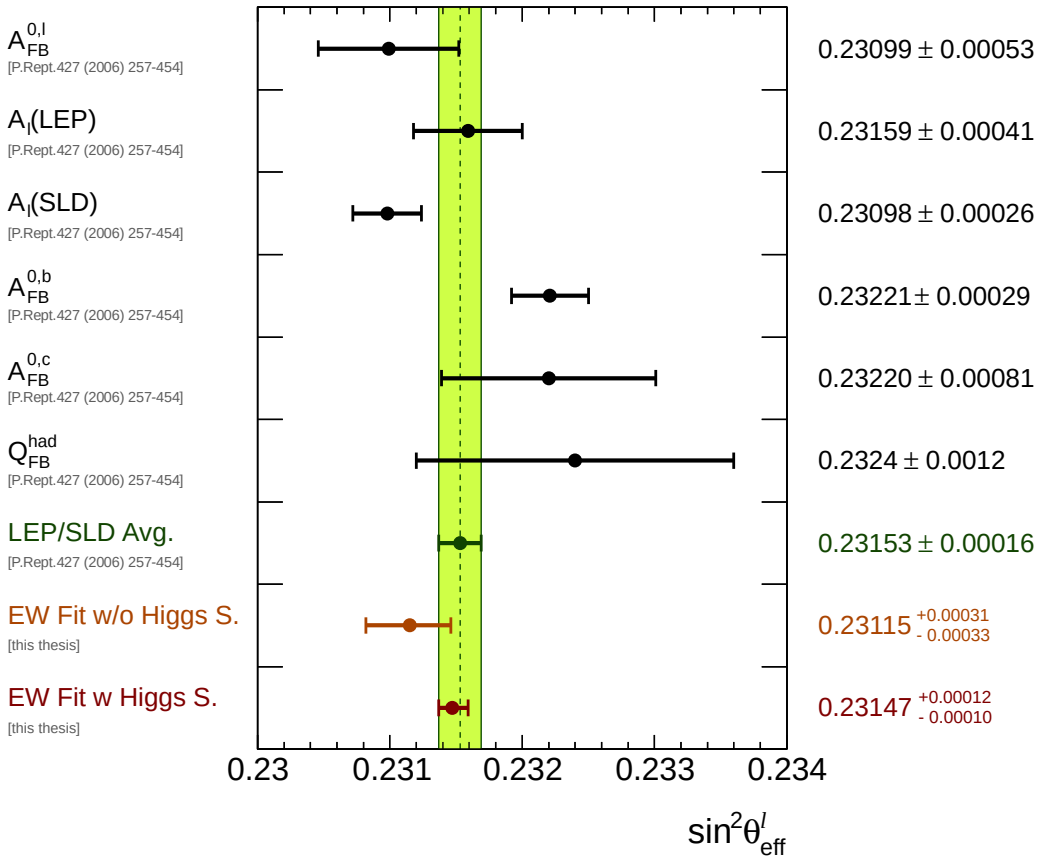

(a)

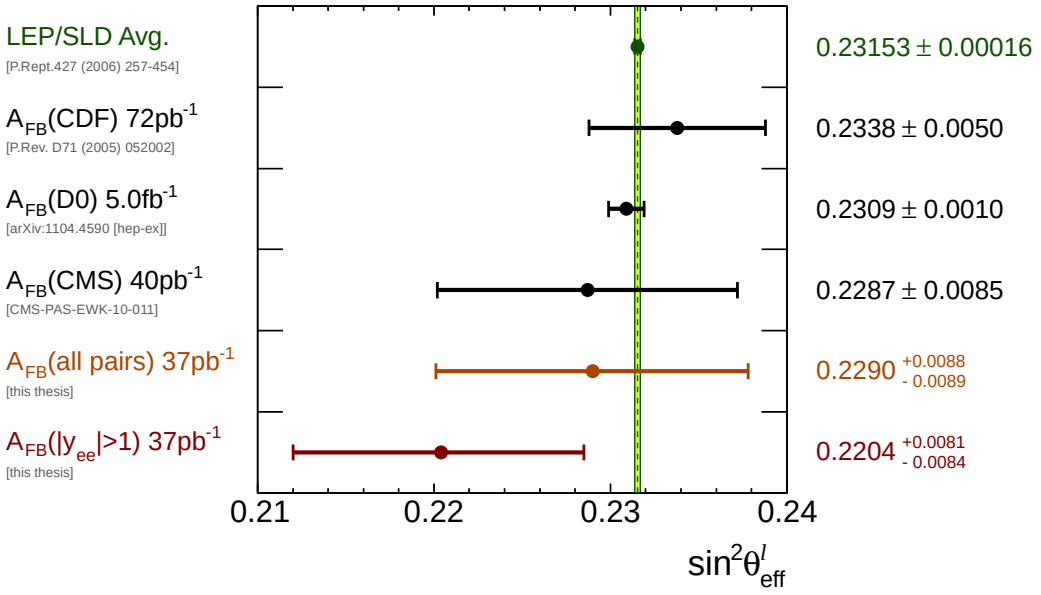

(b)

Figure 9.1: Summary of different determinations of the effective weak mixing angle: (a) Results from LEP and SLD and the electroweak fits, (b) results from hadron colliders. In both plots the LEP/SLD average is displayed by the green band.

limit of 166 GeV, while by considering the direct Higgs searches the Higgs mass has been determined to be $M_H = 125\,^{+8}_{-10}$ GeV with the 95% CL upper limit of 146 GeV. Recently, the ATLAS and CMS collaborations have presented updates on the Higgs boson search [80, 81]. Both experiments have observed a broad excess of events with respect to the background in the region of 140 GeV, which is in agreement with the 95% CL upper limit from the electroweak fits. Nevertheless, more data is required to confirm whether the observed excess is a statistical fluctuation or not.[1]

In this thesis also the data taken in 2010 with the ATLAS detector corresponding to an integrated luminosity of 37.4 pb^{-1} has been analyzed. Several electron performance studies — electron trigger rates and efficiencies as well as time dependent rate studies of $Z/\gamma^* \to e^+e^-$ candidates — indicate stable detector conditions for the measurement of electron candidates. The electroweak induced forward-backward asymmetry of $pp \to Z/\gamma^* \to e^+e^-$ events has been presented at detector level as well as after a detector unfolding. For both measurements, a good agreement with the SM expectation is observed. From the forward-backward asymmetry at detector level, the value of the effective weak mixing angle is determined by comparing the data results to MC simulations generated with different values of $\sin^2\theta^\ell_{\text{eff}}$. By applying a rapidity cut on the di-electron system ($|y_{ee}| > 1$) the value of $\sin^2\theta^\ell_{\text{eff}}$ is extracted more accurately than without any rapidity cut. The values with and without the rapidity cut are shown in fig. 9.1(b) by the red and orange dots, respectively. They are compared to various determinations from hadron colliders. All values agree with the LEP/SLD average [18] denoted by the green band.

All measurements performed in this thesis agree with the SM. Nevertheless, from the constraints of the electroweak precision data allowed regions in the parameter space of new physics models can be estimated. New physics contributions appearing predominantly through vacuum polarizations can be parametrized by the oblique parameters. In this thesis the widely used S, T, U parameters [3, 4] have been determined from the electroweak precision observables

$$S = 0.04 \pm 0.10\,, \qquad T = 0.05 \pm 0.11\,, \qquad U = 0.08 \pm 0.11\,, \tag{9.4}$$

with large correlations between the parameters. These results have been used to revisit constraints on new physics models, like models with a sequential fourth fermion generation, the inert-Higgs doublet model, the littlest Higgs model with T-parity conservation, and models with large extra dimensions. In contrast to the SM, heavy Higgs bosons (few 100 GeV) can be realized in these models by the cancellation of large Higgs contributions to the oblique parameters with those from new physics theory.

Additionally, the impact on the Drell–Yan cross-section and the forward-backward asymmetry from unparticles and large extra dimensions are studied at generator level with the Pythia8 MC generator [5]. Proton-proton interactions at a center-of-mass energy of 14 TeV are assumed. For specific parameter settings significant changes of the cross-section as well as the forward-backward asymmetry can be achieved. In this context, the measurement of the forward-backward asymmetry can provide a possibility to confirm non-SM contributions to the Drell–Yan spectrum or even to determine the parameters of the new physics theory.

[1] Both collaborations believe that the fluctuation is not significant [80, 81].

APPENDIX A

Number of Forward and Backward Events

The following tables contain the number of selected forward and backward events for each invariant mass bin for the CC and the CF selection, respectively. In addition, the numbers of background events are given. They consist of QCD and electroweak background events. However, the QCD background dominates. The QCD background has been determined by scaling the $\cos(\theta_{\mathrm{CS}})$ distributions of the di-jet QCD MC sample by the number of expected QCD background events, as described in chapter 7. The events of the electroweak background are added according to their cross-section. Only the errors from the QCD background is taken into account. The barycenter ($\langle m_{ee} \rangle$) for each invariant mass bin is determined from data events.

Mass Bin	$\langle m_{ee} \rangle$	**Data Events**		**Background Events**	
		N_F	N_B	N_F	N_B
$60 < m_{ee} < 66$ GeV	62.9 GeV	66	83	$25.5^{+3.5}_{-9.5}$	$24.8^{+3.5}_{-9.5}$
$66 < m_{ee} < 70$ GeV	68.0 GeV	62	74	$15.4^{+2.3}_{-6.1}$	$15.5^{+2.3}_{-6.1}$
$70 < m_{ee} < 76$ GeV	73.4 GeV	109	133	$19.8^{+2.8}_{-7.6}$	$18.8^{+2.8}_{-7.6}$
$76 < m_{ee} < 80$ GeV	78.2 GeV	171	186	$12.2^{+1.8}_{-4.9}$	$12.1^{+1.8}_{-4.9}$
$80 < m_{ee} < 86$ GeV	83.7 GeV	733	727	$14.9^{+2.2}_{-6.0}$	$14.7^{+2.2}_{-6.0}$
$86 < m_{ee} < 88$ GeV	87.1 GeV	693	677	$4.5^{+0.7}_{-1.8}$	$4.4^{+0.7}_{-1.8}$
$88 < m_{ee} < 90$ GeV	89.1 GeV	992	978	$4.2^{+0.6}_{-1.7}$	$4.1^{+0.6}_{-1.7}$
$90 < m_{ee} < 92$ GeV	91.0 GeV	1086	1052	$3.7^{+0.6}_{-1.5}$	$3.6^{+0.6}_{-1.5}$
$92 < m_{ee} < 95$ GeV	93.2 GeV	819	816	$5.3^{+0.8}_{-2.2}$	$5.3^{+0.8}_{-2.2}$
$95 < m_{ee} < 100$ GeV	96.9 GeV	283	236	$8.3^{+1.2}_{-3.3}$	$8.3^{+1.2}_{-3.3}$
$100 < m_{ee} < 105$ GeV	102.2 GeV	84	56	$7.9^{+1.2}_{-3.3}$	$8.2^{+1.2}_{-3.3}$
$105 < m_{ee} < 110$ GeV	107.0 GeV	58	37	$6.8^{+1.0}_{-2.7}$	$6.4^{+1.0}_{-2.7}$
$110 < m_{ee} < 116$ GeV	112.7 GeV	43	19	$7.1^{+1.1}_{-2.9}$	$7.3^{+1.1}_{-2.9}$
$116 < m_{ee} < 125$ GeV	120.1 GeV	38	28	$8.8^{+1.3}_{-3.5}$	$9.0^{+1.3}_{-3.5}$
$125 < m_{ee} < 250$ GeV	160.9 GeV	92	66	$38.1^{+5.6}_{-14.9}$	$38.2^{+5.6}_{-14.9}$
$250 < m_{ee} < 1000$ GeV	361.2 GeV	11	5	$6.1^{+0.9}_{-2.3}$	$5.9^{+0.9}_{-2.3}$

Table A.1: Number of forward and backward events for data and background in case of central–central selection.

Mass Bin	$\langle m_{ee} \rangle$	**Data Events**		**Background Events**	
		N_F	N_B	N_F	N_B
$60 < m_{ee} < 66$ GeV	62.8 GeV	23	37	$10.9^{+1.5}_{-4.8}$	$10.7^{+1.5}_{-4.8}$
$66 < m_{ee} < 70$ GeV	68.0 GeV	27	32	$6.0^{+0.9}_{-2.8}$	$6.1^{+0.9}_{-2.8}$
$70 < m_{ee} < 76$ GeV	73.4 GeV	55	71	$8.3^{+1.1}_{-3.6}$	$7.5^{+1.1}_{-3.6}$
$76 < m_{ee} < 80$ GeV	78.1 GeV	95	89	$4.0^{+0.5}_{-1.8}$	$3.8^{+0.5}_{-1.8}$
$80 < m_{ee} < 86$ GeV	83.6 GeV	344	327	$4.9^{+0.7}_{-2.4}$	$5.2^{+0.7}_{-2.4}$
$86 < m_{ee} < 88$ GeV	87.1 GeV	322	288	$1.6^{+0.2}_{-0.8}$	$1.6^{+0.2}_{-0.8}$
$88 < m_{ee} < 90$ GeV	89.1 GeV	408	416	$1.5^{+0.2}_{-0.7}$	$1.4^{+0.2}_{-0.7}$
$90 < m_{ee} < 92$ GeV	91.0 GeV	418	406	$1.3^{+0.2}_{-0.6}$	$1.3^{+0.2}_{-0.6}$
$92 < m_{ee} < 95$ GeV	93.2 GeV	335	264	$1.9^{+0.3}_{-0.9}$	$1.9^{+0.3}_{-0.9}$
$95 < m_{ee} < 100$ GeV	96.8 GeV	121	91	$2.5^{+0.4}_{-1.2}$	$2.5^{+0.4}_{-1.2}$
$100 < m_{ee} < 105$ GeV	102.2 GeV	36	18	$1.8^{+0.3}_{-0.9}$	$2.0^{+0.3}_{-0.9}$
$105 < m_{ee} < 110$ GeV	107.3 GeV	20	13	$1.8^{+0.2}_{-0.7}$	$1.6^{+0.2}_{-0.7}$
$110 < m_{ee} < 116$ GeV	112.9 GeV	14	3	$1.8^{+0.3}_{-0.9}$	$1.9^{+0.3}_{-0.9}$
$116 < m_{ee} < 125$ GeV	119.8 GeV	15	8	$2.0^{+0.3}_{-0.9}$	$2.2^{+0.3}_{-0.9}$
$125 < m_{ee} < 250$ GeV	153.9 GeV	34	23	$7.1^{+1.0}_{-3.2}$	$7.3^{+1.0}_{-3.2}$
$250 < m_{ee} < 1000$ GeV	283.7 GeV	5	0	$0.6^{+0.1}_{-0.2}$	$0.6^{+0.1}_{-0.2}$

Table A.2: Number of forward and backward events for data and background in case of central–central selection and the rapidity cut $|y_{ee}| > 1$.

Mass Bin	$\langle m_{ee} \rangle$	**Data Events**		**Background Events**	
		N_F	N_B	N_F	N_B
$60 < m_{ee} < 66$ GeV	62.8 GeV	16	27	$10.5^{+3.2}_{-6.4}$	$9.4^{+3.2}_{-6.4}$
$66 < m_{ee} < 70$ GeV	67.9 GeV	18	11	$7.2^{+2.2}_{-4.4}$	$6.3^{+2.2}_{-4.4}$
$70 < m_{ee} < 76$ GeV	73.2 GeV	38	43	$10.6^{+3.4}_{-6.8}$	$9.8^{+3.4}_{-6.8}$
$76 < m_{ee} < 80$ GeV	78.0 GeV	35	45	$7.0^{+2.3}_{-4.7}$	$6.8^{+2.3}_{-4.7}$
$80 < m_{ee} < 86$ GeV	83.6 GeV	188	192	$9.9^{+3.2}_{-6.5}$	$9.2^{+3.2}_{-6.5}$
$86 < m_{ee} < 88$ GeV	87.0 GeV	169	146	$3.4^{+1.0}_{-2.0}$	$3.0^{+1.0}_{-2.0}$
$88 < m_{ee} < 90$ GeV	89.0 GeV	201	167	$3.4^{+1.1}_{-2.1}$	$3.1^{+1.1}_{-2.1}$
$90 < m_{ee} < 92$ GeV	91.0 GeV	208	190	$2.9^{+0.9}_{-1.9}$	$2.8^{+0.9}_{-1.9}$
$92 < m_{ee} < 95$ GeV	93.3 GeV	200	171	$4.5^{+1.3}_{-2.6}$	$3.8^{+1.3}_{-2.6}$
$95 < m_{ee} < 100$ GeV	97.1 GeV	83	76	$7.4^{+2.1}_{-4.3}$	$6.3^{+2.1}_{-4.3}$
$100 < m_{ee} < 105$ GeV	102.6 GeV	39	21	$5.7^{+1.9}_{-3.8}$	$5.5^{+1.9}_{-3.8}$
$105 < m_{ee} < 110$ GeV	107.0 GeV	13	13	$5.8^{+1.8}_{-3.7}$	$5.3^{+1.8}_{-3.7}$
$110 < m_{ee} < 116$ GeV	112.8 GeV	21	9	$6.4^{+2.0}_{-4.0}$	$5.7^{+2.0}_{-4.0}$
$116 < m_{ee} < 125$ GeV	119.9 GeV	24	13	$8.8^{+2.8}_{-5.6}$	$8.2^{+2.8}_{-5.6}$
$125 < m_{ee} < 250$ GeV	169.2 GeV	86	63	$61.5^{+19.9}_{-40.2}$	$57.8^{+19.9}_{-40.2}$
$250 < m_{ee} < 1000$ GeV	371.2 GeV	38	21	$37.0^{+12.9}_{-26.2}$	$36.1^{+12.9}_{-26.2}$

Table A.3: Number of forward and backward events for data and background in case of central–forward selection.

Mass Bin	$\langle m_{ee} \rangle$	**Data Events**		**Background Events**	
		N_F	N_B	N_F	N_B
$60 < m_{ee} < 66$ GeV	62.8 GeV	16	27	$10.2^{+3.0}_{-3.7}$	$9.2^{+3.0}_{-3.7}$
$66 < m_{ee} < 70$ GeV	67.9 GeV	18	11	$7.0^{+2.1}_{-2.6}$	$6.2^{+2.1}_{-2.6}$
$70 < m_{ee} < 76$ GeV	73.2 GeV	38	43	$10.3^{+3.2}_{-4.0}$	$9.5^{+3.2}_{-4.0}$
$76 < m_{ee} < 80$ GeV	78.0 GeV	35	45	$6.8^{+2.2}_{-2.7}$	$6.6^{+2.2}_{-2.7}$
$80 < m_{ee} < 86$ GeV	83.6 GeV	188	192	$9.7^{+3.1}_{-3.8}$	$8.9^{+3.1}_{-3.8}$
$86 < m_{ee} < 88$ GeV	87.0 GeV	169	146	$3.3^{+1.0}_{-1.2}$	$2.9^{+1.0}_{-1.2}$
$88 < m_{ee} < 90$ GeV	89.0 GeV	201	167	$3.3^{+1.0}_{-1.2}$	$3.0^{+1.0}_{-1.2}$
$90 < m_{ee} < 92$ GeV	91.0 GeV	208	190	$2.8^{+0.9}_{-1.1}$	$2.7^{+0.9}_{-1.1}$
$92 < m_{ee} < 95$ GeV	93.3 GeV	200	171	$4.3^{+1.3}_{-1.5}$	$3.7^{+1.3}_{-1.5}$
$95 < m_{ee} < 100$ GeV	97.1 GeV	83	76	$7.2^{+2.0}_{-2.5}$	$6.1^{+2.0}_{-2.5}$
$100 < m_{ee} < 105$ GeV	102.6 GeV	39	21	$5.6^{+1.8}_{-2.2}$	$5.3^{+1.8}_{-2.2}$
$105 < m_{ee} < 110$ GeV	107.0 GeV	13	13	$5.6^{+1.7}_{-2.1}$	$5.0^{+1.7}_{-2.1}$
$110 < m_{ee} < 116$ GeV	112.8 GeV	21	9	$6.1^{+1.9}_{-2.3}$	$5.4^{+1.9}_{-2.3}$
$116 < m_{ee} < 125$ GeV	119.9 GeV	24	13	$8.2^{+2.6}_{-3.1}$	$7.6^{+2.6}_{-3.1}$
$125 < m_{ee} < 250$ GeV	164.1 GeV	80	48	$49.0^{+15.5}_{-19.1}$	$45.5^{+15.5}_{-19.1}$
$250 < m_{ee} < 1000$ GeV	347.6 GeV	19	9	$17.7^{+6.1}_{-7.6}$	$17.2^{+6.1}_{-7.6}$

Table A.4: Number of forward and backward events for data and background in case of central–forward selection and the rapidity cut $|y_{ee}| > 1$.

APPENDIX B

Systematic Uncertainties of Unfolded A_{FB}

In the unfolding of the forward-backward asymmetry, several sources of systematic uncertainties arise, namely from the background subtraction, the energy scale, the energy resolution, the identification scale factors, pile-up re-weighting, PDF uncertainty, and the ambiguity of the $\sin^2\theta^{\ell}_{\text{eff}}$ value assumed in the acceptance correction. The values of the systematic uncertainties from the energy scale, the energy resolution, and identification scale factors are estimated by shifting the correction factors by their uncertainties, as given in section 7.1.1. The maximum shifts in the A_{FB} values are taken as systematic uncertainty. In case of pile-up re-weighting the difference between the results with the additional pile-up re-weighting and with the default pile-up configuration (in average 2.2 vertices) is considered as systematic uncertainty. For the background subtraction the maximum shifts in the A_{FB} determination, when applying the uncertainties from appendix A, are used as systematic error. In case of the PDF uncertainty, 52 error PDF sets provided by the CT10 collaboration [235] are used. They have been determined by varying the PDF parameters in positive and negative direction along the i-th eigenvector. Following the description in [235] the PDF uncertainty can be computed by

$$\Delta^{\pm}A^{i}_{\text{FB}} = \sqrt{\sum_{i=1}^{26}(A^{i}_{\text{FB}}(f_i^{\pm}) - A^{i}_{\text{FB}}(f_0))^2}\,, \tag{B.1}$$

where f_i^+ (f_i^-) stands for a PDF with a positive (negative) variation along the i-th eigenvector (f_0 is the default PDF set). Hence, two different uncertainties are derived, one for positive and one for negative variations. Finally, the maximum value of both uncertainties is taken as systematic PDF uncertainty. To account for the ambiguity of the $\sin^2\theta^{\ell}_{\text{eff}}$ value, assumed in the acceptance correction, the unfolded A_{FB} distributions of re-weighted $\sin^2\theta^{\ell}_{\text{eff}}$ samples are used (*cf.* section 8.4). The difference in each mass bin between the unfolded result of the ATLAS simulated Pythia $Z \to ee$ events and the unfolded distributions when using the result of eq. (8.9) and shifting it by the statistical uncertainties is taken as systematic error.

Mass Bin	Background	Energy Scale	Energy Resolution	ID Scale Factors	Pile-Up	PDF	$\sin^2\theta^{\ell}_{\text{eff}}$	Total
$60 < m_{ee} < 66$ GeV	7.6 / 12.5	2.3 / 0.2	1.3 / 0.0	1.8 / 0.0	1.3 / 0.0	0.9 / 8.9	3.6 / 0.8	9.14 / 15.39
$66 < m_{ee} < 70$ GeV	2.8 / 9.4	6.3 / 0.6	0.0 / 0.0	0.6 / 0.0	0.0 / 0.0	0.1 / 8.3	3.7 / 2.4	7.85 / 12.78
$70 < m_{ee} < 76$ GeV	5.6 / 11.8	1.0 / 1.0	0.0 / 1.6	0.0 / 1.6	0.0 / 1.6	0.5 / 5.8	4.9 / 5.0	7.50 / 14.34
$76 < m_{ee} < 80$ GeV	3.5 / 6.5	0.0 / 8.1	0.8 / 2.3	1.2 / 0.0	0.8 / 0.0	1.8 / 2.3	7.5 / 7.2	8.61 / 12.99
$80 < m_{ee} < 86$ GeV	0.6 / 0.9	1.4 / 7.2	1.5 / 1.2	1.6 / 0.0	1.5 / 0.0	2.0 / 1.3	9.0 / 9.6	9.75 / 12.14
$86 < m_{ee} < 88$ GeV	0.1 / 0.1	1.1 / 1.5	0.6 / 0.3	0.6 / 0.0	0.6 / 0.0	1.6 / 1.4	8.9 / 9.9	9.18 / 10.08
$88 < m_{ee} < 90$ GeV	0.0 / 0.0	0.8 / 0.0	0.1 / 0.1	0.1 / 0.0	0.1 / 0.0	1.3 / 1.4	8.4 / 9.3	8.56 / 9.44
$90 < m_{ee} < 92$ GeV	0.0 / 0.1	0.9 / 0.0	0.0 / 0.1	0.0 / 0.2	0.0 / 0.1	1.2 / 1.3	8.0 / 8.8	8.18 / 8.92
$92 < m_{ee} < 95$ GeV	0.1 / 0.0	0.5 / 1.4	0.3 / 0.2	0.0 / 0.5	0.0 / 0.2	1.2 / 1.2	7.8 / 8.6	7.87 / 8.82
$95 < m_{ee} < 100$ GeV	1.1 / 0.4	0.0 / 1.8	1.9 / 0.8	0.0 / 1.2	0.0 / 0.8	1.0 / 2.2	6.8 / 9.2	7.18 / 9.80
$100 < m_{ee} < 105$ GeV	7.2 / 3.3	3.0 / 2.5	3.6 / 1.8	0.0 / 2.5	0.0 / 1.8	1.7 / 3.6	4.0 / 8.3	9.62 / 10.60
$105 < m_{ee} < 110$ GeV	10.8 / 5.2	0.0 / 16.4	0.7 / 2.1	0.0 / 3.0	0.0 / 2.1	6.3 / 2.1	3.0 / 5.6	12.84 / 18.69
$110 < m_{ee} < 116$ GeV	28.6 / 9.6	0.0 / 3.1	0.6 / 0.3	0.6 / 0.4	0.6 / 0.0	6.4 / 3.5	4.5 / 2.7	29.68 / 11.01
$116 < m_{ee} < 125$ GeV	31.5 / 3.8	7.3 / 0.0	2.4 / 1.5	2.4 / 0.0	2.4 / 0.0	2.3 / 11.0	3.7 / 2.1	32.91 / 11.92
$125 < m_{ee} < 250$ GeV	88.2 / 0.0	1.3 / 0.0	0.0 / 0.7	0.0 / 1.0	0.0 / 0.2	0.0 / 20.4	4.0 / 3.0	88.25 / 20.69
$250 < m_{ee} < 1000$ GeV	122.8 / 0.0	2.8 / 5.3	2.3 / 0.9	0.0 / 1.4	0.0 / 0.9	69.5 / 16.0	19.9 / 0.0	142.56 / 16.96

Table B.1: Systematic uncertainties arsing from various sources for the unfolded forward-backward asymmetry. For each invariant mass bin the asymmetric uncertainty is given (+/-)$\times 10^{-4}$.

Bibliography

[1] H. Flacher *et al.*, Revisiting the Global Electroweak Fit of the Standard Model and Beyond with Gfitter, Eur.Phys.J. **C60**, 543 (2009), (note erratum http://www.springerlink.com/content/j0535mg347173up4/), arXiv:0811.0009.

[2] R. Brun and F. Rademakers, Root: An object oriented data analysis framework, Nucl. Instrum. Meth. **A389**, 81 (1997).

[3] M. E. Peskin and T. Takeuchi, A New constraint on a strongly interacting Higgs sector, Phys. Rev. Lett. **65**, 964 (1990).

[4] M. E. Peskin and T. Takeuchi, Estimation of oblique electroweak corrections, Phys. Rev. **D46**, 381 (1992).

[5] T. Sjostrand, S. Mrenna, and P. Z. Skands, A Brief Introduction to PYTHIA 8.1, Comput.Phys.Commun. **178**, 852 (2008), arXiv:0710.3820.

[6] Wikipedia, Elementary particle interactions, July, 2011, http://en.wikipedia.org/wiki/File:Elementary_particle_interactions.svg.

[7] H. Fritzsch, M. Gell-Mann, and H. Leutwyler, Advantages of the Color Octet Gluon Picture, Phys.Lett. **B47**, 365 (1973), Introduces the term 'color'.

[8] R. Ellis, W. Stirling, and B. Webber, QCD and collider physics, Camb.Monogr.Part.Phys.Nucl.Phys.Cosmol. **8**, 1 (1996).

[9] S. L. Glashow, Partial symmetries of weak interactions, Nucl. Phys. **22**, 579 (1961).

[10] A. Salam, Weak and electromagnetic interactions, Originally printed in Svartholm: Elementary Particle Theory, Proceedings Of The Nobel Symposium Held 1968 At Lerum, Sweden*, Stockholm 1968, 367-377.

[11] S. Weinberg, A model of leptons, Phys. Rev. Lett. **19**, 1264 (1967).

[12] P. W. Higgs, Broken symmetries and the masses of gauge bosons, Phys. Rev. Lett. **13**, 508 (1964).

[13] P. W. Higgs, Broken symmetries, massless particles and gauge fields, Phys. Lett. **12**, 132 (1964).

[14] F. Englert and R. Brout, Broken symmmtry and the mass of gauge vector mesons, Phys. Rev. Lett. **13**, 321 (1964).

[15] WMAP Collaboration, E. Komatsu *et al.*, Seven-Year Wilkinson Microwave Anisotropy Probe (WMAP) Observations: Cosmological Interpretation, Astrophys.J.Suppl. **192**, 18 (2011), `arXiv:1001.4538`.

[16] U. Baur, S. Keller, and W. K. Sakumoto, Qed radiative corrections to z boson production and the forward backward asymmetry at hadron colliders, Phys. Rev. D **57**, 199. 53 p (Jul, 1997).

[17] U. Baur, O. Brein, W. F. L. Hollik, C. Schappacher, and D. Wackeroth, Electroweak radiative corrections to neutral-current drell-yan processes at hadron colliders, Phys. Rev. D **65**, 033007. 39 p (Aug, 2001).

[18] ALEPH Collaboration, DELPHI Collaboration, L3 Collaboration, OPAL Collaboration, SLD Collaboration, LEP Electroweak Working Group, SLD Electroweak Group, SLD Heavy Flavour Group, Precision electroweak measurements on the Z resonance, Phys.Rept. **427**, 257 (2006), `hep-ex/0509008`.

[19] S. Bennett and C. E. Wieman, Measurement of the 6S –¿ 7S transition polarizability in atomic cesium and an improved test of the Standard Model, Phys.Rev.Lett. **82**, 2484 (1999), `hep-ex/9903022`.

[20] SLAC E158 Collaboration, P. Anthony *et al.*, Precision measurement of the weak mixing angle in Moller scattering, Phys.Rev.Lett. **95**, 081601 (2005), `hep-ex/0504049`.

[21] NuTeV Collaboration, G. Zeller *et al.*, A Precise determination of electroweak parameters in neutrino nucleon scattering, Phys.Rev.Lett. **88**, 091802 (2002), `hep-ex/0110059`.

[22] D0, V. M. Abazov *et al.*, Measurement of $\sin^2\theta_{\rm eff}^{\rm lept}$ and Z-light quark couplings using the forward-backward charge asymmetry in $p\bar{p} \to Z/\gamma^* \to e^+e^-$ events with $L = 5.0$ fb^{-1} at $\sqrt{s} = 1.96$ TeV, (2011), `arXiv:1104.4590`.

[23] CDF Collaboration, D. E. Acosta *et al.*, Measurement of the forward-backward charge asymmetry of electron positron pairs in $p\bar{p}$ collisions at $\sqrt{s} = 1.96$ TeV, Phys.Rev. **D71**, 052002 (2005), `hep-ex/0411059`.

[24] CMS Collaboration, Forward-backward asymmetry of di-lepton pairs and the weak-mixing angle, (2011), CMS-PAS-EWK-10-011.

[25] S. Drell and T.-M. Yan, Massive Lepton Pair Production in Hadron-Hadron Collisions at High-Energies, Phys.Rev.Lett. **25**, 316 (1970).

[26] S. Drell and T.-M. Yan, Partons and their Applications at High-Energies, Annals Phys. **66**, 578 (1971).

[27] H1 and ZEUS, HERA Combined Results, July, 2011, https://www.desy.de/h1zeus/combined_results/index.php?do=proton_structure.

[28] V. Gribov and L. Lipatov, Deep inelastic e p scattering in perturbation theory, Sov.J.Nucl.Phys. **15**, 438 (1972).

[29] G. Altarelli and G. Parisi, Asymptotic Freedom in Parton Language, Nucl.Phys. **B126**, 298 (1977).

[30] Y. L. Dokshitzer, Calculation of the Structure Functions for Deep Inelastic Scattering and e+ e- Annihilation by Perturbation Theory in Quantum Chromodynamics., Sov.Phys.JETP **46**, 641 (1977).

[31] E. Kuraev, L. Lipatov, and V. S. Fadin, The Pomeranchuk Singularity in Nonabelian Gauge Theories, Sov.Phys.JETP **45**, 199 (1977).

[32] I. Balitsky and L. Lipatov, The Pomeranchuk Singularity in Quantum Chromodynamics, Sov.J.Nucl.Phys. **28**, 822 (1978).

[33] A. D. Martin, R. G. Roberts, W. J. Stirling, and R. S. Thorne, Parton distributions and the LHC: W and Z production, Eur. Phys. J. **C14**, 133 (2000), `hep-ph/9907231`.

[34] M. Baak *et al.*, Updated Status of the Global Electroweak Fit and Constraints on New Physics, (2011), * Temporary entry *, `arXiv:1107.0975`.

[35] D. Y. Bardin *et al.*, ZFITTER v.6.21: A semi-analytical program for fermion pair production in e^+e^- annihilation, Comput. Phys. Commun. **133**, 229 (2001), `hep-ph/9908433`.

[36] A. B. Arbuzov *et al.*, ZFITTER: A semi-analytical program for fermion pair production in e^+e^- annihilation, from version 6.21 to version 6.42, Comput. Phys. Commun. **174**, 728 (2006), `hep-ph/0507146`.

[37] G. Montagna, F. Piccinini, O. Nicrosini, G. Passarino, and R. Pittau, TOPAZ0: A Program for computing observables and for fitting cross-sections and forward - backward asymmetries around the Z0 peak, Comput.Phys.Commun. **76**, 328 (1993).

[38] G. Montagna, O. Nicrosini, F. Piccinini, and G. Passarino, TOPAZ0 4.0: A New version of a computer program for evaluation of deconvoluted and realistic observables at LEP-1 and LEP-2, Comput.Phys.Commun. **117**, 278 (1999), `hep-ph/9804211`.

[39] V. Novikov, L. Okun, A. N. Rozanov, and M. Vysotsky, LEPTOP, (1995), `hep-ph/9503308`.

[40] V. A. Novikov, L. B. Okun, A. N. Rozanov, and M. I. Vysotsky, Mass of the Higgs versus fourth generation masses, JETP Lett. **76**, 127 (2002), `hep-ph/0203132`.

[41] J. Erler, Global fits to electroweak data using GAPP, (1999), `hep-ph/0005084`.

[42] J. Erler and P. Langacker (in: Review for Particle Data Group), Review of particle physics, J. Phys. **G37**, 075021 (2010).

[43] Electroweak working group, D. Y. Bardin *et al.*, Electroweak working group report, (1997), Prepared for Workshop Group on Precision Calculations for the Z Resonance (2nd meeting held Mar 31, 3rd meeting held Jun 13), Geneva, Switzerland, 14 Jan 1994, CERN-YELLOW-95-03A, `hep-ph/9709229`.

[44] LEP Electroweak Working Group (LEP EWWG), Status of July 2010, http://lepewwg.web.cern.ch/LEPEWWG/.

[45] A. Hoecker, H. Lacker, S. Laplace, and F. Le Diberder, A new approach to a global fit of the ckm matrix, Eur. Phys. J. **C21**, 225 (2001), `hep-ph/0104062`.

[46] CKMfitter Group, J. Charles *et al.*, CP violation and the CKM matrix: Assessing the impact of the asymmetric B factories, Eur. Phys. J. **C41**, 1 (2005), `hep-ph/0406184`.

[47] M. Goebel, A global standard model fit at the electroweak scale, Diploma thesis, University Hamburg, 2008.

[48] F. James and M. Roos, Minuit: A system for function minimization and analysis of the parameter errors and correlations, Comput. Phys. Commun. **10**, 343 (1975).

[49] A. Hoecker *et al.*, TMVA: Toolkit for multivariate data analysis, (2007), CERN-OPEN-2007-007, `physics/0703039`.

[50] M. Awramik, M. Czakon, A. Freitas, and G. Weiglein, Precise prediction for the W-boson mass in the standard model, Phys. Rev. **D69**, 053006 (2004), `hep-ph/0311148`.

[51] M. Awramik, M. Czakon, A. Freitas, and G. Weiglein, Complete two-loop electroweak fermionic corrections to $\sin^2\theta^{\rm lept}_{\rm eff}$ and indirect determination of the Higgs boson mass, Phys. Rev. Lett. **93**, 201805 (2004), `hep-ph/0407317`.

[52] M. Awramik, M. Czakon, and A. Freitas, Electroweak two-loop corrections to the effective weak mixing angle, JHEP **11**, 048 (2006), `hep-ph/0608099`.

[53] M. Awramik, M. Czakon, A. Freitas, and B. Kniehl, Two-loop electroweak fermionic corrections to $\sin^2\theta^{b\bar{b}}_{\rm eff}$, Nucl.Phys. **B813**, 174 (2009), `arXiv:0811.1364`.

[54] D. Y. Bardin and G. Passarino, The standard model in the making: Precision study of the electroweak interactions, Oxford, UK: Clarendon (1999) 685 p.

[55] K. Hagiwara, S. Matsumoto, D. Haidt, and C. Kim, A Novel approach to confront electroweak data and theory, Z.Phys. **C64**, 559 (1994), Order of authors changed in journal, `hep-ph/9409380`.

[56] K. Hagiwara, Electroweak studies at Z factories, Ann.Rev.Nucl.Part.Sci. **48**, 463 (1998).

[57] G.-C. Cho and K. Hagiwara, Supersymmetry versus precision experiments revisited, Nucl.Phys. **B574**, 623 (2000), hep-ph/9912260.

[58] G.-C. Cho, K. Hagiwara, Y. Matsumoto, and D. Nomura, The MSSM confronts the precision electroweak data and the muon g-2, (2011), * Temporary entry *, arXiv:1104.1769.

[59] A. A. Akhundov, D. Y. Bardin, and T. Riemann, Electroweak One Loop Corrections to the Decay of the Neutral Vector Boson, Nucl. Phys. **B276**, 1 (1986).

[60] D. Y. Bardin, S. Riemann, and T. Riemann, Electroweak one loop corrections to the decay of the charged vector boson, Z. Phys. **C32**, 121 (1986).

[61] R. Barbieri, M. Beccaria, P. Ciafaloni, G. Curci, and A. Vicere, Two loop heavy top effects in the standard model, Nucl. Phys. **B409**, 105 (1993).

[62] J. Fleischer, O. V. Tarasov, and F. Jegerlehner, Two loop heavy top corrections to the rho parameter: A simple formula valid for arbitrary higgs mass, Phys. Lett. **B319**, 249 (1993).

[63] G. Degrassi, S. Fanchiotti, F. Feruglio, B. P. Gambino, and A. Vicini, Two loop electroweak top corrections: Are they under control?, Phys. Lett. **B350**, 75 (1995), hep-ph/9412380.

[64] G. Degrassi, F. Feruglio, A. Vicini, S. Fanchiotti, and P. Gambino, Two-loop corrections for electroweak processes, (1995), hep-ph/9507286.

[65] G. Degrassi, P. Gambino, and A. Vicini, Two-loop heavy top effects on the mz-mw interdependence, Phys. Lett. **B383**, 219 (1996), hep-ph/9603374.

[66] G. Degrassi and P. Gambino, Two-loop heavy top corrections to the z0 boson partial widths, Nucl. Phys. **B567**, 3 (2000), hep-ph/9905472.

[67] B. A. Kniehl, Two Loop Corrections to the Vacuum Polarizations in Perturbative QCD, Nucl. Phys. **B347**, 86 (1990).

[68] ZFITTER Code (version 6.42), July, 2011, /afs/cern.ch/user/b/bardindy/public/ZF6_42.

[69] P. A. Baikov, K. G. Chetyrkin, and J. H. Kuhn, Order α_s^4 QCD Corrections to Z and τ Decays, Phys. Rev. Lett. **101**, 012002 (2008), arXiv:0801.1821.

[70] A. Czarnecki and J. H. Kühn, Nonfactorizable qcd and electroweak corrections to the hadronic z boson decay rate, Phys. Rev. Lett. **77**, 3955 (1996), hep-ph/9608366.

[71] R. Harlander, T. Seidensticker, and M. Steinhauser, Complete corrections of o(alpha alpha(s)) to the decay of the z boson into bottom quarks, Phys. Lett. **B426**, 125 (1998), hep-ph/9712228.

[72] Tevatron Electroweak Working Group and CDF and D0 Collaborations, Updated Combination of CDF and D0 Results for the Mass of the W Boson, (2009), arXiv:0908.1374.

[73] Tevatron Electroweak Working Group, Combination of CDF and D0 Results on the Width of the W boson, (2010), arXiv:1003.2826.

[74] T. E. W. Group, Combination of CDF and DO results on the mass of the top quark using up to 5.8 fb-1 of data, (2011), * Temporary entry *, arXiv:1107.5255.

[75] M. Davier, A. Hoecker, B. Malaescu, and Z. Zhang, Reevaluation of the Hadronic Contributions to the Muon g-2 and to alpha(MZ), Eur. Phys. J. **C71**, 1515 (2011), arXiv:1010.4180.

[76] The ALEPH, DELPHI, L3 and OPAL Collaborations, and LEP Working Group for Higgs Boson Searches, R. Barate *et al.*, Search for the standard model Higgs boson at LEP, Phys. Lett. **B565**, 61 (2003), hep-ex/0306033.

[77] T. CDF, D. Collaborations, t. T. N. Phenomena, and H. W. Group, Combined CDF and D0 Upper Limits on Standard Model Higgs Boson Production with up to 8.6 fb-1 of Data, (2011), * Temporary entry *, arXiv:1107.5518.

[78] ATLAS Collaboration, G. Aad *et al.*, Limits on the production of the Standard Model Higgs Boson in pp collisions at $\sqrt{s} = 7$ TeV with the ATLAS detector, (2011), CERN-PH-EP-2011-076 (2011), arXiv:1106.2748.

[79] CMS Collaboration, S. Chatrchyan *et al.*, Measurement of WW Production and Search for the Higgs Boson in pp Collisions at $\sqrt{s} = 7$ TeV, Phys. Lett. **B699**, 25 (2011), arXiv:1102.5429.

[80] ATLAS Colaboration, Update of the Combination of Higgs Boson Searches in 1.0 to 2.3 fb^{-1} of *pp* Collisions Data Taken at $\sqrt{s} = 7$ TeV with the ATLAS Experiment at the LHC, (Aug, 2011).

[81] CMS Colaboration, Combination of Higgs Searches, (Aug, 2011).

[82] Particle Data Group, K. Nakamura *et al.*, Review of particle physics, J.Phys.G **G37**, 075021 (2010).

[83] P. Skands and D. Wicke, Non-perturbative QCD effects and the top mass at the Tevatron, Eur. Phys. J. **C52**, 133 (2007), hep-ph/0703081.

[84] D. Wicke and P. Z. Skands, Non-perturbative QCD Effects and the Top Mass at the Tevatron, (2008), arXiv:0807.3248.

[85] A. H. Hoang, A. Jain, I. Scimemi, and I. W. Stewart, Infrared Renormalization Group Flow for Heavy Quark Masses, (2008), arXiv:0803.4214.

[86] A. H. Hoang and I. W. Stewart, Top Mass Measurements from Jets and the Tevatron Top-Quark Mass, (2008), arXiv:0808.0222.

[87] D0 Collaboration, V. M. Abazov *et al.*, Determination of the pole and MSbar masses of the top quark from the ttbar cross section, (2011), arXiv:1104.2887.

[88] D0 Collaboration, V. M. Abazov *et al.*, Measurement of the top quark pair production cross section in the lepton+jets channel in proton-antiproton collisions at $\sqrt{s}$=1.96 TeV, (2011), arXiv:1101.0124.

[89] U. Langenfeld, S. Moch, and P. Uwer, Measuring the running top-quark mass, Phys. Rev. **D80**, 054009 (2009), arXiv:0906.5273.

[90] K. Hagiwara, R. Liao, A. D. Martin, D. Nomura, and T. Teubner, $(g-2)_\mu$ and $\alpha(M_Z^2)$ re-evaluated using new precise data, J. Phys. **G38**, 085003 (2011), arXiv:1105.3149.

[91] M. Davier, S. Descotes-Genon, A. Hocker, B. Malaescu, and Z. Zhang, The Determination of alpha(s) from Tau Decays Revisited, Eur.Phys.J. **C56**, 305 (2008), arXiv:0803.0979.

[92] CDF and D0 Collaborations, Combination of CDF and D0 Results on the Mass of the Top Quark, (2010), arXiv:1007.3178.

[93] G. Altarelli, R. Barbieri, and F. Caravaglios, Nonstandard analysis of electroweak precision data, Nucl. Phys. **B405**, 3 (1993).

[94] G. Altarelli, R. Barbieri, and F. Caravaglios, Electroweak precision tests: A concise review, Int. J. Mod. Phys. **A13**, 1031 (1998), hep-ph/9712368.

[95] C. P. Burgess, S. Godfrey, H. Konig, D. London, and I. Maksymyk, A Global fit to extended oblique parameters, Phys. Lett. **B326**, 276 (1994), hep-ph/9307337.

[96] R. Barbieri, A. Pomarol, R. Rattazzi, and A. Strumia, Electroweak symmetry breaking after LEP-1 and LEP-2, Nucl. Phys. **B703**, 127 (2004), hep-ph/0405040.

[97] C. P. Burgess, The Effective use of precision electroweak measurements, Pramana **45**, S47 (1995), hep-ph/9411257.

[98] S. Weinberg, Implications of Dynamical Symmetry Breaking: An Addendum, Phys.Rev. **D19**, 1277 (1979), (For original paper see Phys.Rev.D13:974-996,1976).

[99] L. Susskind, Dynamics of Spontaneous Symmetry Breaking in the Weinberg-Salam Theory, Phys.Rev. **D20**, 2619 (1979).

[100] J. R. Ellis, G. L. Fogli, and E. Lisi, Technicolor and precision electroweak data revisited, Phys.Lett. **B343**, 282 (1995).

[101] M. Golden and L. Randall, Radiative corrections to electrweak parameters in technicolor theories, Nucl. Phys. **B361**, 3 (1991).

[102] R. Sundrum and S. D. Hsu, Walking technicolor and electroweak radiative corrections, Nucl.Phys. **B391**, 127 (1993), hep-ph/9206225.

[103] C. P. Burgess, S. Godfrey, H. Konig, D. London, and I. Maksymyk, Model independent global constraints on new physics, Phys. Rev. **D49**, 6115 (1994), hep-ph/9312291.

[104] N. G. Deshpande and E. Ma, Pattern of Symmetry Breaking with Two Higgs Doublets, Phys. Rev. **D18**, 2574 (1978).

[105] R. Barbieri, L. J. Hall, and V. S. Rychkov, Improved naturalness with a heavy Higgs: An alternative road to LHC physics, Phys. Rev. **D74**, 015007 (2006), hep-ph/0603188.

[106] L. Lopez Honorez, E. Nezri, J. F. Oliver, and M. H. G. Tytgat, The inert doublet model: An archetype for dark matter, JCAP **0702**, 028 (2007), hep-ph/0612275.

[107] M. Gustafsson, E. Lundstrom, L. Bergstrom, and J. Edsjo, Significant gamma lines from inert Higgs dark matter, Phys. Rev. Lett. **99**, 041301 (2007), astro-ph/0703512.

[108] E. Lundstrom, M. Gustafsson, and J. Edsjo, The Inert Doublet Model and LEP II Limits, Phys. Rev. **D79**, 035013 (2009), arXiv:0810.3924.

[109] T. Hambye, F. S. Ling, L. Lopez Honorez, and J. Rocher, Scalar Multiplet Dark Matter, JHEP **07**, 090 (2009), arXiv:0903.4010.

[110] S. Andreas, M. H. Tytgat, and Q. Swillens, Neutrinos from Inert Doublet Dark Matter, JCAP **0904**, 004 (2009), arXiv:0901.1750.

[111] E. M. Dolle and S. Su, The Inert Dark Matter, Phys. Rev. **D80**, 055012 (2009), arXiv:0906.1609.

[112] L. Lopez Honorez and C. E. Yaguna, The inert doublet model of dark matter revisited, JHEP **09**, 046 (2010), arXiv:1003.3125.

[113] L. Lopez Honorez and C. E. Yaguna, A new viable region of the inert doublet model, JCAP **1101**, 002 (2011), arXiv:1011.1411.

[114] B. Holdom *et al.*, Four Statements about the Fourth Generation, PMC Phys. **A3**, 4 (2009), arXiv:0904.4698.

[115] B. Holdom, Approaching a strong fourth family, Phys.Lett. **B686**, 146 (2010), * Temporary entry *, arXiv:1001.5321.

[116] W.-S. Hou, CP Violation and Baryogenesis from New Heavy Quarks, Chin. J. Phys. **47**, 134 (2009), arXiv:0803.1234.

[117] K. Belotsky, M. Khlopov, and K. Shibaev, Stable quarks of the 4th family?, (2008), * Brief entry *, arXiv:0806.1067.

[118] ATLAS Collaboration, Search for Fourth Generation Quarks Decaying to $W^+qW^-q \to l^+l^-\nu\nu qq$ in pp collisions at $\sqrt{s} = 7$ TeV with the ATLAS Detector, ATLAS-CONF-2011-022 (2011).

[119] CMS Collaboration, S. Chatrchyan *et al.*, Search for a Heavy Bottom-like Quark in pp Collisions at $\sqrt{s} = 7$ TeV, Phys. Lett. **B701**, 204 (2011), arXiv:1102.4746.

[120] CDF Collaboration, J. Conway *et al.*, CDF/PUB/TOP/PUBLIC/10395 (2011).

[121] CDF Collaboration, T. Aaltonen *et al.*, Search for heavy bottom-like quarks decaying to an electron or muon and jets in $p\bar{p}$ collisions at $\sqrt{s} = 1.96$ TeV, (2011), arXiv:1101.5728.

[122] C. J. Flacco, D. Whiteson, and M. Kelly, Fourth generation quark mass limits in CKM-element space, (2011), arXiv:1101.4976.

[123] C. J. Flacco, D. Whiteson, T. M. P. Tait, and S. Bar-Shalom, Direct Mass Limits for Chiral Fourth-Generation Quarks in All Mixing Scenarios, Phys. Rev. Lett. **105**, 111801 (2010), arXiv:1005.1077.

[124] L3 Collaboration, P. Achard *et al.*, Search for heavy neutral and charged leptons in e+ e- annihilation at LEP, Phys. Lett. **B517**, 75 (2001), hep-ex/0107015.

[125] A. Arhrib and W.-S. Hou, Effect of fourth generation CP phase on $b \to s$ transitions, Eur. Phys. J. **C27**, 555 (2003), hep-ph/0211267.

[126] W.-S. Hou, M. Nagashima, and A. Soddu, Large time-dependent CP violation in B_s^0 system and finite D^0 - $\bar{D}^0$ mass difference in four generation standard model, Phys. Rev. **D76**, 016004 (2007), hep-ph/0610385.

[127] W.-S. Hou, M. Nagashima, and A. Soddu, Enhanced $K(L) \to \pi^0\nu\bar{\nu}$ from direct CP violation in $B \to K\pi$ with four generations, Phys. Rev. **D72**, 115007 (2005), hep-ph/0508237.

[128] W.-S. Hou, H.-n. Li, S. Mishima, and M. Nagashima, Fourth generation CP violation effect on $B \to K\pi$, ϕK and ρK in NLO PQCD, Phys. Rev. Lett. **98**, 131801 (2007), hep-ph/0611107.

[129] A. Soni, A. K. Alok, A. Giri, R. Mohanta, and S. Nandi, The Fourth family: A Natural explanation for the observed pattern of anomalies in B^- CP asymmetries, Phys. Lett. **B683**, 302 (2010), arXiv:0807.1971.

[130] F. J. Botella, G. C. Branco, and M. Nebot, Small violations of 3 x 3 unitarity, the phase in B0(S) - anti-B0(S) mixing and visible $t \to cZ$ decays at the LHC, J. Phys. Conf. Ser. **171**, 012058 (2009).

[131] O. Eberhardt, A. Lenz, and J. Rohrwild, Less space for a new family of fermions, Phys. Rev. **D82**, 095006 (2010), arXiv:1005.3505.

[132] M. Bobrowski, A. Lenz, J. Riedl, and J. Rohrwild, How much space is left for a new family of fermions?, Phys. Rev. **D79**, 113006 (2009), arXiv:0902.4883.

[133] A. Soni, A. K. Alok, A. Giri, R. Mohanta, and S. Nandi, SM with four generations: Selected implications for rare B and K decays, Phys. Rev. **D82**, 033009 (2010), arXiv:1002.0595.

[134] A. J. Buras *et al.*, Patterns of Flavour Violation in the Presence of a Fourth Generation of Quarks and Leptons, JHEP **09**, 106 (2010), arXiv:1002.2126.

[135] H. Lacker and A. Menzel, Simultaneous Extraction of the Fermi constant and PMNS matrix elements in the presence of a fourth generation, JHEP **07**, 006 (2010), arXiv:1003.4532.

[136] J. Erler and P. Langacker, Precision Constraints on Extra Fermion Generations, Phys. Rev. Lett. **105**, 031801 (2010), arXiv:1003.3211.

[137] P. H. Frampton, P. Q. Hung, and M. Sher, Quarks and leptons beyond the third generation, Phys. Rept. **330**, 263 (2000), hep-ph/9903387.

[138] CDF and D0 Collaborations, T. Aaltonen *et al.*, Combined Tevatron upper limit on gg-¿H-¿W+W- and constraints on the Higgs boson mass in fourth-generation fermion models, (2010), arXiv:1005.3216.

[139] CMS Colaboration, SM Higgs Combination, (Jul, 2011).

[140] B. Holdom, Negative T from a dynamical left-handed neutrino mass, Phys.Rev. **D54**, 721 (1996), hep-ph/9602248.

[141] H.-J. He, N. Polonsky, and S.-f. Su, Extra families, Higgs spectrum and oblique corrections, Phys. Rev. **D64**, 053004 (2001), hep-ph/0102144.

[142] B. Holdom, The Discovery of the fourth family at the LHC: What if?, JHEP **0608**, 076 (2006), hep-ph/0606146.

[143] G. D. Kribs, T. Plehn, M. Spannowsky, and T. M. P. Tait, Four generations and Higgs physics, Phys. Rev. **D76**, 075016 (2007), arXiv:0706.3718.

[144] M. S. Chanowitz, Bounding CKM Mixing with a Fourth Family, Phys. Rev. **D79**, 113008 (2009), arXiv:0904.3570.

[145] M. S. Chanowitz, Higgs Mass Constraints on a Fourth Family: Upper and Lower Limits on CKM Mixing, Phys.Rev. **D**, 035018 (2010), arXiv:1007.0043.

[146] M. Hashimoto, Constraints on Mass Spectrum of Fourth Generation Fermions and Higgs Bosons, Phys.Rev. **D81**, 075023 (2010), arXiv:1001.4335.

[147] N. Arkani-Hamed, A. G. Cohen, and H. Georgi, Electroweak symmetry breaking from dimensional deconstruction, Phys. Lett. **B513**, 232 (2001), hep-ph/0105239.

[148] N. Arkani-Hamed, A. G. Cohen, T. Gregoire, and J. G. Wacker, Phenomenology of electroweak symmetry breaking from theory space, JHEP **08**, 020 (2002), hep-ph/0202089.

[149] N. Arkani-Hamed, A. G. Cohen, E. Katz, and A. E. Nelson, The littlest Higgs, JHEP **07**, 034 (2002), hep-ph/0206021.

[150] C. Csaki, J. Hubisz, G. D. Kribs, P. Meade, and J. Terning, Big corrections from a little Higgs, Phys. Rev. **D67**, 115002 (2003), hep-ph/0211124.

[151] J. L. Hewett, F. J. Petriello, and T. G. Rizzo, Constraining the littlest Higgs. ((U)), JHEP **10**, 062 (2003), hep-ph/0211218.

[152] C. Csaki, J. Hubisz, G. D. Kribs, P. Meade, and J. Terning, Variations of little Higgs models and their electroweak constraints, Phys. Rev. **D68**, 035009 (2003), hep-ph/0303236.

[153] M. Perelstein, M. E. Peskin, and A. Pierce, Top quarks and electroweak symmetry breaking in little Higgs models, Phys. Rev. **D69**, 075002 (2004), hep-ph/0310039.

[154] T. Han, H. E. Logan, B. McElrath, and L.-T. Wang, Phenomenology of the little Higgs model, Phys. Rev. **D67**, 095004 (2003), hep-ph/0301040.

[155] H.-C. Cheng and I. Low, TeV symmetry and the little hierarchy problem, JHEP **09**, 051 (2003), hep-ph/0308199.

[156] H.-C. Cheng and I. Low, Little hierarchy, little Higgses, and a little symmetry, JHEP **08**, 061 (2004), hep-ph/0405243.

[157] J. Hubisz and P. Meade, Phenomenology of the littlest Higgs with T-parity, Phys. Rev. **D71**, 035016 (2005), hep-ph/0411264.

[158] J. Hubisz, P. Meade, A. Noble, and M. Perelstein, Electroweak precision constraints on the littlest Higgs model with T parity, JHEP **01**, 135 (2006), hep-ph/0506042.

[159] M. Asano, S. Matsumoto, N. Okada, and Y. Okada, Cosmic positron signature from dark matter in the littlest Higgs model with T-parity, Phys.Rev. **D75**, 063506 (2007), hep-ph/0602157.

[160] J. Casas, J. R. Espinosa, and I. Hidalgo, Implications for new physics from fine-tuning arguments. II. Little Higgs models, JHEP **0503**, 038 (2005), hep-ph/0502066.

[161] N. Arkani-Hamed, S. Dimopoulos, and G. R. Dvali, The hierarchy problem and new dimensions at a millimeter, Phys. Lett. **B429**, 263 (1998), hep-ph/9803315.

[162] I. Antoniadis, N. Arkani-Hamed, S. Dimopoulos, and G. R. Dvali, New dimensions at a millimeter to a Fermi and superstrings at a TeV, Phys. Lett. **B436**, 257 (1998), hep-ph/9804398.

[163] M. Shifman, LARGE EXTRA DIMENSIONS: Becoming acquainted with an alternative paradigm, Int. J. Mod. Phys. **A25**, 199 (2010), arXiv:0907.3074.

[164] D. J. Kapner *et al.*, Tests of the gravitational inverse-square law below the dark-energy length scale, Phys. Rev. Lett. **98**, 021101 (2007), hep-ph/0611184.

[165] Particle Data Group, G. F. Giudice and J. D. Wells, Extra dimensions (in: Review of particle physics), J. Phys. **G37**, 075021 (2010).

[166] S. Hannestad and G. G. Raffelt, Stringent neutron-star limits on large extra dimensions, Phys. Rev. Lett. **88**, 071301 (2002), hep-ph/0110067.

[167] G. F. Giudice, R. Rattazzi, and J. D. Wells, Quantum gravity and extra dimensions at high-energy colliders, Nucl. Phys. **B544**, 3 (1999), hep-ph/9811291.

[168] T. Han, J. D. Lykken, and R.-J. Zhang, On Kaluza-Klein states from large extra dimensions, Phys. Rev. **D59**, 105006 (1999), hep-ph/9811350.

[169] J. L. Hewett, Indirect collider signals for extra dimensions, Phys. Rev. Lett. **82**, 4765 (1999), hep-ph/9811356.

[170] G. F. Giudice and A. Strumia, Constraints on extra dimensional theories from virtual graviton exchange, Nucl. Phys. **B663**, 377 (2003), hep-ph/0301232.

[171] R. Contino, L. Pilo, R. Rattazzi, and A. Strumia, Graviton loops and brane observables, JHEP **06**, 005 (2001), hep-ph/0103104.

[172] G. Landsberg, Collider Searches for Extra Spatial Dimensions and Black Holes, (2008), arXiv:0808.1867.

[173] S. Ask, Search for extra dimensions at LEP, (2004), hep-ex/0410004.

[174] CMS Collaboration, S. Chatrchyan *et al.*, Search for Large Extra Dimensions in the Diphoton Final State at the Large Hadron Collider, JHEP **05**, 085 (2011), arXiv:1103.4279.

[175] ATLAS Collaboration, G. Aad *et al.*, Search for new phenomena with the monojet and missing transverse momentum signature using the ATLAS detector in $\sqrt{s} = 7$ TeV proton-proton collisions, (2011), CERN-PH-EP-2011-090 (2011), arXiv:1106.5327.

[176] Muon G-2 Collaboration, G. W. Bennett *et al.*, Final report of the muon E821 anomalous magnetic moment measurement at BNL, Phys. Rev. **D73**, 072003 (2006), hep-ex/0602035.

[177] L. Evans and P. Bryant, LHC Machine, JINST **3**, S08001 (2008).

[178] O. S. Bruning *et al.*, LHC Design Report. 1. The LHC Main Ring, (2004).

[179] LHC Images, July, 2011,
http://lhc-machine-outreach.web.cern.ch/lhc-machine-outreach/lhc_in_pictures.htm.

[180] S. Catani *et al.*, QCD, (2000), `hep-ph/0005025`.

[181] ATLAS Collaboration, G. Aad *et al.*, The ATLAS Experiment at the CERN Large Hadron Collider, JINST **3**, S08003 (2008).

[182] A. Yamamoto *et al.*, Progress in ATLAS central solenoid magnet, IEEE-Trans.Appl.Supercond. **10**, 353 (2000).

[183] G. Aad *et al.*, ATLAS pixel detector electronics and sensors, JINST **3**, P07007 (2008).

[184] A. Abdesselam *et al.*, The barrel modules of the ATLAS semiconductor tracker, Nucl.Instrum.Meth. **A568**, 642 (2006).

[185] E. Abat *et al.*, The ATLAS TRT end-cap detectors, JINST **3**, P10003 (2008).

[186] ATLAS TRT Collaboration, E. Abat *et al.*, The ATLAS TRT barrel detector, JINST **3**, P02014 (2008).

[187] ATLAS Collaboration, ATLAS liquid argon calorimeter: Technical design report, (1996).

[188] A. Artamonov *et al.*, The ATLAS forward calorimeters, JINST **3**, P02010 (2008).

[189] The ATLAS Collaboration, G. Aad *et al.*, Expected Performance of the ATLAS Experiment - Detector, Trigger and Physics, (2009), `arXiv:0901.0512`.

[190] CERN Report No. ATL-PHYS-PUB-2011-006, 2011 (unpublished).

[191] W. Lampl *et al.*, CERN Report No. ATL-LARG-PUB-2008-002. ATL-COM-LARG-2008-003, 2008 (unpublished).

[192] ATLAS Collaboration, Electron performance measurements with the atlas detector in 2010 lhc proton-proton collision data, in preparation .

[193] ATLAS Collaboration, Performance of the atlas trigger system in 2010, in preparation .

[194] *ATLAS level-1 trigger: Technical Design Report*, Technical Design Report ATLAS (CERN, Geneva, 1998).

[195] P. Jenni, M. Nessi, M. Nordberg, and K. Smith, *ATLAS high-level trigger, data-acquisition and controls: Technical Design Report*, Technical Design Report ATLAS (CERN, Geneva, 2003).

[196] ATLAS Collaboration, CERN Report No. ATLAS-CONF-2011-114, 2011 (unpublished).

[197] T. Fonseca-Martin *et al.*, Event reconstruction algorithms for the atlas trigger, J. Phys.: Conf. Ser. **119**, 022022 (2008).

[198] A. Hocker *et al.*, Overview of the High Level Trigger Steering and Selection for the ATLAS experiment at the LHC, IEEE Trans.Nucl.Sci. **55**, 165 (2008).

[199] P. Bell *et al.*, CERN Report No. ATL-DAQ-PUB-2009-005, 2009 (unpublished).

[200] V. Lendermann *et al.*, Combining Triggers in HEP Data Analysis, Nucl.Instrum.Meth. **A604**, 707 (2009), `arXiv:0901.4118`.

[201] ATLAS Collaboration, Atlas experiment - public results, July, 2011, https://twiki.cern.ch/twiki/bin/view/AtlasPublic/WebHome.

[202] P. Waller, CERN Report No. ATL-DAPR-PROC-2010-001, 2010 (unpublished).

[203] ATLAS, G. Aad *et al.*, Luminosity Determination in pp Collisions at $\sqrt{s} = 7$ TeV Using the ATLAS Detector at the LHC, Eur. Phys. J. **C71**, 1630 (2011), `arXiv:1101.2185`.

[204] P. Jenni and M. Nessi, CERN Report No. CERN-LHCC-2004-010. LHCC-I-014, 2004 (unpublished), revised version number 1 submitted on 2004-03-22 14:56:11.

[205] P. Jenni, M. Nordberg, M. Nessi, and K. Jon-And, *ATLAS Forward Detectors for Measurement of Elastic Scattering and Luminosity*, Technical Design Report (CERN, Geneva, 2008).

[206] H. Burkhardt and P. Grafström, Report No. LHC-PROJECT-Report-1019. CERN-LHC-PROJECT-Report-1019, 2007 (unpublished).

[207] W. Kozanecki *et al.*, Interaction-Point Phase-Space Characterization using Single-Beam and Luminous-Region Measurements at PEP-II, Nucl.Instrum.Meth. **A607**, 293 (2009).

[208] S. van der Meer, CERN Report No. CERN-ISR-PO-68-31. ISR-PO-68-31, 1968 (unpublished).

[209] CERN Report No. ATLAS-CONF-2011-011, 2011 (unpublished).

[210] M. Dobbs *et al.*, Les Houches guidebook to Monte Carlo generators for hadron collider physics, p. 411 (2004), Compiled by the Working Group on Quantum Chromodynamics and the Standard Model, `hep-ph/0403045`.

[211] A. Buckley *et al.*, General-purpose event generators for LHC physics, Physics Reports (2011), * Temporary entry *, `arXiv:1101.2599`.

[212] M. Dobbs and J. B. Hansen, The HepMC C++ Monte Carlo event record for High Energy Physics, Comput.Phys.Commun. **134**, 41 (2001).

[213] HepMC, July, 2011, http://lcgapp.cern.ch/project/simu/HepMC/.

[214] B. Andersson, G. Gustafson, G. Ingelman, and T. Sjostrand, Parton Fragmentation and String Dynamics, Phys.Rept. **97**, 31 (1983).

[215] T. Sjostrand, Status of Fragmentation Models, Int.J.Mod.Phys. **A3**, 751 (1988).

[216] G. Marchesini and B. Webber, Simulation of QCD Jets Including Soft Gluon Interference, Nucl.Phys. **B238**, 1 (1984).

[217] B. Webber, A QCD Model for Jet Fragmentation Including Soft Gluon Interference, Nucl.Phys. **B238**, 492 (1984).

[218] T. Sjostrand, S. Mrenna, and P. Z. Skands, PYTHIA 6.4 Physics and Manual, JHEP **0605**, 026 (2006), `hep-ph/0603175`.

[219] S. Frixione and B. R. Webber, Matching NLO QCD computations and parton shower simulations, JHEP **0206**, 029 (2002), `hep-ph/0204244`.

[220] S. Frixione, F. Stoeckli, P. Torrielli, and B. R. Webber, NLO QCD corrections in Herwig++ with MC@NLO, JHEP **01**, 053 (2011), `arXiv:1010.0568`.

[221] G. Corcella *et al.*, HERWIG 6.5: an event generator for Hadron Emission Reactions With Interfering Gluons (including supersymmetric processes), JHEP **01**, 010 (2001), `hep-ph/0011363`.

[222] GEANT4, S. Agostinelli *et al.*, GEANT4: A Simulation toolkit, Nucl.Instrum.Meth. **A506**, 250 (2003).

[223] J. Allison *et al.*, Geant4 developments and applications, IEEE Trans.Nucl.Sci. **53**, 270 (2006).

[224] M. Paterno, Calculating Efficencies and Their Uncertainties, May, 2003, http://home.fnal.gov/paterno/images/effic.pdf.

[225] Private communication with Michele Dieli (talk given in internal ATLAS meeting).

[226] M. Meyer, Untersuchung der Elektrontriggereffizienzen am ATLAS-Detektor mithilfe der Tag-and-Probe-Methode, (2011), Bachelor Thesis.

[227] Atlas, G. Aad *et al.*, Measurement of the $W \to l\nu$ and $Z/\gamma^* \to ll$ production cross sections in proton-proton collisions at $\sqrt{s} = 7$ TeV with the ATLAS detector, JHEP **12**, 060 (2010), `arXiv:1010.2130`.

[228] A. D. Martin, W. J. Stirling, and R. S. Thorne, MRST partons generated in a fixed-flavour scheme, Phys. Lett. **B636**, 259 (2006), `hep-ph/0603143`.

[229] A. Sherstnev and R. S. Thorne, Parton Distributions for LO Generators, Eur. Phys. J. **C55**, 553 (2008), `arXiv:0711.2473`.

[230] CERN Report No. ATL-PHYS-PUB-2011-008, 2011 (unpublished).

[231] P. M. Nadolsky *et al.*, ImpliFBcations of CTEQ global analysis for collider observables, Phys. Rev. **D78**, 013004 (2008), `arXiv:0802.0007`.

[232] J. C. Collins and D. E. Soper, Angular Distribution of Dileptons in High-Energy Hadron Collisions, Phys.Rev. **D16**, 2219 (1977).

[233] ATLAS, CERN Report No. ATL-PHYS-PUB-2009-037. ATL-COM-PHYS-2009-099, 2009 (unpublished), CSC note.

[234] H. Yin, Measurement of the Forward-Backward Charge Asymmetry(A_{FB}) using $p\bar{p} \to Z/\gamma^* \to e^+e^-$ events in $\sqrt{s} = 1.96$ TeV, (2010), Ph.D. Thesis (advisor: Liang Han).

[235] H.-L. Lai *et al.*, New parton distributions for collider physics, Phys. Rev. **D82**, 074024 (2010), arXiv:1007.2241.

[236] S. Alioli, P. Nason, C. Oleari, and E. Re, A general framework for implementing NLO calculations in shower Monte Carlo programs: the POWHEG BOX, JHEP **06**, 043 (2010), arXiv:1002.2581.

[237] G. F. Veramendi, A measurement of forward-backward charge asymmetry of electron-positron pairs in proton-antiproton collision at 1.8 TeV, (2003), Ph.D.Thesis (Advisor: Young-kee Kim).

[238] S. Ask, Simulation of Z plus Graviton/Unparticle Production at the LHC, Eur.Phys.J. **C60**, 509 (2009), arXiv:0809.4750.

[239] S. Ask *et al.*, Real Emission and Virtual Exchange of Gravitons and Unparticles in Pythia8, Comput.Phys.Commun. **181**, 1593 (2010), arXiv:0912.4233.

[240] J. Hewett and T. Rizzo, Collider Signals of Gravitational Fixed Points, JHEP **0712**, 009 (2007), arXiv:0707.3182.

[241] H. Georgi, Unparticle physics, Phys.Rev.Lett. **98**, 221601 (2007), hep-ph/0703260.

[242] H. Georgi, Another odd thing about unparticle physics, Phys.Lett. **B650**, 275 (2007), arXiv:0704.2457.

[243] A. Delgado, J. R. Espinosa, and M. Quiros, Unparticles Higgs Interplay, JHEP **0710**, 094 (2007), arXiv:0707.4309.

[244] T. Kikuchi and N. Okada, Unparticle Dark Matter, Phys.Lett. **B665**, 186 (2008), arXiv:0711.1506.

[245] S.-L. Chen, X.-G. He, X.-P. Hu, and Y. Liao, Thermal unparticles: A New form of energy density in the universe, Eur.Phys.J. **C60**, 317 (2009), arXiv:0710.5129.

[246] H. Georgi and Y. Kats, Unparticle self-interactions, JHEP **1002**, 065 (2010), arXiv:0904.1962.

[247] K. Cheung, W.-Y. Keung, and T.-C. Yuan, Collider Phenomenology of Unparticle Physics, Phys.Rev. **D76**, 055003 (2007), arXiv:0706.3155.

[248] M. Kumar, P. Mathews, V. Ravindran, and A. Tripathi, Unparticle physics in diphoton production at the CERN LHC, Phys.Rev. **D77**, 055013 (2008), arXiv:0709.2478.

Danksagung

Ich möchte mich an dieser Stelle bei allen Personen bedanken, die mich während meiner Doktorarbeit begleitet und unterstützt haben. Besonderer Dank gilt dabei folgenden Personen:

- Bei Prof. Dr. Johannes Haller bedanke ich mich für die Betreuung (insbesondere für die zahlreichen Diskussionen) und die Unterstützung während meiner Doktorarbeit.
- Prof. Dr. Joachim Mnich für die Übernahme des Zweitgutachtens der Dissertation.
- Prof. Dr. Peter Schleper für die Übernahme des Zweitgutachtens der Disputation.
- Der Gfitter Gruppe danke ich für die gute Zusammenarbeit. Insbesondere möchte ich mich bei Andreas Höcker für die vielen anregenden Gespräche bedanken.
- Concerning electron reconstruction and identification as well as questions to the ATLAS trigger system I thank: Takanori Kono, Karsten Köneke, and Mohamed Aharrouche.
- Für die lockere und angenehme Arbeitsatmosphäre bedanke ich mich bei meiner Arbeitsgruppe (speziell bei Martin Wildt, Mark Terwort, Dörthe Ludwig, Dennis Petschull, Tiago Perez). Außerdem bei allen Korrekturlesern und den Zuhörern des Disputations-Probevortrages.
- Meiner Freundin Kristin danke ich, dass sie immer mitgefiebert hat und dass sie eine super Korrekturleserin war. Freue mich sehr auf unsere zukünftige gemeinsame Zeit. ☺
- Zum Schluss bedanke ich mich bei meiner Familie (insbesondere meinen Eltern) dafür, dass sie immer für mich da ist.

Vielen Dank!